

DELFT UNIVERSITY OF TECHNOLOGY
FUGRO GEOSERVICES B.V.
DELTARES

Influence of Multiple Thin Soft Layers on the Cone Resistance in Intermediate Soils

DEVELOPMENT OF A CORRECTION FACTOR FROM NUMERICAL AND
PHYSICAL MODELS

M.SC. THESIS

by

T.I. VAN DER LINDEN

February 2016



Influence of Multiple Thin Soft Layers on the Cone Resistance in Intermediate Soils

Development of a correction factor from numerical and physical models

by

T.I. van der Linden

to obtain the degree of Master of Science at Delft University of Technology

Student number: 1504584

Committee: Prof.dr. M.A. Hicks
Dr. A. Askarinejad
Ir. F.J.M. Hoefsloot
Ir. D.A. de Lange
Dr. F. Pisanò



Administrative data

Student

T.I. (Toon) van der Linden
Nieuwe Langendijk 59b
2611 VJ Delft, NL
toonvdl@gmail.com
+31 6 1751 0131

Graduation committee

Prof.dr. M.A. (Michael) Hicks - Chairman
Delft University of Technology
Faculty of Civil Engineering and Geosciences, Room 00.060
M.A.Hicks@tudelft.nl
+31 15 27 87433

Dr. A. (Amin) Askarinejad - Supervisor Geo-Engineering section
Delft University of Technology
Faculty of Civil Engineering and Geosciences, Room 00.510
A.Askarinejad@tudelft.nl
+31 15 27 83326

Ir. F.J.M. (Flip) Hoefsloot - Daily supervisor Fugro
Principal Consultant, Fugro GeoServices B.V.
F.Hoefsloot@fugro.com
+31 70 311 1314

Ir. D.A. (Dirk) de Lange - Daily supervisor Deltares
Jr. Researcher/Consultant, Deltares
Dirk.deLange@deltares.nl
+31 88 335 7288

Dr. F. (Federico) Pisanò - Supervisor Offshore Engineering section
Delft University of Technology
Faculty of Civil Engineering and Geosciences, Rooms 00.500 and 2.82
F.Pisano@tudelft.nl
+31 15 27 88030

Addresses

Delft University of Technology Faculty of Civil Eng. and Geosciences Section Geo-Engineering	Fugro GeoServices B.V. Geotechnical Division	Deltares Unit Geo-engineering
Stevinweg 1 Postbus 5048 2600 GA Delft, NL citg.tudelft.nl	Veurse Achterweg 10 Postbus 63 2260 AB Leidschendam, NL www.fugro.com	Boussinesqweg 1 Postbus 177 2600 MH Delft, NL www.deltares.nl

Abbreviations

CPT	Cone Penetration Test
CRR	Cyclic Resistance Ratio
CSR	Cyclic Stress Ratio
EERI	Earthquake Engineering Research Institute
FC	Fines Content
FE	Finite Element
GEF	Geotechnical Exchange Format
M_L	Richter local magnitude
M_w	Moment magnitude
MSF	Magnitude Scaling Factor
NAP	Reference height used for altitude measurements in The Netherlands
NEN-EN	European standard accepted to be a Dutch standard
NPR	Nederlandse Praktijkrichtlijn, Dutch guideline
PGA	Peak Ground Acceleration [m/s ²]
SPT	Standard Penetration Test
WC	Water content

Symbols

C_N	Correction factor for the local stress level [-]
D_{cell}	Cell radius [mm]
D_{eq}	Equivalent pile diameter [m]
G	Elastic shear modulus [MPa]
H	Absolute layer thickness [mm]
H_{ratio}	Ratio between differences in layer thickness [-]
K_0	Neutral earth pressure coefficient [-]
K_H	Thin layer correction factor [-]
K_α	Correction factor for static shear stress [-]
K_σ	Correction factor for isotropic stress state [-]
Q	Normalised cone resistance [-]
$Q_{char,clay}$	Normalised characteristic cone resistance for clay [-]
$Q_{char,ratio}$	Ratio of normalised characteristic cone resistances for sand and clay [-]

$Q_{char,sand}$	Normalised characteristic cone resistance for sand [-]
$R_{d,e}$	Relative density based on void ratio [-]
$R_{d,n}$	Relative density based on porosity [-]
S_u	Undrained shear strength [kPa]
Δq_{c1N}	Adjustment in the cone resistance for the fines content [MPa]
α_p	Pile class factor [-]
β	Pile tip shape factor [-]
δ	Vertical displacement at the centre of a loaded region [mm]
η	Dimensionless penetration resistance [-]
γ_L	Factor of safety against liquefaction [-]
μ	Mean of a series of values [var.]
ν	Poisson's ratio [-]
ψ	Dilatancy angle [°]
σ	Standard deviation of a series of values [var.]
σ'_v	Effective vertical stress at the moment of testing [kPa]
σ'_{v0}	Initial effective vertical stress [kPa]
σ_v	Total vertical stress [kPa]
φ	Angle of internal friction [°]
a	Cone area ratio [-]
a	Cone radius [mm]
d_{cone}	Cone diameter [mm]
e	Void ratio = $V_{voids}/V_{solids} = \frac{n}{1-n}$ [-]
e_{max}	Maximum void ratio [-]
e_{min}	Minimum void ratio [-]
f_s	Measured sleeve friction [MPa]
g	Gravitational acceleration [m/s ²]
h_c	Critical depth [mm]
n	Porosity = $V_{voids}/V_{total} = \frac{e}{1+e}$ [-]
n_{max}	Maximum porosity [-]
n_{min}	Minimum porosity [-]
p_0	Uniform stress over a disc-shaped region [MPa]
p_a	Atmospheric pressure, $p_a = 0.1$ MPa

q_c^*	Equivalent thick layer cone resistance or characteristic cone resistance [MPa]
$q_{b,max}$	Maximum pile tip resistance [MPa], with maximum value of 15 MPa
$q_{c,I,gem}$	Mean value of cone resistances over trajectory I [MPa]
$q_{c,II,gem}$	Mean value of cone resistances over trajectory II [MPa]
$q_{c,III,gem}$	Mean value of cone resistances over trajectory III [MPa]
q_{c1Ncs}	Equivalent characteristic cone resistance [MPa]
q_{c1N}	Normalised cone resistance [MPa]
q_{cA}	Thin layer cone resistance [MPa]
q_{cB}	Thick layer cone resistance [MPa]
$q_{char,sand}$	Characteristic cone resistance for sand [MPa]
q_c	Measured cone resistance [MPa]
q_t	Corrected total cone resistance [MPa]
r_d	Shear stress reduction factor [-]
s	Factor which accounts for the cross-sectional shape of the pile tip [-]
t_{sus}	Number of standard deviations by which x_{sus} differs from μ [-]
u_2	Pore pressure acting behind the cone [MPa]

Acknowledgements

First and foremost I would like to thank the members of the graduation committee for their support and knowledge provided during the project. Although not officially part of the committee I would like to thank Ruud Stoevelaar as well, whose enthusiasm was very motivating

In order to achieve the quality of the soil samples obtained during testing, the input, help, experience and eye for details of Ferry Schenkeveld proved to be crucial. He taught me that sample preparation is an art in itself, something that not many people are capable of doing. I am pleased that I have had him as teacher in physical modelling. During the long hours in the *Geohal* of Deltares conversations with him (and often monologues) were pleasant distractions of the work that was needed to be done. I would also like to express my gratitude to Rob Zwaan and the people of the *Geohal* and workshop for the help provided during testing, who showed that (almost) nothing is impossible.

Proper data can only be obtained with well working measuring equipment, so I would like to thank Rob Greeve, Pieter Noordmans and the people of the Fugro equipment department for providing the testing equipment and their support and flexibility when problems occurred with the equipment during testing. Also the help and curiosity of Wim Nohl, Berry Schoenmaker and the people of the Fugro office in Leidschendam proved to be of great value in order to keep the project going.

And last but certainly not least I would like to thank my family and friends for their perpetual support.

Toon van der Linden
February 10, 2016

Preface

This document contains the final report of the graduation research on the influence of multiple thin soft layers on the cone resistance in intermediate soils. This thesis is the concluding project of the MSc track of Geo-Engineering at the faculty of Civil Engineering and Geosciences of Delft University of Technology. The project was supported by and has been conducted for a major part at Fugro GeoServices and Deltares.

The recent earthquakes in the province of Groningen in the northern part of The Netherlands provide a significant amount of new research opportunities, since there are still issues to solve with earthquakes and earthquake associated issues in Dutch (soil) conditions. Direct motivation for researching the influence of thin layers on the cone resistance, measured during a cone penetration test (CPT), is the potential occurrence of liquefaction in these layers caused by earthquakes.

In the main report theory is discussed, starting with an introduction to the problem and towards the end focussing on methods to model cone resistance in thin layers and result analysis. Besides the main report a lot of work done during this research is described in the appendices, especially when it comes to describing the physical modelling phase.

Abstract

In this thesis research is presented on the influence of multiple thin soft layers on the cone resistance and an attempt has been made to develop a correction factor from numerical and physical models. The presence of thin layers causes difficulties with determination of the liquefaction potential of sand deposits containing thin clay layers using cone penetration testing (CPT) data, including the cone resistance. Understanding the behaviour of the cone resistance in layered deposits and correcting the cone resistance is believed to help finding a solution.

In this research numerical models are presented to simulate the cone resistance in deposits with multiple layers. Using numerical models a range of correction factors is determined for different soil compositions, concluding that correction factors for the cone resistance depend mainly on the ratio of characteristic resistances of sand and clay. Physical modelling has been performed for validation of the numerical models and for correction factor determination. Layered samples were artificially built and tested using a cone, which besides measuring cone resistance also contained a friction sleeve and an u_2 pore pressure transducer. Cross-sections have been made of tested samples to obtain an indication of the penetration process. Since a limited amount of test results were obtained complete validation was not possible in this research, although the available test results could considerably well be simulated using the numerical models. Feasibility of performing tests on layered samples and obtaining results has been demonstrated.

Samenvatting

In deze afstudeerthesis is onderzoek gedaan naar de invloed op de conusweerstand van meerdere dunne, zachte lagen en is er een poging gedaan om correctiefactoren te bepalen aan de hand van numerieke en fysische modellen. De aanwezigheid van dunne lagen leidt tot problemen bij het bepalen van de verwekingsgevoeligheid van kleilaag-bevattende zandafzettingen. Hierbij wordt gebruik gemaakt van sondeerdata, waaronder de conusweerstand. Het begrijpen van het gedrag van de conusweerstand in gelaagde afzettingen en het corrigeren van de conusweerstand worden beschouwd als hulpmiddelen om tot een oplossing te komen.

In dit onderzoek worden numerieke modellen gebruikt om de conusweerstand te simuleren in gelaagde grond met meerdere opeenvolgende dunne lagen. Aan de hand van de numerieke modellen is een reeks aan correctiefactoren bepaald voor verschillende grondsamenstellingen, waaruit volgt dat correctiefactoren ten behoeve van de conusweerstand voornamelijk afhankelijk zijn van de verhouding tussen karakteristieke weerstanden van zand en klei. Fysische modellen zijn beproefd ter validatie van de numerieke modellen en ten behoeve van correctiefactorbepaling. Gelaagde monsters, kunstmatig opgebouwd, zijn beproefd met een conus die naast het meten van de conusweerstand in staat was om mantelwrijving en waterdruk (u_2) te registreren. Doorsnedes van beproefde monsters zijn gemaakt om een indicatie te krijgen van het penetratieproces. Aangezien een beperkt aantal proefresultaten verkregen zijn, is volledige validatie van de numerieke modellen niet mogelijk in dit onderzoek, hoewel de beschikbare testresultaten op redelijke wijze gesimuleerd konden worden met behulp van de numerieke modellen. De haalbaarheid van het samenstellen en beproeven van gelaagde monsters en het verkrijgen van resultaten uit deze proeven is aangetoond in dit onderzoek.

Contents

Abbreviations	vii
Symbols	vii
Acknowledgements	viii
Preface	ix
Abstract	x
Samenvatting	xi
1 Introduction	1
1.1 Background	1
1.1.1 Flaser bedding	2
1.1.2 CPT and evaluating liquefaction potential	2
1.2 Research	3
1.2.1 Questions	3
1.2.2 Objectives and approach	4
1.2.3 Boundaries and limitations	4
1.2.4 Reading this report	4
2 Cone penetration testing and layered subsoil	6
2.1 Cone penetration testing	6
2.2 Penetration mechanism	9
2.2.1 Mechanisms in clay and sand	9
2.2.2 Critical depth	13
2.2.3 Soi state	14
2.3 Thin layer descriptions and corrections	15
2.4 Available research on physical modelling	16
3 Research implementation	19
3.1 Numerical analysis	19
3.1.1 Vreugdenhil et al. (1994) model	19
3.1.2 Koppejan method	25
3.1.3 Comparing the modelling methods	26
3.2 Physical modelling of thin layers	27
4 Results	29
4.1 Test results	29
4.2 Normalisation	30
4.3 Test results versus models	32
4.4 Correcting the cone resistance	35
4.4.1 Correcting 8 cm layering	35
4.4.2 Correcting 2 cm layering	37
4.4.3 Correction factors from simulations	38
4.4.4 Determination of a relationship	41
4.5 Correcting field data	42
5 Remarks	46

6	Conclusions and recommendations	47
6.1	Conclusions	47
6.1.1	Research question and objective	47
6.1.2	General conclusions	47
6.1.3	Conclusions on physical modelling	48
6.2	Recommendations	48
6.2.1	General recommendations	48
6.2.2	Recommendations on physical modelling	49
	References	52
	Bibliography	55
	Appendices	
A	CPT based liquefaction evaluation	A-1
B	Classifying soil using the Robertson et al. (1986) method	B-1
C	Borehole logs and description	C-1
D	Method of Vreugdenhil et al. (1994)	D-1
E	Method of Koppejan	E-1
F	Numerical scenarios	F-1
G	Factual testing report	G-1
H	Data management	H-1
I	Full page figures	I-1

1 Introduction

1.1 Background

In 1959 natural gas was discovered near Slochteren in the province of Groningen, The Netherlands by the Nederlandse Aardolie Maatschappij (NAM), and thus in 1963 exploitation of the 2800 billion m³ gas field started (NAM (2015)). Since then 2073 billion m³ of gas has been extracted (by the end of 2013), which has caused a significant decrease in pressure in the reservoir over the years at a mean depth of 3 km beneath ground level (NAM (2013)).

Because of this pressure release by gas exploitation, redistribution of stresses causes movements mostly along already existing cracks and faults. These movements cause earthquakes, and since they are considered to be a result of human activities they are called ‘induced’ earthquakes. On December 5, 1991 the first earthquake recognised to be induced was measured in Groningen, although it is believed that the earthquakes measured in the area since 1986 can be classified as induced earthquakes. Since then the number of earthquakes as well as the earthquake magnitude have increased, illustrated in figure 1.1. Soil subsidence in the area is also considered to be caused by exploitation activities. Figure 1.1 also displays the contour line of the area which has subsided at least 18 cm, which surrounds the area in which most earthquakes are measured. As of today, the earthquake with largest magnitude had a moment magnitude (M_w) of 3.6 (Dost and Kraaijpoel (2013)) recorded near Huizinge, and it is believed that the maximum magnitude will increase in the future (NAM (2013)).

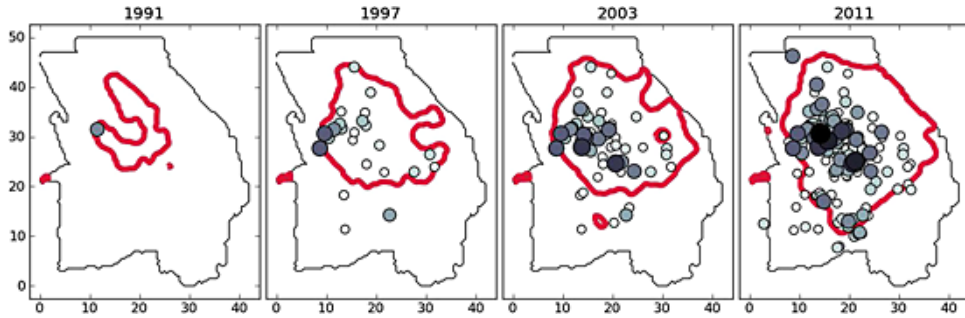


Figure 1.1: Observed earthquakes with $M_L \geq 1.5$ on the map of the gas field, together with the 0.18 m compaction contour for several years, after NAM (2013). Size and colour of the dots indicate the earthquake magnitudes.

Earthquakes cause different types of waves reaching the upper layers near ground level. Besides having effect on structures at ground level, these waves also affect soil behaviour and soil-structure interaction. One of the phenomena that may occur during earthquakes is liquefaction of loosely packed, (partly) saturated (sand) layers, during which the soil loses its strength and stiffness due to excess pore pressure taking over effective soil stresses. This type of soil behaviour has been recorded during larger tectonic earthquakes, e.g. the 1964 Alaska and Niigata earthquakes and more recently during the 2011 Christchurch and Tohoku earthquakes. Although the earthquakes in Groningen are not expected to reach magnitudes like the earthquakes mentioned before, ground accelerations, which are considered to be leading when looking at soil and structure behaviour during earthquakes, may reach considerable levels. Soil conditions in Groningen can be characterized as Holocene clay, peat and sand deposits on top of Pleistocene sand deposits (Beranek (1987)), thus it is believed that the soil may be susceptible to liquefaction (especially in the loose sand layer) as a result of induced earthquakes.

Until the more regular appearance of earthquakes, Dutch standards did not take seismic loads into account because it was believed that the existing standard provided a sufficient level of structural safety, also for earthquakes already occurring in The Netherlands. Because the lack

of experience with induced earthquakes and the fact that most of the buildings in the northern part of The Netherlands are built using unreinforced brickworks, a guideline for designing and reviewing earthquake resistance of existing and already built buildings has been published in December 2015: the ‘Nederlandse Praktijkrichtlijn 9998’ (NPR 9998) by the Nederlands Normalisatie-instituut (2015). This guideline can be used for designing structures in earthquake-prone areas in northern parts of the Netherlands.

1.1.1 Flaser bedding

One particular feature of the sand deposits in Groningen (known in Dutch as ‘wadzand’) is that they contain thin layers of clay/silt material, known as ‘flaser beds’. An example of this type of sand deposit can be found in figure 1.2.



Figure 1.2: Detail from a borehole log containing flaser bedding deposits

These layers can be characterized as fine sand with quasi regular sequences of 10 - 300 mm of vertical distance with small (10 - 20 cm width) and thin (3 - 15 mm thick) clay/silt bands with fine sand (from personal communication). Because of their small size it is hard to give an accurate estimation of their true properties from CPT data and to classify these layers, thus their influence on the liquefaction potential of the sand layer is uncertain. Therefore it is interesting to look at the influence of these multiple thin layers on the cone resistance, and to provide a way to correct the original data to ‘clean soil’ data (in this report referred to as characteristic data) for calculation purposes. One of the calculations using CPT data is the evaluation of the liquefaction potential of soil layers.

1.1.2 CPT and evaluating liquefaction potential

In the NPR a method is presented to determine the factor of safety against liquefaction based on data from cone penetration tests (CPTs), derived from the method presented by Idriss and Boulanger (2008). The method is more extensively described in appendix A. This method also uses CPT data as input, but the CPT data measured in flaser bedding deposits and other deposits containing thin layers may not give a good reflection of the true properties of the thin sand and clay layers due to their size.

Some of the factors used in the NPR depend directly on the cone resistance and some on the total and effective stresses, determined from CPT data by soil classification.

Especially in thin sand layers the cone resistance reaches significantly lower values than their characteristic cone resistances would be corresponding to the density of the sand. This causes determination of lower resistances to cyclic stresses and thus lower factors of safety, while higher resistances would better represent the true situation.

Classification can be performed with a method proposed by Robertson, Campanella, et al. (1986), in which soil is classified looking at cone resistance and friction ratio. The method proposed by Robertson, Campanella, et al. (1986) is described in appendix B. Depending on these two characteristics, the layer is assigned to one of the 12 zones which each represent a different soil type with associated unit weight. Since there are no ‘transition’ zones between the zones and the difference in soil properties between two neighbouring zones can be significant, a small error in CPT data can cause incorrect classification with big difference in unit weight and thus a larger error in soil stress determination. In the paper of Robertson and Fear (1995) a definition of the same problem considering classification is well defined:

“Thin sand layers embedded in soft clay deposits are often incorrectly classified as silty sands based on the CPT soil behaviour type charts. Hence, a slightly improved classification can be achieved if the cone resistance is first corrected for layer thickness before applying the classification charts”.

It can be concluded that the cone resistance is an essential parameter in the liquefaction evaluation and that it is important to have an accurate estimation of the cone resistance compared to the actual subsoil conditions.

To be able to improve interpretation of CPT data and use this interpretation for better input for evaluation of the liquefaction potential is something worth researching. Correcting the cone resistance for the thin layers to come to characteristic cone resistances for the type of bedding considered could be a way of improving CPT data interpretation. Therefore the main topic of this thesis can be described as investigating the "influence of thin soft layers on the cone resistance in intermediate sand layers".

1.2 Research

In this section the research questions, objectives and steps as well as the boundaries and limitations are discussed. At the end a guideline of how to read this report can be found.

1.2.1 Questions

The main research question "What is the influence of multiple thin soft layers on the cone resistance of the intermediate sand layers and in which way can the CPT data be corrected for thin layers?" can be answered by answering the following sub-questions:

- In what way do thin layers influence the cone resistance, looking at both the cone resistance and the classification process which is used for the determination of soil stresses (which are used in the liquefaction evaluation)?
- Can a correction also be derived from theory, e.g. from Vreugdenhil et al. (1994)?
- Can the thin layer correction proposed by Robertson and Fear (1995) also be used for the situation in Groningen?
- Are other models available for simulating the cone resistance?
- Is there a convenient method of conducting physical tests for validation of the models described?

1.2.2 Objectives and approach

The aim of this research is see whether it is possible to design an experiment in a convenient and effective way in terms of time and means, which would be used for validation of calculation models. The main objectives of the research are:

- Learning about existing theories on cone resistance in multiple thin layers;
- Being able to define test setups and carry out tests using this/these setup(s);
- Deriving an expression from the test results for a correction in order to obtain a characteristic sand cone resistance from the measured cone resistance, and applying this correction on field data in a plausible way;
- Providing results that may be useful for calculations considering liquefaction potential of sands with multiple thin layers;

To reach the objectives and to be able to answer the research question(s) an idea of the differences in penetration mechanism in thin layers is formed and a look is taken into results of previous researches. In order to be able to correct the cone resistance different methods of simulating the cone resistance are selected and validated with physical test results. Correction factors resulting from test results and simulations are compared and an attempt is made to define a relationship for determination of a correction factor. Lastly it is attempted to correct CPT data from the field using results from this research.

1.2.3 Boundaries and limitations

The boundaries and limitations concerning this thesis project can be summarized as follows:

- Only the influence of thin layers with equal thicknesses for the soft and stiff layers were considered;
- Only shallow conditions between 0 and 1 m depth are considered;
- Only fully saturated conditions are considered;
- Soil samples used in laboratory tests were be artificially built (no samples from the field will be used for testing);
- Physical testing will be the main source for validation of considered numerical models;
- Testing will take place with penetration rates which in combination with sampling frequency give a sufficient level of detail over depth. This can mean that penetration rate is lowered is sampling frequency cannot be raised.

1.2.4 Reading this report

In the first part a short introduction is given on cone penetration testing, after which relevant research on the penetration mechanism occurring during cone penetration testing, description of thin layers and physical modelling of thin layers is discussed. Next the research implementation is discussed. First the numerical part in which the methods of simulating cone resistance in layered soils are presented after which a brief overview of the physical modelling part is discussed. In the third part the results are discussed and an attempt is made to present a correction method for correcting the cone resistance for thin layers, and a connection with field data is made. The last part is reserved for remarks, conclusions and recommendations in which also feedback will be given on the research questions stated in this section.

Right behind the main report are the relevant appendices located to which multiple references are made in the main report. Most appendices are merely an addition to the report, except perhaps for appendix G. This appendix contains the factual testing report, and has the actual contents of a separate report. For understanding how the tests were performed it is necessary

to go through this appendix as well, since it contains important information. It was considered to be too much for the main report, so the main report does not go deep into the testing phase, only the results are extensively discussed.

2 Cone penetration testing and layered subsoil

This chapter gives an overview of the penetration mechanism in layered soils and researches on penetration through layered soils, both theoretical and physical.

2.1 Cone penetration testing

A common method of conducting soil investigation in regions with soft soil deposits is the cone penetration test (CPT). During cone penetration testing a cone penetrometer is pushed into the soil. During pushing several types of resistances and pressures can be measured. Every type of soil has characteristic values for the resistances that can be measured, therefore the interpretation CPT data can give a fairly good indication of soil properties. This type of soil investigation is widely used in The Netherlands and a considerable amount of parameters for foundation engineering purposes are derived from CPT data.

According to Lunne et al. (1997) during a CPT "*a cone on the end of a series of rods is pushed into the ground at a constant rate and continuous or intermittent measurements are made of the resistance to penetration of the cone*". The total force on the cone divided by the projected area of the cone gives the cone resistance q_c , and the total force acting on the friction sleeve divided by the surface area of the friction sleeve gives the sleeve friction f_s . A common extension in the use of the cone penetrometer is the use of pore pressure transducers for measuring the local pore pressure in the soil. When pore pressure transducers are installed on the cone penetrometer it is called a piezocone, but for convenience the piezocone is referred to as 'cone' in this report. In figure 2.1a the locations of the cone, friction sleeve and pore pressure filters on a simplification of a cone penetrometer can be found. Usually only one of the pore pressure transducers is added to the cone penetrometer, where u_1 is located in the cone, u_2 on the 'shoulder' of the penetrometer between the cone and friction sleeve and u_3 is located above the friction sleeve. Pore pressure measurements depend considerably on the locations of the pore pressure transducers. Figure 2.1b gives a detailed overview of the features of a piezocone, although penetrometers with other configurations are common as well.

Although cone penetrometers are available in different dimensions, a regular cone penetrometer used in the field has a cone area of 10 cm^2 , meaning a cone diameter of 35.7 mm, and a cone angle (apex) of 60° . For special purposes cones with a diameter between 25 mm and 50 mm may be used without the application of correction factors. The shape and dimensions of a normal cone according to Dutch standards can be found in figure 2.2. In this figure '1' stands for the minimal allowable cone shape after wearing effects, '2' for the maximum allowable cone shape, d_c represents the diameter of the cylindrical part of the penetrometer, h_c is the length of the cylindrical part of the cone and h_e is the height of the conical part of the cone.

The measurements made by the sensors are transferred through a cable connected to the cone to a data-acquisitioning device, which also records depth measurements. Data-acquisition produces data which is conveniently manageable for processing and calculating purposes. An example of an CPT result (normally referred to as CPT) can be found in figure 2.3. Besides cone resistance, sleeve friction and pore pressures many more features of soil behaviour can be examined using other types of sensors and devices mounted on the cone, such as seismic properties, temperature and conductivity. However, these features are not considered in this thesis.

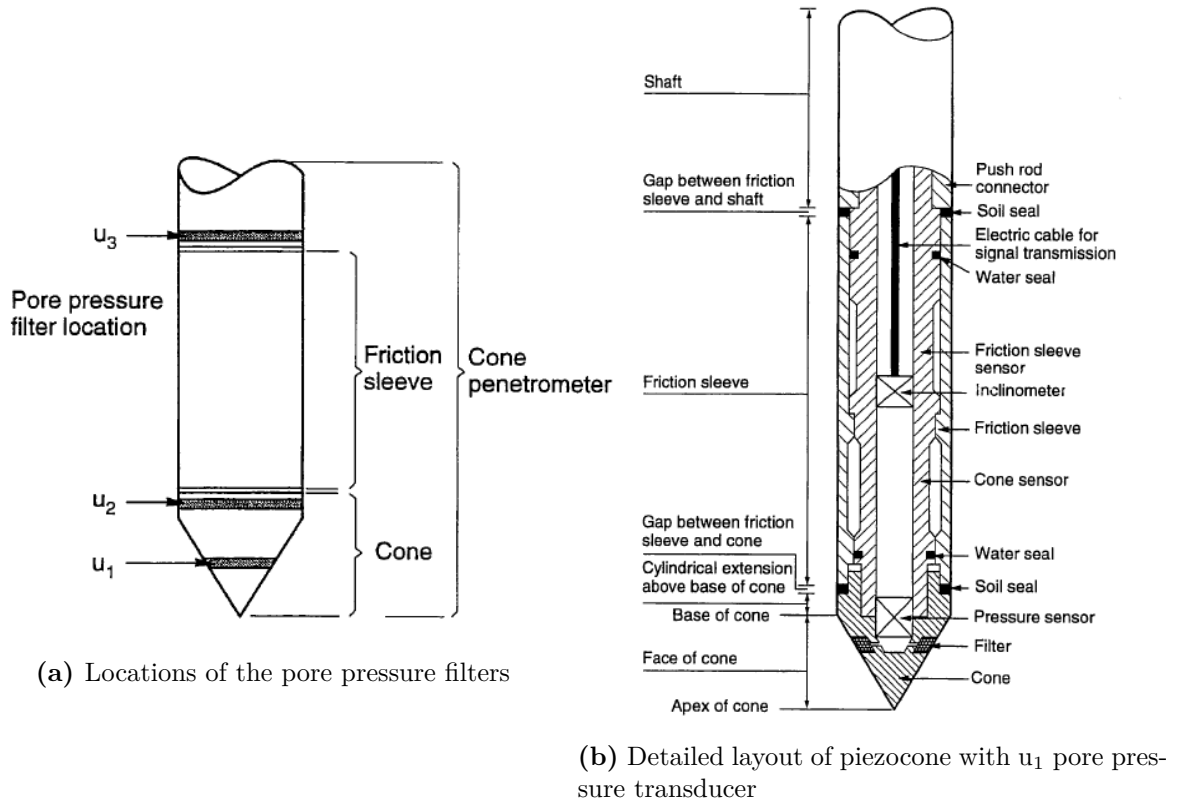


Figure 2.1: Overall layout of (piezo)cone penetrometers (figures after Lunne et al. (1997)).

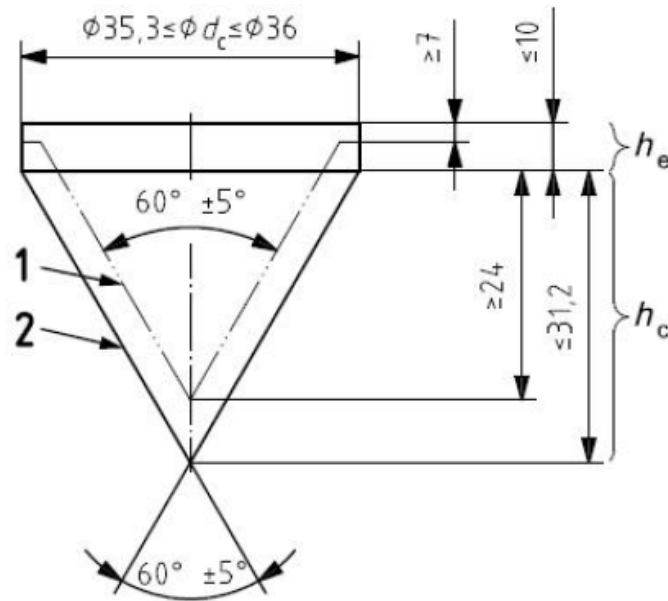


Figure 2.2: Dimensions and standards regarding tolerance for a 10 cm² cone (after Nederlands Normalisatie-instituut (2012)).

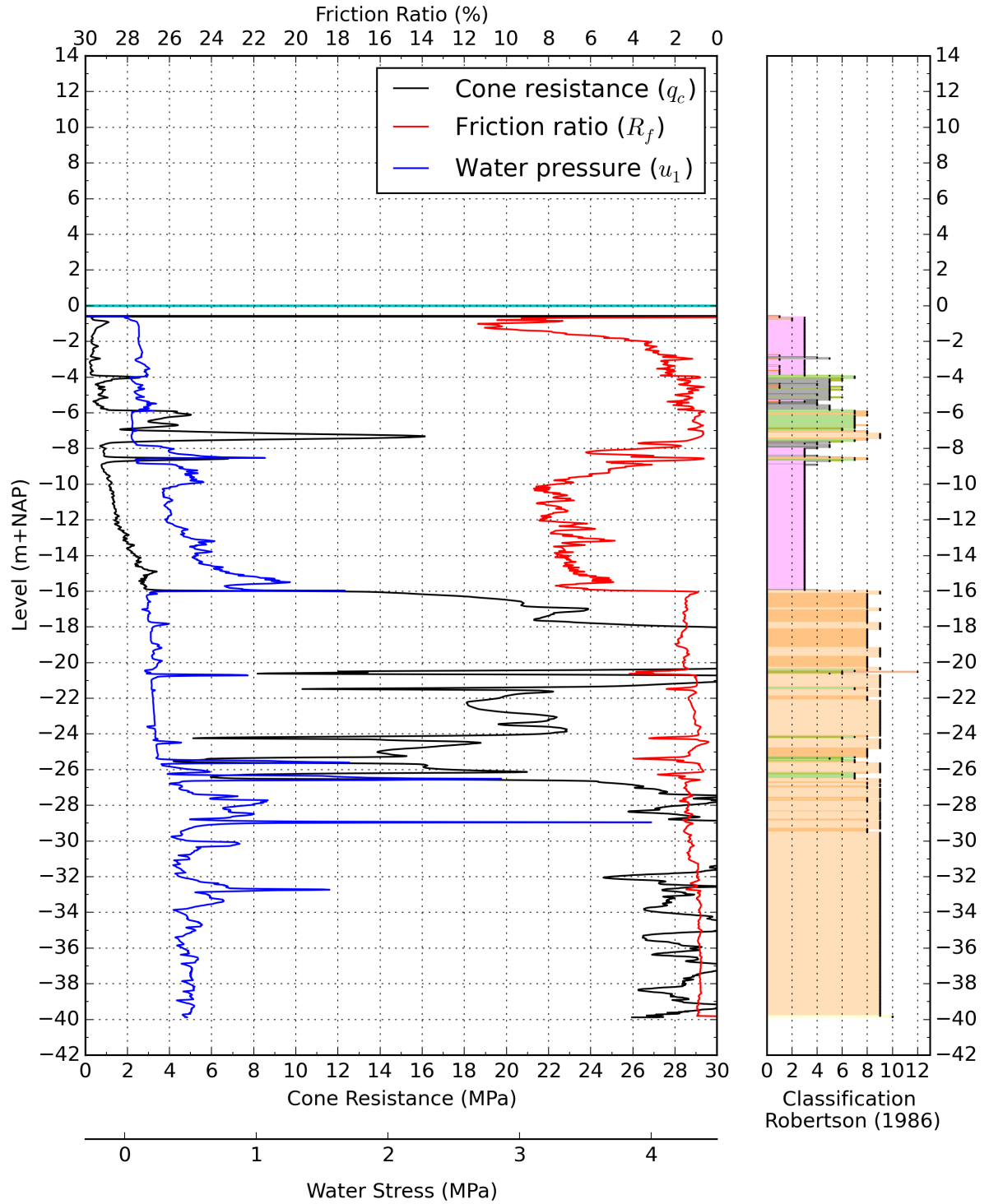


Figure 2.3: Example of data from CPT measurements

2.2 Penetration mechanism

Studying the mechanism occurring in soil during cone penetration can help to understand why the cone resistance develops in layered soils the way it does. The theory of Prandtl, which describes a solution for the problem of a strip load on a half plane, provides a basis for many theories of how a failure surface develops as a cone penetrates through the soil. The shapes of the failure surfaces presented in this section are all more or less derived from this theory, often adjusted by other authors.

2.2.1 Mechanisms in clay and sand

During penetration in soil large plastic strains are forming, but also elastically deformed regions can be distinguished. This is visualised by Muromachi (1981) based on experimental penetrations, shown in figure 2.4, where zone (3) is marked with dense vertical black lines.

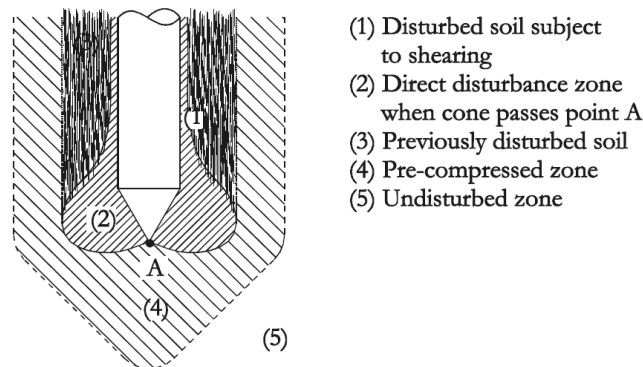


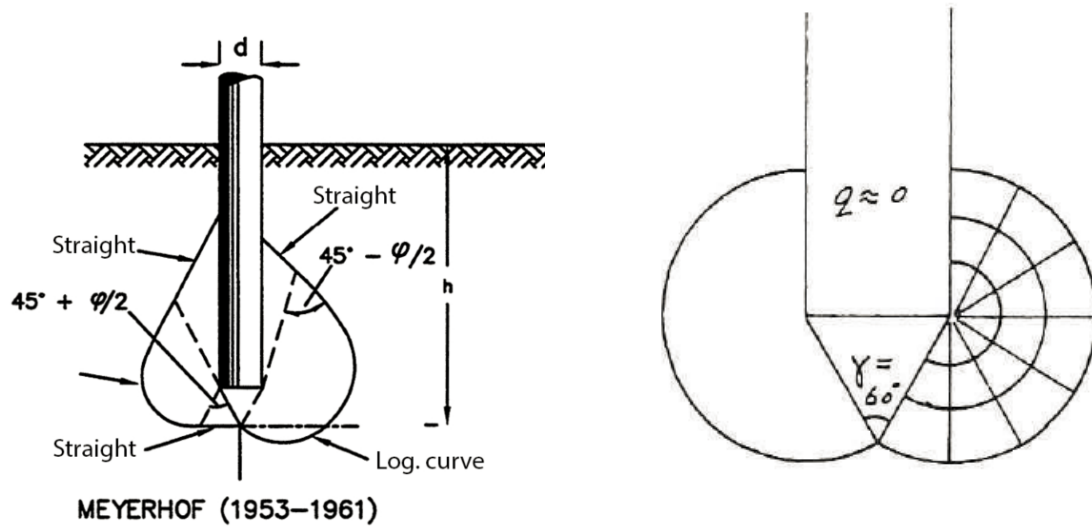
Figure 2.4: Zones of influence during cone penetration, after Silva and Bolton (2004), modified from Muromachi (1981)

The theory of Prandtl defines failure surfaces, in which stress state of the soil is assumed to be critical. This part of the soil takes a large contribution in the total tip resistance experienced by the pile or cone penetrometer. Understanding and defining the shape of these surfaces throughout the process of penetration through layered soil can help in understanding the behaviour of the measured cone resistance in such circumstances.

The shape of the failure surfaces depends on the strength and stiffness parameters of the soil and differs with different types of soil, displayed in figure 2.5. In sand logarithmic spirals with straight parts to the pile shaft are a typical feature due to its frictional properties, for clay the shape of the failure surface is rather circular and smaller compared to surfaces found in sand. The shape of the failure surface depends on the angle of internal friction φ . If φ is considered to be 0° the circular shape shown in figure 2.5b appears. Although φ is not 0° for clays and therefore the true shape of the failure surface is not perfectly circular, clay is less frictional than sand and to illustrate the difference in failure surface a circular shape is chosen for clay.

Arshad et al. (2014) have investigated the penetration mechanism of a cone using the digital image correlation (DIC) technique. With this technique soil displacements were monitored during the penetration process. Figure 2.6 shows the soil displacements for penetration at different levels in a sand with 85% relative density.

Figure 2.6a clearly shows failure shape formation according to Prandtl. As the cone progresses however, the vectors turn primarily vertically instead of radially, meaning that the sand is pushed downward and which could mean that particle crushing occurs. It can be concluded that the shape of the failure zone changes as stress level increases.



(a) Penetration through sand, after Lubking (1997) (b) Penetration through clay, after Smits (1977)

Figure 2.5: Failure surfaces and their typical shapes

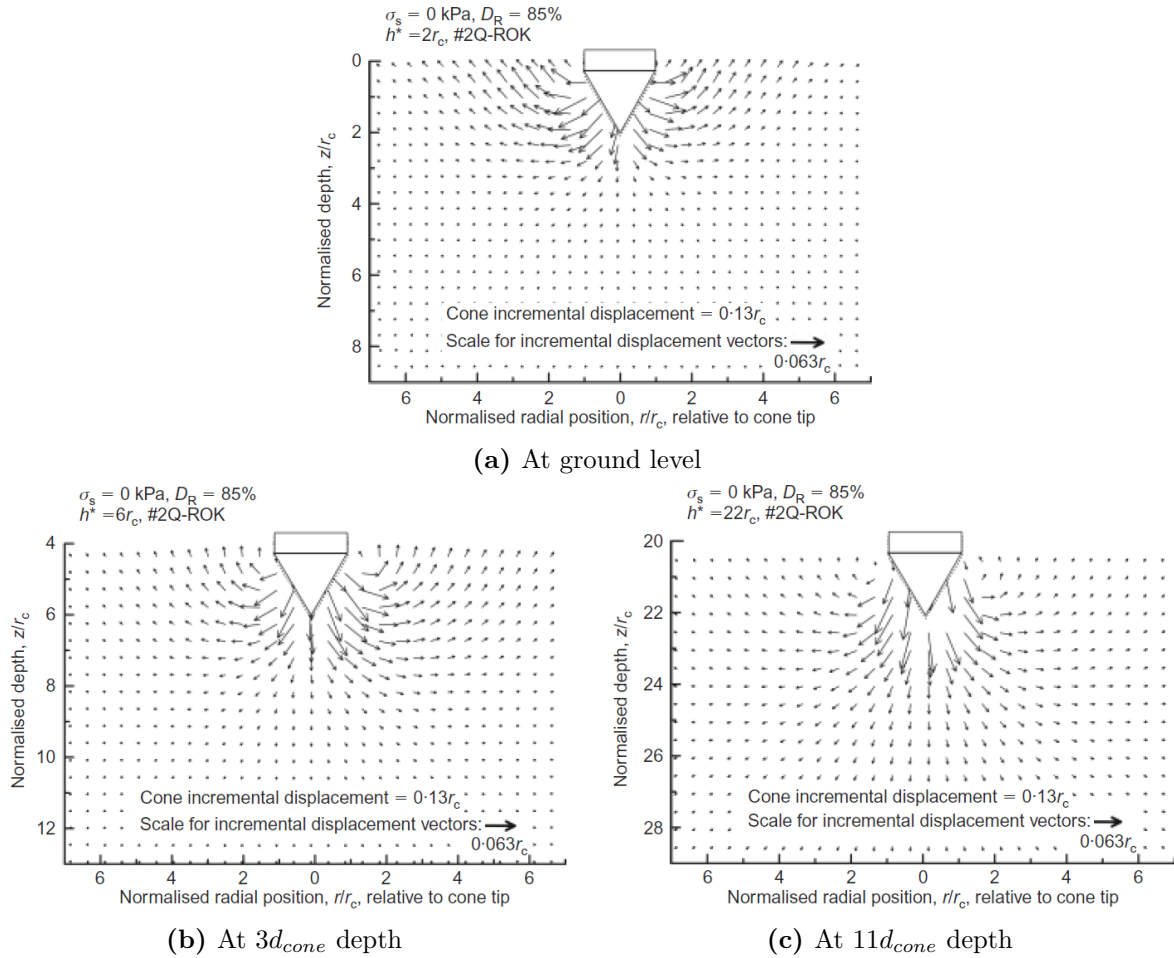


Figure 2.6: Soil displacements during penetration at different depths (r_c = cone radius), after Arshad et al. (2014)

Figures 2.7, 2.8 and 2.9 give an indication of how the failure surfaces may develop during the penetration process in different layering. These figures are not proven scientifically but merely an estimation based on the two separate shapes of the failure surfaces of sand and clay. During drawing of the shapes the cone area and stress level were not considered. However when comparing the figures with the results from Arshad et al. (2014) in figure 2.6, it can be concluded that figures 2.7, 2.8 and 2.9 are more valid for shallow penetration than for deep penetration.

When a penetrometer approaches a clay layer from a uniform sand layer, failure surfaces change in shape throughout the process. This is illustrated in figure 2.7. As the failure surface interferes with the layer boundary (fig. 2.7, stage 2; continuing in stage 3) it adapts below the interface the shape it would have in the clay layer. Above the layer interface (e.g. stage 3) the failure zone adapts the shape it has in sand again, but now the failure surface is smaller because the zone ‘starts’ in clay. This causes the failure zone above the layer interface to be smaller than it would be in uniform sand.

Drawing with the same method the failure surfaces for penetration through a three-layer system with a thin layer thickness $0.8d_{cone}$ shown in figure 2.8, the same pattern emerges as for the two-layered system until the cone tip reaches the bottom clay-sand interface (fig. 2.8, stage 3). Below this interface the cone tip experiences resistance from the sand layer again, but the clay layer causes the failure surface above the clay layer not to be able to develop as it would in uniform sand (stage 7). This could correspond to the fact that in the Dutch method of determining pile bearing capacity for the part of the soil up to $8D$ above the pile tip that contributes to the pile bearing capacity, the minimum encountered cone resistance is allowed to be used in calculations.

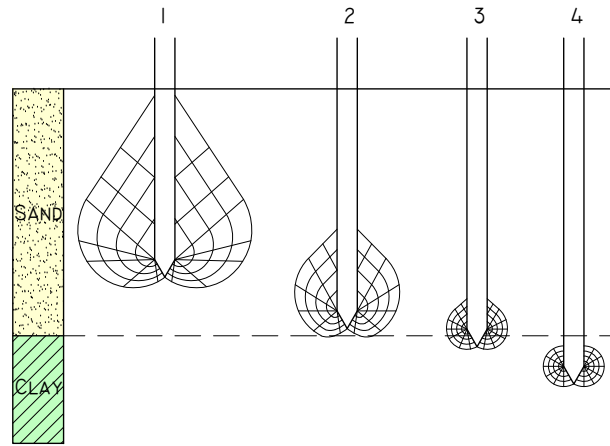


Figure 2.7: Indication of the development of failure surfaces in a 2-layer system during penetration

A comparable pattern can be drawn for a five-layer system with thin layer thickness $0.8 d_{cone}$, shown in figure 2.9. The main difference is that when the cone is completely in the layered part (stages 4 and 5 in fig. 2.9) the failure surface changes slightly between shapes characteristic to sand and clay.

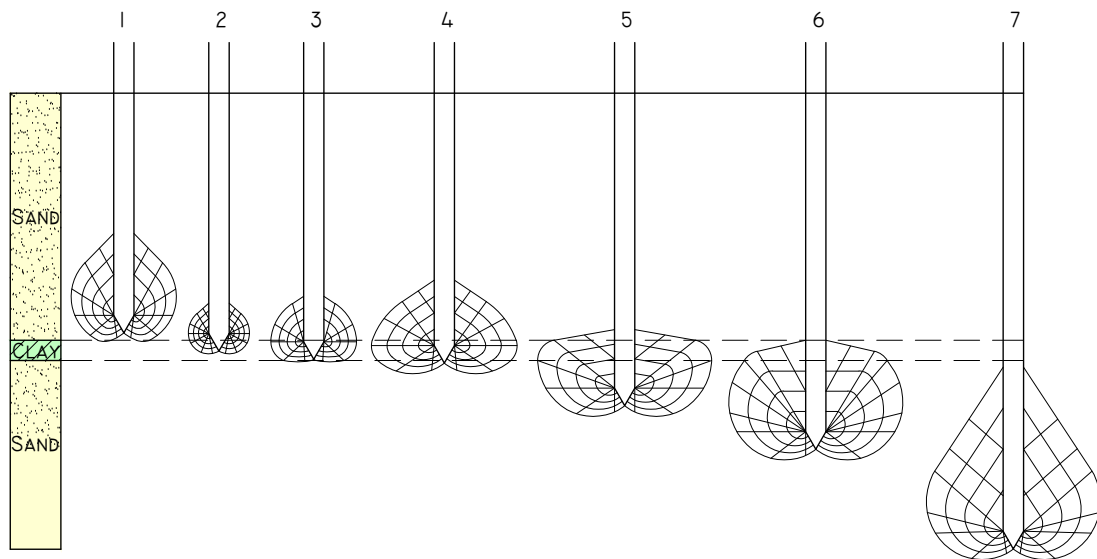


Figure 2.8: Indication of the development of failure surfaces in a 3-layer system during penetration

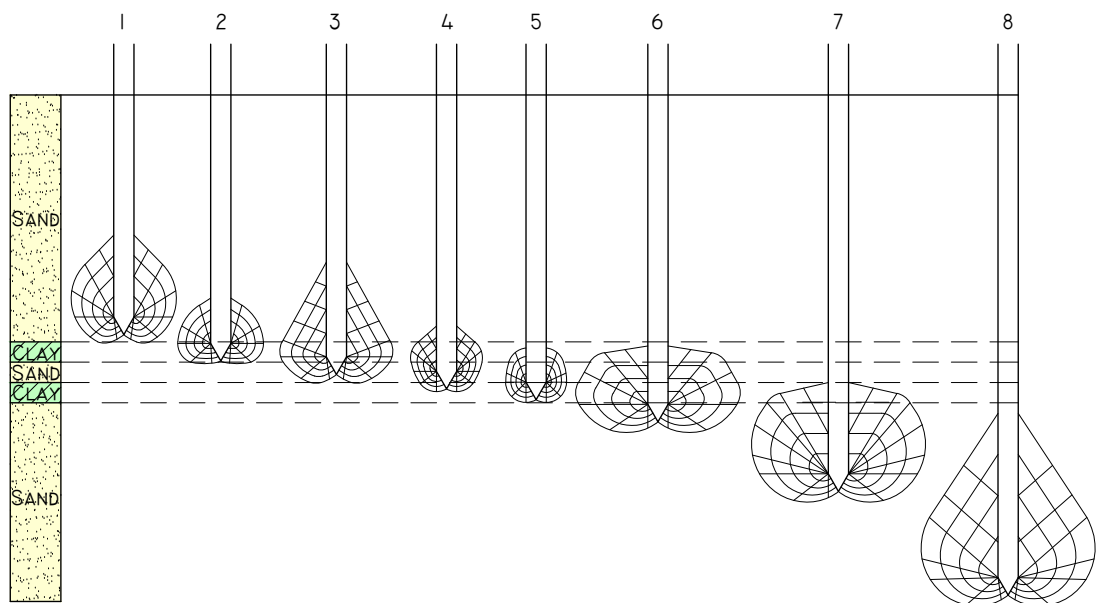


Figure 2.9: Indication of the development of failure surfaces in a 5-layer system during penetration

2.2.2 Critical depth

Looking at the figures in the previous section 2.2.1, it can be concluded that the cone will not encounter full penetration resistance characteristic for a soil layer when a layer of soil is entered, especially from ground level. From ground level the cone first requires a certain penetration before the failure surfaces around the cone penetrometer do not change any more and therefore before they reached their ultimate shape. The depth at which full penetration resistance is reached is called the critical depth. Figure 2.10 displays how this process takes place and how cone resistance and failure surfaces develop along the process. The critical depth is especially important to be considered when performing shallow CPTs, which was the case during the experiments described in appendix G. Several authors have described critical depth and formulated relationships to describe how large this depth is in certain situations, which are described below.

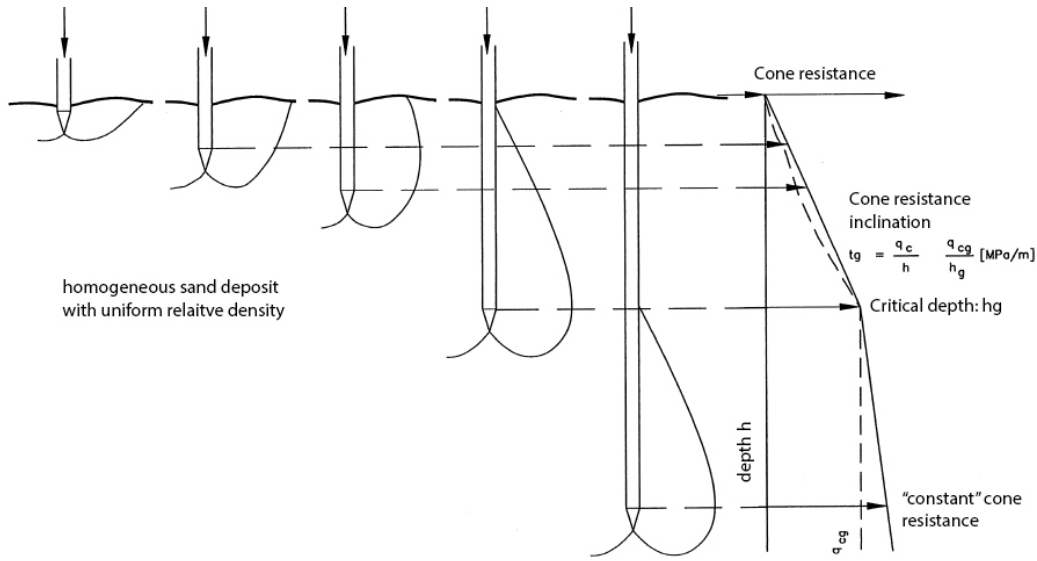


Figure 2.10: Development of the failure surface around a penetrating cone reaching below critical depth, after Lubking (1997)

According to Meyerhof (1952) for non compressible soils the relationship for critical depth can be defined from theory as

$$\frac{h_c}{d_{cone}} = \tan \left(45 + \frac{\varphi}{2} \right) \cdot e^{\pi \tan(\varphi)} \quad (2.1)$$

where h_c is the critical depth, d_{cone} the cone diameter and φ the angle of internal friction. Teferra (1975) conducted research on critical depth and derived empirical and theoretical relationships for critical depth. The empirical work of Teferra (1975) resulted in the following equation:

$$\frac{h_c}{d_{cone}} = (3.28 \pm 0.63) \cdot (10 \cdot q_c)^{0.407} \quad (2.2)$$

where q_c is the cone resistance when critical depth has been reached in MPa. Puech (1974) also related critical depth empirically to cone resistance:

$$\frac{h_c}{d} = \frac{25 \cdot (1 + 0.1q_c)}{\sqrt{d}} \quad (2.3)$$

where q_c is the cone resistance in MPa and d the cone diameter in cm. As there are different equations for critical depth, it is believed that the relationship that sets the critical depth at the lowest level (so which gives the largest depth) should be the governing relationship for sample design. An example of determining the level of critical depth during physical modelling can be found in section G.1.2 of appendix G.

2.2.3 Soi state

The magnitude of penetration resistance in sand depends mainly on the angle of internal friction φ , of which an increase can come from higher relative densities. A large φ implies a larger dilatancy angle ψ , which means that during shearing a higher volume increase occurs, causing higher penetration resistances. Not only does the volume increase, but also the area which is experiencing shear is larger. This causes the critical depth to be deeper for soils with higher relative densities and thus higher values of φ , illustrated in figure 2.11.

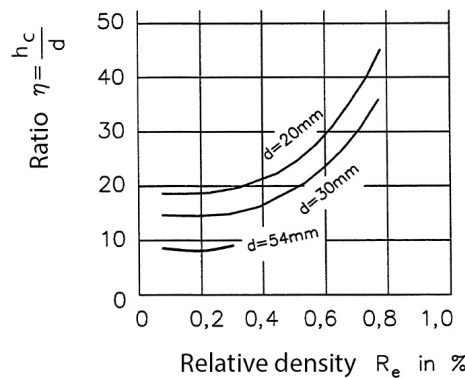


Figure 2.11: Relationship between critical depth and relative density, after Lubking (1997)

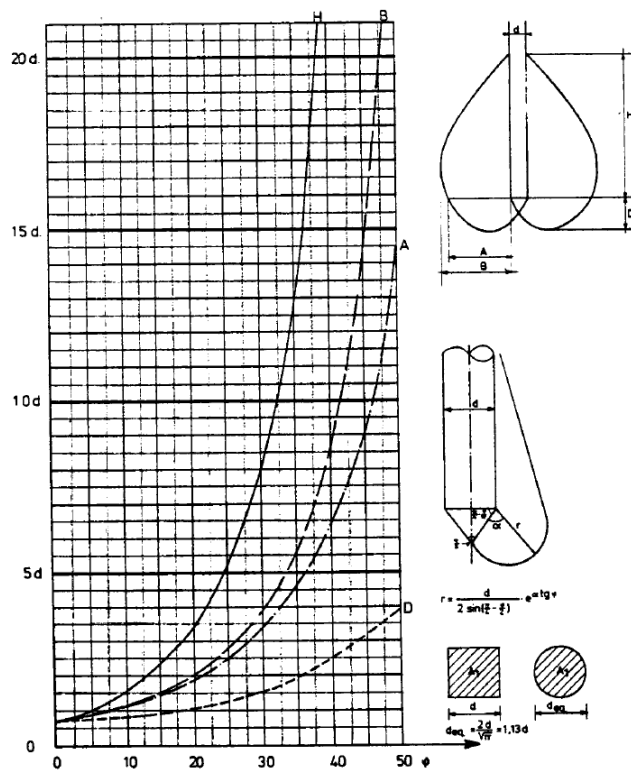


Figure 2.12: Shape sizes of the failure surfaces in sand for different angles of internal friction according to the theory of Prandtl, after Douwes Dekker (1984)

Besides the vertical distance of pile penetration, a higher angle of internal friction also causes a larger horizontal plane in which penetration causes failure surfaces, also due to higher values of ψ . This is characterised in figure 2.12.

From Houslsby and Hitchman (1989) it is concluded that the cone resistance in a calibration chamber is more influenced by horizontal effective stresses than by vertical effective stresses. Most experiments on artificially prepared samples are conducted in bounded environments. Taking into account that higher angles of internal friction cause larger areas in the soil affected by penetration, it can be concluded that if boundaries are too close to the penetration location and the soil is relatively dense the rigidity of the boundaries can have an effect on the penetration resistance due to horizontal stresses. When conducting physical tests the effect of the boundaries on measurements should be as small possible when research is focussed on soil properties instead of boundary effects. Considering the physical tests conducted for this research cell size effects are discussed in section G.1.3 of appendix G.

2.3 Thin layer descriptions and corrections

One of the first researches to give a relationship for describing penetration resistance in layered systems was Geuze (1961). Geuze (1961) described a way to extrapolate the resistance measured with a penetrometer of diameter b to the tip resistance of a pile of diameter B , displayed in figure 2.13.

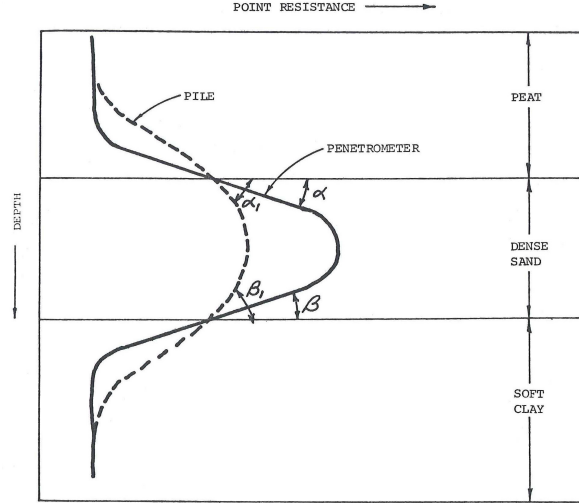


Figure 2.13: Penetration resistance of a three-layer system according to Geuze (1961) (after Treadwell (1976))

The relationship proposed by Geuze (1961):

$$\frac{\tan \alpha}{\tan \alpha_1} = \frac{\tan \beta}{\tan \beta_1} = \frac{b}{B} \quad (2.4)$$

where the angles are defined as displayed in figure 2.13. Although this relationship does not directly describe the penetration resistance in a layered system, it may help understanding the difference in measured cone resistance between different penetrometer sizes.

Vreugdenhil et al. (1994) provided an analytical method to describe cone resistance in thin layers based on a simplified linear elastic solution, which was used by Yue and Yin (1999) for developing their layered elastic model. Robertson and Fear (1995) used the method of Vreugdenhil et al. (1994) to produce a correction for thin layers for determination of an equivalent thick-layer cone resistance K_H , see figure 2.14. In this method q_{cB} equals the measured cone resistance of the surrounding layer, q_{cA} the measured cone resistance of the thin layer and q_c^* the equivalent thick layer (or characteristic) cone resistance of the thin layer, with $q_c^* = K_H \cdot q_{cA}$. According to Youd and Idriss (2001) this is valid for the situation in which a stiff layer is embedded between two soft layers. Whether this method gives a valid correction for the situation in Groningen, where the thin layers are considered to be soft compared to the sand, is something that is investigated in this research. Joer et al. (1996) provided equations to describe the solution of Vreugdenhil et al. (1994) for a certain number of layers, which was used in this research to model multiple layers described in section 3.1.1.

Besides the models presented above which are used in this research to describe the cone resistance other numerical studies to model the effect of layering on cone resistance were performed by Ahmadi and Robertson (2005), Xu and Lehane (2008) and Walker and Yu (2010). Because these studies either used specific (FE) programmes or involved only 2-layered systems, these studies are not elaborated here.

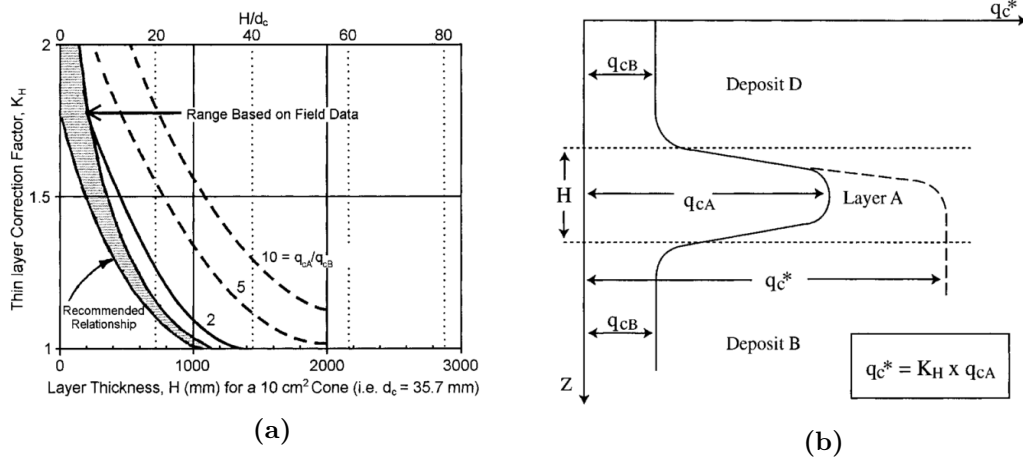


Figure 2.14: Determination of a thin-layer correction factor K_H (after Youd and Idriss (2001), modified from Robertson and Fear (1995).)

2.4 Available research on physical modelling

Some experiments have been carried out to investigate the effect of soil layering on CPT measurements. In most cases the test setup consisted of a two or three layer sample configuration.

Treadwell (1976) performed cone penetration tests on three-layer and five-layer samples, using Monterey No. 0 sand (fine sand). Variety between layers was achieved by differences in sand density, where loose sand was prepared with a relative density of 5% to 12% and dense sand with 76% to 86%. Tests were conducted with cone apex angles of 30° , 60° and 180° , while the base diameter of the penetrometer had a different diameter than the shaft (base 2.03 cm, shaft 1.59 cm). Also a smaller cone was used for testing the five-layer configurations. Figures 2.15 and 2.16 show examples of test results for the three- and five-layer system tested with cone apex angle of 60° (α being the semi-apex angle).

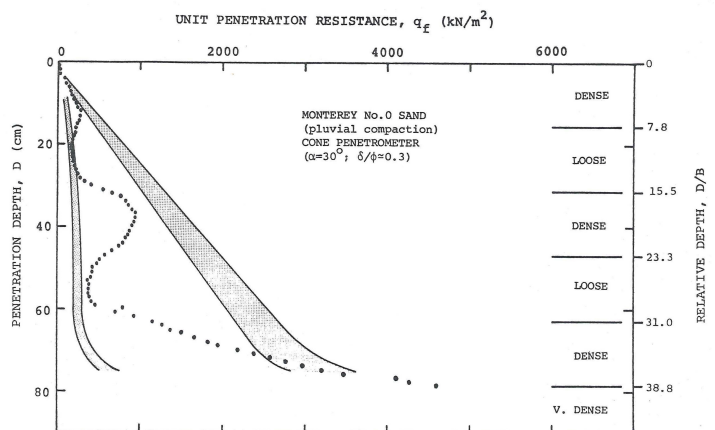
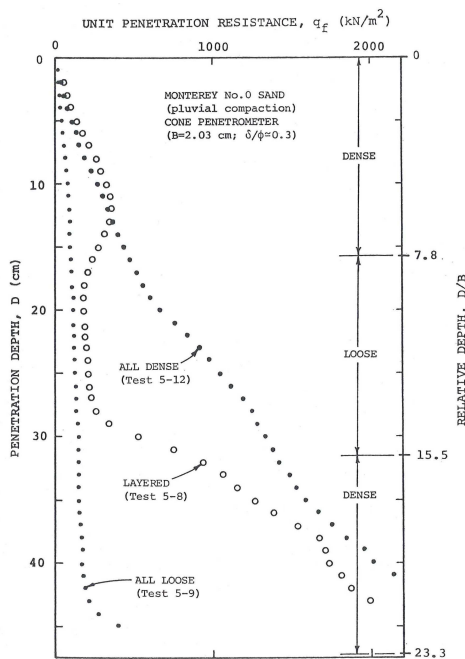


Figure 2.15: Results for three-layered system, after Treadwell (1976) **Figure 2.16:** Results from Treadwell for five-layered system, after Treadwell (1976)

Silva and Bolton (2004) performed centrifuge penetration tests on a 30 cm high sand sample, containing three layers of sand of two different fractions with a same relative density of 75%. Results show that at certain distances from layer interfaces the cone reacts on the layer below because of the fraction difference of the two types of sand.

Xu (2007) performed centrifuge penetration tests on multiple configurations of layering, including a two-layered system with sand and clay layering. This last configuration contained a layer sand with 96% relative density above a clay layer. Result of tests with a 16 mm cone can be found in figure 2.17. Although only a two-layered system with sand and clay was tested, these results can be very useful when studying cone resistance near sand-clay layer interfaces. For example, the distance above the sand-clay interface at which the cone reacts on the presence of the clay layer is $3.8d_{cone}$.

Młynarek et al. (2012) performed penetrometer tests on a three layered system with a clay layer of various size embedded between two sand layers, in which a relationship between correction factor and clay layer thickness is presented for a three layered system. It should be noted that the research of Młynarek et al. (2012) focusses on correcting the cone resistance for clay layers, where this research aims to look primarily to sand layers as well as clay layers. The results considering the cone resistance can be found in figure 2.18.

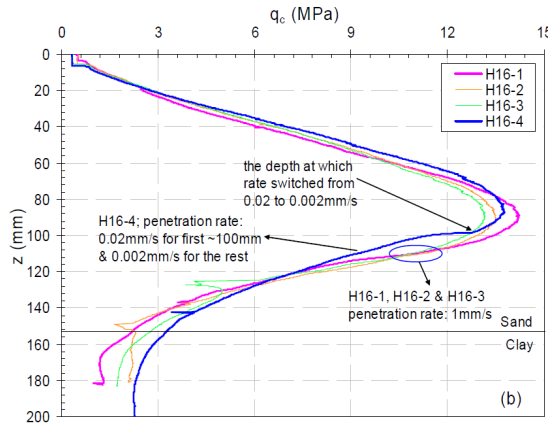


Figure 2.17: Results for the two-layered system with dense sand on top of a clay layer tested with a 16 mm cone, after Xu (2007)

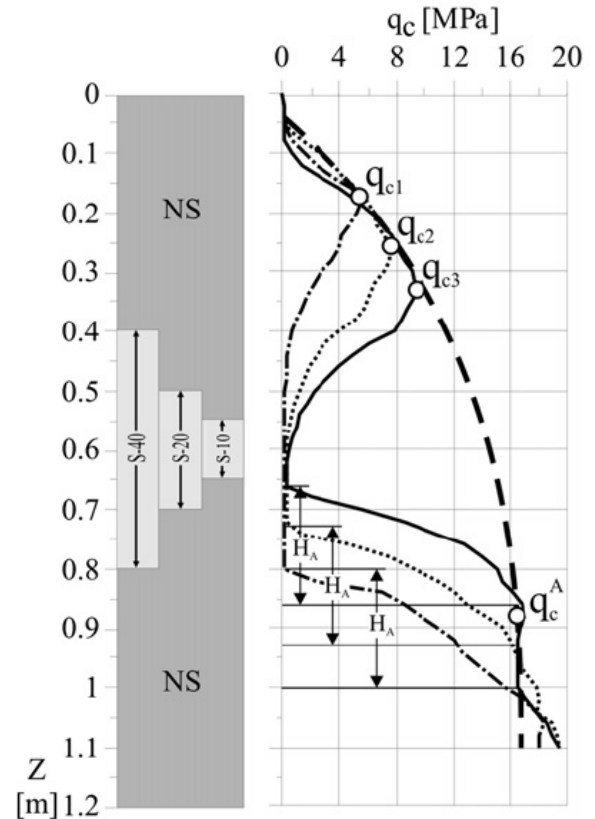


Figure 2.18: Changes of cone resistance with depth for different thicknesses of clay layer, after Młynarek et al. (2012)

Mo (2014) also performed centrifuge penetration tests on layered sand samples with different relative densities. This research distinguishes itself from others since particle image velocimetry (PIV) techniques were used to monitor the penetration process, rarely done on layered samples. In this research also three layers was the maximum number of layers tested per sample. In a publication about this research by Mo, Marshall, and Yu, H. A. (2015) the method

of Vreugdenhil et al. (1994) for simulating cone resistance is used. The fact that only three layers were tested and that only sand was used, make it not very usable for the multiple thin layer problem because it is believed that the penetration mechanisms in sand and clay differ. However, the PIV technique and application of the theory of Vreugdenhil et al. (1994) make it a very interesting research.

It can be concluded that few research is done on physically modelling penetration of layered soil samples, especially samples with multiple sand and clay layers. Most researches are focussed on a single layer surrounded by a material with different properties, which is also where the correction factor proposed by Robertson and Fear (1995) is based on. Whether this correction factor is also valid for multiple soil layers is something that needs investigation, which is attempted in this research.

3 Research implementation

3.1 Numerical analysis

In order to understand how the cone resistance behaves when passing through multiple layers, an attempt has been made to model the penetration resistance using an analytical elastic model proposed by Vreugdenhil et al. (1994) and clarified by Joer et al. (1996) compared with elastic finite element calculations, and the Koppejan-method used in the Dutch version of Eurocode 7 (*NEN 9997-1* (2012)). The results of these models and methods are compared to each other as well.

The model of Vreugdenhil et al. (1994) was chosen since it is a very convenient solution to the penetration problem and recognised and used in recent research (Mo, Marshall, and Yu, H. A. (2015)). It was chosen to adjusting the Koppejan method since this empirical method also gives straightforward results and is widely used for determination of pile bearing capacity in The Netherlands, therefore more or less proven in practice.

3.1.1 Vreugdenhil et al. (1994) model

As stated in section 2.3, Vreugdenhil et al. (1994) provided a method based on elasticity for estimating the measured penetration resistance within a thin layer. Although an elastic solution does not seem to fit with a problem where plastic strains play a major role, the use of an elastic model is justified by stating that not the actual penetration process but the influence of nearby layers of soil is considered.

The only parameters for characterizing the properties of the soil layer used in this method are the elastic shear modulus G and the layer thickness, from which the distance between cone and layer interface is derived. It is assumed that the shear modulus of each layer is proportional to the cone resistance of that layer, meaning that the relative difference in shear modulus between the layers can be a good representation of the relative difference in characteristic resistance (that is the cone resistance if a layer would be infinite thick). Another assumption is that the layers are incompressible, meaning that ν has a value of 0.5.

The method gives a separate equation for the penetration resistance for each separate layer. Therefore the layer interfaces define the boundaries between the governing equations for each layer. For example, the penetration resistance of a two-layer system has a slightly different equation above the boundary between the two layers than below this boundary. An example of how the solution for a two-layered system may look like can be found in figure 3.1. This solution involves a dimensionless penetration resistance η instead of the measured cone resistance q_c . Equations and their derivations for the penetration resistance both above and below the interface can be found in appendix D.

It can be concluded that at a certain distance from the interface the calculated resistance (which would be the in situ measured resistance) approaches the characteristic soil resistance, which is something that would be expected. This resistance resembles the resistance that would be measured if the soil would only consist of that particular type of soil. When looking at figure 3.1a, it seems that a smooth transition between the layers has been accomplished, but from figure 3.1b it can be concluded that near the interface the two equations show significantly different behaviour although the solutions seem to connect at the interface.

In order to generate a simulation for multiple layers, Joer et al. (1996) presented a generalised form of the equations given by Vreugdenhil et al. (1994) for evaluation of a multi-layered situa-

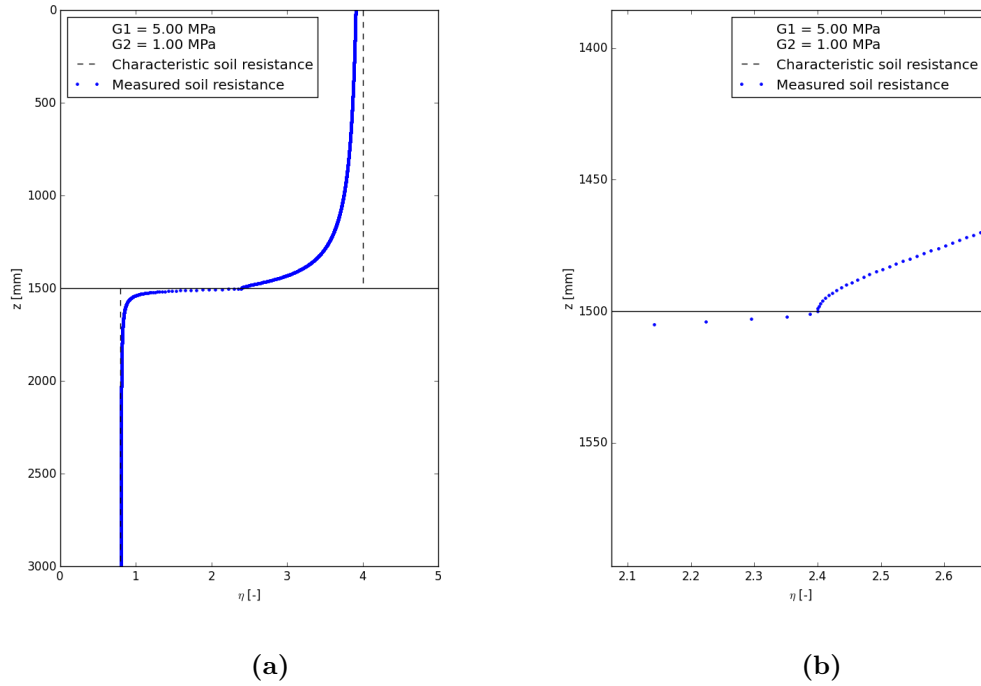


Figure 3.1: Dimensionless response as cone passes through interface between two layers with different shear moduli. Figure 3.1b focuses on the interface shown in figure 3.1a.

tion. Equations for this method can be found in appendix D.3. This method has been used to simulate a 7.6 m deep soil profile, consisting of six layers with different thicknesses and elastic shear moduli. The result of this example can be found in figure 3.2. In this figure the equations for η of each layer over the whole depth have been plotted in faint grey, while the governing equations in each layer have been highlighted using coloured dots.

It can be concluded that for a minimum thickness of 200 mm the transitions between layers are quite smooth and that the overall course of the penetration resistance seems plausible.

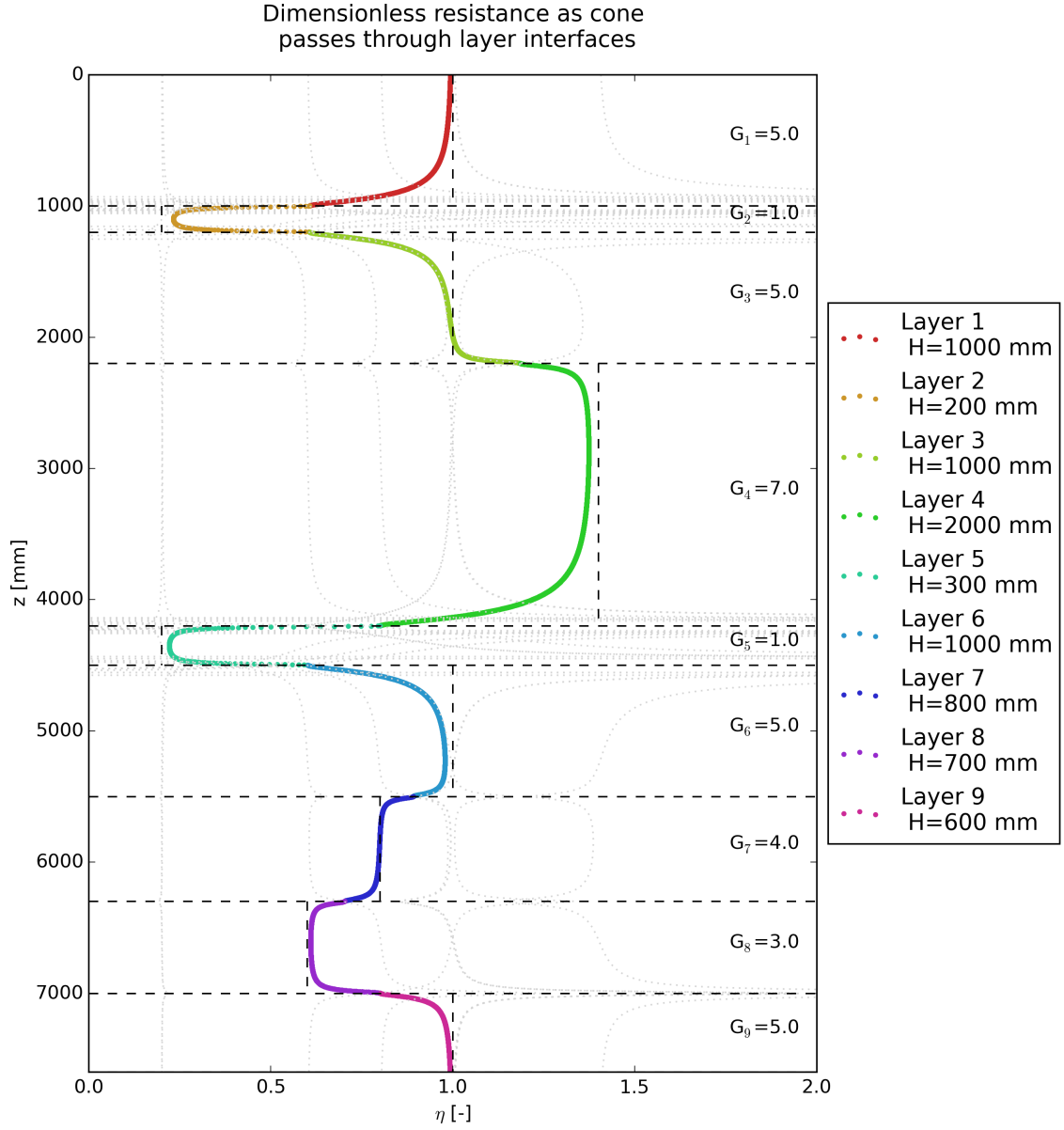


Figure 3.2: Dimensionless resistance result for a simulation with six layers. The horizontal dashed lines mark the boundaries between the layers, the vertical dashed lines show the characteristic dimensionless penetration resistance for their corresponding layer.

Finite element calculations

Since the method of Vreugdenhil et al. (1994) is an elastic method, it is believed that a numerical finite element (FE) calculation using a linear elastic material model should give comparable results. Therefore the FE program PLAXIS 2D was used for modelling the cone resistance.

The calculation considers an axisymmetric 2 m deep soil profile. The material model of the soil layer is linear elastic, and so the only parameters that are needed to be assigned are shear modulus G and Poisson's ratio ν , of which the latter is set equal to 0.5 (similar to the assumption of incompressibility by Vreugdenhil et al. (1994)). An example of a generated mesh and the detail around the cone/pile tip can be found in figure 3.3.

Since Vreugdenhil applies a uniform pressure p_0 , the pressure applied by the cone is repre-

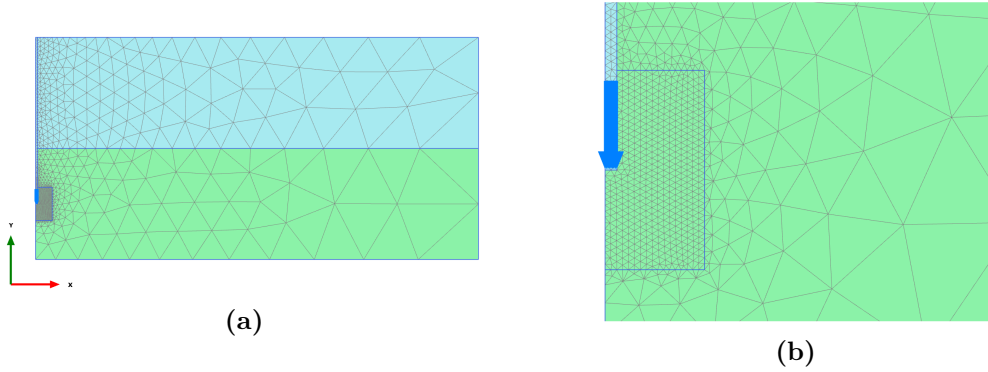


Figure 3.3: Example mesh and detail around the cone tip.

sented by a uniform load (instead of uniform displacement). After calculation with PLAXIS 2D the maximum displacement is taken for calculation of the dimensionless penetration resistance defined by Vreugdenhil et al. (1994), illustrated in figure 3.4. Because of the axisymmetry of the model, it is assumed that the maximum displacement can be found at the left corner node of the loaded line, representing the centre of the cone. This corresponds to the location where Vreugdenhil et al. (1994) defined their location of the displacement δ . The value for maximum

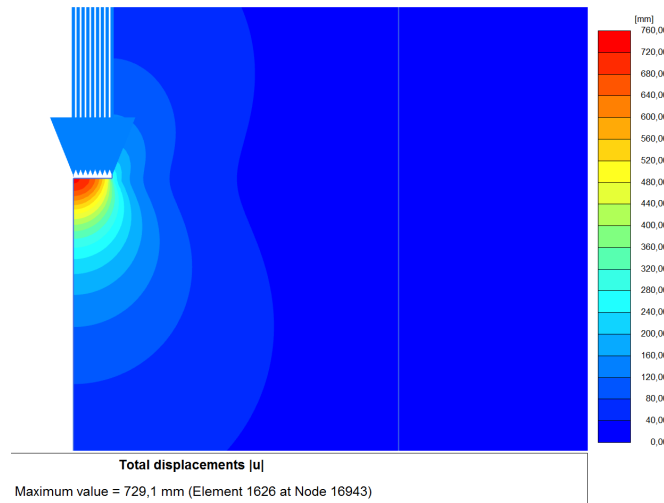


Figure 3.4: Example of the displacements calculated by PLAXIS 2D.

displacement is then used as δ to calculate the dimensionless penetration resistance defined by Vreugdenhil et al. (1994):

$$\eta = \frac{p_0 a}{G_1 \delta} \quad (3.1)$$

Where η is the dimensionless penetration resistance, p_0 the uniform stress over the disc-shaped region, a the cone radius, G_1 the elastic shear modulus of the top layer and δ the vertical displacement at the centre of the loaded region.

By calculating the maximum displacement for different levels of the cone tip, the penetration resistance according to Vreugdenhil et al. (1994) can be calculated. This way similar figures as shown in figure 3.1 can be made, only now showing FE results instead of results calculated with the Vreugdenhil et al. (1994) model. An example of such result can be found in figure 3.5. The input parameters for the soil types in the PLAXIS model can be found in table 3.1.

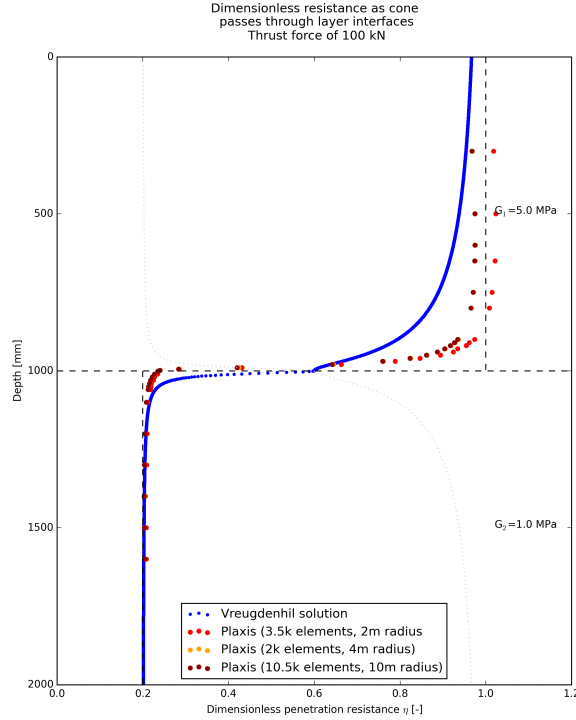


Figure 3.5: Example of calculated η with results from PLAXIS 2D for different mesh setups.

Table 3.1: Overview of the soil parameters for the axisymmetric PLAXIS model

	Mat. model	Drain. type	γ_{unsat}	γ_{sat}	G	ν
Top layer	Lin. elast.	Drained	0.0 kN/m ³	0.0 kN/m ³	5.0 MPa	0.5
Bottom layer	Lin. elast.	Drained	0.0 kN/m ³	0.0 kN/m ³	1.0 MPa	0.5

It can be concluded that different mesh setups give different results. The 3.5k mesh used is a uniform mesh with no densifications around the pile tip, the other two mesh setups did have these densifications. It can be concluded that the densified meshes give similar results. It can be concluded that especially the densification around the cone tip gives more comparable results and that the width of the mesh is less important.

In this research the use of the FE method (FEM) only focussed on the elastic solution and comparison with the method of Vreugdenhil et al. (1994). It could be considered to use more complex material models which would better describe soil behaviour (e.g. introduce plasticity with the Mohr-Coulomb model), since soil is certainly not a purely elastic material. Since the FEM is not good at dealing with large deformations in the mesh, using FEM is not the best

method of solving the problem of cone penetration. This can partly be solved by using the PLAXIS option to update the mesh after every calculation step and to only consider small strains, but here still errors in the mesh can occur. One solution could be to use the material point method (MPM), which is capable of dealing with large strains. More about the use of MPM for large strain problems is published for example by Wieńkowski ([2004](#)).

3.1.2 Koppejan method

The Koppejan method involves an empirical model for determining the pile tip resistance for foundations, which is widely used in foundation engineering and which has been included in Dutch standards (*NEN 9997-1* (2012)). Since there is software available which uses the Koppejan method for calculating pile tip resistances, a first attempt has been made to model the method using this software. The program *DFoundations*, produced by Deltares, has been used to calculate the pile tip resistances, in which the ‘standard’ cone diameter (36 mm) represents the pile diameter. The input soil profile is the characteristic values of the cone resistance for the layers, illustrated in figure 3.6.

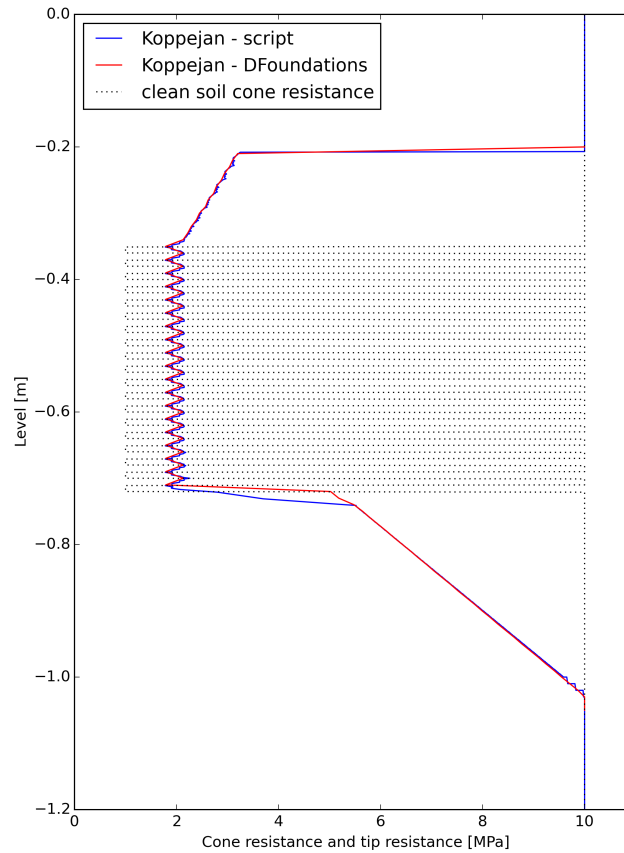


Figure 3.6: Example profile input and results for *DFoundations* and script with 1 cm thick layers. The q_c varies between values of 1 MPa and 10 MPa.

The program calculates the pile tip resistances over a certain depth with certain vertical calculation interval, using the characteristic cone resistances as the ‘original CPT’. It is believed that the tip resistances the method calculates may resemble the penetration resistance the cone experiences during testing. The equation for the Koppejan method can be found in appendix E.

DFoundations does not allow the vertical calculation interval to be smaller than 0.01 m, which becomes a problem when the virtual cone resistance needs to be calculated for layers smaller than 0.01 m. Also not more than 150 calculation steps are allowed. Therefore a script in the Python programming language has been written allowing very small calculation intervals without limiting the amount of calculation steps. The script first reads and interprets the GEF-file (Geotechnical Exchange Format in which raw CPT data is stored) with the characteristic q_c

values and then calculates the tip resistance over full depth with preferred calculation interval (which has been set to 0.001 m as default). The script also allows the area of surrounding soil influencing the cone resistance to be adjusted, where the original method of describes the area to reach $8D_{eq}$ above the pile tip and between $0.7D_{eq}$ and $4D_{eq}$ below pile tip level. These distances of influence are called ‘iteration distances’ in the remaining parts of this report. These levels could be adjusted, especially when looking at the difference of shapes of the failure surfaces for different conditions, shown in figure 2.12. The script with another way of validation can be found in appendix E.

3.1.3 Comparing the modelling methods

Figure 3.5 also includes the solution from Vreugdenhil et al. (1994) for a two-layered system with similar ratio in G_1 and G_2 . It can be observed that the PLAXIS solution gives a smoother solution on the interface and that the interface influences the penetration resistance at less distance than for the solution from Vreugdenhil et al. (1994). Since the PLAXIS calculations have been put on hold, only the Koppejan and Vreugdenhil calculations for multiple thin layers can be compared. These two methods of modelling thin layer cone resistance will be used in the remaining part of this research.

Figure 3.7 shows the situation for 1 cm thick layers with a characteristic resistance of alternately 1 and 10 MPa.

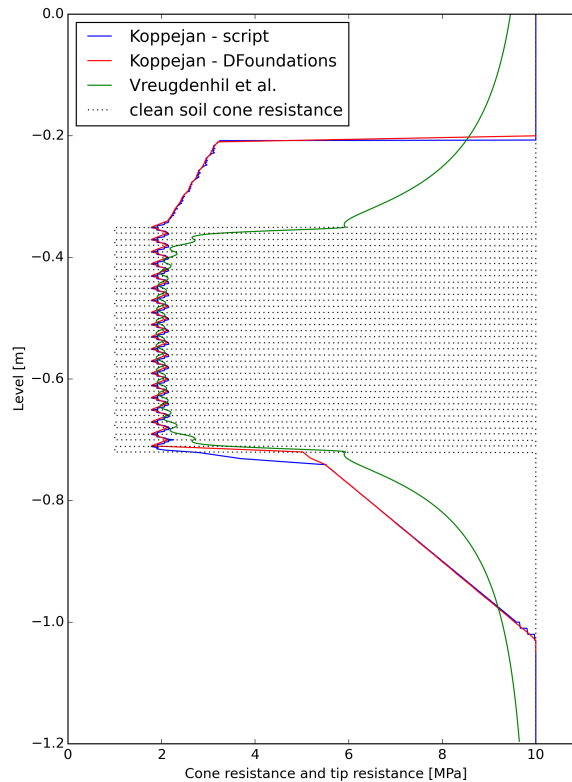


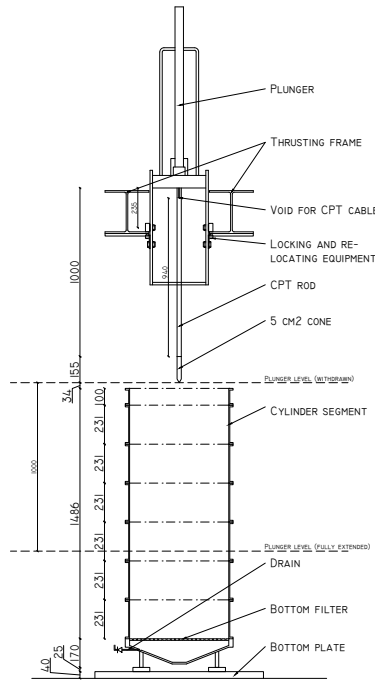
Figure 3.7: Example profile with the same input as shown in figure 3.6 and results for *DFoundations*, script and Vreugdenhil with 1 cm thick layers. The q_c varies between values of 1 MPa and 10 MPa.

Looking at the centre of the thin layer zone, it can be concluded that Koppejan and Vreugdenhil give similar results. More configurations and their results are presented in appendix F. In this appendix also solutions for other iteration distances than included in the original method of Koppejan are included.

3.2 Physical modelling of thin layers

In order to validate the Vreugdenhil et al. (1994) and Koppejan methods, cone penetration tests were performed in artificially built soil samples containing sand and clay layers were subjected to cone penetration. This section contains merely a short description of the tests, since an extensive description of the test setups and results as well as other indicative tests can be found in appendix G. This appendix also describes the considerations that came to light during design of the tests. It is therefore recommended to have appendix G within reach when detailed understanding of the tests and surrounding processes and decisions is desired.

The main goal of the tests, besides checking the Vreugdenhil et al. (1994) and Koppejan methods, was to see whether correction factors for thin layers could be obtained from physical modelling. If the models fairly match the test results, these models can be used to investigate correction factors for other sample configurations. It was unknown whether it was feasible to prepare samples with clay layering and therefore the tests can also be characterised as a feasibility study on preparing thin layer samples.



(a) Equipment configuration for tests on the first sample (b) A sample about to be penetrated for penetration testing

Figure 3.8: Test setup used for testing layered samples

The test were conducted in a circular steel cylinder with an inner diameter of 58.9 cm, which could be built up with cell elements to reach certain height. Choosing this cylinder diameter has implications for choosing the cone size. This consideration is further elaborated in section G.1.3 of appendix G. For the tests use was made of Baskarp sand and Vingerling clay, described in appendix G, which were built up artificially to obtain a sample configuration of which the dimensions of the layers are precisely known. Samples were tested with a 5 cm² cone ($d_{cone} = 25$ mm) containing u_2 pore pressure transducers which was able to penetrate the soil for one meter of depth. The test setup is displayed in figure 3.8. For most tests sample height was 1.2 m in order to avoid the bottom plate from influencing measurements.

Since the multiple layer model of Vreugdenhil et al. (1994), who use the shear modulus G to describe a soil layer, has been used previously, it was preferred to know the ratio of characteristic shear moduli as well. This parameter can be obtained by comparing the characteristic cone resistances of both clay and sand, since the assumption Vreugdenhil et al. (1994) make is $G_1/G_2 = q_{c,1}/q_{c,2}$. For sand preparation, methods were used which gave a reasonable level of homogeneity in the sand. In order to know the local relative density of the sand besides the bulk density for different preparation methods, local relative density measurements were taken.

To obtain the characteristic cone resistances of sand, the cylinder was filled and compacted to obtain a single homogeneous sand layer. The characteristic cone resistance of clay was obtained by testing a 30 cm thick clay between two sand layers. Determination of the required layer thickness for the characteristic resistance in clay was done with the Vreugdenhil et al. (1994) model, for which a G_1/G_2 -ratio of 10 was assumed on beforehand. The model showed that the penetration resistance in a layer of 30 cm would approximate the characteristic cone resistance. Two other samples were prepared with sand and clay layers, the first sample containing three clay layers with a layer thickness of 8 cm each and the second sample containing ten layers of 2 cm. In the layered part of the samples sand and clay layers had an equal thickness. Layer thicknesses were chosen based on general differences in behaviour of the Vreugdenhil et al. (1994) and Koppejan models together with practical considerations of vertical space within the meter of testing depth that was available.

An overview of the configurations of the samples subjected to penetration testing can be found in table 3.2. During tests on the first two samples it turned out that the boundary effects on the measurements in the sand were too large for these results to be useful. From tests on sample 2 the characteristic resistance of clay was determined, since boundary effects are believed not to have influenced resistance measurements in the clay. Since it was believed that the relative density of samples 1 and 2 was too high, tests on samples 3 and 4 were performed to see what effect a lower relative density would have on measurements. Besides that this seemed still too dense, the preparation technique used for samples 3 and 4 was considered not to be ideal for preparing layered samples. Therefore a different technique was used for samples 5, 6 and 7, where the results of the tests on sample 7 were used for determining the characteristic resistance of sand.

Table 3.2: Testing program

Sample nr.	Layering	Est. sand $R_{d,e}$
1	-	91.6%
2	one 30 cm clay layer	91.6%
3	-	74.0%
4	-	74.0%
5	three 8 cm clay layers	55.0%
6	ten 2 cm clay layers	55.0%
7	-	55.0%

Multiple tests at different locations on the sample were performed to have an indication of the reliability of the measurements. For the tests involving layering after the last tests the cone penetrometer and extension rod were left in the sample to make a cross-section of the sample along the cone rod. This way deformations as a result of cone penetration could be observed and more clues could be gained of why CPT data would behave like measured. Figures of the cross-sections can be found in appendices G and I.

4 Results

This chapter presents the most relevant test results from penetration tests on the different samples characterised in table 3.2. Since this research focusses mainly on cone resistance data, this chapter only presents the results and analysis of cone resistance measurements. A complete overview and description of the tests can be found in G. The appendix also presents results of other measured parameters: sleeve friction and pore pressure measurements.

In this chapter all levels are normalised with respect to the cone diameter. This means that depth is divided by the cone diameter: z/d_{cone} . This makes the results presented comparable with other research done with different cone diameters.

4.1 Test results

The results of tests providing usable results can be found in figure 4.1. Only the results are presented of the tests that are considered useful for further analysis and correction factor generation. Numbers of the tests correspond to the numbers of the samples of which an overview is found in table 4.1.

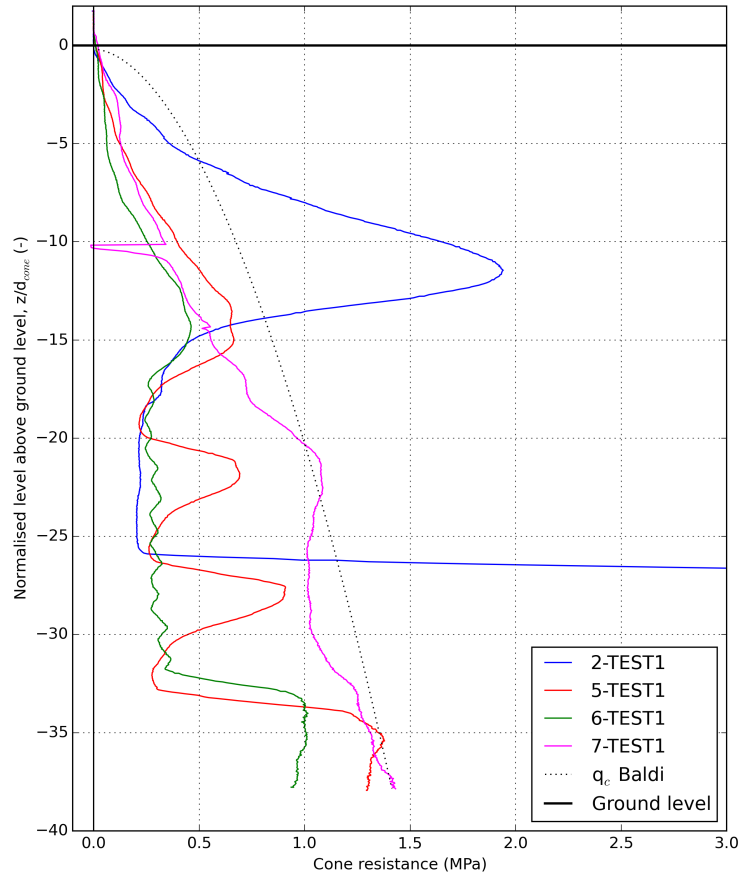


Figure 4.1: Cone resistance results for relevant tests

Table 4.1: Sample properties of the relevant tests

Sample nr.	Layering	Est. sand $R_{d,e}$
2-TEST1	one 30 cm clay layer	91.6%
5-TEST1	three 8 cm clay layers	55.0%
6-TEST1	ten 2 cm clay layers	55.0%
7-TEST1	no layering	55.0%

In this figure the relationship between relative density and cone resistance according to Baldi et al. (1986) has been fitted. The relationship of Baldi et al. (1986) can be written as

$$q_c = C_0 \cdot \sigma_v'^{C_1} \cdot \exp(C_2 \cdot R_d) \quad (4.1)$$

where C_0 , C_1 and C_2 are parameters for certain types of sand. Baldi et al. (1986) present parameters for Ticino sand to be $C_0 = 157$, $C_1 = 0.55$ and $C_2 = 2.41$. Adjusting C_0 to 127 gives the line drawn in figure 4.1, which is based on measurement fitting and not on an existing study to the parameters of Baldi et al. (1986) for Baskarp sand. Comparing the fitted line with the result of 7-TEST1, it can be concluded that the decrease in cone resistance between a depth of $23d_{cone}$ and $33d_{cone}$ can come from local inhomogeneity, and so that over this depth the relationship of Baldi et al. (1986) can be preferred.

The resistance in the bottom 8 cm sand layer of 5-TEST1 is higher than in the top 8 cm sand layer. Local density measurements (see figure G.60 of appendix G) show that the bottom intermediate layer was more dense than the rest of the sand in the sample, so therefore the sand resistance of the top 8 cm sand layer will be leading in further analyses.

In almost every test a small inclination in the overall trend can be observed, which is caused by increasing stress level over depth. In order to make the results usable for calculation, the results are normalised for the effective stress level, described in section 4.2.

4.2 Normalisation

Since the results show significant differences over depth, normalisations were applied on the test data. Two different methods for determining the normalised cone resistance Q are used. The method of Lunne et al. (1997) includes the total and effective vertical stress for normalisation, written as

$$Q_t = \frac{q_t - \sigma_{v0}}{\sigma_{v0}'} \quad (4.2)$$

where q_t is the corrected total cone resistance. This type of resistance is defined as

$$q_t = q_c + u_2(1 - a) \quad (4.3)$$

where q_c is the measured cone resistance, u_2 the pore pressure behind the cone and a the cone area ratio, determined during cone calibration to be 0.5.

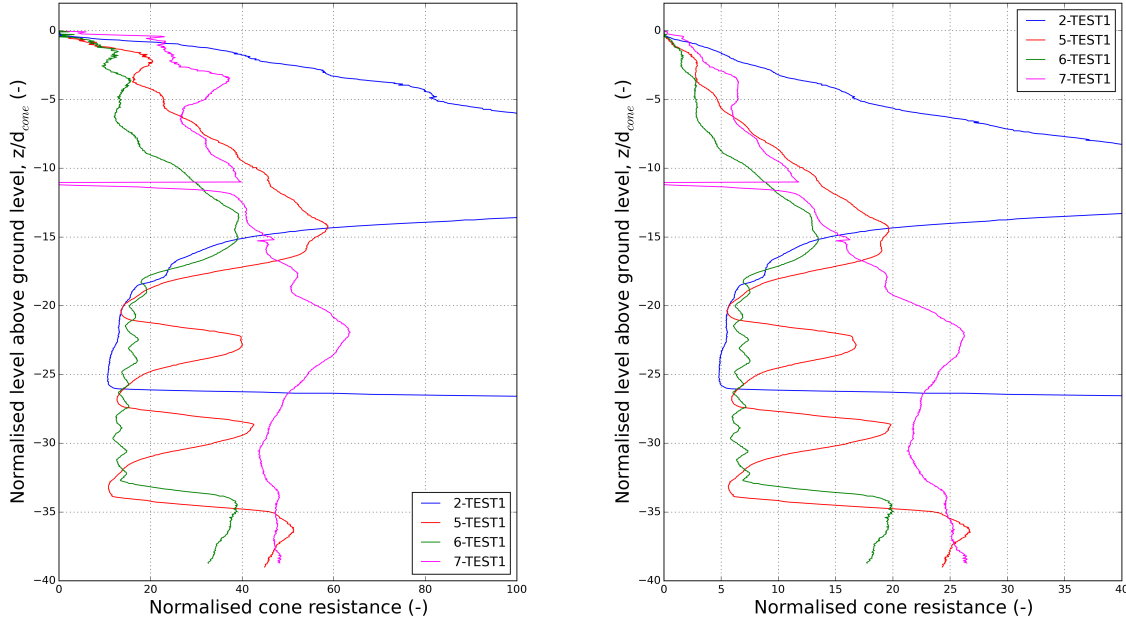
The method of Liao and Whitman (1986) includes the square root of the effective stress for determination of a correction factor for the local stress level:

$$C_N = \sqrt{\frac{1}{\sigma_{v0}'}} \quad (4.4)$$

where σ_{v0}' is the initial effective stress. In order to come to a dimensionless normalised cone resistance, the method of Liao and Whitman (1986) as well as the cone resistance is adjusted with a constant value for the atmospheric pressure p_a of 0.1 MPa:

$$Q_N = \frac{q_c}{p_a} \cdot \sqrt{\frac{p_a}{\sigma_{v0}'}} \quad (4.5)$$

which is also used in currently valid guidelines (e.g. Nederlands Normalisatie-instituut (2015)).



(a) Normalisation (Q_t) according to Lunne et al. (1997) (b) Normalisation (Q_N) according to Liao and Whitman (1986), adjusted with p_a

Figure 4.2: Results for the normalised cone resistance for relevant tests

Figure 4.2 shows the results after normalisation with the two different methods. The method of Lunne et al. (1997) corrects the results giving another inclination (e.g. resistances for test 6-TEST1 are declining in the layered section of the sample), while the adjusted method of Liao and Whitman (1986) results in normalised cone resistances without any inclination. It was therefore decided to continue analysing the results using the adjusted normalisation method of Liao and Whitman (1986) (equation (4.5)), although it should be mentioned that the presented methods of normalisation are usually not applied to shallow CPTs as the tests done for this research can be classified. For convenience the parameter Q_N is referred to as Q .

From the normalised measurements the characteristic normalised cone resistances for sand and clay could be determined, which are needed when comparing the test results with simulations is desired. Figure 4.3 displays the determination of the characteristic cone resistances. From figure 4.1 it can be concluded that the penetration resistance in clay does not need correction to obtain a characteristic cone resistance, since already a vertical trend can be observed in the clay layer. Therefore the characteristic cone resistance for clay is taken at a depth of $22d_{cone}$ and not at the point where the normalised cone resistance is most vertical. For determination of the characteristic normalised cone resistance in sand, the decrease between $23d_{cone}$ and $33d_{cone}$ is ignored according to the fit from the relationship of Baldi et al. (1986) described before.

Comparing the normalised cone resistances in figure 4.2b of test 6-TEST1 with the results of 5-TEST1 and 7-TEST1 below a depth of $35d_{cone}$, it can be concluded that the bottom sand layer has been slightly looser compacted for 6-TEST1. Therefore a characteristic normalised cone resistance for the sand $Q_{char,sand}$ in sample 6 is determined to be 19.6, which is used in further calculations.

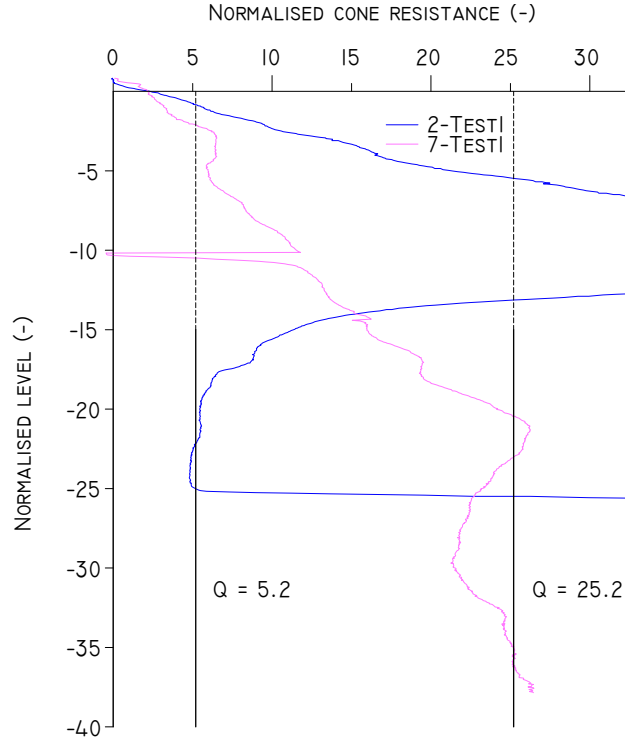


Figure 4.3: Characteristic normalised cone resistances $Q_{char,sand} = 25.2$ and $Q_{char,clay} = 5.2$

4.3 Test results versus models

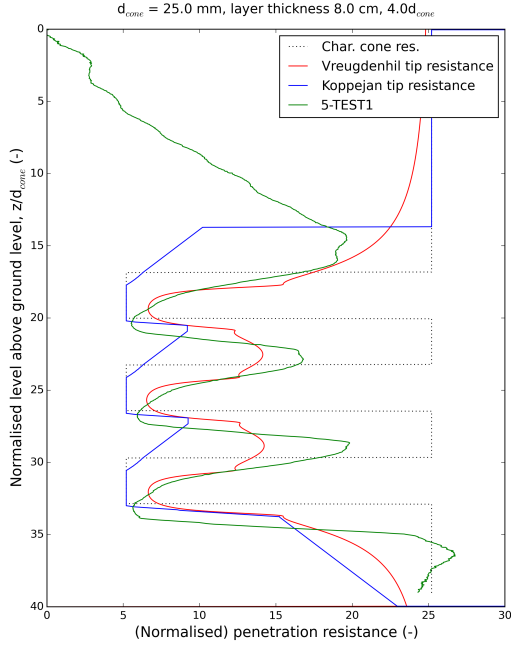
The results are compared with the simulated results of the Vreugdenhil et al. (1994) and Koppejan models. The input for the models were GEF files, containing the levels at which the clay and sand layers were prepared during sample preparation and the characteristic normalised cone resistances determined in section 4.2. Figure 4.4 shows the measurements of the tests on the 8 cm layers together with their corresponding simulations, figure 4.5 shows these results for the tests on the 2 cm layers.

For the 8 cm layers, the Vreugdenhil et al. (1994) seems to follow the overall trend in measured cone resistance quite well, only the maximum cone resistances in the 8 cm sand layers show differences with the simulations. The resistance at the sand-to-clay boundary interfaces for the middle and bottom clay layers shows no difference between measurements and simulations. When a correction factor would be determined based on the model of Vreugdenhil et al. (1994) the factor would be overestimated compared to what the factor would be determined based on CPT data.

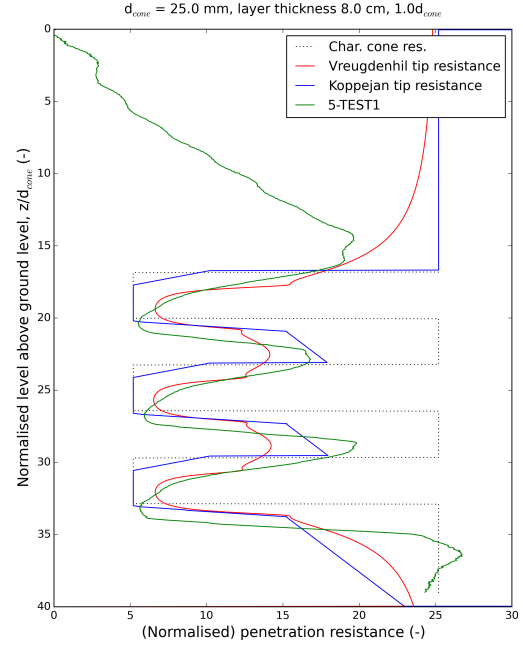
It can be concluded from figure 4.4a that the Koppejan model does not give results comparable to measurements when choosing a value between $0.7d_{cone}$ and $4d_{cone}$ for trajectory I and II (see appendix E). Therefore the iteration distance was adjusted to a distance between $0.7d_{cone}$ and $1.0d_{cone}$, giving results of figure 4.4b. In this figure the peak resistances in the 8 cm sand layers are better represented by the Koppejan model, also when considering that the bottom 8 cm sand layer contained sand with slightly higher relative densities, resulting in higher (but unknown) characteristic cone resistances.

For the 2 cm layers, the Vreugdenhil et al. (1994) model seems to follow the same trend as the measurements, but the simulated cone resistances are higher in the layered part. This overestimation of the cone resistance leads to underestimation of the correction factor for sand. For the Koppejan model calculations are made similar to the situation with 8 cm layers. In this

case $4d_{cone}$ iteration distance below the cone seem to give better fitting than when making this distance smaller, like $1d_{cone}$ shown in figure 4.5b. It seems therefore reasonable to conclude that when layer become smaller than the cone diameter the iteration distance of Koppejan should be lower than $1d_{cone}$ below the cone.

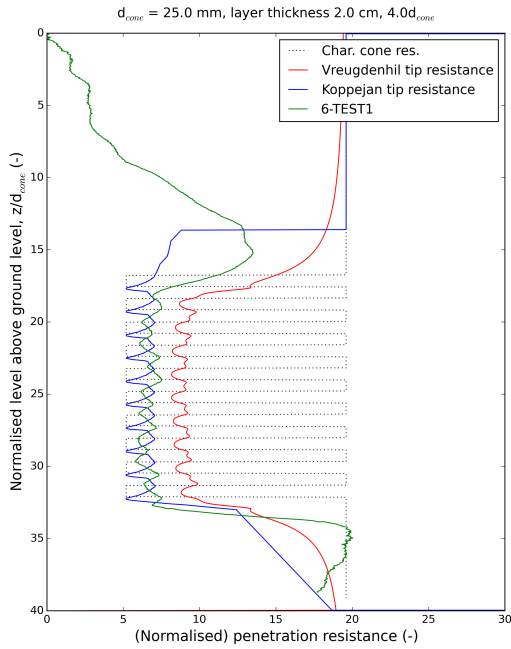


(a) $4d_{cone}$ iteration distance

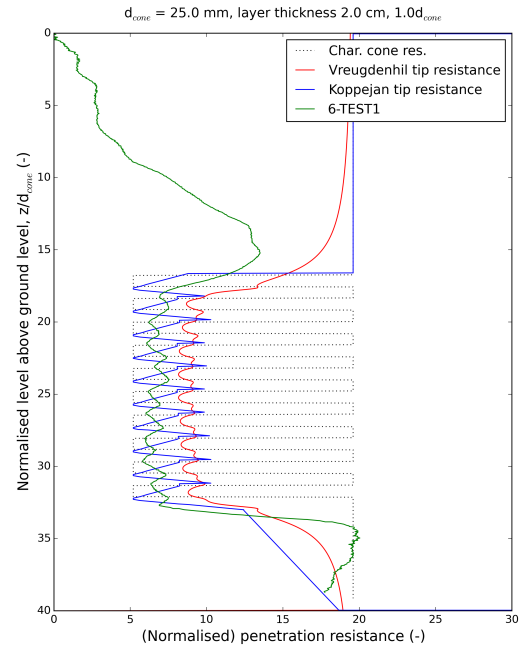


(b) $1d_{cone}$ iteration distance

Figure 4.4: Comparing the normalised cone resistance to model simulations for 8 cm layers



(a) $4d_{cone}$ iteration distance



(b) $1d_{cone}$ iteration distance

Figure 4.5: Comparing the normalised cone resistance to model simulations for 2 cm layers

Based on these results it is concluded that a fair approximation can be made using the Vreugdenhil et al. (1994) and Koppejan simulations, and therefore that these models could be used for developing curves for correction factors at different ratios of characteristic cone resistances. It seems that for layer thicknesses larger than $1d_{cone}$ the Koppejan model with an iteration distance up to $1d_{cone}$ gives the best approaching maximum resistance, while for layer thicknesses smaller than $1d_{cone}$ the Koppejan model with an iteration distance up to $4d_{cone}$ gives the best approximation. For thin layers the minimum solution is found well before the iteration distance reaches $4d_{cone}$. For example, $1.5d_{cone}$ of iteration distance gives very similar results as simulations up to $4d_{cone}$ iteration distance for the situation in figure 4.5, meaning that instead of $4d_{cone}$ also $1.5d_{cone}$ can be determined to be a reasonable iteration distance. The solution of the Vreugdenhil et al. (1994) model gives results located between both Koppejan approaches and seems not to be the best approach when looking comparing it with test results.

4.4 Correcting the cone resistance

This section describes the steps to come to correcting the cone resistance for thin layer effects. First correction factors are determined for the tests data, after which curves for correction factor with different ratios of characteristic cone resistances are presented. Next an attempt is made to setup a relationship for describing correction factor in different situations and the connection with field data is made.

Since the main problem with thin layers is that the cone resistance in small sand layers is so low that the layer is classified incorrectly, focus will be on correcting the cone resistance of the sand layers. However, the correction factors for the clay found during experiments are also presented here but not further elaborated.

Correction factors depend for a large amount on determination of characteristic resistances and the ratio of sand and clay layers. The difference between the characteristic resistance for sand of the 8 cm and 2 cm configuration illustrates that even in a controlled laboratory environment it is still a challenge to obtain these characteristic cone resistances, especially for sand. In field situations the characteristic resistances cannot be measured, and so these need to be assumed or estimated based on for example relative density, which could prove to be quite uniform when flaser bedding is considered. This should be kept in mind when going through the analyses below.

4.4.1 Correcting 8 cm layering

Figure 4.6 shows the basis of how correction takes place for 8 cm layers. Layer boundaries as they are implemented during sample preparation are drawn as horizontal lines, the grey area defines the amount of resistance that needs to be corrected in the direction of the arrows drawn in each separate layer. For each layer the characteristic normalised cone resistance matching the layer is divided by the normalised cone resistance data. The result of this computation is given in figure 4.7a. Since only a correction for sand is considered a detail of the correction factors in the sand layer is displayed in figure 4.7b.

In order not to overestimate the correction factor, in each layer the lowest correction factor should be chosen as the factor that can correct the cone resistance for layering. Since the bottom 8 cm sand layer was denser than the sand in other parts of the sample, the correction factor in this layer is not used. This leads to a correction factor of 1.50 for sand layers in a configuration of 8 cm layering (sand and clay layers of equal thickness) with a ratio in characteristic cone resistances of $Q_{char, ratio} = 4.85 (=25.2/5.2)$.

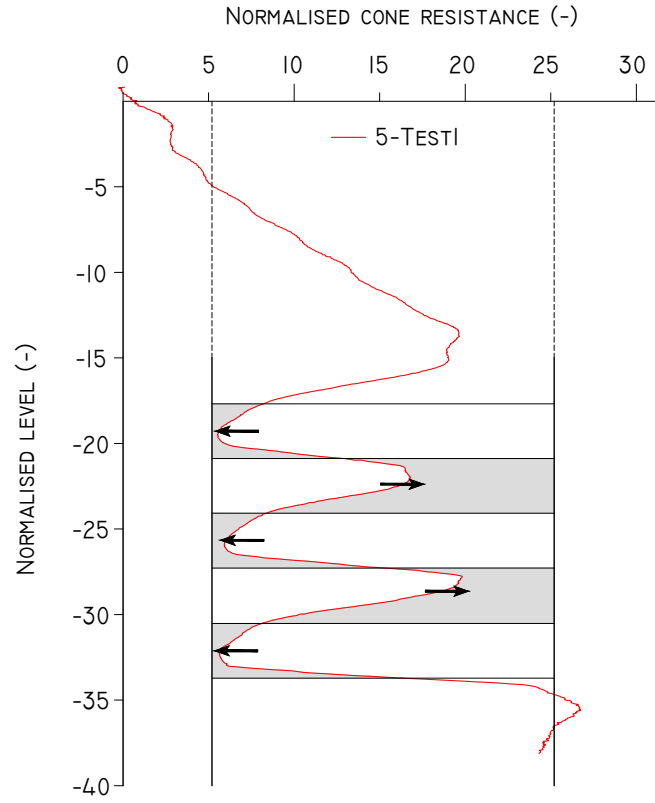
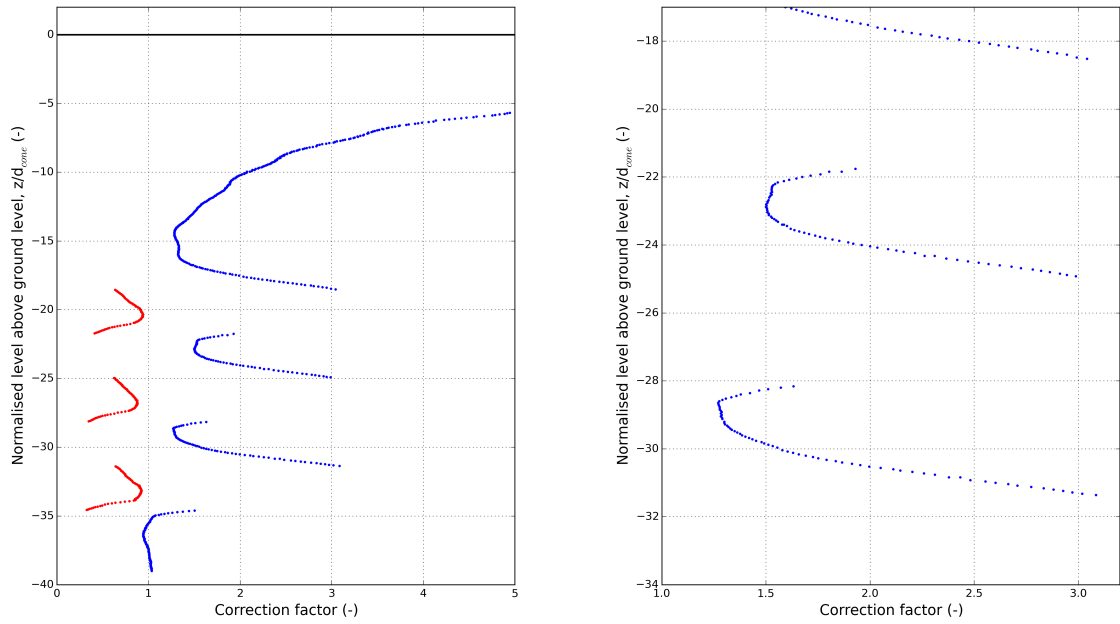


Figure 4.6: Correction principle for 8 cm configuration



(a) Correction factors for 8 cm sand layers (red = corr. in clay, blue = corr. in sand) **(b)** Detail of correction factor in the sand layers

Figure 4.7: Correcting CPT data of tests on 8 cm layers

4.4.2 Correcting 2 cm layering

Figure 4.8 shows the basis of how correction takes place for 2 cm layers. As explained before, it was decided that the characteristic normalised cone resistance $Q_{char,sand}$ for this sample is 1.96, which is drawn in the figure. The same method of correction has been applied as for the

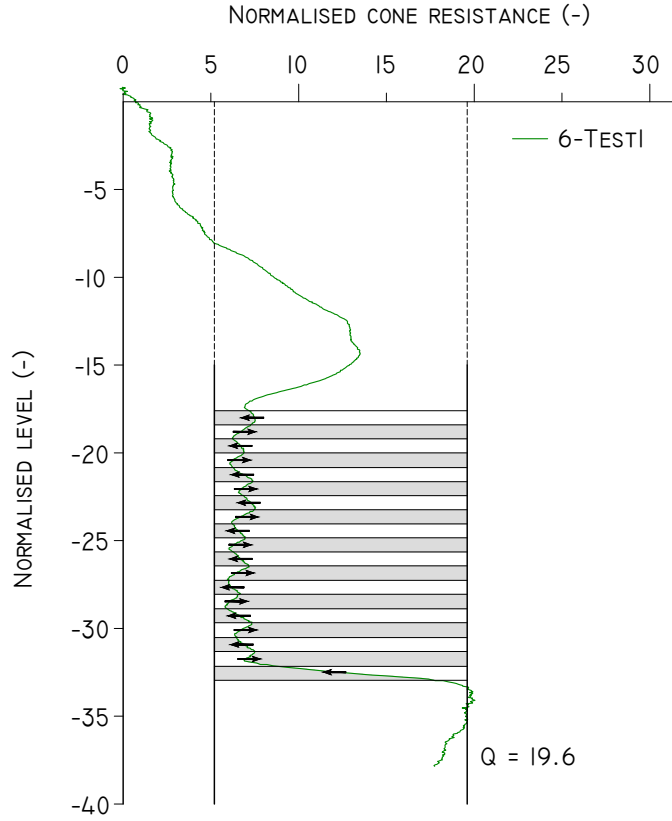


Figure 4.8: Correction principle for 2 cm configuration

8 cm layering configuration. The result of this computation is given in figure 4.9a, and a detail of the correction factors in the sand layer is displayed in figure 4.9b.

Again the lowest values for the correction factor for each layer are taken as leading correction factor. For the bottom 2 cm sand layer the first value of the correction factor is taken into account, since in the bottom part the thin layer cone resistance gradually returns to the characteristic resistance of the sand below the thin layers. Taking the mean value of the minimum correction factors for each layer combined gives an overall correction factor of 2.74 for sand layers in a configuration of 2 cm layering (sand and clay layers of equal thickness) with a ratio in characteristic cone resistances of $Q_{char, ratio} = 3.77 (=19.6/5.2)$.

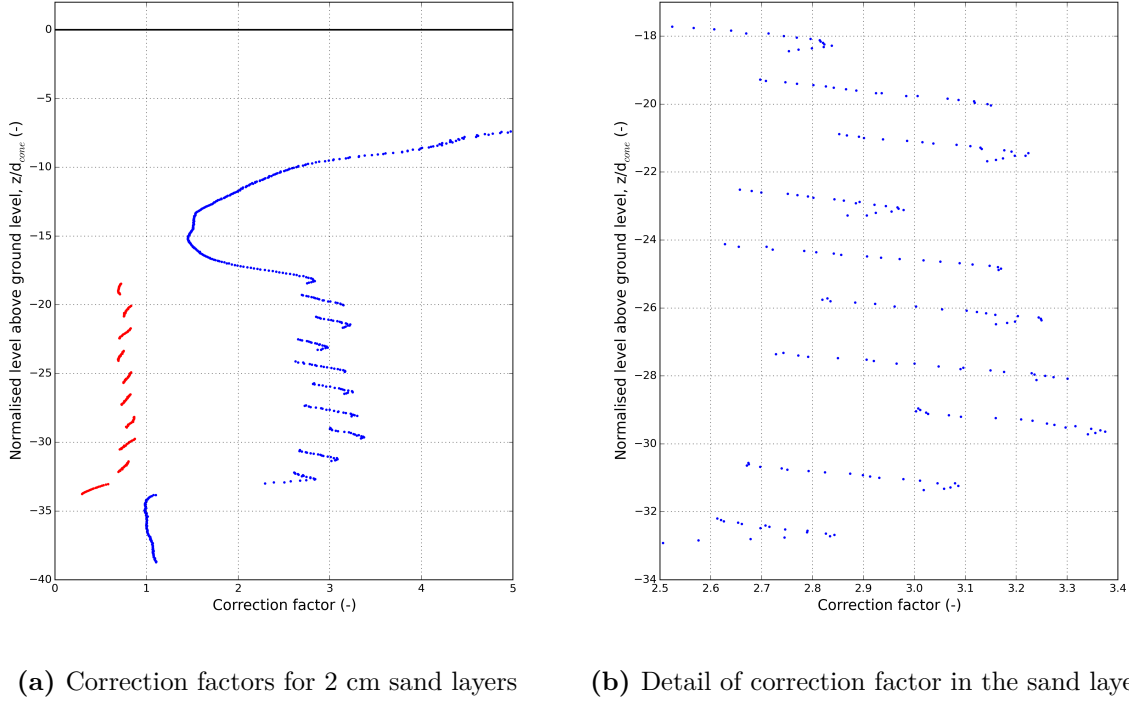


Figure 4.9: Correcting CPT data of tests on 2 cm layers

4.4.3 Correction factors from simulations

The method used for determining the correction factor for the measurements can also be applied on simulations. This way a range of correction factors for different layer thicknesses and characteristic resistance ratios can be calculated. Results of simulations with characteristic resistance ratios 10, 5, 4.85, 3.77 and 2 including test results can be found in figure 4.10. The simulated correction factors were determined with scenarios including multiple layers (>3 layer in total) comparable to the scenarios presented in appendix F.

Figure 4.10 also contains the recommended relationship for results obtained with a 10 cm^2 cone, drawn as a black line after Robertson and Fear (1995). The equation for this relationship:

$$K_H = 0.5 \cdot \left(\frac{H}{1000} - 1.45 \right)^2 + 1.0 \quad (4.6)$$

This relationship, in which H represents layer thickness, was developed based on the work of Vreugdenhil et al. (1994) for single thin layers and is also drawn in figure 2.14. In order to have a conservative correcting method the $Q_{char, ratio}$ was assumed to be 2 for this relationship, since the corrections found in this research are considered to be rather large. Although the results have been normalised for the cone diameter, it can be observed that for layer thicknesses larger than $2d_{cone}$ a significant amount of computed correction factors (also for higher values of $Q_{char, ratio}$) and one correction factor derived from test results are smaller than the recommended relationship. It can therefore be concluded that as the cones become smaller in diameter the correction factors become smaller as well.

Since figure 4.10 does not give a clear overview of how the correction factors develop for each $Q_{char, ratio}$ separately, figure 4.11 shows figures for $Q_{char, ratio}$ of 10, 5, 2, and for the ratios corresponding to the ratios from test results and the correction factors from these test results (see sections 4.4.1 and 4.4.2). The area of interest has also been highlighted. It is defined as the area in which the layer thickness is smaller than the cone diameter, which is considered also to be the definition of thin layers.

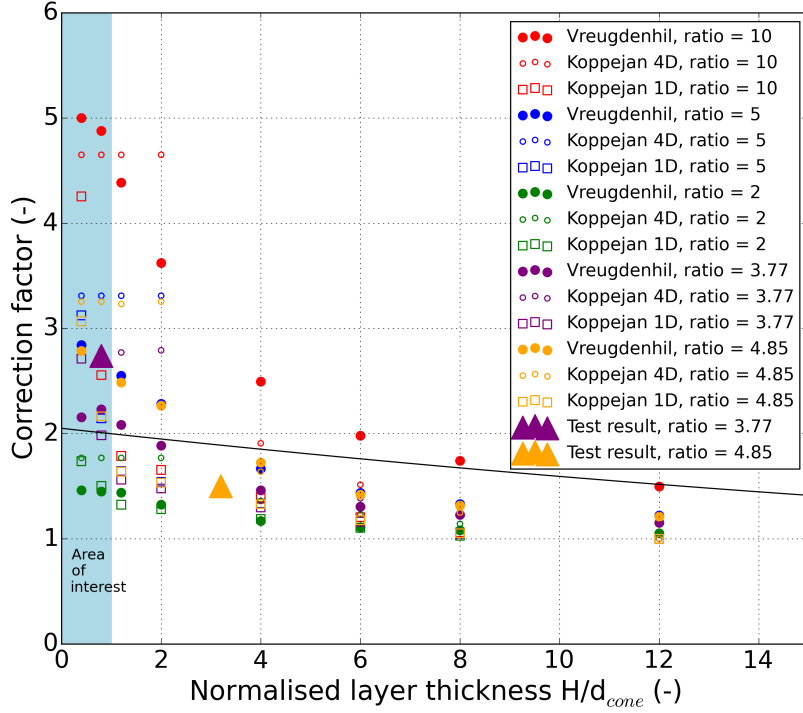


Figure 4.10: Computed correction factors and factors from experiments for a 5 cm² cone and different ratios in characteristic cone resistance, including recommended relationship for a 10 cm² cone

From figures 4.11e and 4.11f it can be concluded that for a layer thickness $< d_{cone}$ the correction factor is approached closely with simulations from the Koppejan method with $4d_{cone}$ of iteration distance below the cone, and for a layer thickness $> d_{cone}$ with simulations from the Koppejan method with $1d_{cone}$ of iteration distance.

The solution from Vreugdenhil et al. (1994) gives for layer thicknesses $< d_{cone}$ correction factors between the two Koppejan methods. The Vreugdenhil et al. (1994) also shows that when layer thicknesses become very small a constant correction factor is calculated, which is also expected looking at the test results of the 2 cm layers. If thinner layers would have been tested it is believed that the cone resistance would average even more, meaning that a correction factor for sand layers would not change much.

Besides a simulation is made of the conditions applicable to the relationship of Robertson and Fear (1995), drawn in figures 4.10 and 4.11d. This relationship was produced for a 10 cm² cone and a $Q_{char,ratio}$ of 2, which is considered to be sufficiently conservative. It can be observed that all calculated correction factors are lower than the proposed relationship. The proposed relationship, however, is produced with simulations of three-layer systems and thus not with multiple thin layers as done in this research.

For each $Q_{char,ratio}$ it can be observed that a bandwidth of solutions is developing between highest and lowest value of the correction factor, often between the solutions of Koppejan for $4d_{cone}$ and $1d_{cone}$ of iteration distance with the solution of Vreugdenhil et al. (1994) in between. For their corresponding values for $Q_{char,ratio}$ the two results from the tests also fall within this bandwidth. Therefore best solution for the Koppejan method could be obtained with an iteration distance between $1d_{cone}$ and $4d_{cone}$.

Since only two correction factors could be determined from the test data it is believed that more tests are needed in order to validate the correction factors produced with the models of Vreugdenhil et al. (1994) and Koppejan and their resulting bandwidth. It is also believed that

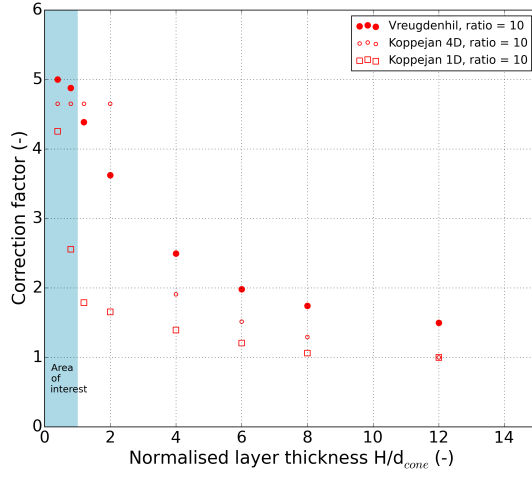
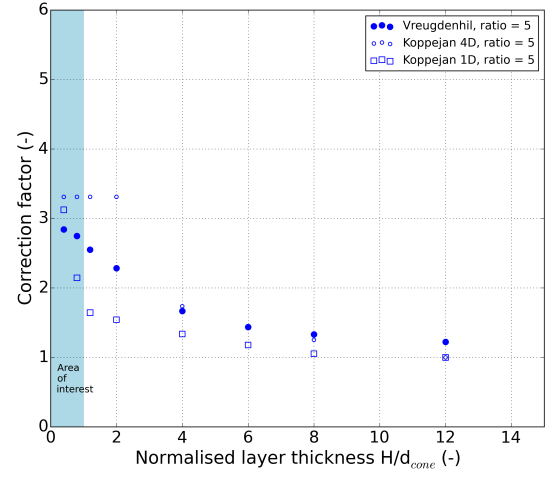
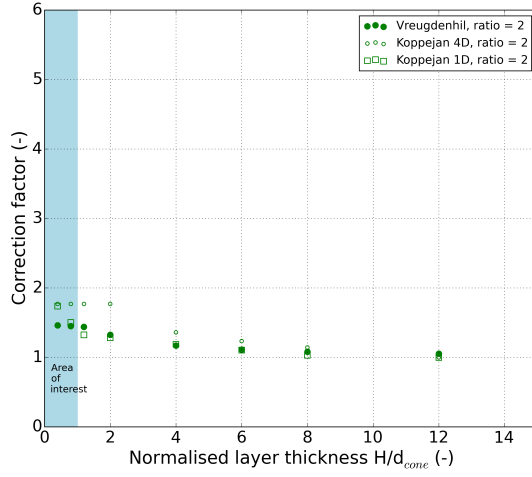
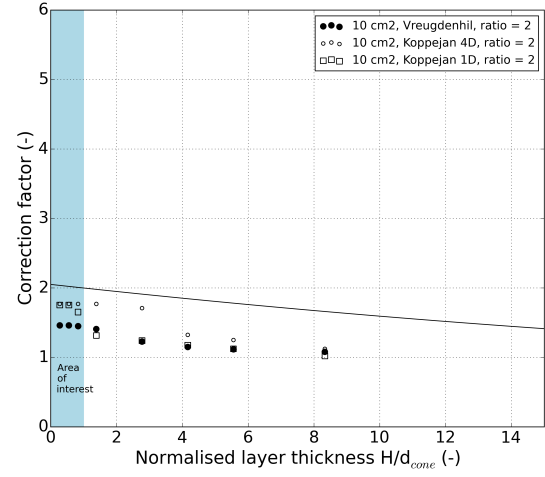
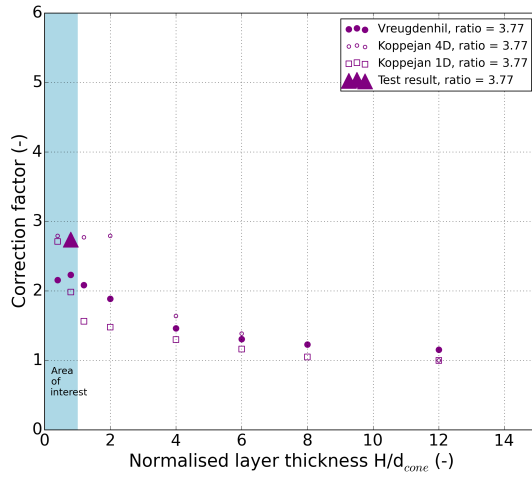
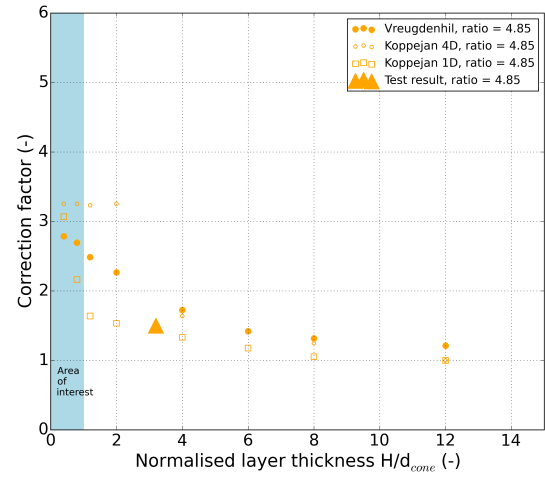

 (a) $Q_{char,ratio} = 10$

 (b) $Q_{char,ratio} = 5$

 (c) $Q_{char,ratio} = 2$

 (d) $Q_{char,ratio} = 2$ for 10 cm^2 cone

 (e) $Q_{char,ratio} = 3.77$, including test result

 (f) $Q_{char,ratio} = 4.85$, including test result

Figure 4.11: Computed correction factors and factors from experiments for different ratios of characteristic cone resistance

different correction factors could be found if tests are conducted at different stress levels. If more tests would be conducted, it is recommended that testing is conducted at higher stress levels as well.

4.4.4 Determination of a relationship

Since only two measurements are available for validating the numerical models, it does not make much sense to come with a detailed correlation for determining the thin layer correction factor for multiple layers. However, the parameters on which the correlation would depend can qualitatively be determined. The figures in section 4.4.3 already give some of these parameters, but there are more which could be important.

Layer thickness (H)

Since thicker layers produce cone resistances approaching characteristic cone resistance, layer thickness (relative to cone size) will have a major influence on the correction factor.

Layer configuration (H_{ratio})

All tests on layered samples presented in this research are done on samples with $H_{ratio}=1$, meaning that the soft and stiff layers have equal thickness. In field situations this may vary considerably, meaning that this feature of flaser bedding and other types of thin layering also needs to be considered when trying to formulate a definition of a correction factor.

Cone size (d_{cone})

Since layer thickness should be considered relative to the size of the cone (e.g. cone diameter), correction factors depend also on cone size.

Characteristic resistances ($q_{char,sand}$ and $q_{char,clay}$)

The magnitude of the difference in penetration mechanisms for sand and clay is determined by their characteristic cone resistances. Correction factor determination makes use of the ratio between these two characteristic resistances, therefore both are needed. Instead of the normalised characteristic cone resistances it is preferred to use the true cone resistance $q_{char,sand}$ and $q_{char,clay}$, since these are the actual measured resistances. This implies that also the stress level needs to be considered.

Stress level (σ'_v)

The correction factors presented in the previous sections are assumed not to depend on stress level, since the characteristic cone resistances are determined using CPT data normalised for stress level. All ratios presented in the previous sections are therefore ratios of normalised characteristic cone resistances, but it is believed that characteristic cone resistances depend more on stress level, since the characteristic cone resistances in this research are obtained from shallow CPT. Eventually it is preferred to be able to distinguish layering at different stress levels without the need of obtaining a correction factor via normalisation of the cone resistance.

Summarising all the above a qualitative formulation of the correction factors for thin layering can be defined as a function, defined as

$$K_H = f(H, H_{ratio}, d_{cone}, q_{char,sand}, q_{char,clay}, \sigma'_v) \quad (4.7)$$

4.5 Correcting field data

Figure 4.12a shows CPT data from the province of Groningen. From these measurements the liquefaction potential is calculated using the methods described in appendix A, shown in figure 4.12b. This figure is the same as the one presented in chapter 1 (figure A.1), and like figure A.1 the two horizontal dashed lines mark the boundaries of the layer that has been classified as flaser bedding during borehole log examination. An overview of the borehole log corresponding to these CPT results can be found in appendix C. The location of the samples taken for the borehole log was close the location where the CPT measurements were taken. It can be observed from figure 4.12b that the NPR method considers a part of the flaser bedding layer to be susceptible to liquefaction.

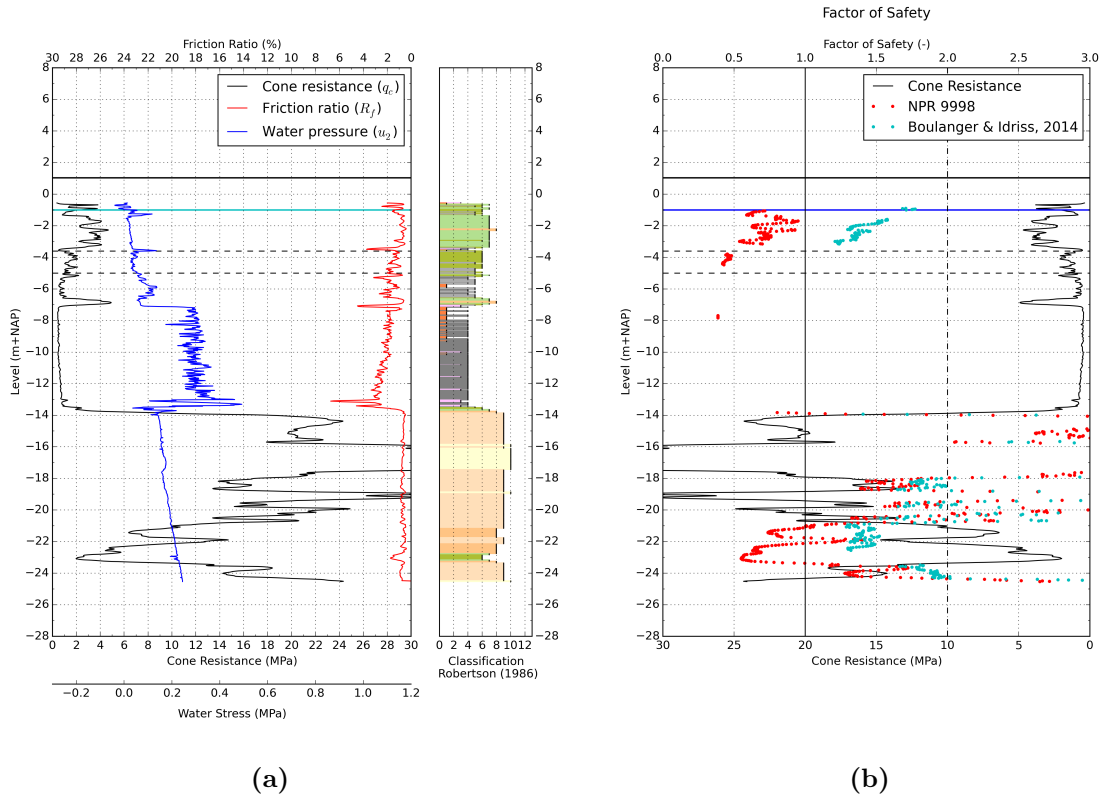


Figure 4.12: An original CPT and the calculated factors of safety according to a preliminary version of the NPR and Boulanger and Idriss (2014) for a typical soil profile in Groningen.

The original CPT shows that the cone resistance in the flaser bedding layer shows many little peaks and does not exceed a value of 2 MPa. Pore pressure in this layer is not showing a perfect linear line like below a depth of NAP -18 m, indicating that the layer does not contain a homogeneous sand layer. It also does not show a significant increase in pore pressure and constant high value for u_2 , meaning that the layer is not a homogeneous clay layer as well. The data originate from a standard GEF-file in which measurements are written every 2 cm of depth. Therefore zooming in on the thin layered part shall not give much more information on the very thin layers. It should be noted that this is the only CPT processed together with borehole inspection used in this report, thus it is unknown how other kind of flaser bedding formations can be characterized using CPT data.

The development of pore pressure during the physical tests from this research can be considered to be comparable to results found in the field test. This kind of pore pressure trend in combination with the cone resistance may be an indication for encountering a flaser bedding layer,

which may be used in other CPT classification processes. During the tests in this research it was found that based on u_2 measurements it is possible to point out the amount of clayey layers in the sample, only estimating the layer thickness is not easy using u_2 measurements.

Comparable to the method of correction by Robertson and Fear (1995) the correction technique used in this research is multiplying the measured cone resistance by a correction factor, defined as

$$q_c^* = K_H \cdot q_{cA} \quad (4.8)$$

where q_c^* is the characteristic cone resistance in the thin sand layers to be used in the liquefaction evaluation, K_H the thin layer correction factor and q_{cA} the measured thin layer cone resistance. Steps for application of the thin layer correction factor are:

1. Measure layer thicknesses from borehole log
2. Draw layering in CPT data corresponding to the borehole log
3. Estimate characteristic resistances, e.g. from nearby thick layers or from estimated $R_{d,e}$ and S_u
4. Investigate relationship for the determined ratio of characteristic cone resistances as shown in section 4.4.3
5. Determine correction factor for different layer thicknesses using the relationship from step 3
6. Apply these on the cone resistance in the sand layers using equation 4.8.

In the following part of this section these steps are applied on a part of the CPT data presented in figure 4.12. An attempt is made to correct the cone resistance.

1. and 2.: Layer thickness determination

Figure 4.13 shows a detailed classification based on the figure of the borehole log. A classification of the complete borehole log has been presented in appendix C. To look at the level of detail of thin layers a more detailed classification is needed.

The black dots represent the cone resistance samples taken with a frequency of 1 Hz at 20 mm/s. It can be concluded that there are very few samples taken in order to determine whether a certain data point is measured in sand or clay, also because it is difficult to say if the spacial variability is such that the same thin layers are present at the CPT location.

Since no higher frequency measurements are available it is believed that it is not correct to apply correction factors on resistances of which it is not certain in which layer these are measured. However, in order to provide some kind of example it is determined that all points in the area classified as flaser bedding can be considered to be measured in sand layers, where the layer thickness is determined at 0.5 cm.

3.: Estimating characteristic resistances

Determining characteristic cone resistances is not straightforward, since the exact characteristics of the soil layers are not known. If for example relative density measurements were available of sand layers, an estimation of the characteristic cone resistance could be made (e.g. by using the relationship by Baldi et al. (1986)).

However, also for this step an approximation can be made. Looking at a depth just below NAP -4.6 m, where more sand is found than clay, an estimation can be made of the ratio in characteristic cone resistances $Q_{char, ratio}$. It is not believed that the characteristic cone resistance in the sand layers is less than two times and more than five times as high as the characteristic resistance in clay. A ratio of 3.5 seems therefore to be reasonable.

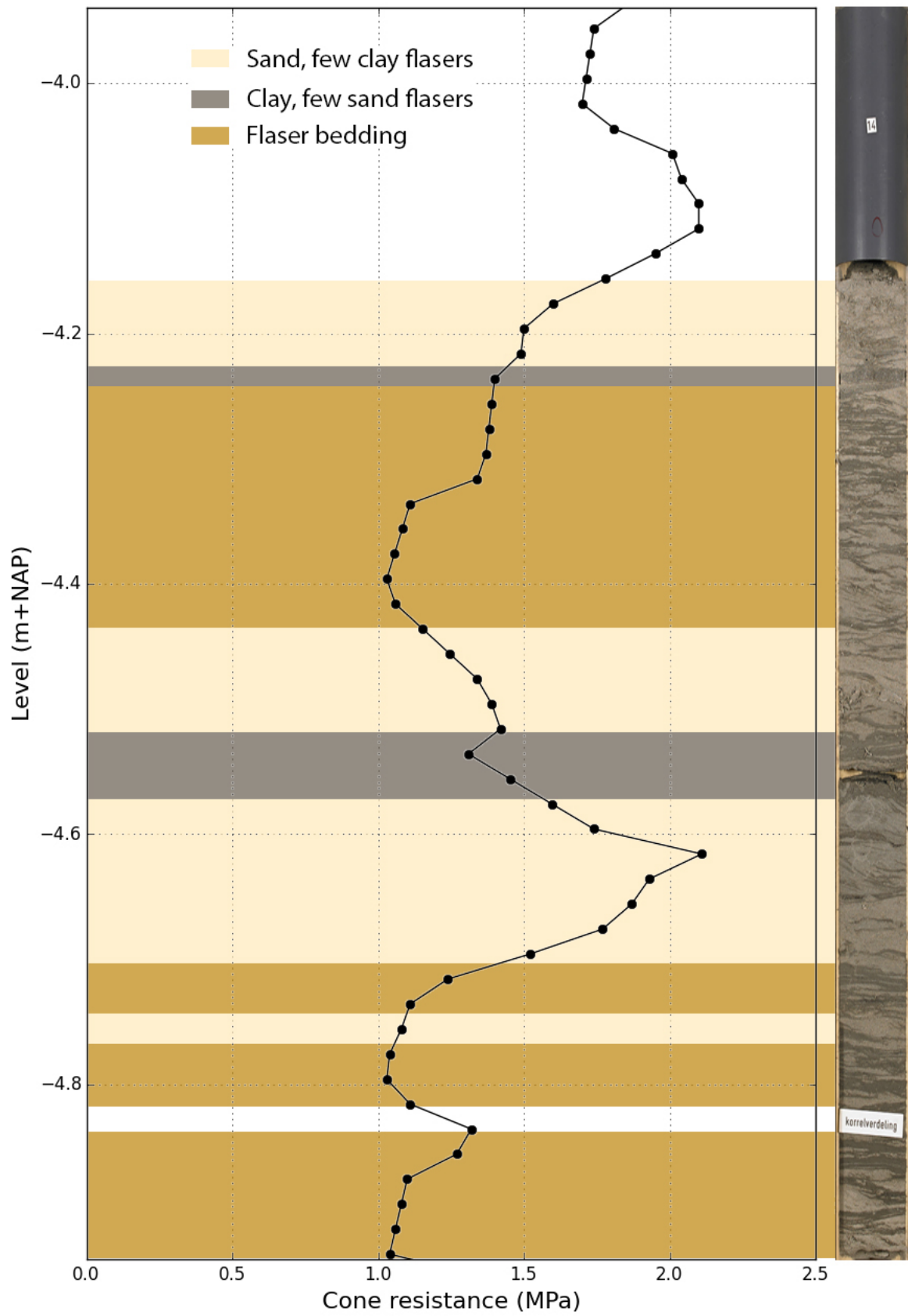


Figure 4.13: Considered section of the borehole log with corresponding measured cone resistance

4. and 5.: Correction factor determination

Since a 10 cm² cone was used ($d_{cone} = 36$ mm), the H/d_{cone} ratio is 0.14. Together with a $Q_{char, ratio}$ of 3.5 a correction factor can be determined. Since it is not yet known which method (Koppejan methods or Vreugdenhil et al. (1994)) is most valid, once again an estimation of the range is needed. Since a ratio of 3.5 approaches a ratio of 3.77, displayed in figure 4.11e, a slightly lower factor should be taken than determined from figure 4.11e. Where this figure gives a factor of 2.8 (also regarding the test result) for $H/d_{cone} = 0.14$, a factor of 2.6 is chosen for a $Q_{char, ratio}$ of 3.5.

6.: Correcting CPT data

The factor determined during the previous steps is used for correcting the cone resistance measured in layers classified to be flaser bedding in figure 4.13. The layer thickness of 0.5 cm seems to be more valid for the flaser bedding layer around NAP -4.3 m than for the bottom part in which more clay seems to be present. Therefore the correction factor of 2.6 can only be applied on the the flaser bedding layer around NAP -4.3 m.

5 Remarks

In order not to lose view on the bigger picture, some remarks to this research need to be made:

- Correction factors depend for a large amount on determination of characteristic resistances. The difference between the characteristic resistance for sand of the 8 cm and 2 cm configuration illustrates that even in a controlled laboratory environment it is still a challenge to obtain these characteristic cone resistances, especially for sand. In field situations the characteristic resistances cannot be measured, and so these need to be assumed or estimated based on for example relative density, which could prove to be quite uniform when flaser bedding is considered.
- One crucial comment in the NPR not been fully appreciated in this research: sand which is situated less than 0.25 m away from a clay-sand layer interface can be neglected during determination of its susceptibility to liquefaction. Therefore, all sand layers of 0.5 m or less bounded by two clay layers can be neglected according to the NPR, simply because the cone resistance in the sand is influenced by the clay layer and thus the characteristic cone resistance is unknown. This research may give an indication on what the cone resistance of the sand within the 0.25 m range would be (characteristically), so that also these sand layers can be evaluated for their susceptibility to liquefaction.
- In this research a penetration rate of 4 mm/s has been applied in order to have a sufficient amount data points over depth. It is not certain whether the correction factors determined with the test results from this research are influenced by the chosen penetration rate and whether a normal penetration rate would give different correction factors.
- Physical modelling conducted with PIV techniques showed that a difference in penetration mechanism can occur (Arshad et al. (2014)) at higher stress levels. Although the correction factors are developed based on normalised data, this feature of cone penetration can cause different correction factors.

6 Conclusions and recommendations

6.1 Conclusions

6.1.1 Research question and objective

The main research question of this thesis was: *What is the influence of multiple thin soft layers on the cone resistance of the intermediate sand layers and in which way can the CPT data be corrected for thin layers?*

Looking at the results of this research, it can be concluded that as layers get thinner, the cone resistance in the layered soil sections approach a value of the cone resistance slightly higher than the cone resistance in clay. This can be best observed comparing test results of tests on samples with 8 cm and 2 cm layering, where for very thin layers it is believed that the layered part will have a cone resistance of about 0.3 MPa, which is closer to the characteristic value of 0.22 MPa for clay than 1.0 MPa for sand. This difference may come from changing shapes of failure surfaces, of which it is believed that in layered soils the failure surface resembles the failure surface for clay more than for sand.

Based on test results and results of cone resistance simulations a range of correction factors has been presented. The results from physical testing could be used for validation of the numerical models, but since a limited amount of results were obtained complete validation was not possible. Correction factors can be applied by multiplying the measured cone resistance in the sand layers with the determined correction factor, which results in determination of design cone resistance. Sleeve friction and pore pressure measurements are not corrected using this factor. Since only two tests resulted in data points usable for validation of computed correction factors more tests are needed to obtain some amount of certainty in the computed correction factors.

The main objective of this thesis was to see whether it would be possible to design an experiment in a convenient and effective way in terms of time and means, which would be used for validation of calculation models. It can be concluded that the physical tests conducted can be well used for validation of the (analytical) models used for simulation. The data from this research may be used for validation of models not considered in this research as well (e.g. FEM or MPM simulations). Artificial samples can be effectively obtained in terms of time, means and reproducibility. If more research would be conducted it is believed that the way the test were conducted in this research can be continued.

6.1.2 General conclusions

- Determination of a correction factor depends on the ratio of characteristic cone resistances, not on absolute values. This implies that the same correction factor can be determined for different soil conditions. It also implies that for finding a corrected cone resistance (which is similar to a characteristic cone resistance) a correction factor is needed, but for determination of a correction factor again the characteristic cone resistance is required. This kind of circular referencing is considered to be the basis of the problem of finding a correction factor in the way proposed in this research.
- Considering the Koppejan method, for thin layers ($H < d_{cone}$) the maximum cone resistance seems to be best approached by an iteration distance of $4d_{cone}$, while for thicker layers ($H > d_{cone}$) the solution with a distance of $1d_{cone}$ seems to better match measured cone resistance for determination of $q_{c,I,gem}$ and $q_{c,II,gem}$. Since for thin layers the minimum solution of Koppejan is found well before reaching $4d_{cone}$, also shorter iteration distances can be chosen.

- The method of Vreugdenhil et al. (1994) in most cases seems to give results in between the large and small iteration distances of the Koppejan method, therefore it mostly does not give the best fitting solution. However, it is believed that it gives decent results considering an elastic analysis for an elasto-plastic problem.
- The correlation from Robertson and Fear (1995) seems to choose a conservative value for the ratio of characteristic resistances. For many higher ratios of characteristic resistances higher correction factors are found in simulations as well from test results. Meanwhile the correlation from Robertson and Fear (1995) seems to overestimate the correction factor for a ratio of characteristic cone resistances of 2.
- Borehole logs are necessary for correction factor determination. For determination of a correction factor the layer thickness is required, which can be best be determined by examining borehole logs. These borings should be taken close enough to the CPT location to make sure that spacial variability in CPT measurements is reasonably small.
- Further research is needed to validate the correction factors presented in chapter 4. At this point only two measurements can be drawn in figure 4.10. Although these measurements are considered to be within range of the simulations, validation requires more measurements, meaning that more tests on layered samples are needed.

6.1.3 Conclusions on physical modelling

- It is feasible to build up layered samples with the materials used in this research. It is also possible to build up the samples such that during testing boundary effects are minimised. It is believed that thinner layers than 2 cm can be prepared as well using the type of clay used in this research.
- It seems not to be possible to eliminate boundary effects from measured data, therefore boundaries affecting measurements is something that needs to be avoided. As long as the sand is loosely to intermediately packed it is believed that boundary effects are not to be noticed in the measurements in the centre of the cell with the dimensions of cell and cone as chosen in this research.
- Cross-sections of penetrated samples give a good indication under which circumstances the data of measured parameters is recorded (see appendix I). The averaging effect observed in the cone resistance of the thin layer test is something that can very well be explained using the accompanying cross-section. Also the behaviour of the pore pressure measurements can be explained using cross-sections. Therefore with relatively little extra work considerable insight can be obtained from these cross-sections.
- Using u_2 pore pressure transducers a good indication of the number of clay layers can be obtained, but the actual layer size is hard to determine, especially for layers thicker than the cone diameter (see results in appendix G).

6.2 Recommendations

6.2.1 General recommendations

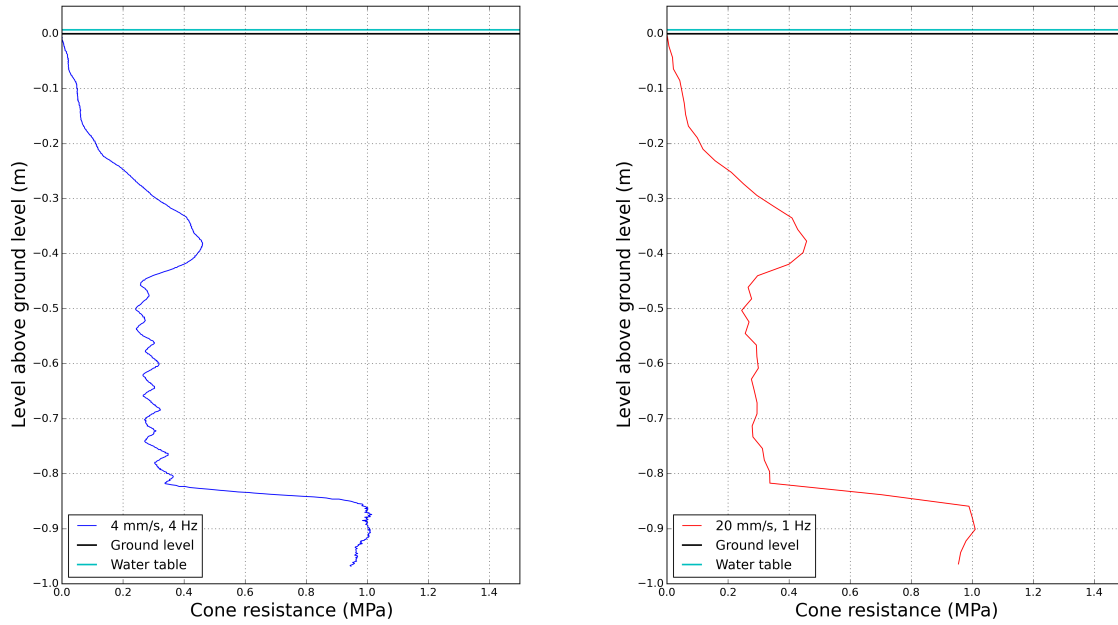
- When trying to detect thin layers, CPTs in the field should be performed with higher sampling frequency. Figure 6.1 gives an indication of how the cone resistance would be presented if the data were recorded at 1 Hz with a penetration rate of 20 mm/s (fig. 6.1b), representing default GEF presentation which is sometimes even field measurement frequency. Comparing it with the way the data was recorded during this research (fig. 6.1a) it can be concluded that field measurements could miss quite a level of detail if presented as a reduced data-set.

Since it was not necessary to detect thin layers in the past but rather thick, stiff layers upon which construction can be founded, it was not necessary to collect data of every millimetre of depth, but for detecting thin layers a smaller registration interval seems necessary. It is believed that the penetration rate of 20 mm/s should be unchanged because of a possible change in shape of the failure. Also the depth interval of GEF files, which 2 cm by default, needs to be considered when investigating thin layers.

- Additional adjustments to the Koppejan method could be made. To see whether the solution better fits on test data, it could be decided to change the principles of the trajectories. It is suggested to look at the trajectories which take the minimum encountered cone resistance as design resistance. It could be possible that taking the actual average of the whole trajectory without using minimum or maximum values could give a better result compared to test measurements.
- Besides adjusting the Koppejan method, the method of Vreugdenhil et al. (1994) could be adjusted as well. For every layer the distance to the cone location is considered, even if the layer is hundreds of times the diameter away from the cone. This feature is covered by parameter h and for multiple layers by h_j , which is believed to be the feature that may be adjusted to come to better fitting simulations.
- An attempt could be made to use cone resistance data as reverse input for the models used to simulate the cone resistance. In this research the input of the simulation models has been the characteristic cone resistance, which gives a simulated cone resistance. If cone resistance measurements from the field could be used to back calculate the characteristic resistances, less effort is needed for determination or estimation of the characteristic cone resistance. If the ratio of characteristic cone resistance does not need to be determined, issues as described in the general conclusions can be avoided. Back calculation could be a solution for the issue with the ratio of characteristic resistance, described as circular referencing. For example, estimation of the characteristic cone resistance in clay could be conveniently done using the rule of thumb $q_c = 20 \cdot S_u$, and with the location of layer interfaces known from borehole logging simulation can be made of the characteristic sand resistance and thus of the measured cone resistance.
- Although it was not within the boundaries of this research, it is believed that sleeve friction measurements are essential as well. Classification methods also make use of sleeve friction data, and so it is important that besides correcting the cone resistance also correcting sleeve friction needs to be considered in future research. Since the friction sleeve is normally considerably larger than the layer thickness, the sleeve friction is averaged over a certain number of layers, not giving a good indication of the actual friction encountered in a single thin layer.

6.2.2 Recommendations on physical modelling

- The change in shape of failure surfaces in layered samples could be investigated using PIV techniques. The shapes of the failure surfaces presented in this report (see section 2.2) are merely a non-proven indication based on separate failure surfaces in clay and sand. A better understanding of these shapes could help with understanding behaviour in cone resistance measurements.
- Physical modelling conducted with PIV techniques showed that a difference in shape of the failure surface (and potentially also change in penetration mechanism) can occur at higher stress levels, which can cause different correction factors. Therefore it is recommended to execute tests with surcharge and to develop a method for conveniently applying surcharge. This can be used to prove whether the correction factors, although normalised, depend on stress level.



(a) One measurement per 1 mm (4 mm/s, 4 Hz) (b) One measurement per 20 mm (20 mm/s, 1 Hz)

Figure 6.1: Presentation of the results of 6-TEST1 with different penetration ratios and sampling frequencies

- If during further research a higher level of resemblance to field conditions is required, a review of the utilised types of sand and clay should be performed. The combination of the chosen types of sand and clay could be an unrealistic combination encountered nowhere in the field. Also the properties of the chosen types may not give clear and optimal results.
- Making cross-sections and taking density samples should be continued. With not much effort a better idea of what happened during penetration and why it happened can be gained. Dismantling samples without examining it more carefully after penetration means that valuable information will be lost.
- The top and bottom layers could be made from clay instead of sand ('turn around' the configuration). It is believed that the phenomenon of critical depth is more of an issue with sand than for clay due to difference in failure surface. Choosing clay instead of sand for the top layer could cause critical depth to be located at shallower depth. If the correction is desired to be applied on thin sand layers there is no need for having large top and bottom sand layers, except that an indication of the characteristic resistance in sand is not available in this case.
- The use of a normal penetration rate of 20 mm/s should be considered in further testing, although some believe that using lower rates is not of great influence on measured cone resistance. When using a rate of 20 mm/s it is required that a sufficiently high sampling frequency can be used. Determining correction factors based on low penetration rates may give different results than when correction factors are determined using a standard penetration rate of 20 mm/s. Results from further testing with a normal penetration rate could indicate whether the penetration rate of 4 mm/s gave reasonable results applicable to field situations.
- To make sure that correction factors are not only applicable to the situation where sand and clay layer have equal thicknesses, tests should be performed on samples with other configu-

rations, where for example sand layers are of larger thickness than clay layers.

- Looking at the results of pore pressure measurements presented in appendix G it can be recommended to consider using u_1 pore pressure transducers, which may give more information for thin layers than u_2 measurements taken in this research.

References

- Ahmadi, M. M. and P. K. Robertson (2004). "Calibration chamber size and boundary effects for CPT qc measurements." In: *Proceedings of ISC-2 on Geotechnical and Geophysical Site Characterization*. Millpress, Rotterdam, pp. 829–833.
- Ahmadi, M. M. and P. K. Robertson (2005). "Thin-layer Effects on the CPT qc Measurement." In: *Canadian Geotechnical Journal* 42, pp. 1302–1317. ISSN: 0008-3674. DOI: [10.1139/t05-036](https://doi.org/10.1139/t05-036).
- Andrus, R. D., P. Piratheepan, B. S. Ellis, J. Zhang, and C. H. Juang (2004). "Comparing liquefaction evaluation methods using penetration-VS relationships." In: *Soil Dynamics and Earthquake Engineering* 24, pp. 713–721. ISSN: 02677261. DOI: [10.1016/j.soildyn.2004.06.001](https://doi.org/10.1016/j.soildyn.2004.06.001).
- Arshad, M., F. Tehrani, M. Prezzi, and R. Salgado (2014). "Experimental study of cone penetration in silica sand using digital image correlation." In: *Geotechnique* (7), pp. 551–569. DOI: [10.1680/geot.13.P.179](https://doi.org/10.1680/geot.13.P.179).
- Baldi, G., R. Bellotti, N. Ghionna, M. Jamiolkowski, and E. Pasqualini (1986). "Interpretation of CPT's and CPTU's. 2nd Part: Drained penetration of sands." In: *4th International Geotechnical Seminar, Field Instrumentation and In-Situ Measurements*. 1985, pp. 143–155.
- Beranek, W. J. (1987). "The Prediction of Damage to Masonry Buildings caused by Subsoil Settlements." In: *Heron* 32(4), pp. 55–93.
- Bolton, M. D., M. W. Gui, J. Laue, R. Renzi, J. Garnier, M. D. Bolton, G. Bagge, and J. F. Corte (1999). "Centrifuge cone penetration tests in sand." In: *Géotechnique* 49(4), pp. 543–552. ISSN: 0016-8505. DOI: [10.1680/geot.1999.49.4.543](https://doi.org/10.1680/geot.1999.49.4.543).
- Boulanger, R. W. and I. M. Idriss (2014). *CPT and SPT Based Liquefaction Triggering Procedures*. Tech. rep. Davis, CA, USA: University of California.
- Dost, B. and D. Kraaijpoel (2013). *The August 16, 2012 earthquake near Huizinge (Groningen)*. Tech. rep. January. De Bilt, The Netherlands: KNMI.
- Douwes Dekker, D. M. (1984). *Soil mechanics for Engineering Purposes, Part I and II - lecture book*.
- Geuze, E. C. W. A. (1961). "Discussions." In: *Proceedings of the Fifth International Conference on Soil Mechanics and Foundation Engineering*. Paris, France, pp. 245–247.
- Houlsby, G. T. and R. Hitchman (1989). "Discussion: Calibration chamber tests of a cone penetrometer in sand." In: *Géotechnique* 39(4), pp. 727–731. ISSN: 0016-8505. DOI: [10.1680/geot.1989.39.4.727](https://doi.org/10.1680/geot.1989.39.4.727).
- Ibsen, L. B. and L. Bodker (1994). *Baskarp Sand No 15*. Tech. rep. Aalborg, Denmark: Aalborg Universitet.
- Idriss, I. M. and R. W. Boulanger (2008). *Soil Liquefaction during Earthquakes*. Tech. rep. Monograph EERI MNO-12. Earthquake Engineering Research Institute.
- Joer, H. A., M. F. Randolph, and Y. H. Liew (1996). "Interpretation of Cone Resistance in Layered Soils." In: *7th Australia New Zealand Conference on Geomechanics: Geomechanics in a Changing World*. Ed. by M. B. Jaksa, W. S. Kaggwa, and D. A. Cameron. Adelaide, Australia, pp. 92–97.
- Kim, K., M. Prezzi, R. Salgado, and W. Lee (2010). "Penetration rate effects on cone resistance measured in a calibration chamber." In: *Proceedings of the 2nd International Symposium on*

- Cone Penetration Testing (CPT '10)*. Huntington Beach, CA, USA, pp. 1025–1030. ISBN: 9780415621366.
- Laboratorium voor Grondmechanica (1982). *Penetrometerproef*. Tech. rep. Delft, The Netherlands: Laboratorium voor Grondmechanica Delft.
- Liao, S. S. C. and R.V. Whitman (1986). “Overburden Correction Factors for SPT in Sand.” In: *Journal of Geotechnical Engineering* 112(3), pp. 373–377. ISSN: 0733-9410. DOI: [10.1061/\(ASCE\)0733-9410\(1986\)112:3\(373\)](https://doi.org/10.1061/(ASCE)0733-9410(1986)112:3(373)).
- Lubking, P. (1997). *Soft Soil Correlaties - 374590*. Tech. rep. Delft, The Netherlands: Grondmechanica Delft.
- Lunne, T., P. K. Robertson, and J. J. M. Powell (1997). *Cone Penetration Testing in Geotechnical Practice*. First edition. Blackie Academic & Professional. ISBN: 0751403938.
- Meijers, P. (2014). *Effecten aardbevingen op kritische infrastructuur - Verwekingsstudie*. Tech. rep. Delft, The Netherlands: Deltares.
- Meyerhof, G. G. (1952). “Recherches sur la force portante des pieux.” In: *Annales de l'Inst. du Bâtiment et des Travaux Publ.* 16.
- Młynarek, Z., S. Gogolik, and J. Póltorak (2012). “The effect of varied stiffness of soil layers on interpretation of CPTU penetration characteristics.” In: *Archives of Civil and Mechanical Engineering* 12, pp. 253–264. DOI: [10.1016/j.acme.2012.03.013](https://doi.org/10.1016/j.acme.2012.03.013).
- Mo, P. Q. (2014). “Centrifuge Modelling and Analytical Solutions for the Cone Penetration Test in Layered Soils.” PhD thesis. University of Nottingham.
- Mo, P. Q., A. M. Marshall, and Yu, H. A. (2015). “Centrifuge modelling of cone penetration tests in layered soils.” In: *Géotechnique* 65(6), pp. 468–481. DOI: [10.1680/geot.14.P.176](https://doi.org/10.1680/geot.14.P.176).
- Muromachi, T. (1981). “Cone penetration testing in Japan.” In: *Cone penetration testing and experience*, pp. 49–75.
- NAM (2013). *Technical Addendum to the Winningsplan Groningen 2013*. Tech. rep. Nederlandse Aardolie Maatschappij BV.
- NAM (2015). *Aardgas uit het Groningen-gasveld*. Nederlandse Aardolie Maatschappij BV. URL: <http://www.namplatform.nl/gaswinning/het-groningen-gasveld.html> (visited on 03/04/2015).
- Nederlands Normalisatie-instituut (2012). *NEN-EN-ISO 22476-1, Geotechnical investigation and testing - Field testing - Part 1: Electrical cone and piezocone penetration test*. Tech. rep. Delft, The Netherlands: Nederlands Normalisatie-instituut.
- Nederlands Normalisatie-instituut (2015). *NPR 9998:2015*. Tech. rep. Delft, The Netherlands: Nederlands Normalisatie-instituut.
- NEN 9997-1* (2012). Tech. rep. Delft, The Netherlands: Nederlands Normalisatie-instituut.
- Poulsen, R., B. N. Nielsen, and L. B. Ibsen (2013). “Correlation between cone penetration rate and measured cone penetration parameters in silty soils.” In: *Proceedings of the 18th International Conference on Soil Mechanics and Geotechnical Engineering*. Paris, France, pp. 603–606.
- Puech, A. et al. (1974). “Contribution to the study of static and dynamic penetrometers.” In: *Proceedings of the 1st European Symposium on Penetration Testing*. Stockholm, Sweden.
- Robertson, P. K., R. G. Campanella, D. Gillespie, and J. Grieg (1986). “Use of piezometer cone data.” In: *In Situ '86*. Blacksburg, VA, USA.

- Robertson, P. K. and C. E. Fear (1995). "Liquefaction of Sands and its Evaluation." In: *IS-Tokyo '95, Proceedings of the 1st International Conference on Earthquake Geotechnical Engineering*. Ed. by K. Ishihara. Balkema, Rotterdam: Tokyo, Japan, pp. 1253–1289.
- Robertson, P. K. and C. E. Wride (1997). "Cyclic liquefaction and its evaluation based on SPT and CPT." In: *NCEER Workshop on Evaluation of Liquefaction Resistance of Soils*.
- Salgado, R., J. K. Mitchell, and M. Jamiolkowski (1998). "Calibration Chamber Size Effects on Penetration Resistance in Sand." In: *Journal of Geotechnical and Geoenvironmental Engineering*(9), pp. 878–888. DOI: [10.1061/\(ASCE\)1090-0241\(1998\)124:9\(878\)](https://doi.org/10.1061/(ASCE)1090-0241(1998)124:9(878)).
- Silva, M. and M. D. Bolton (2004). "Centrifuge penetration tests in saturated layered sands." In: *Proceedings ISC-2 on Geotechnical and Geophysical Site Characterization*. Ed. by Viana da Fonseca and Mayne. Millpress, Rotterdam, pp. 377–384.
- Smits, F. P. (1977). "Sonderen in zand - een theoretische basis voor analyse van de conusweerstand." In: *Proceedings of FUGRO Sondeersymposium*, pp. 31–42.
- Taylor, J. R. (1997). *An Introduction to Error Analysis, second edition*. University Science Books. ISBN: 0-935702-42-3.
- Teferra, A. (1975). "Beziehungen zwischen Reibungswinkel, Lagerungsdichte und Sondierwiderständen nichtbindiger Böden mit verschiedener Kornverteilung." *Forschungsberichte aus Bodenmechanik und Grundbau*. TH-Aachen.
- Treadwell, D. D. (1976). "The influence of gravity, prestress, compressibility, and layering on soil resistance to static penetration." PhD thesis. University of California at Berkeley.
- Van der Poel, J. T. and F. M. Schenkeveld (1998). "A preparation technique for very homogeneous sand models and CPT research." In: *Proceedings of the International Conference on Centrifuge Modelling (Centrifuge '98)*. Ed. by T. Kimura, O. Kusakabe, and J. Takemura. Balkema, Rotterdam: Tokyo, Japan, pp. 149–154. ISBN: 9054109866.
- Vreugdenhil, R., R. Davis, and J. Berrill (1994). "Interpretation of Cone Penetration Results in Multilayered Soils." In: *International Journal for Numerical and Analytical Methods in Geomechanics* 18, pp. 585–599. ISSN: 0363-9061. DOI: [10.1002/nag.1610180902](https://doi.org/10.1002/nag.1610180902).
- Walker, J. and H. S. Yu (2010). "Analysis of the cone penetration test in layered clay." In: *Géotechnique* 60(12), pp. 939–948. ISSN: 0016-8505. DOI: [10.1680/geot.7.00153](https://doi.org/10.1680/geot.7.00153).
- Wiąckowski, Z. (2004). "The material point method in large strain engineering problems." In: *Computer Methods in Applied Mechanics and Engineering* 193(39-41), pp. 4417–4438. DOI: [10.1016/j.cma.2004.01.035](https://doi.org/10.1016/j.cma.2004.01.035).
- Xu, X. (2007). "Investigation of the End Bearing Performance of Displacement Piles in Sand." PhD Thesis. The University of Western Australia.
- Xu, X. and B. M. Lehane (2008). "Pile and penetrometer end bearing resistance in two-layered soil profiles." In: *Géotechnique* 58(3), pp. 187–197. ISSN: 0016-8505. DOI: [10.1680/geot.2008.58.3.187](https://doi.org/10.1680/geot.2008.58.3.187).
- Youd, T. L. and I. M. Idriss (2001). "Liquefaction Resistance of Soils : Summary Report From the 1996 NCEER and 1998 NCEER/NSF Workshops on Evaluation of Liquefaction Resistance of Soils." In: *Journal of Geotechnical and Geoenvironmental Engineering* 127(April), pp. 297–313.
- Yue, Z. Q. and J. H. Yin (1999). "Layered elastic model for analysis of cone penetration testing." In: *International Journal for Numerical and Analytical Methods in Geomechanics* 23(8), pp. 829–843.

Bibliography

- Baziar, M. H. and R. Ziaie Moayed (2006). "Evaluation of Cone Penetration Resistance in Loose Silty Sand Using Calibration Chamber." In: *International Journal of Civil Engineering* 4(2), pp. 106–119.
- Gui, M. W. and D. S. Jeng (2009). "Application of cavity expansion theory in predicting centrifuge cone penetration resistance." In: *The Open Civil Engineering Journal* 3, pp. 1–6. ISSN: 18741495. DOI: [10.2174/1874149500903010001](https://doi.org/10.2174/1874149500903010001).
- Korff, M., H. M. G. Kruse, T. P. Stoutjesdijk, J. Bredeveld, G. A. Van der Ham, P. Holscher, G. De Lange, P. Meijers, E. Vastenburger, T. Vermaas, and M. A. T. Visschedijk (2013). *Effecten geïnduceerde aardbevingen op kritische infrastructuur Groningen*. Tech. rep. Deltares.
- Krage, C. P. and J. T. DeJong (2014). "Variable Penetration Rate Cone Testing in Sands with Fines." MA thesis. Davis, CA, USA: University of California.
- Mo, P. Q., A. M. Marshall, and H. S. Yu (2014). "Cavity expansion analysis for the interpretation of CPT data in layered soils." In: *Proceedings of the 3rd International Symposium on Cone Penetration Testing (CPT '14)*. Las Vegas, NV, USA, pp. 331–338.
- Robertson, P. K. (1990). "Soil classification using the cone penetration test." In: *Canadian Geotechnical Journal* 27, pp. 151–158. ISSN: 0008-3674. DOI: [10.1139/t90-014](https://doi.org/10.1139/t90-014).
- Robertson, P. K. (2009). "Interpretation of cone penetration tests - a unified approach." In: *Canadian Geotechnical Journal* 46, pp. 1337–1355. ISSN: 0008-3674. DOI: [10.1139/T09-065](https://doi.org/10.1139/T09-065).
- Salgado, R. (2013). "The mechanics of cone penetration: Contributions from experimental and theoretical studies." In: *Geotechnical and Geophysical Site Characterization 4*. Ed. by Coutinho and Mayne. Taylor & Francis Group, pp. 131–153. ISBN: 9780415621366. DOI: [10.1201/b13251-9](https://doi.org/10.1201/b13251-9).
- Sturm, H. (2013). "The tip resistance in layered soils during static penetration." In: *Proceedings of the 18th International Conference on Soil Mechanics and Geotechnical Engineering*. Paris, France, pp. 817–820.

A CPT based liquefaction evaluation

Contents

A.1	Liquefaction evaluation in the NPR	A-2
A.2	NPR 9998 method	A-3
A.3	Boulanger and Idriss (2014) method	A-4

This appendix describes the methods used in the NPR and used by Boulanger and Idriss (2014) for evaluating the liquefaction potential of soil layers based on CPT data.

Figure A.1 shows a cone resistance result for a typical Groningen soil profile together with the result of the calculations for evaluation of the liquefaction potential described in section A.1. Classification of this layer has been done examining the accompanying borehole log. The two horizontal dashed lines mark the boundaries of the layer that has been classified as flaser bedding during borehole log examination. Factor of safety calculation is done considering a PGA value of $0.24 g$ and $M_w = 5$. A photo of the layer containing flaser bedding from the borehole log can be found in figure C.1 together with a description in table C.1 in appendix C.

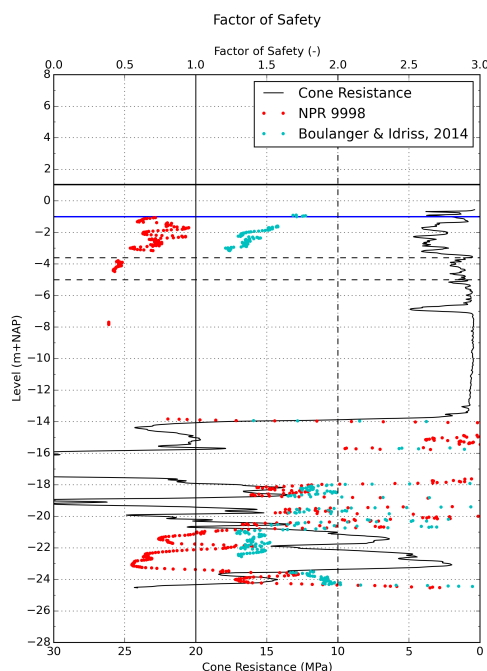


Figure A.1: Cone resistance data and the calculated factors of safety according the NPR and Boulanger and Idriss (2014) for a typical soil profile in Groningen.

Figure A.1 shows that the NPR method calculates a factor of safety below 0.5 for a part of the flaser bedding, while the method of Boulanger and Idriss (2014) considers the layer not to be susceptible to cyclic liquefaction. Although it is mentioned the NPR does not decide whether to include FC in determination of the normalised cone resistance. In figure A.1 the fines content has not been taken into account and a slightly different r_d factor has been implemented which has been used in a preliminary version of the NPR. This can explain the discrepancy between the safety factors of the NPR and Boulanger and Idriss (2014) methods.

A.1 Liquefaction evaluation in the NPR

Looking at the geotechnical aspect of the NPR 9998, liquefaction is considered to be one of the most important hazards during earthquakes. In the code NEN-EN 1998-5 annex B, a method for calculating susceptibility to soil to liquefaction is given based on the method of Youd and Idriss (2001). For induced earthquakes this method is believed to provide an insufficient level of safety, and therefore a more recent method is used in the NPR as described in EERI MNO-12 by Idriss and Boulanger (2008). This method describes how liquefaction susceptibility can be evaluated using CPT (or SPT) data (see section 2.1). The latest update of this method from Boulanger and Idriss (2014) makes some changes in the 2008 method and thus shows differences with the NPR method. This update is not implemented in the NPR.

Meijers (2014) has conducted tests on undisturbed and artificially built soil samples from Groningen and compared the liquefaction susceptibility derived from testing with the susceptibility according to EERI MNO-12. Similar results were found and so it was concluded that the method of EERI MNO-12 is applicable to the situation in Groningen, which forms the basis for the method used in the NPR. The method in the NPR consists of determining the factor of safety against cyclic liquefaction γ_L , defined as

$$\gamma_L = \frac{CRR_{7.5}}{CSR} \cdot MSF \cdot K_\sigma \cdot K_\alpha \quad (\text{A.1})$$

where γ_L is the factor of safety against liquefaction at certain level, $CRR_{7.5}$ the Cyclic Resistance Ratio at earthquake magnitude $M_w = 7.5$, CSR the Cyclic Stress Ratio, MSF the Magnitude Scaling Factor, K_σ a correction factor for isotropic stress state and K_α a correction factor for static shear stress.

NEN-EN 1998-5 recommends a safety factor of 1.25 as a limiting value below which a soil is considered to be susceptible to (complete) liquefaction. According to the NPR, up to a safety factor of 2.0 generation of excess pore pressure should be taken into account, which can be described as partial liquefaction.

The factors used to calculate the factor of safety consist of empirical correlations, of which some depend directly or indirectly on the (normalised) cone resistance (see section 2.1):

- The cyclic resistance ratio (CRR) can be seen as the resistance of soil to liquefaction. $CRR_{7.5}$ depends entirely on the normalised cone resistance q_{c1N} .
- CSR can be considered as the level of cyclic loading on the soil caused by an earthquake (Andrus et al. (2004)). It partly depends on total and effective vertical stresses. For determining these stresses, cone resistance and friction ratio can be used for soil classification and thus for unit weight and stress determination.
- K_σ depends on both effective stress and normalised cone resistance, where the effective stress can be estimated from cone resistance and friction ratio as well.

The MSF and K_α are not determined using data derived from CPTs.

The NPR method is derived from EERI MNO-12 by Idriss and Boulanger (2008), which is an earlier version of Boulanger and Idriss (2014). Therefore the way the factor of safety against liquefaction is calculated in both methods considered is the same, namely equation A.1. The parameters are calculated in different ways comparing both methods. Only the CSR is calculated the same way in both methods and is defined as

$$CSR = 0.65 \cdot \frac{PGA}{g} \frac{\sigma_v}{\sigma'_v} r_d \quad (\text{A.2})$$

where PGA is the peak ground acceleration in m/s^2 , g the gravitational acceleration in m/s^2 , σ_v the total vertical stress in kPa, σ'_v the effective vertical stress before an earthquake in kPa and r_d is a shear stress reduction factor over depth.

In the next sections determination of the parameters from equation (A.1) is considered.

A.2 NPR 9998 method

The NPR method is published in Nederlands Normalisatie-instituut (2015), appendix E. The next sections describe the method presented in appendix E of the NPR.

Determination of $\text{CRR}_{7.5}$

First, a correction factor for the local stress level is defined as

$$C_N = \left(\frac{p_a}{\sigma'_v} \right)^m \quad (\text{A.3})$$

where C_N is a overburden correction factor for the local stress level, p_a the atmospheric pressure ($p_a = 0.1$ MPa), σ'_v the effective vertical stress at the moment of testing in MPa and m is a dimensionless parameter, for which from a practical point of view a value of 0.5 is taken. The normalised cone resistance q_{c1N} is determined as

$$q_{c1N} = \frac{C_N \cdot q_c}{p_a} \quad (\text{A.4})$$

where q_c is the measured cone resistance in MPa and p_a the atmospheric pressure assumed to be 0.1 MPa (= 100 kPa). The NPR notes that the effect of the FC could also be taken into account by adding a function of the FC to the normalised cone resistance according to

$$q_{c1Ncs} = q_{c1N} + \Delta q_{c1N} \quad (\text{A.5})$$

where

$$\Delta q_{c1N} = 5.4 + \left(\frac{q_{c1N}}{16} \right) \cdot \exp \left(1.63 + \frac{9.7}{\text{FC} + 0.01} - \frac{15.7}{(\text{FC} + 0.01)^2} \right) \quad (\text{A.6})$$

where the fines content depends on q_{c1N} and the $\text{CRR}_{7.5}$, used as a percentage. If q_{c1Ncs} is calculated its value should be used instead of the value for q_{c1N} .

Next, $\text{CRR}_{7.5}$ is determined as

$$\text{CRR}_{7.5} = \exp \left(\frac{q_{c1N}}{540} + \left(\frac{q_{c1N}}{67} \right)^2 - \left(\frac{q_{c1N}}{80} \right)^3 + \left(\frac{q_{c1N}}{114} \right)^4 - 3 \right) \quad (\text{A.7})$$

Determination of r_d

This factor takes account for the assumption that the CSR is not constant over depth. Its value determined in the NPR is equal to the way it is presented in method of Boulanger and Idriss (2014), found in the next section.

Determination MSF

The MSF takes into account duration effects like the number and relative amplitudes of loading cycles on the triggering of liquefaction (Boulanger and Idriss (2014)). In general a larger earthquake will generate longer signals with more load cycles, which results in a lower value for the MSF. It is currently assumed that for the situation in Groningen a maximum expected value of magnitude would be $M_w = 5.0$. According to the method in EERI MNO-12, for earthquakes

with a magnitude $M_w \leq 5.0$ the MSF is equal to 1.8, which is the value used in the calculations according to the NPR. In the NPR it is stated that if it is concluded that account has to be taken for higher magnitude earthquakes than currently expected, the value of the MSF should be used during calculation.

Determination K_σ

This factor takes into account that at higher stress levels with the same CSR the liquefaction potential increases. K_σ is calculated using the following equations

$$C_\sigma = \frac{1}{37.3 - 8.27 \cdot q_{c1N}^{0.264}} \quad \text{with } C_\sigma \leq 0.3 \quad (\text{A.8})$$

$$K_\sigma = 1 - C_\sigma \ln \left(\frac{\sigma'_v}{p_{ref}} \right) \quad \text{with } K_\sigma \leq 1.1 \quad (\text{A.9})$$

where p_{ref} is equal to 100 kPa.

Determination K_α

The factor K_α takes into account ground level orientation. The NPR considers only a horizontally oriented ground level for which K_α is equal to 1. If ground level is not horizontal, the value of K_α can be found in Idriss and Boulanger (2008).

A.3 Boulanger and Idriss (2014) method

The method of Boulanger and Idriss (2014) as described in the following sections are taken from Boulanger and Idriss (2014). Compared to the NPR method, there is quite some difference in determination of $CRR_{7.5}$ and r_d .

Determination of $CRR_{7.5}$

Determination of $CRR_{7.5}$ depends on the parameter q_{c1Ncs} , the equivalent clean sand cone resistance. The difference compared to q_{c1N} is that the equivalent cone resistance is adjusted for the fines content FC by adding Δq_{c1N} to the normalised cone resistance q_{c1N} , written as

$$q_{c1Ncs} = q_{c1N} + \Delta q_{c1N} \quad (\text{A.10})$$

where q_{c1Ncs} is the equivalent clean sand cone resistance in MPa, q_{c1N} the normalised cone resistance in MPa and Δq_{c1N} is an adjustment for the fines content: $\Delta q_{c1N} = f(FC)$. Similar to the NPR method also a correction factor for the local stress level is defined as

$$C_N = \left(\frac{p_a}{\sigma'_v} \right)^m \leq 1.7 \quad (\text{A.11})$$

with m defined as

$$m = 1.338 - 0.249 \cdot q_{c1Ncs}^{0.264} \quad (\text{A.12})$$

and p_a the atmospheric pressure assumed to be 100 kPa and σ'_v is the effective vertical stress in kPa. The normalised cone resistance is determined as follows with

$$q_{c1N} = C_N \frac{q_c}{p_a} \quad (\text{A.13})$$

For determining the influence of the fines, the FC is determined according to Robertson and Wride (1997). First the cone resistance and friction ratio are normalised:

$$Q = \left(\frac{q_c - \sigma_{vc}}{p_a} \right) \left(\frac{p_a}{\sigma'_v} \right)^n \quad (\text{A.14})$$

$$F = \left(\frac{f_s}{q_c - \sigma_v} \right) \cdot 100\% \quad (\text{A.15})$$

where q_c is the measured cone resistance and f_s is the measured sleeve friction, both in MPa, and n is a factor that varies from 0.5 in sands to 1.0 in clays.

$$I_c = \left[(3.47 - \log(Q))^2 + (1.22 + \log(F)) \right]^{0.5} \quad (\text{A.16})$$

Where I_c is a soil behaviour type index for determining the FC as

$$FC = 80 (I_c + C_{FC}) - 137 \quad (\text{A.17})$$

It is assumed that the fitting parameter C_{FC} that is determined based on site-specific data, is equal to 0.

$$\Delta q_{c1N} = \left(11.9 + \frac{q_{c1N}}{14.6} \right) \exp \left(1.63 - \frac{9.7}{FC + 2} - \left(\frac{15.7}{FC + 2} \right)^2 \right) \quad (\text{A.18})$$

Now q_{c1N} and Δq_{c1N} combined form q_{c1Ncs} , which is used to determine $CRR_{7.5}$:

$$CRR_{7.5} = \exp \left(\frac{q_{c1Ncs}}{113} + \left(\frac{q_{c1Ncs}}{1000} \right)^2 - \left(\frac{q_{c1Ncs}}{140} \right)^3 + \left(\frac{q_{c1Ncs}}{137} \right)^4 - 2.80 \right) \quad (\text{A.19})$$

Because q_{c1Ncs} is needed to determine m , which is needed to ultimately determine q_{c1Ncs} itself, some iteration is needed. It seems that with a number of two or three iterations the solution is sufficiently stable, so not a lot of effort is needed for determination of the CRR.

Determination of r_d

This factor takes account for the assumption that the CSR is not constant over depth. It can be determined using the equations below.

$$r_d = \exp(\alpha(z) + \beta(z) \cdot M) \quad (\text{A.20})$$

$$\alpha(z) = -1.012 - 1.126 \cdot \sin \left(\frac{z}{11.73} + 5.133 \right) \quad (\text{A.21})$$

$$\beta(z) = 0.106 + 0.118 \cdot \sin \left(\frac{z}{11.28} + 5.142 \right) \quad (\text{A.22})$$

Determination MSF

In the 2014 method, Boulanger and Idriss (2014) give an expression for the MSF which is also used in the previous version presented in the EERI MNO-12. This expression is applicable for sands:

$$MSF = 6.9 \cdot \exp \left(\frac{-M_w}{4} \right) - 0.058 \leq 1.8 \quad (\text{A.23})$$

Boulanger and Idriss (2014) make a remark on the maximum value of the equation above: "*The value of 1.8 is obtained by considering the time series of stress induced by a small magnitude earthquake to be dominated by single pulse of stress (...), with all other stress cycles to be sufficiently small to neglect*". Considering that the earthquakes in Groningen are of relative small magnitude and are also mostly dominated by a single pulse, it seems fair to take a value for the MSF of 1.8. Besides this, Boulanger and Idriss (2014) in the 2014 version also give a more general form for sands and clays:

$$MSF_{max} = 1.09 + \left(\frac{q_{c1Ncs}}{180} \right)^3 \leq 2.2 \quad (\text{A.24})$$

$$MSF = 1 + (MSF_{max} - 1) \left(8.64 \exp \left(\frac{-M}{4} \right) - 1.325 \right) \quad (\text{A.25})$$

This method of calculating the MSF is only noted here, but not taken into account with the calculations presented in the report.

Determination K_σ

This factor is determined similar to the NPR method:

$$C_\sigma = \frac{1}{37.3 - 8.27 \cdot q_{c1Ncs}^{0.264}} \leq 0.3 \quad (\text{A.26})$$

$$K_\sigma = 1 - C_\sigma \ln \left(\frac{\sigma'_v}{p_{ref}} \right) \leq 1.1 \quad (\text{A.27})$$

Where p_{ref} is equal to 100 kPa.

Determination K_α

Similar to the NPR method, K_α takes ground level orientation and accompanying stress situation into account. In this thesis orientation of ground level is considered to be horizontal, making K_α equal to 1.

B Classifying soil using the Robertson et al. (1986) method

Robertson, Campanella, et al. (1986) developed a method to classify soil using CPT data. At a certain depth at which cone resistance and sleeve friction measurements are available, the soil can be assigned to one of the twelve zones based on cone resistance and friction ratio. The diagram used for classification can be found in figure B.1.

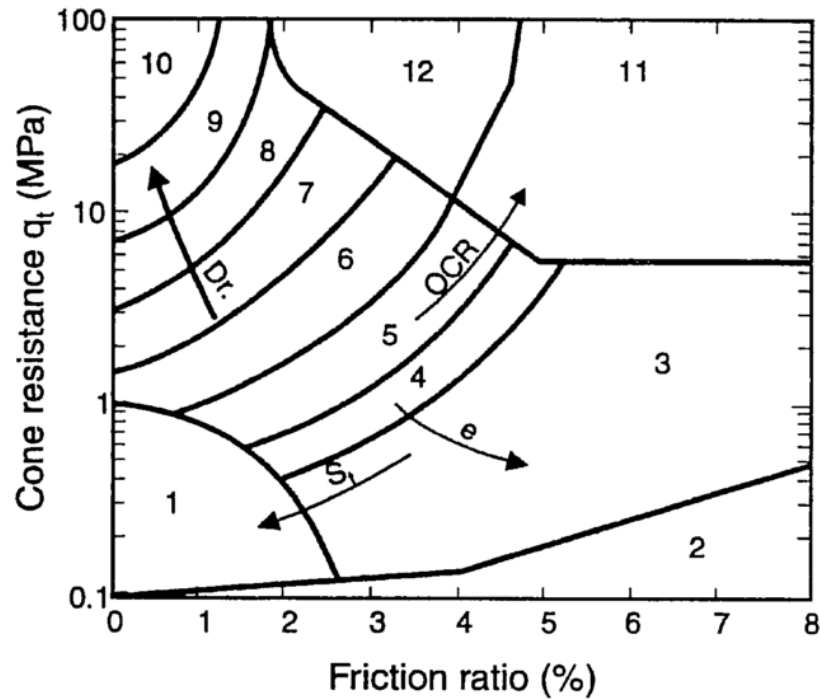


Figure B.1: Simplified soil behaviour type classification for standard electric friction cone, after Robertson, Campanella, et al. (1986) .

After assigning a classification zone to the measurements at certain depth, the unit weight is estimated using table B.1. These unit weights are used for estimation of the vertical stresses, used in the liquefaction evaluation.

Table B.1: Estimates of unit weights based on soil description, from Lunne et al. (1997)

Zone	Soil behaviour type	Approx. unit weight [kN/m ³]
1	Sensitive fine grained	17.5
2	Organic material	12.5
3	Clay	17.5
4	Silty clay to clay	18
5	Clayey silt to silty clay	18
6	Sandy silt to clayey silt	18
7	Silty sand to sandy silt	18.5
8	Sand to silty sand	19
9	Sand	19.5
10	Gravelly sand to sand	20
11	Very stiff fine grained (OC or cemented)	20.5
12	Sand to clayey sand (OC or cemented)	19

C Borehole logs and description

Table C.1: Geological description borehole 1, displayed in figure C.1.

Base level [m relative NAP]	Description	Deposition	Judgement liquefaction susceptibility	Grain size distr.
-1.3	Sandy clay with few sand inclusions, grey, sand in lamina	Tidal channel	Not susceptible	
-2.9	Fine sand, laminated, with few clay flasers (notably at base and top)	Tidal channel	Susceptible	-1.85 - 2.7
-3.6	Sand and clay, (very) irregular layered	Tidal channel	Not susceptible	
-5	Sand and clay, laminated (flaser bedding), grey	Tidal channel	Not susceptible	-4.85
-6.5	Clay with many very fine sand lenses (with shelly material), clay intervals up to 30 cm, sand intervals to 3 cm, black (anoxic)	Tidal channel	Not susceptible	
-7	Sand, fine, laminated, very little organic matter, slightly silty	Tidal channel	Susceptible	-6.75
-10.5	Clay with sand inclusions, minor perturbation	Lagoonal	Not susceptible	
-13.3	Clay ("bekkenklei"), organic (no roots), dark grey	Lagoonal	Not susceptible	
-15	Sand ("dekzand II"), fine, finely laminated, 5cm organic top ("podzol")	Wind blown	Not susceptible	-14.46

Table C.2: Geological description borehole 2

Base level [m relative NAP]	Description	Deposition	Judgement liquefaction susceptibility	Grain size distr.
-1.5	Sand and clay, mixed on top, in lamina (flasers/lenses), lowest 50 cm	Tidal channel	Not susceptible	
-3.4	Sand with little clay, laminated	Tidal channel	Susceptible	-1.84
-12.8	Sand and clay, relative much fine organic material (dark), in lamina	Tidal channel	Not susceptible	-3.54 - 4.74 - 7.74 - 9.44
-14.2	Clay ("bekkenklei"), organic (no roots), dark grey	Lagoonal	Not susceptible	
-16	Sand ("dekzand II"), fine, finely laminated, 5cm organic top ("podzol")	Wind blown	Not susceptible	
-13.3	Clay ("bekkenklei"), organic (no roots), dark grey	Lagoonal	Not susceptible	
-15	Sand ("dekzand II"), fine, finely laminated, 5cm organic top ("podzol")	Wind blown	Not susceptible	-14.46

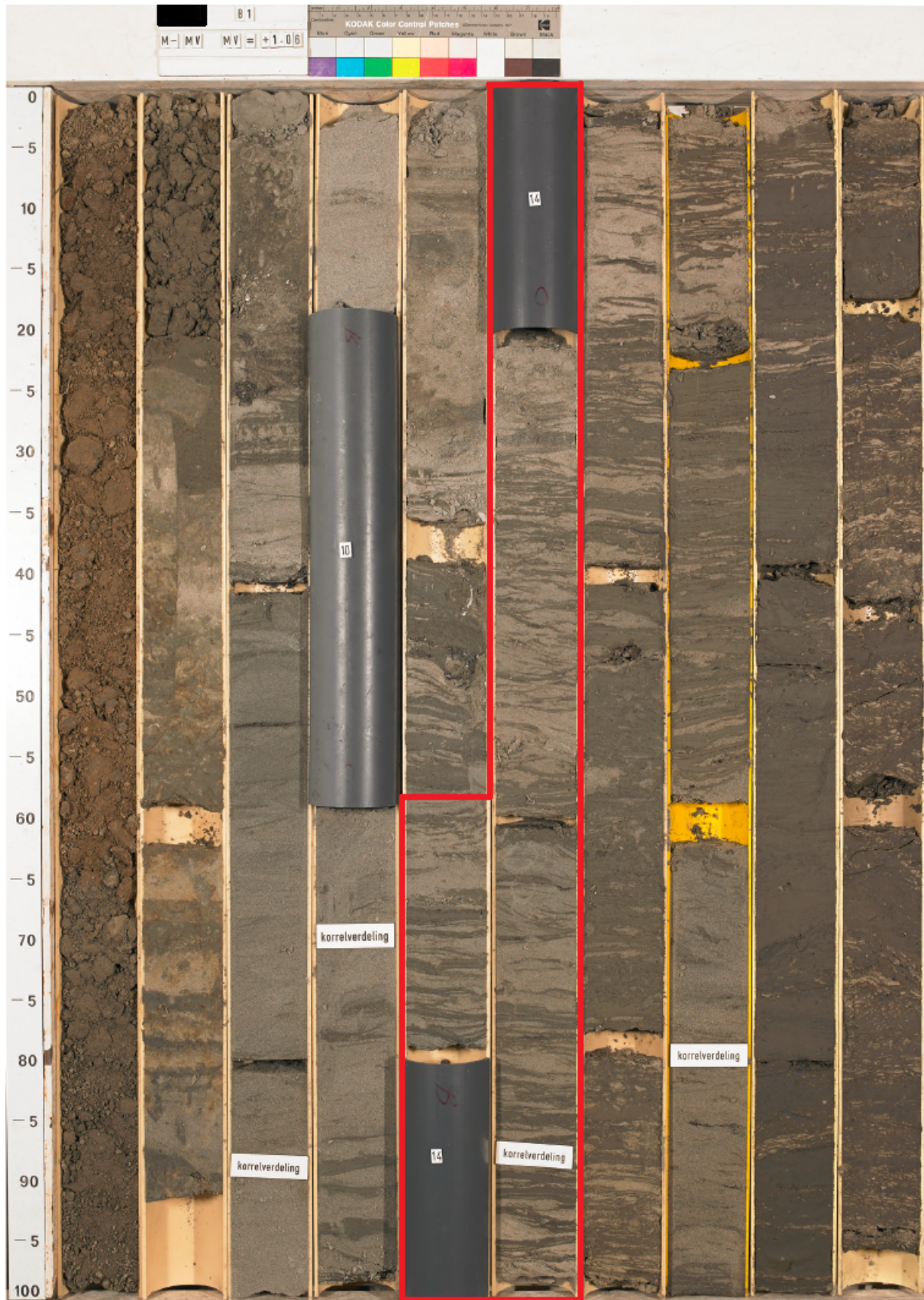


Figure C.1: Cross section of the borehole log accompanying the CPT shown in figure A.1 containing flaser bedding. The flaser bedding layer is marked in red.

D Method of Vreugdenhil et al. (1994)

Contents

D.1 Penetration resistance above interface	D-2
D.2 Penetration resistance below interface	D-3
D.3 Generalisation by Joer et al.	D-4
D.4 Script	D-5

This appendix describes the method of the elastic thin layer model, derived by Vreugdenhil et al. (1994) with additional clarification by Joer et al. (1996). Vreugdenhil et al. (1994) derived a method to describe the change in penetration resistance between two or more subsequent layers. Vreugdenhil et al. (1994) noted that an elastic model may appear to be a very poor one for a problem in which large plastic strains occur near the cone tip. The use of the model is justified by stating that it is not desired to model the penetration process, but the effect on the cone resistance of nearby layers of soil.

The first part of the appendix describes the problem of elasticity regarding the penetration problem and derives the dimensionless penetration resistance for a two-layer system, the second part gives a method to describe the penetration resistance for a number of N layers.

Vreugdenhil considers two linearly elastic, incompressible half spaces in bonded contact, as shown in figure D.1. A disc-shaped region represents a cone with radius a , on which an uniform load of p_0 is considered, instead of an uniform displacement. The disc-shaped region is considered to be at distance h from the layer interface, where is defined to be positive above the interface and negative below.

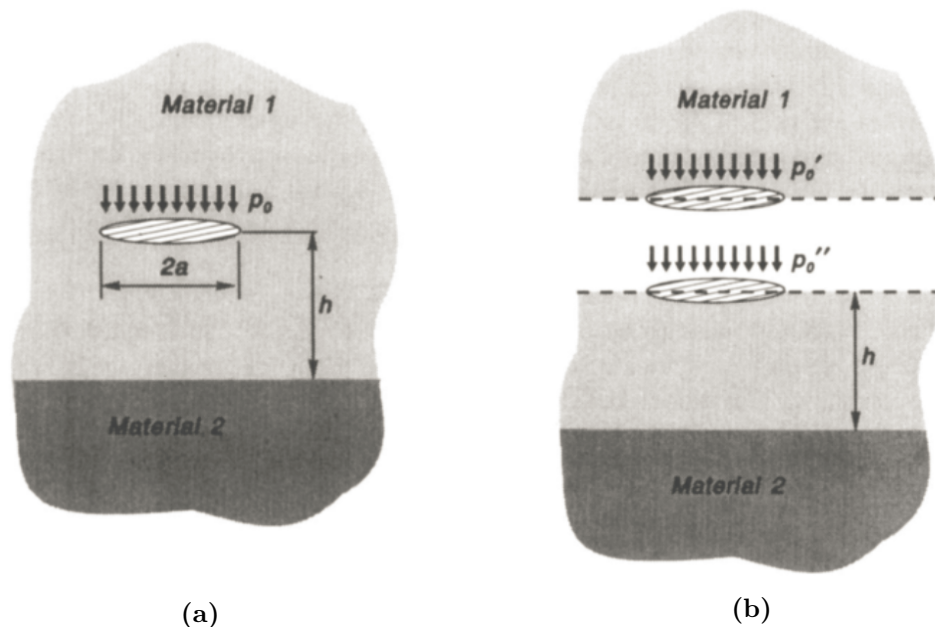


Figure D.1: Representation of CPT by circular uniform load (a) and decomposition into two half-space problems (b) (after Vreugdenhil et al. (1994)).

The two half-space solutions shown in figure D.1b can be combined to an infinite space problem shown in figure D.1a by making assumptions considering the displacements and loads:

$$\delta' = \delta'' = \delta \quad (\text{D.1})$$

$$p'_0 + p''_0 = p_0 \quad (\text{D.2})$$

The dimensionless penetration resistance parameter, which is used extensively in the publication by Vreugdenhil et al. (1994), is a function of the uniform load, radius of the disc-shaped region, shear modulus of the top layer and the vertical deflection at the centre of the loaded region.

$$\eta = \frac{p_0 a}{G_1 \delta} \quad (\text{D.3})$$

Vreugdenhil et al. (1994) use the vertical deflection δ to come to a definition of η , in which the deflection for the upper half-space and lower half-space are defined. Since the definition of the deflections of the half-spaces varies for each layer, each layer also has its own governing definition of η . In the two-layer situation therefore also two equations for η need to be defined. In the next sections the derivations for the resistance equations above and below the interface are given.

D.1 Penetration resistance above interface

Derivation of the dimensionless penetration resistance for load points above the interface between the two layers starts with the definition of the vertical deflections in the two half-space problems:

$$\delta' = \frac{p'_0 a}{2G_1} \quad (\text{D.4})$$

and

$$\delta'' = \frac{p''_0 a}{2G_1} - \frac{p''_0}{2G_1} \frac{a^2}{\sqrt{a^2 + h^2}} + \frac{p''_0}{2G_2} \frac{a^2}{\sqrt{a^2 + h^2}} \quad (\text{D.5})$$

Since the upper half-space in the top layer is homogeneous, δ' is obtained by integrating Boussinesq's point-load solution over the disc-shaped region. The lower half-space in the top layer is considered to be layered, and so δ'' is obtained by an approximation based on Boussinesq's solution in which the relative displacements in the two layers are combined. On the right hand side of equation (D.5), the difference between the first and second term represent the relative shortening of thickness h , and the third term represents the displacement of the half-space of the lower material below the depth h .

For convenience, r is defined as:

$$r = \frac{a}{\sqrt{a^2 + h^2}} \quad (\text{D.6})$$

So equation (D.5) can be rewritten as:

$$\delta'' = \frac{p''_0 a}{2G_1} - \frac{p''_0 a}{2G_1} r + \frac{p''_0 a}{2G_2} r \quad (\text{D.7})$$

Using the assumption shown in equation (D.1), the following equation can be composed and rewritten.

$$\frac{p'_0 a}{2G_1} = \frac{p''_0 a}{2G_1} - \frac{p''_0 a}{2G_1} r + \frac{p''_0 a}{2G_2} r \quad (\text{D.8})$$

$$p'_0 \frac{1}{G_1} = p''_0 \left(\frac{1}{G_1} - \frac{1}{G_1} r + \frac{1}{G_2} r \right) \quad (\text{D.9})$$

Using equation (D.2) for p'_0 :

$$p_0 = p''_0 \left(2 - r + \frac{G_1}{G_2} r \right) \quad (\text{D.10})$$

Again using equation (D.2), now for p''_0 :

$$p_0 = (p_0 - p'_0) \left(2 - r + \frac{G_1}{G_2} r \right) \quad (\text{D.11})$$

Using equation (D.4) for p'_0 :

$$p_0 \left(1 - r + \frac{G_1}{G_2} r \right) = \frac{2\delta G_1}{a} \left(2 - r + \frac{G_1}{G_2} r \right) \quad (\text{D.12})$$

This gives:

$$\delta = \frac{p_0 a}{2G_1} \left(\frac{1 - r + \frac{G_1}{G_2} r}{2 - r + \frac{G_1}{G_2} r} \right) \quad (\text{D.13})$$

Using the definition of η from equation (D.3) and the definition of λ :

$$\lambda_i = \left(1 - \frac{G_i}{G_{i+1}} \right) \frac{a}{\sqrt{a^2 + h^2}} = \left(1 - \frac{G_i}{G_{i+1}} \right) r = r - \frac{G_i}{G_{i+1}} r \quad (\text{D.14})$$

Gives:

$$\eta = 2 \left(\frac{2 - \lambda_1}{1 - \lambda_1} \right) \quad \text{for } h > 0 \quad (\text{D.15})$$

D.2 Penetration resistance below interface

Derivation of the dimensionless penetration resistance for load points below the interface between the two layers also starts with the definition of the vertical deflection in the two half-space problems:

$$\delta' = \frac{p'_0 a}{2G_2} - \frac{p'_0}{2G_2} \frac{a^2}{\sqrt{a^2 + h^2}} + \frac{p'_0}{2G_1} \frac{a^2}{\sqrt{a^2 + h^2}} \quad (\text{D.16})$$

and

$$\delta'' = \frac{p''_0 a}{2G_2} \quad (\text{D.17})$$

An almost similar situation occurs below the interface as above, except that now the upper half-space is considered to be layered and the lower half-space to be homogeneous. Definition of the terms in equations (D.16) and (D.17) is similar to the terms in the equations above the interface, except that attention needs to be paid to which half-space the terms apply.

For convenience, r is defined as:

$$r = \frac{a}{\sqrt{a^2 + h^2}} \quad (\text{D.18})$$

So equation (D.16) can be rewritten as:

$$\delta' = \frac{p'_0 a}{2G_2} - \frac{p'_0 a}{2G_2} r + \frac{p'_0 a}{2G_1} r \quad (\text{D.19})$$

Using the assumption shown in equation (D.1), the following equation can be composed and rewritten.

$$\frac{p'_0 a}{2G_2} - \frac{p'_0 a}{2G_2} r + \frac{p'_0 a}{2G_1} r = \frac{p''_0 a}{2G_2} \quad (\text{D.20})$$

$$p'_0 \left(\frac{1}{G_2} - \frac{1}{G_2} r + \frac{1}{G_1} r \right) = p''_0 \frac{1}{G_2} \quad (\text{D.21})$$

Using equation (D.2) for p'_0 :

$$p'_0 \left(2 - r + \frac{G_2}{G_1} r \right) = p_0 \quad (\text{D.22})$$

Again using equation (D.2), now for p''_0 :

$$(p_0 - p''_0) \left(2 - r + \frac{G_2}{G_1} r \right) = p_0 \quad (\text{D.23})$$

Using equation (D.17) for p_0'' :

$$p_0 \left(1 - r + \frac{G_2}{G_1} r \right) = \frac{2\delta G_2}{a} \left(2 - r + \frac{G_2}{G_1} r \right) \quad (\text{D.24})$$

This gives:

$$\delta = \frac{p_0 a}{2G_2} \left(\frac{1 - r + \frac{G_2}{G_1} r}{2 - r + \frac{G_2}{G_1} r} \right) \quad (\text{D.25})$$

Using the definition of η from equation (D.3) and the definition of λ :

$$\lambda_i = \left(1 - \frac{G_i}{G_{i+1}} \right) \frac{a}{\sqrt{a^2 + h^2}} = \left(1 - \frac{G_i}{G_{i+1}} \right) r = r - \frac{G_i}{G_{i+1}} r \quad (\text{D.26})$$

And the definition of stiffness ratio k :

$$k_i = \frac{G_{i+1}}{G_1} \quad (\text{D.27})$$

Gives:

$$\eta = 2k_1 \left(\frac{2 + k_1 \lambda_1}{1 + k_1 \lambda_1} \right) \quad \text{for } h \leq 0 \quad (\text{D.28})$$

Considering equations (D.15) and (D.28), the situation where $h \rightarrow \infty$ gives a resistance of $\eta \rightarrow 4$, and where $h \rightarrow -\infty$ a resistance of $\eta \rightarrow 4k_1$. This can be seen in figure 3.1a, where at the bottom of the two-layer problem the penetration resistance approaches the value of $4 \cdot 1.00/5.00 = 0.8$.

D.3 Generalisation by Joer et al.

Joer et al. (1996) give a more generalised version of the solution presented by Vreugdenhil et al. (1994), in which a number of N interfaces and consequently a number of $N+1$ layers are considered. The penetration resistance is modified compared to the method of Vreugdenhil et al. (1994) to have a value of 1 at the top of the penetration problem. In a similar way to Vreugdenhil et al. (1994) the stiffness ratio is defined:

$$k_i = \frac{G_{i+1}}{G_1} \quad i = 0, 1, 2, 3, \dots, N \quad (\text{D.29})$$

For convenience, the definition of λ is adjusted to the definition from Vreugdenhil et al. (1994):

$$\lambda_j = \left[\frac{1}{k_{j-1}} - \frac{1}{k_j} \right] \frac{a}{\sqrt{a^2 + h_j^2}} \quad j = 1, 2, 3, \dots, N \quad (\text{D.30})$$

The penetration resistance within the i^{th} layer (q_{ci}) then is:

$$q_{ci} \approx \eta_i q_{c1}^* = \frac{k_{i-1}}{2} \left(\frac{2 + A_i - B_i}{(1 + A_i)(1 - B_i)} \right) q_{c1}^* \quad (\text{D.31})$$

In which q_{ci} represents the characteristic cone resistance of layer the i^{th} layer and q_{c1}^* the characteristic cone resistance of the first layer. The normalised stiffness η_i is comparable to η used by Vreugdenhil et al. (1994). The main difference is that η_1 used by Joer et al. (1996) at $h \rightarrow \infty$ approaches a value of 1, where η_1 used by Vreugdenhil et al. (1994) approaches a value of 4. The values for A_i and B_i are defined as follows:

$$A_1 = 0 \quad A_i = k_{i-1} \sum_{j=1}^{j=i-1} \lambda_j \quad i = 2, 3, 4, \dots, (N+1) \quad (\text{D.32})$$

$$B_{N+1} = 0 \quad B_i = k_{i-1} \sum_{j=N}^{j=i} \lambda_j \quad i = 1, 2, 3, \dots, N \quad (\text{D.33})$$

D.4 Script

```
1  # -*- coding: utf-8 -*-
2  """
3  Created on Thu Apr 30 09:45:15 2015
4
5  @author: Toon van der Linden
6
7  Joer (1996) model for N layers
8  """
9  import time
10 import math
11 import numpy as np
12 import matplotlib.pyplot as plt
13
14 plt.close("all")
15
16 SaveFig = True
17 PlotVlines = True
18 Scenario = 1
19
20 """ INPUT """
21 Gmax = 10.0
22 Gmin = 1.0
23
24 if Scenario == 1:
25     H = np.array([1000,200,1000,2000,300,1000,800,700,600,400])
26     G = np.array([5.0,1.0,5.0,7.0,1.0,5.0,4.0,3.0,5.0,2.0])
27     NrOfLayers = 10
28 if Scenario == 2:
29     H = np.array([500,100,500,2000,300,1000,800,700,600,400])
30     G = np.array([1.0,0.5,1.0,7.0,1.0,5.0,4.0,3.0,5.0,2.0])
31     NrOfLayers = 10
32 if Scenario == 3:
33     H = np.array([300,80,80,80,80,80,300])
34     G = np.array([Gmax,Gmin,Gmax,Gmin,Gmax,Gmin,Gmax])
35     NrOfLayers = 7
36
37 Interfaces = np.zeros(NrOfLayers+1)
38 for x in range(1,len(Interfaces)):
39     Interfaces[x] = sum(H[0:x])
40 TotDepth = sum(H[0:NrOfLayers])
41 dz = 1
42 a = 12.5
43
44 """ CALCULATIONS """
45 StartTime = time.time()
46
47 z = np.linspace(0,TotDepth,((TotDepth/dz)+1))
48 InterfaceLoc = np.zeros(len(Interfaces))
49 for x in range(0,len(Interfaces)):
50     InterfaceLoc[x] = min(range(len(z)), key=lambda i: abs(z[i]-Interfaces[x]))
51 zovera = z/a
52
53 k = np.zeros(NrOfLayers)
54 k[0] = 1.0
55 for x in range(0,NrOfLayers):
56     k[x] = G[x]/G[0]
57
```



```

58 h = np.zeros([len(z),NrOfLayers-1])
59 for x in range(0,NrOfLayers-1):
60     h[0,x] = sum(H[0:x+1])
61
62 for x in range(1,len(z)):
63     for y in range(0,NrOfLayers-1):
64         h[x,y] = h[x-1,y]-dz
65
66 lam = np.zeros([len(z),NrOfLayers-1])
67 for x in range(0,NrOfLayers-1):
68     lam[:,x] = (1/k[x]-1/k[x+1])*a/np.sqrt(a**2+h[:,x]**2)
69
70 A = np.zeros([len(z),NrOfLayers])
71 for x in range(0,len(z)):
72     for y in range(1,NrOfLayers):
73         A[x,y] = k[y]*sum(lam[x,range(0,y)])
74
75 B = np.zeros([len(z),NrOfLayers])
76 for x in range(0,len(z)):
77     for y in range(0,NrOfLayers-1):
78         B[x,y] = k[y]*sum(lam[x,range(y,NrOfLayers-1)])
79
80 eta = np.zeros([len(z),NrOfLayers])
81
82 for x in range(0,NrOfLayers):
83     eta[:,x] = (k[x]/2)*((2+A[:,x]-B[:,x])/((1+A[:,x])*(1-B[:,x])))
84
85 EndTime = time.time()
86 RunTime = EndTime-StartTime
87 print "Running time", RunTime, "s"
88
89 xminplot = 0
90 xmaxplot = math.ceil(max(k))
91
92 """ COLORMAP """
93 import colorsys
94 HSV_tuples = [(x*1.0/NrOfLayers, 0.80, 0.80) for x in range(NrOfLayers)]
95 RGB_tuples = map(lambda x: colorsys.hsv_to_rgb(*x), HSV_tuples)
96 """ export rgb to plotting variables """
97
98 colorlist = RGB_tuples
99 colorgray = 'LightGray'
100 colors = np.arange(0,100,100/NrOfLayers)
101 labels1 = []
102 Gtext = []
103 for x in range(0,NrOfLayers):
104     labels1.append('Layer '+str(x+1))
105     Gtext.append('G$_'+ str(x+1)+'$=')
106 labels2 = []
107 for x in range(0,NrOfLayers):
108     labels2.append(labels1[x]+'\\n H='+str(H[x])+ ' mm')
109 Glabels = []
110 for x in range(0,len(G)):
111     Glabels.append(str(G[x]))
112
113 EtaList = np.zeros(len(z))
114
115 def Plotting():
116     fig = plt.figure(figsize=(10,11))

```

```

117 ax = plt.subplot(111)
118 ax.set_title('Dimensionless resistance as conen passes through layer interfaces',
    y = 1.02)
119 ax.set_xlabel("$\eta$ [-]") # eta = dimensionless penetration resistance
120 ax.set_ylabel("z [mm]")
121 for x in range(0,NrOfLayers):
122     ax.text(xmaxplot-0.12*xmaxplot,Interfaces[x]+0.5*H[x],Gtext[x]+str(G[x]))
123 for x in range(0,NrOfLayers):
124     zmin = InterfaceLoc[x]
125     zmax = InterfaceLoc[x+1]
126     ax.plot(eta[0:zmin,x],z[0:zmin],colorgray,ls='dotted')
127     ax.plot(eta[zmax:len(z),x],z[zmax:len(z)],colorgray,ls='dotted')
128     ax.scatter(eta[zmin:zmax,x],z[zmin:zmax],c=colorlist[x],edgecolor=colorlist[x],
        s=5,label=labels2[x])
129     EtaList[zmin:zmax] = eta[zmin:zmax,x]
130 for x in range(0,len(Interfaces)-1):
131     ax.axhline(y=Interfaces[x+1],color='k',ls='dashed')
132 ax.set_ylim(TotDepth,0)
133 ax.set_xlim(xminplot,xmaxplot)
134 box = ax.get_position()
135 ax.set_position([box.x0, box.y0, box.width * 0.83, box.height])
136 ax.legend(loc='center left', bbox_to_anchor=(1, 0.5))
137 if PlotVlines == True:
138     for x in range(0,NrOfLayers):
139         ax.plot((k[x],k[x]),(Interfaces[x],Interfaces[x+1]),'k--')
140 if SaveFig == True:
141     fig.savefig('Joer1996.png', dpi=300)
142 plt.show()
143
144 fig2 = plt.figure(figsize=(10,11))
145 ax2 = plt.subplot(111)
146 ax2.set_title('Dimensionless resistance as cone\n passes through layer interfaces'
    , y = 1.02)
147 ax2.set_xlabel("Computed cone resistance [MPa]") # eta = dimensionless penetration
    resistance
148 ax2.set_ylabel("z [mm]")
149 for x in range(0,NrOfLayers):
150     zmin = InterfaceLoc[x]
151     zmax = InterfaceLoc[x+1]
152     ax2.plot(eta[0:zmin,x],z[0:zmin],colorgray,ls='dotted')
153     ax2.plot(eta[zmax:len(z),x],z[zmax:len(z)],colorgray,ls='dotted')
154     ax2.scatter(eta[zmin:zmax,x]*G[0],z[zmin:zmax],c=colorlist[x],edgecolor=
        colorlist[x],s=5,label=labels2[x])
155     EtaList[zmin:zmax] = eta[zmin:zmax,x]
156 for x in range(0,len(Interfaces)-1):
157     ax2.axhline(y=Interfaces[x+1],color='k',ls='dashed')
158 ax2.set_ylim(TotDepth,0)
159 ax2.set_xlim(0,50)
160 box = ax2.get_position()
161 ax2.set_position([box.x0, box.y0, box.width * 0.83, box.height])
162 ax2.legend(loc='center left', bbox_to_anchor=(1, 0.5))
163 if PlotVlines == True:
164     for x in range(0,NrOfLayers):
165         ax2.plot((k[x]*G[0],k[x]*G[0]),(Interfaces[x],Interfaces[x+1]),'k--')
166 if SaveFig == True:
167     fig2.savefig('Joer1996.png', dpi=300)
168 plt.show()
169
170 Plotting()

```

E Method of Koppejan

Contents

E.1	Method for CPT simulation	E-1
E.2	Script	E-3
E.3	Validation with DFoundations	E-7

The Koppejan method (also known as the Dutch method) is used originally for calculating the pile tip resistance of foundation piles. In this thesis, the method was used to simulate the measured cone resistance. A fictional soil profile (example in figure 3.6) with characteristic values of q_c is used as true soil resistances to calculate the pile tip resistance and thus simulate what the cone resistance would be with such profile.

Because available software able of calculating the pile tip resistance with the Koppejan method does not allow calculation intervals to be smaller than 0.01 m, a new script was needed to be able to calculate intervals smaller than 0.01 m and thus to be able to simulate layers thinner than 0.01 m. This appendix briefly describes the main equation used for the method and presents the script developed for calculation.

E.1 Method for CPT simulation

The equation for determining the maximum pile tip resistance as presented in [NEN 9997-1 \(2012\)](#):

$$q_{b,max} = \frac{1}{2} \cdot \alpha_p \cdot \beta \cdot s \left(\frac{q_{c,I,gem} + q_{c,II,gem}}{2} + q_{c,III,gem} \right) \quad (E.1)$$

Where $q_{b,max}$ is the maximum generated pile tip resistance, α_p a pile class factor, β a pile tip shape factor, s a pile tip cross-section factor, $q_{c,I,gem}$ the mean value of cone resistances over trajectory 1, $q_{c,II,gem}$ the mean value of cone resistances over trajectory 2 and $q_{c,III,gem}$ the mean value cone resistances over trajectory 3. For modelling the CPT process, α_p , β and s are each considered to be equal to 1.0.

The trajectories can be described as follows:

- **Trajectory I:** starts at pile tip level and ends at a level of at least $0.7 \cdot D_{eq}$ and at most $4 \cdot D_{eq}$ below pile tip level. The endpoint of the trajectory must be chosen between these two levels such that $q_{b,max}$ is as small as possible.
- **Trajectory II:** starts at the endpoint of trajectory I and ends at pile tip level. The governing cone resistance in the trajectory cannot be higher than a value previously encountered in trajectory II.
- **Trajectory III:** starts at pile tip level and ends at a level of $8 \cdot D_{eq}$ above pile tip level. The governing cone resistance in the trajectory cannot be higher than a value previously encountered in trajectory III. The first value of trajectory III is the minimum value of trajectory II.

The trajectories are illustrated for two examples in figure E.1.

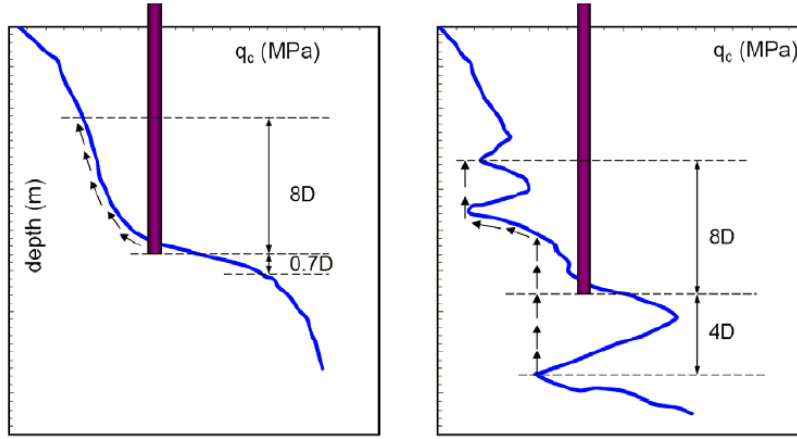


Figure E.1: Example of trajectory determination for the Koppejan method (after Xu (2007)).

In this thesis it is assumed that when calculating the various mean cone resistances over the different trajectories and apply them in the equation above, $q_{b;max}$ would represent the measured cone resistance. The script presented in the next section can deal with different iteration

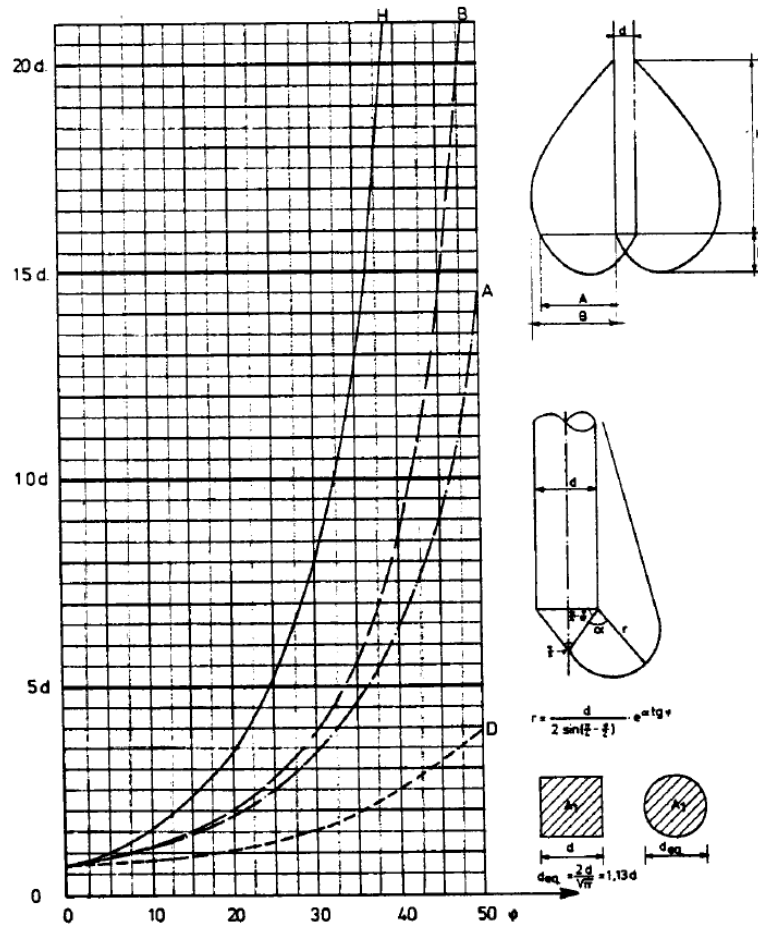


Figure E.2: Shape sizes of the failure surfaces in sand for different angles of internal friction according to the theory of Prandtl, after Douwes Dekker (1984)

distances than $4d_{cone}$ for trajectory I. Figure E.2 shows the variation of failure surface size with varying angle of internal friction. Parameter D stands for the distance of influence below the pile tip, and it can be concluded that according to the theory with the logarithmic spiral planes of the Prandtl-theory for an angle of internal friction of 50° soil influences the pile tip over a

vertical distance of $4d_{cone}$.

Since this value of internal friction is rarely reached, lower values than $4d_{cone}$ can be valid to be used as iteration distance for trajectory I and II. These distances can be adjusted in the script according to figure E.2. Appendix F presents results of different iteration distances and different sample configurations.

E.2 Script

```
1  # -*- coding: utf-8 -*-
2  """
3  Created on Fri Jun 12 15:12:25 2015
4
5  @author: Toon van der Linden
6
7  Koppejan
8  """
9  import numpy as np
10 import os
11 import re
12 import time
13 import matplotlib.pyplot as plt
14
15 plt.close("all")
16 StartTime = time.time()
17 """ INPUT PARAMETERS """
18 LogFile = True
19
20 GEFfileNumber = 1 # Number of GEF file to be used from directory, shown when PrintDirectory()
    is called
21 dz = 0.01 # Vertical calculation interval [m]
22 Dcone = 0.025 # Cone diameter [m]
23 KoppejanMin = 4.0 #KoppejanMin*Dcone for bottom iteration location relative to pile tip level
24 KoppejanMax = 8.0 #KoppejanMax*Dcone for top iteration location relative to pile tip level
25
26 """ IMPORTING CPT DATA """
27
28 def PrintDirectory():
29     execfile('DirectoryPrinter.py')
30
31 GEFfiles = os.listdir('C:\Users\Toon\Documents\TU Delft\CIE5060-09 (MSc thesis) - PC\GEF\
    ArtificialGEF')
32 FileName = GEFfiles[GEFfileNumber]
33 print '\nFile used for calculation: ',FileName
34
35 PathName = os.path.join("C:\Users\Toon\Documents\TU Delft\CIE5060-09 (MSc thesis) - PC\GEF\
    ArtificialGEF",FileName)
36 FileLoad = open(PathName)
37 RawData = FileLoad.readlines()
38 FileLoad.close()
39 FileLoad = open(PathName)
40 TextData = FileLoad.read()
41 FileLoad.close()
42
43 """ GEF FILE INTERPRETATION """
44 # Only GEF files in Dutch are recognized by this script
45 for x in range(0,len(RawData)): # Locating and storing groundlevel
46     if '#ZID=' in RawData[x]:
47         temp = re.findall(r'\d+', RawData[x])
48         GroundLevel = eval(temp[1]+'.'+temp[2])
49         if re.findall(r'-' , RawData[x]) == ['-']:
50             GroundLevel = GroundLevel*-1
51
```

```

52 for x in range(0,len(RawData)): # Locating and storing pre-excavation
53     if RawData[x].find("voorgegraven diepte") != -1:
54         temp6 = re.findall(r'\d+', RawData[x])
55         PreExcDepth = eval(temp6[1]+'.'+temp6[2])
56     if TextData.find("voorgegraven diepte") == -1:
57         PreExcDepth = 0.0
58
59 for x in range(0,len(RawData)): # Locating and storing number of columns in GEF file
60     if '#COLUMN=' in RawData[x]:
61         temp = re.findall(r'\d+', RawData[x])
62         ColNr = eval(temp[0])
63
64 for x in range(0,len(RawData)): # Locating pore pressure column
65     if RawData[x].find("Waterdruk") != -1 or RawData[x].find("Waterspanning") != -1:
66         temp = re.findall(r'\d+', RawData[x])
67         ColNr_WP = eval(temp[0])
68         if RawData[x].find("u1") != -1:
69             utype=1
70         if RawData[x].find("schouder") != -1 or RawData[x].find("u2") != -1:
71             utype=2
72     elif TextData.find("Waterdruk schouder") == -1 and TextData.find("Waterspanning") == -1:
73         ColNr_WP = np.NaN
74
75 for x in range(0,len(RawData)): # Locating CPT depth column
76     if RawData[x].find("Gecorrigeerde diepte") != -1 or RawData[x].find("gecorrigeerde diepte")
77         != -1 or RawData[x].find("Sondeerlengte") != -1:
78         temp = re.findall(r'\d+', RawData[x])
79         ColNr_Depth = eval(temp[0])
80     if TextData.find("Gecorrigeerde diepte") == -1 and TextData.find("gecorrigeerde diepte") ==
81         -1 and TextData.find("Sondeerlengte") == -1:
82         ColNr_Depth = np.NaN
83
84 for x in range(0,len(RawData)): # Locating friction ratio column
85     if RawData[x].find("Wrijvingsgetal") != -1:
86         temp = re.findall(r'\d+', RawData[x])
87         ColNr_FrRat = eval(temp[0])
88     if TextData.find("Wrijvingsgetal") == -1:
89         ColNr_FrRat = np.NaN
90
91 for x in range(0,len(RawData)): # Locating local friction column
92     if RawData[x].find("Wrijvingsweerstand fs") != -1 or RawData[x].find("Lokale wrijving") !=
93         -1:
94         temp = re.findall(r'\d+', RawData[x])
95         ColNr_LocFr = eval(temp[0])
96     if TextData.find("Wrijvingsweerstand fs") == -1 and TextData.find("Lokale wrijving") == -1:
97         ColNr_LocFr = np.NaN
98
99 for x in range(0,len(RawData)): # Locating cone resistance column
100     if RawData[x].find("Conusweerstand qc") != -1 or RawData[x].find("Puntdruk") != -1:
101         temp = re.findall(r'\d+', RawData[x])
102         ColNr_ConeRes = eval(temp[0])
103     if TextData.find("Conusweerstand qc") == -1 and TextData.find("Puntdruk") == -1:
104         ColNr_FrRat = np.NaN
105
106 for x in range(0,len(RawData)): # Locating time column
107     if RawData[x].find("Tijd,") != -1:
108         temp = re.findall(r'\d+', RawData[x])
109         ColNr_Time = eval(temp[0])
110     if TextData.find("Tijd,") == -1:
111         ColNr_Time = np.NaN
112
113 for x in range(0,len(RawData)): # Locating classification column
114     if RawData[x].find("Classificatie zone Robertson") != -1:
115         temp = re.findall(r'\d+', RawData[x])
116         ColNr_Class = eval(temp[0])

```

```

114     if TextData.find("Classificatie zone Robertson") == -1:
115         ColNr_Class = np.NaN
116
117 for x in range(0,len(RawData)): # Locating start of measurement data
118     if RawData[x] == '#EOH=\n':
119         StartCPTloc = x+1
120         break
121
122 temp = (len(RawData)-StartCPTloc)
123 DataMatrix = np.zeros((temp,ColNr))
124 for x in range(0,temp): # Importing measurement data in matrix
125     DataMatrix[x,:] = np.asarray(RawData[x+StartCPTloc].split()).astype(np.float)
126
127 # Assigning various parameters from matrix columns to different arrays
128 if type(ColNr_Depth) == int:
129     Data_Depth = DataMatrix[:,ColNr_Depth-1]
130 if type(ColNr_ConeRes) == int:
131     Data_ConeRes = DataMatrix[:,ColNr_ConeRes-1]
132 if type(ColNr_LocFr) == int:
133     Data_LocFr = DataMatrix[:,ColNr_LocFr-1]
134 if type(ColNr_FrRat) == int:
135     Data_FrRat = DataMatrix[:,ColNr_FrRat-1]
136 if type(ColNr_WP) == int:
137     Data_WP = DataMatrix[:,ColNr_WP-1]
138 if type(ColNr_Class) == int:
139     Data_Class = DataMatrix[:,ColNr_Class-1]
140
141 Depth = Data_Depth
142 ConeR = Data_ConeRes
143 LocalFr = Data_LocFr
144 FrRat = Data_FrRat
145
146 # Handling of out-of-range data
147 for x in range(0,len(FrRat)):
148     if FrRat[x] < -999:
149         FrRat[x] = 0
150
151 temp = int(round((max(Depth)-min(Depth))/dz))
152 CalcDepth = np.linspace(min(Depth),max(Depth),temp+1) # Creating array for storing calculation
153               results with size according to vertical calculation interval dz
154
155 """ INTERPOLATE CONE RES. FROM GEF TO COMPUTABLE ARRAY """
156 # Re-defining GEF qc data to array with size equal to result array size
157 Calcqc = np.ones(len(CalcDepth))*np.NaN
158 for x in range(0,len(Calcqc)):
159     for y in range(0,len(Depth)):
160         if CalcDepth[x] == Depth[y]:
161             Calcqc[x] = Data_ConeRes[y]
162         elif CalcDepth[x] > Depth[y] and CalcDepth[x] < Depth[y+1]:
163             temp = (CalcDepth[x]-Depth[y])/(Depth[y+1]-Depth[y])
164             Calcqc[x] = Data_ConeRes[y]+(Data_ConeRes[y+1]-Data_ConeRes[y])*temp
165
166 """ CALCULATING KOPPEJAN """
167
168 qc1gem = np.ones(len(CalcDepth))*np.NaN # Creating empty trajectory arrays
169 qc2gem = np.ones(len(CalcDepth))*np.NaN
170 qc3gem = np.ones(len(CalcDepth))*np.NaN
171 prmax = np.ones(len(CalcDepth))*np.NaN
172 qbmax = np.ones(len(CalcDepth))*np.NaN
173
174 KoppejanRange = np.linspace(0.7,KoppejanMin,(KoppejanMin-0.7)*10+1) # Trajectory 1 and 2
175               iteration range
176
177 if LogFile == True: # Creating a log file for debugging purposes
178     log_file = open("Koppejan-V3_log.txt","w")

```



```

177
178 StartLoopTime = time.time()
179 for x in range(0,len(CalcDepth)): # Starting calculation loop for every calc. depth
180     TopLevel = CalcDepth[x] - KoppejanMax*Dcone # Defining KoppejanMax*Dcone above cal. level
181     TopLoc = min(range(len(CalcDepth)),key=lambda i: abs(CalcDepth[i]-TopLevel)) # Finding
        nearest location in array
182     prmax[x] = 100*max(Calcqc) # Setting initial value prmax at calc. depth loc. before
        iterating
183     for w in range(0,len(KoppejanRange)): # Starting 0.7D-4D loop
184         KjD = KoppejanRange[w]
185         if LogFile == True: # Log file commands
186             log_file.write('Koppejan distance: ')
187             log_file.write(str(KjD))
188             log_file.write(' at Level of: ')
189             log_file.write(str(CalcDepth[x]))
190             log_file.write('\n')
191         BotLevel = CalcDepth[x] + KjD*Dcone # Defining lower calc. level
192         BotLoc = min(range(len(CalcDepth)),key=lambda i: abs(CalcDepth[i]-BotLevel))
193         if BotLoc-x == 0.0:
194             if LogFile == True: # Log file commands
195                 log_file.write('Iteration counter: ')
196                 log_file.write(str(iterationcount))
197                 log_file.write('\n')
198                 log_file.write('Location in array: ')
199                 log_file.write(str(BotLoc))
200                 log_file.write('\n')
201         if BotLoc - x != 0.0:
202             qc1gem[x] = sum(Calcqc[x:BotLoc])/(BotLoc-x) # Determining value for qc1gem
203             BotRange = Calcqc[x:BotLoc]
204             qc2traj = np.ones(abs(BotLoc-x))*np.NaN
205             qc2traj[len(qc2traj)-1] = Calcqc[BotLoc]
206             for y in range(len(qc2traj)-2,-1,-1): # Defining trajectory for qc2
207                 if BotRange[y] <= qc2traj[y+1]:
208                     qc2traj[y] = BotRange[y]
209                 if BotRange[y] > qc2traj[y+1]:
210                     qc2traj[y] = qc2traj[y+1]
211             qc2gem[x] = sum(qc2traj)/(BotLoc-x) # Determining value for qc2gem
212             if x - TopLoc != 0.0:
213                 TopRange = Calcqc[TopLoc:x]
214                 qc3traj = np.ones(x-TopLoc)*np.NaN
215                 qc3traj[len(qc3traj)-1] = qc2traj[0]
216                 for y in range(len(qc3traj)-2,-1,-1): # Defining trajectory for qc3
217                     if TopRange[y] <= qc3traj[y+1]:
218                         qc3traj[y] = TopRange[y]
219                     if TopRange[y] > qc3traj[y+1]:
220                         qc3traj[y] = qc3traj[y+1]
221             qc3gem[x] = sum(qc3traj)/(x-TopLoc) # Determining value for qc3gem
222             temp_pr = 0.25*qc1gem[x]+0.25*qc2gem[x]+0.5*qc3gem[x]
223             if LogFile == True:
224                 log_file.write('qc1gem: ')
225                 log_file.write(str(qc1gem[x]))
226                 log_file.write(' qc2gem: ')
227                 log_file.write(str(qc2gem[x]))
228                 log_file.write(' qc3gem: ')
229                 log_file.write(str(qc3gem[x]))
230                 log_file.write('\n')
231                 log_file.write('temp: ')
232                 log_file.write(str(temp_pr))
233                 log_file.write('\n')
234             if temp_pr < prmax[x]: # Choosing the smallest prmax as ultimate value
235                 prmax[x] = temp_pr
236         if LogFile == True:
237             log_file.write('prmax taken: ')
238             log_file.write(str(prmax[x]))
239             log_file.write('\n\n')

```



```

240     qbmax[x] = prmax[x]
241
242     if LogFile == True:
243         log_file.close()
244
245     LoopTime = time.time() - StartLoopTime
246     print 'Loop time: ', LoopTime, 'seconds'
247
248     prmax = np.ones(len(CalcDepth))*np.NaN
249     for x in range(0, len(prmax)): # Calculating the pile tip resistance according to Koppejan
250         prmax[x] = 0.25*qc1gem[x] + 0.25*qc2gem[x] + 0.5*qc3gem[x]
251
252     """ PLOTTING """
253     plt.figure(figsize=(9,11))
254     plt.plot(Calcqc, CalcDepth, c='blue')
255     plt.plot(qbmax, CalcDepth, c='red')
256     plt.xlim(0, 11)
257     plt.gca().invert_yaxis()
258     plt.show()
259
260     EndTime = time.time() - StartTime
261     print 'Running time: ', EndTime, 'seconds'
    
```

E.3 Validation with DFoundations

Whether the script gives pile tip resistances corresponding to results of calculations from field tests, results from the script were compared to results from the program *DFoundations*. A GEF file from a CPT performed in Groningen analysed in *DFoundations* simulating a 0.036 m circular driven cast-in-place pile. Since *DFoundations* only allows a maximum number of calculation points of 150, only a part of the CPT was analysed with a calculation interval of 0.02 m. For the script the same GEF file was used with a cone diameter of 36 mm, standard $4d_{cone}$ and $8d_{cone}$ iteration distances and a calculation interval of 0.02 m. The results can be found in figure E.3.

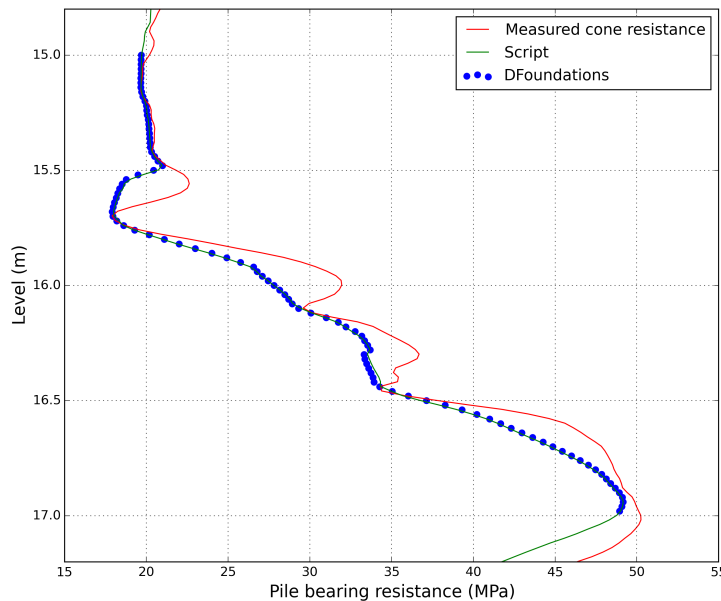


Figure E.3: Results of calculations for DFoundations and script

Since the calculations points of *DFoundations* and the script show almost exact overlap it was concluded that the script operates correctly and can be used for further analysis.

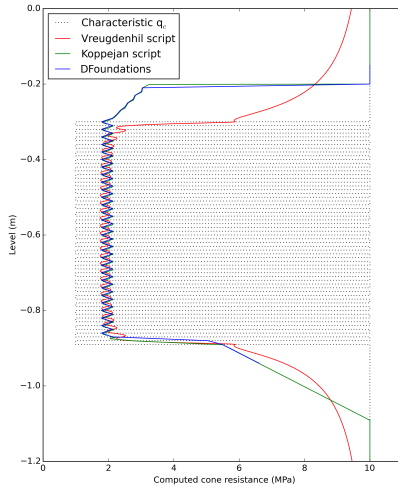
F Numerical scenarios

In order to determine which sample configurations are worth for physical modelling different scenarios have been determined and tested with the methods of Vreugdenhil et al. and Koppejan. In the figures presented in this appendix the results for different configurations can be found, where the characteristic resistance of sand and clay has been set at 10 MPa and 1 MPa respectively. It can be concluded that for each thin layers (1 and 2 cm thick), medium layers (5 and 10 cm thick) and thick layers (20 and 50 cm) results are comparable. Each category of thickness (thin, medium and thick) shows similar behaviour of models within the configurations of that category. For this reason it is determined that different configurations that can be used for physical modelling should be chosen within each category.

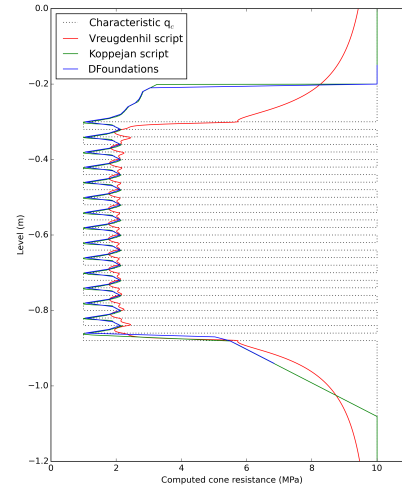
Other figures in this appendix show model simulations for a cone diameter as used during testing. Also different iteration distances were applied for determining trajectory I and II for the Koppejan method, described in appendix E. Since the iteration distance of $0.7d_{cone}$ - $4d_{cone}$ may be too large for the layered sample configurations tested in the lab, besides an iteration distance of $4d_{cone}$ also simulations are presented with $2d_{cone}$ $1.5d_{cone}$ and $1d_{cone}$. Table F.1 shows an overview of the simulated scenarios. Since adjusting this distance is not possible with DFoundations, results for DFoundations are not included in these figures.

Table F.1: Overview of the tested scenarios

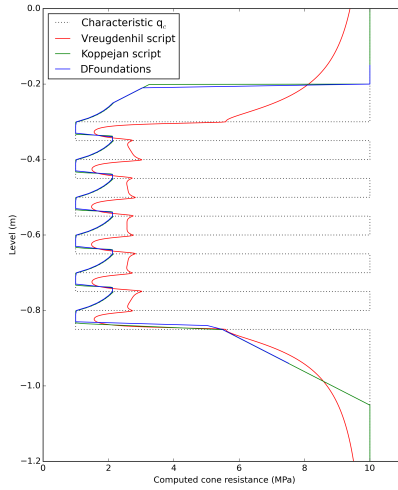
Cone diameter	Koppejan iteration dist.	Figure
36 mm	$4.0d_{cone}$ and DFound.	F.1
36 mm	$4.0d_{cone}$	F.2
36 mm	$1.5d_{cone}$	F.3
25 mm	$4.0d_{cone}$	F.4
25 mm	$2.0d_{cone}$	F.5
25 mm	$1.5d_{cone}$	F.6
25 mm	$1.0d_{cone}$	F.7



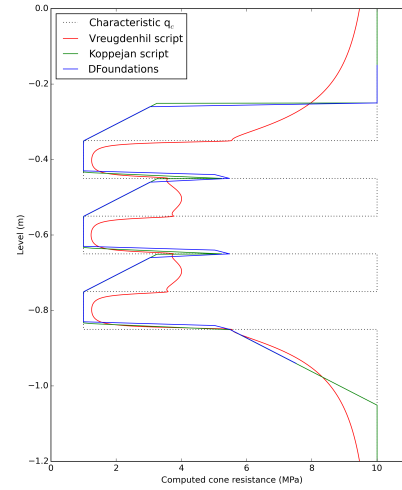
(a) 1 cm layers



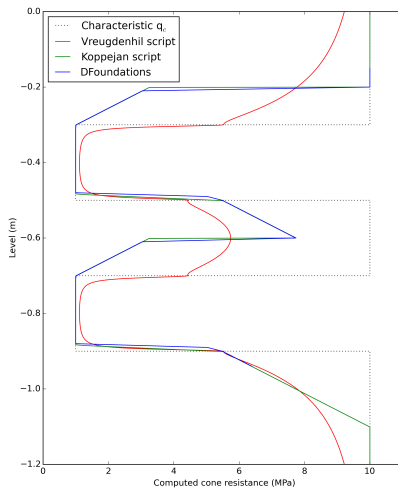
(b) 2 cm layers



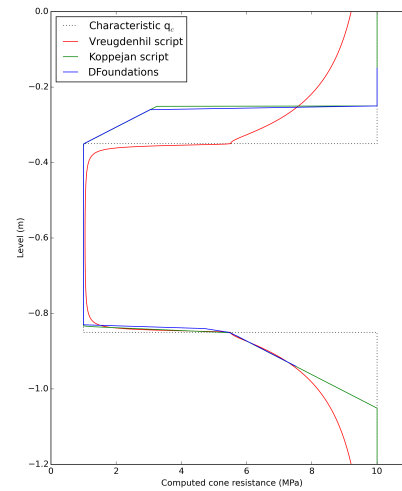
(c) 5 cm layers



(d) 10 cm layers

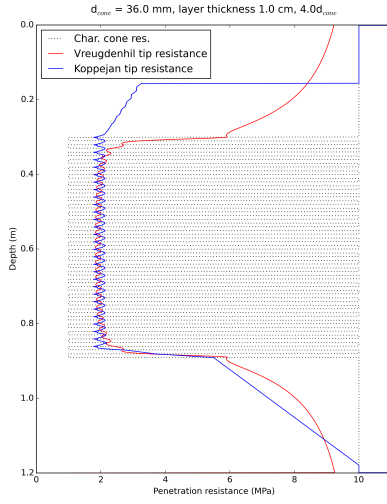


(e) 20 cm layers

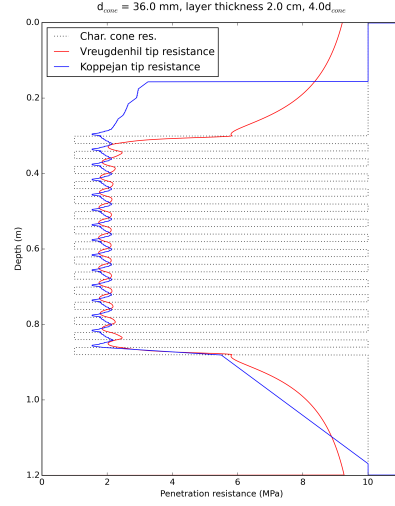


(f) 50 cm layer

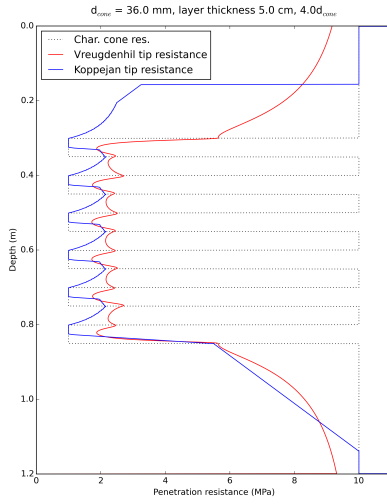
Figure F.1: Comparing the DFoundations solution with the solutions from the Koppejan script and Vreugdenhil



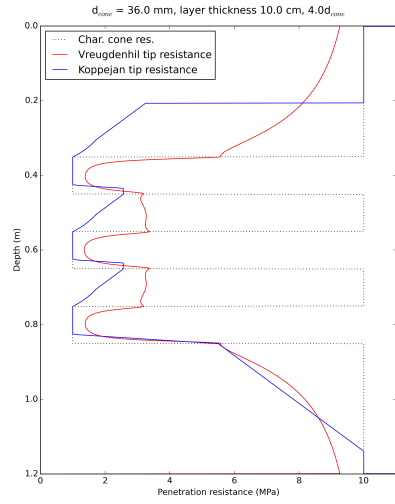
(a) 1 cm layers



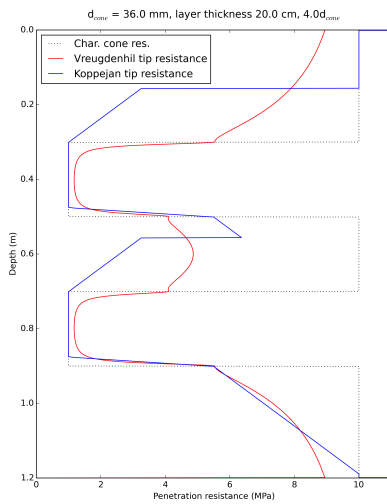
(b) 2 cm layers



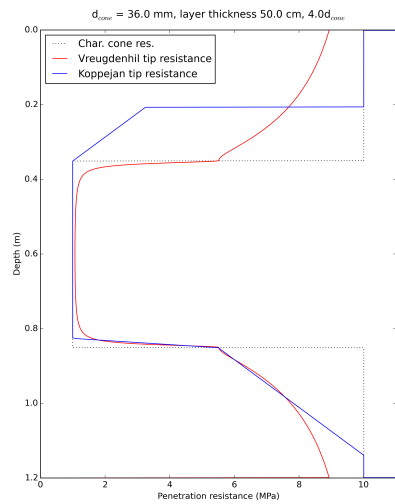
(c) 5 cm layers



(d) 10 cm layers

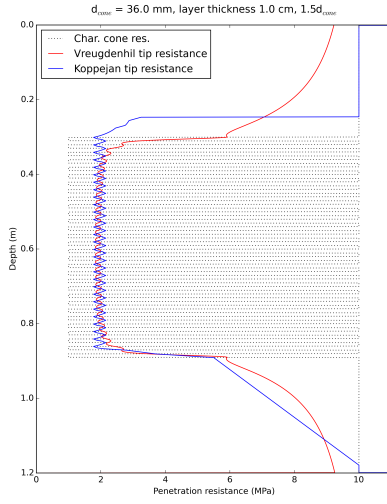


(e) 20 cm layers

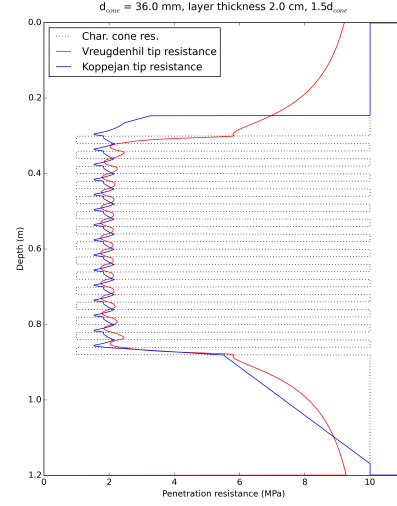


(f) 50 cm layer

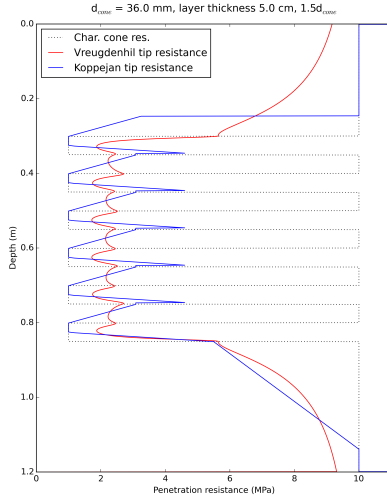
Figure F.2: Different scenarios with a 36 mm cone, iteration range for Koppejan trajectory 1 between 0.7 and 4.0 d_{cone}



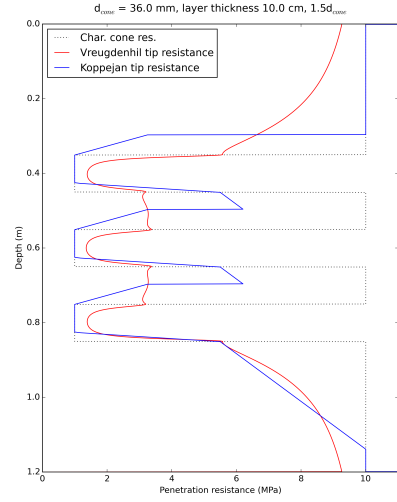
(a) 1 cm layers



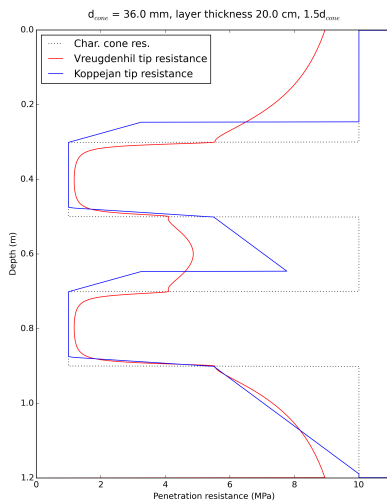
(b) 2 cm layers



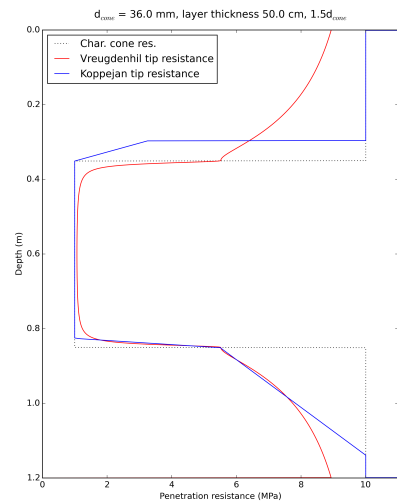
(c) 5 cm layers



(d) 10 cm layers

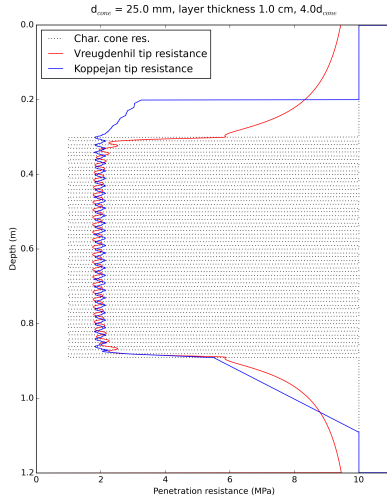


(e) 20 cm layers

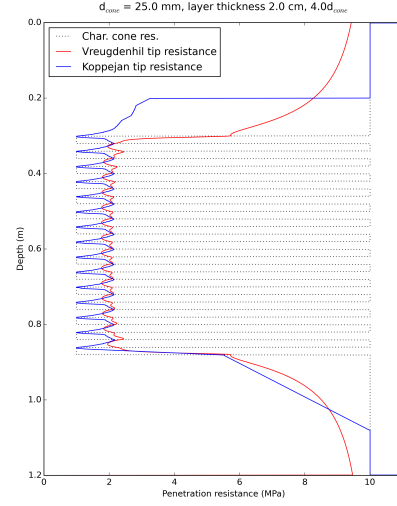


(f) 50 cm layer

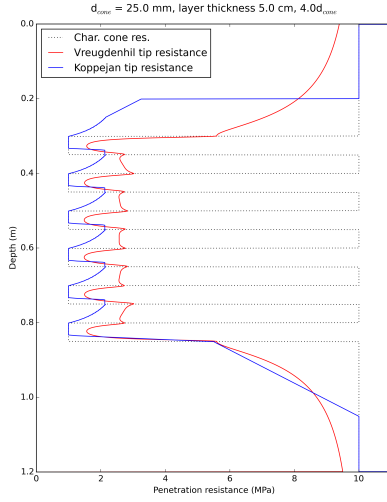
Figure F.3: Different scenarios with a 36 mm cone, iteration range for Koppejan trajectory 1 between 0.7 and $1.5 d_{\text{cone}}$



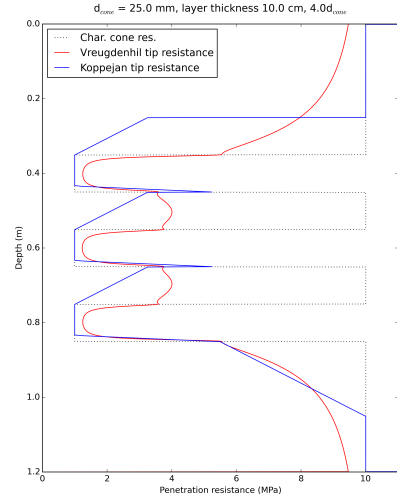
(a) 1 cm layers



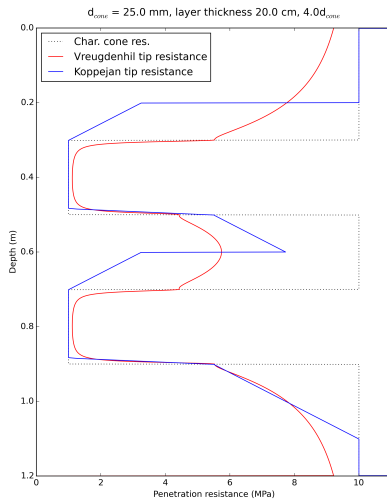
(b) 2 cm layers



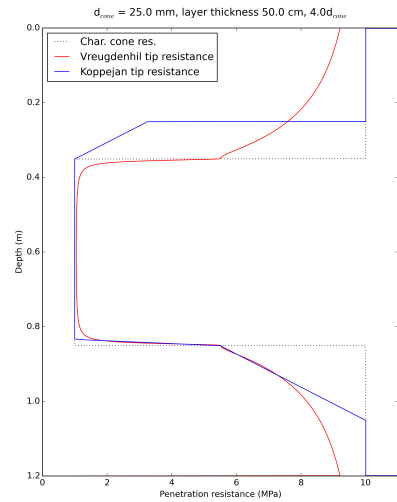
(c) 5 cm layers



(d) 10 cm layers

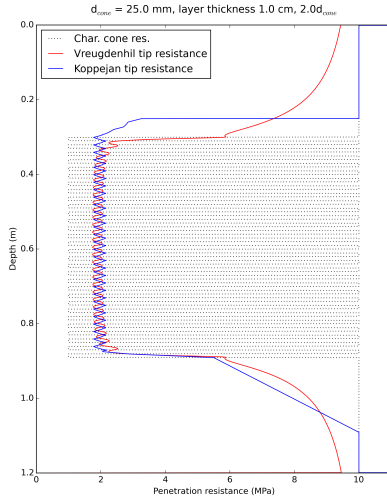


(e) 20 cm layers

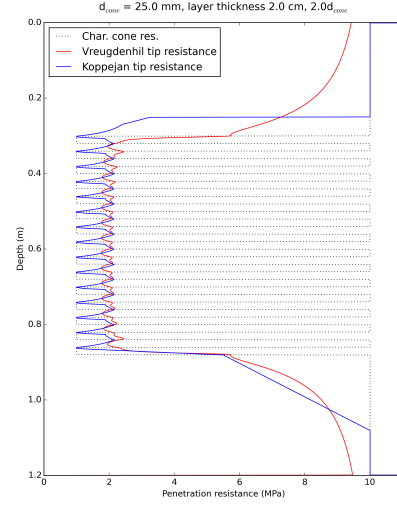


(f) 50 cm layer

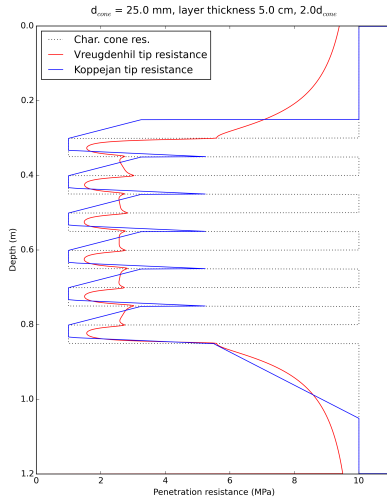
Figure F.4: Different scenarios with a 25 mm cone, iteration range for Koppejan trajectory 1 between 0.7 and 4.0 d_{cone}



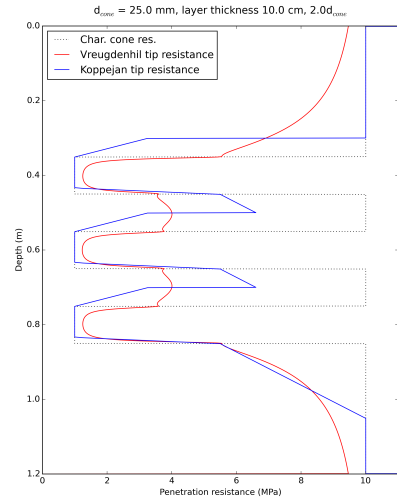
(a) 1 cm layers



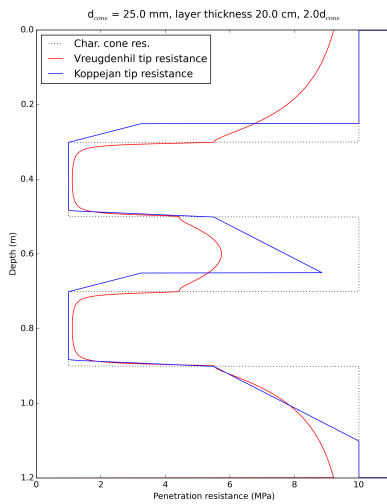
(b) 2 cm layers



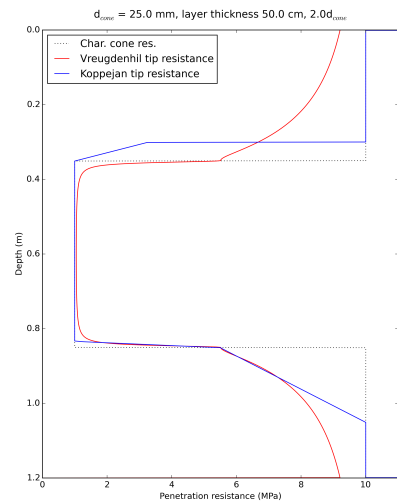
(c) 5 cm layers



(d) 10 cm layers

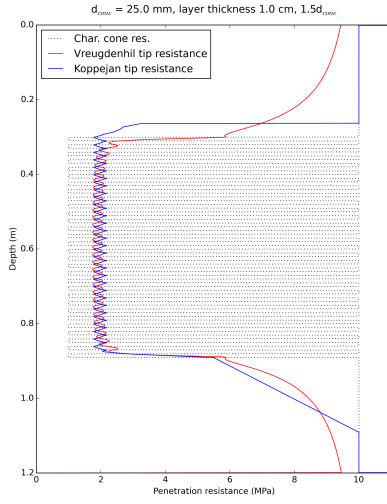


(e) 20 cm layers

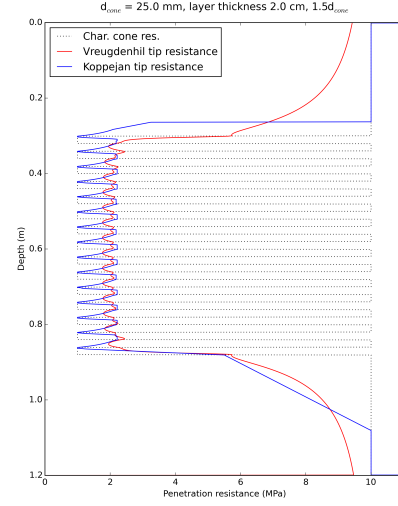


(f) 50 cm layer

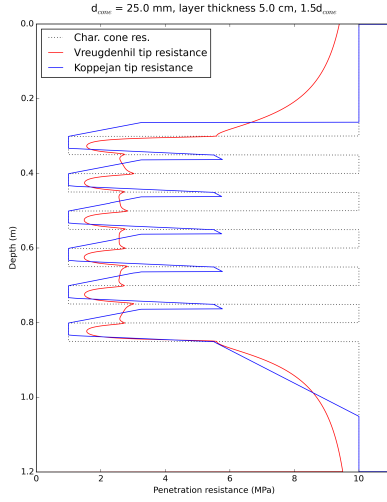
Figure F.5: Different scenarios with a 25 mm cone, iteration range for Koppejan trajectory 1 between 0.7 and 2.0 d_{cone}



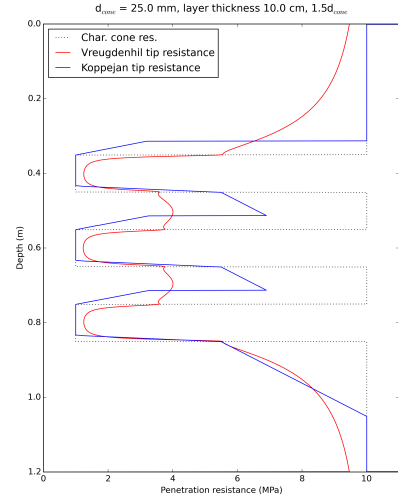
(a) 1 cm layers



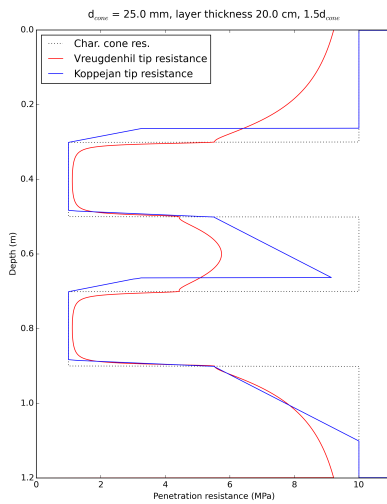
(b) 2 cm layers



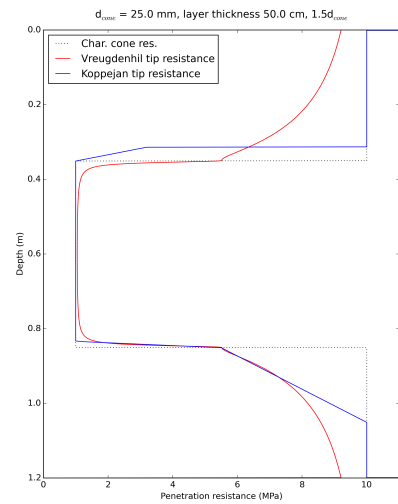
(c) 5 cm layers



(d) 10 cm layers

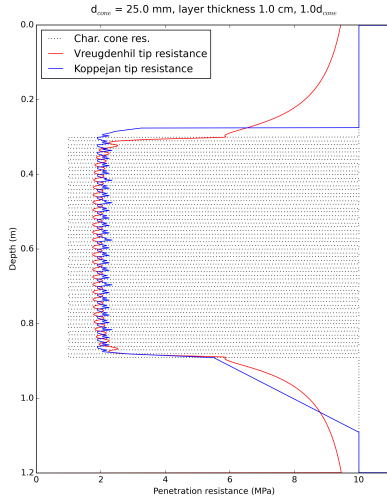


(e) 20 cm layers

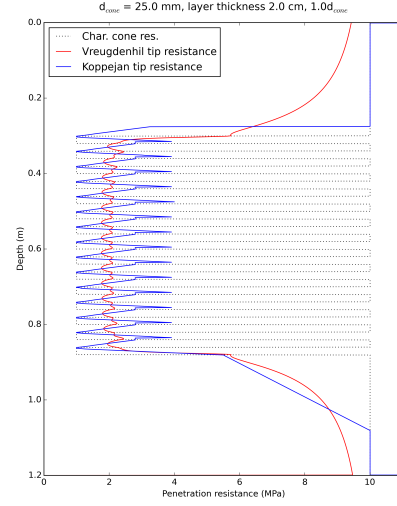


(f) 50 cm layer

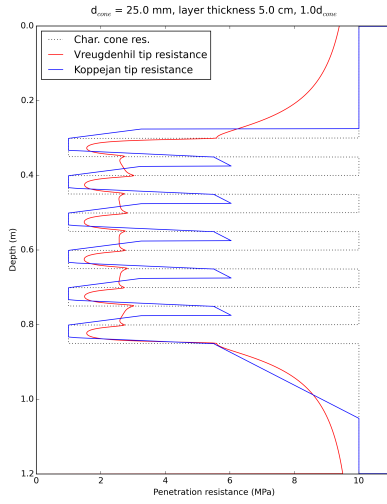
Figure F.6: Different scenarios with a 25 mm cone, iteration range for Koppejan trajectory 1 between 0.7 and $1.5 d_{\text{cone}}$



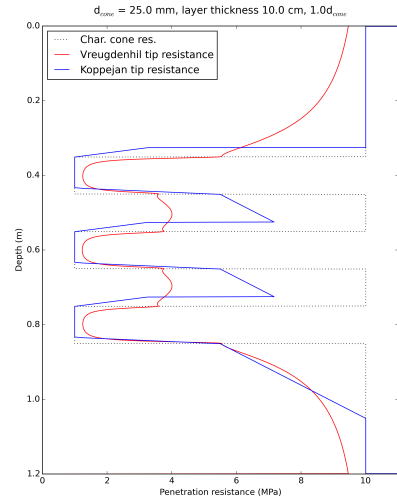
(a) 1 cm layers



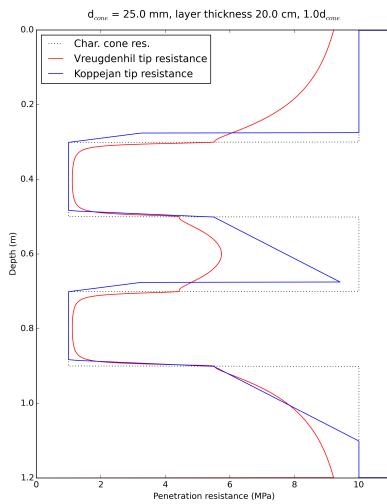
(b) 2 cm layers



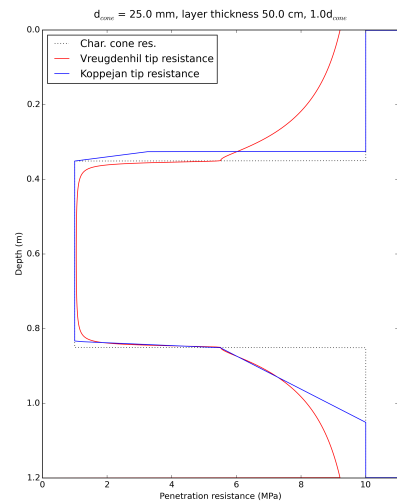
(c) 5 cm layers



(d) 10 cm layers



(e) 20 cm layers



(f) 50 cm layer

Figure F.7: Different scenarios with a 25 mm cone, iteration range for Koppejan trajectory 1 between 0.7 and $1.0 d_{\text{cone}}$

G Factual testing report

Contents

G.1	Considerations	G-2
G.1.1	Cone properties and dimensions	G-2
G.1.2	Influence of top and bottom boundary	G-3
G.1.3	Cell size effects	G-3
G.1.4	Sample pressurisation	G-6
G.1.5	Multiple tests on one sample	G-7
G.1.6	Layer thicknesses	G-7
G.1.7	Sand density	G-7
G.1.8	Penetration rate	G-7
G.1.9	Repeatability	G-8
G.2	Indicative tests Baskarp sand	G-8
G.2.1	Sieving characteristics	G-8
G.2.2	Minimum and maximum density	G-11
G.2.3	Previously conducted tests	G-12
G.3	Indicative tests Vingerling clay	G-13
G.3.1	Atterberg limits	G-13
G.3.2	Undrained shear strength and water content	G-14
G.3.3	Previously conducted tests	G-14
G.3.4	Swelling of Vingerling clay	G-18
G.4	Preparation techniques	G-19
G.4.1	Sand preparation	G-19
G.4.2	Clay preparation	G-23
G.5	Experimental setup	G-25
G.5.1	Cell and driving equipment	G-25
G.5.2	Cone and data-acquisition	G-27
G.6	Testing procedure	G-30
G.6.1	Data processing	G-30
G.6.2	Sample dismantling	G-31
G.7	Sample 1: Uniform dense sand layer	G-32
G.7.1	Sample configuration	G-32
G.7.2	Tests	G-33
G.7.3	Results	G-34
G.7.4	Sample dismantling	G-37
G.7.5	Conclusions	G-38
G.8	Sample 2: Single 30 cm clay layer between dense sand layers	G-39
G.8.1	Sample configuration	G-39
G.8.2	Results	G-40
G.8.3	Dismantling	G-44
G.8.4	Conclusions	G-46
G.9	Sample 3: Uniform medium dense sand layer	G-47
G.9.1	Sample configuration	G-47
G.9.2	Results	G-48
G.9.3	Dismantling	G-51
G.9.4	Conclusions	G-51

G.10 Sample 4: Two layered medium dense sand layers	G-52
G.10.1 Sample configuration	G-52
G.10.2 Results	G-53
G.10.3 Dismantling	G-56
G.10.4 Conclusions	G-57
G.11 Sample 5: Three 8 cm clay layers between medium sand layers . . .	G-58
G.11.1 Sample configuration	G-58
G.11.2 Results	G-59
G.11.3 Dismantling	G-63
G.11.4 Conclusions	G-65
G.12 Sample 6: Ten 2 cm clay layers between medium sand layers	G-66
G.12.1 Sample configuration	G-66
G.12.2 Results	G-66
G.12.3 Dismantling	G-71
G.12.4 Conclusions	G-73
G.13 Sample 7: Uniform medium sand layer	G-74
G.13.1 Sample configuration	G-74
G.13.2 Results	G-74
G.13.3 Dismantling	G-78
G.13.4 Conclusions	G-78

G.1 Considerations

The most ideal testing situation would be to have a very big sampling tank in which multiple tests can be conducted on one sample with negligible boundary effects on the penetration resistance. Since time and means were limited, it was chosen to prepare the sample in a cylinder with certain dimensions. Because multiple samples need to be tested in a limited amount of time, the cylinder could not be too large. A large cylinder would mean that sample preparation would take longer and that a uniform sample quality could become more uncertain. At the same time, a small cylinder would influence measurements considerably, making them less valuable for comparison with results from other research and for the sake of repeatability of the tests. Balance had to be found in order to come to an acceptable test setup. This section contains a description of the decisions and consideration made in order to get to a test setup.

G.1.1 Cone properties and dimensions

In order to minimize boundary effects on the penetration resistance measurements, it was preferred to use a cone with small diameter. But since the thin layers in Groningen are much thinner than the cone diameter used for in-situ CPTs, it would mean that when using a small cone the layers in the prepared sample need to be extremely thin in order to resemble in-situ testing. When using a standard 10 cm² cone, no scaling needs to be applied to the thin layers, which are already hard to prepare. It proved that the boundary effects were much more of an issue than the dimensions of the soil layers, so therefore the use of a 5 cm² cone is justified, equalling a cone diameter of 25 mm.

It was believed that the cone penetrometer should be able to measure pore pressures. From CPT data from field situations, detection of small clay layers seems to be more convenient using pore pressure transducers on the cone penetrometer. The pressure sensor seems to be more sensitive for a change in the penetrated type of soil, so the use of a piezocone for this research was preferred as well.

G.1.2 Influence of top and bottom boundary

According to *NEN 9997-1* (2012), the vertical zone of influence above the pile tip reaches up to 8 times the equivalent pile diameter. In order to eliminate the influence of the top boundary of the sample, relevant measurements are not taken until penetration has reached a minimum depth of 8 times the equivalent pile diameter, and so it is not necessary to build up layers above this minimum depth. Regarding this test, where the equivalent pile diameter is equal to the diameter of the cone (25 mm), it seems relevant to build up layers below a depth of at least $8 \cdot 0.025 \approx 20$ cm, but an even larger depth is preferred.

Section 2.2.2 provides a couple of definitions of critical depth, which in sense is the depth until which the top boundary influences measurements. It is stated that the value which gives the largest critical depth should be the governing value for critical depth. Three definitions have been given. For the situation with a sand with relative density of 50% situation the parameters are estimated such that $\varphi = 32^\circ$, $\gamma = 19.68$ kN/m³, $d_{cone} = 0.025$ m and $q_c = 1.0$ MPa at critical depth.

$$\frac{h_c}{d_{cone}} = \tan \left(45^\circ + \frac{\varphi}{2} \right) \cdot e^{\pi \tan(\varphi)} = \tan \left(45^\circ + \frac{32^\circ}{2} \right) \cdot e^{\pi \tan(32^\circ)} = 12.85 \quad (G.1)$$

$$\frac{h_c}{d_{cone}} = (3.28 \pm 0.63) \cdot (10 \cdot q_c)^{0.407} = (3.28 \pm 0.63) \cdot (10 \cdot 1.0)^{0.407} = 8.37 \pm 1.61 \quad (G.2)$$

$$\frac{h_c}{d} = \frac{25 \cdot (1 + 0.1q_c)}{\sqrt{d}} = \frac{25 \cdot (1 + 0.1 \cdot 1.0)}{\sqrt{2.5}} = 17.39 \quad (G.3)$$

According to these calculations for this situation, critical depth should be set at $17.39d_{cone}$ below ground level. This means that below a depth of 43.5 cm full penetration resistance is reached and that layering could be installed at that depth. Regarding the differences between the calculated critical depths the governing depth of 43.5 cm is quite uncertain.

In order to let the resistance reach its characteristic value before the bottom of the cylinder is reached, it was also preferred to prepare at least the bottom 20 cm without layering. Since in calibration chambers from other laboratories sample heights of 1 - 1.5 m can be reached (Salgado et al. (1998)), it seemed reasonable that it is possible to prepare 1.2 m high samples, depending on the equipment available. With the two zones of 30 cm that do not contain layering, 60 cm of vertical space was left for preparing layers.

G.1.3 Cell size effects

Salgado et al. (1998) and Ahmadi and Robertson (2004) studied the size effects of the calibration chamber size on the penetration resistance in sand, while Bolton et al. (1999) studied the size effects during centrifuge cone penetration tests. Salgado et al. (1998) pictured different zones of influence based on cavity expansion theory. The zones of influence are shown in figure G.1. The ideal situation would be when $B > A > R$, or at least that $B > R$. At this point it is believed that the cone resistance would be influenced significantly by the boundaries. Besides cone diameter the size of R depends on the relative density of the sand and therefore on the neutral earth pressure coefficient K_0 through φ . Making sure the cone diameter and K_0 are small enough results in a situation where $B > R$.

Salgado et al. and Ahmadi and Robertson distinguish four types of boundary conditions, which are displayed in figure G.2.

The test setup with rigid cylinder walls that was used in this research resembles a combination of BC2 and BC3, with the bottom boundary condition from BC2 and top condition from BC3. For convenience BC3 is considered to resemble the situation occurring during this project, since

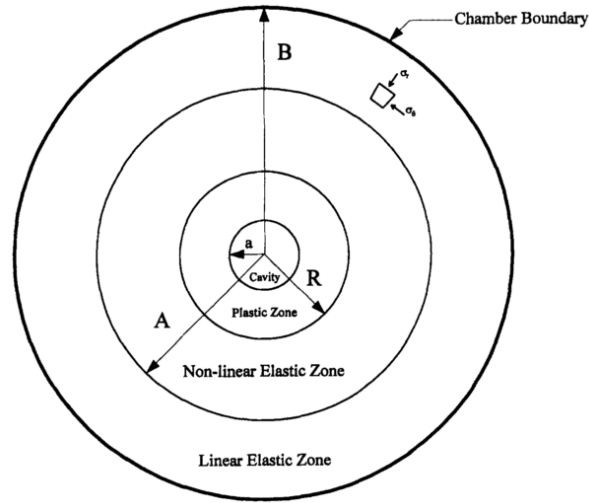
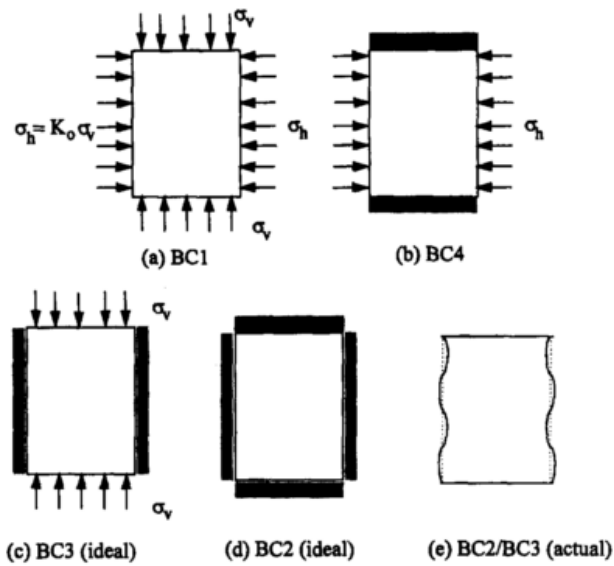


Figure G.1: Classification of zones of influence in calibration chamber (after Salgado et al. (1998)).



Type of Boundary Conditions	Lateral Boundary Conditions	Top and Bottom Boundary Conditions
BC1	Constant Stress	Constant Stress
BC2	No displacement	No displacement
BC3	No displacement	Constant Stress
BC4	Constant Stress	No displacement

Figure G.2: Types of boundary conditions in calibration chamber tests (after Salgado et al. (1998)).

the walls of the cell can be regarded as rigid. Ahmadi and Robertson (2004) provided a numerical modelling procedure for the penetration procedure, and plotted the predicted tip resistance against the chamber diameter to cone diameter ratio ($D_{\text{chamber}}/D_{\text{cone}}$). The results for different sand densities can be found in figure G.3.

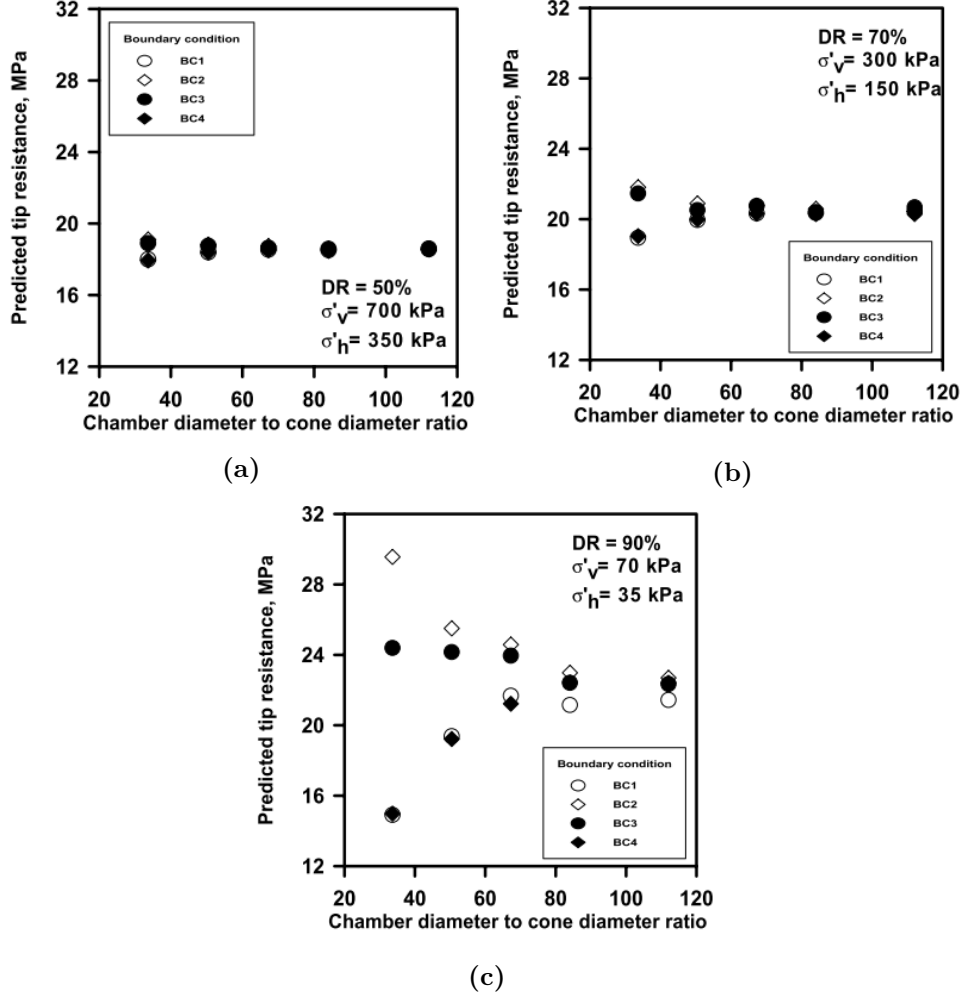


Figure G.3: Effect of chamber size and boundary condition on tip resistance for different sand densities (after Ahmadi and Robertson (2004)).

From these numerical simulations, it can be concluded that for BC3 higher values of $D_{\text{chamber}}/D_{\text{cone}}$ around 30 give relatively constant tip resistances for relative densities of 50%. It was therefore assumed that $D_{\text{chamber}}/D_{\text{cone}} = 30$ would be sufficient to avoid boundary effects in the measurements, although results for lower ratios have not been presented. Since the preferred cone size would be 25 mm, this would mean that at the diameter of the cylinder needs to be at least $30 \cdot 0.025 = 0.75$ m.

Bolton et al. (1999) evaluated size effects in centrifuge CPT tests in sand. Bolton et al. (1999) give in the diagram showed in figure G.4 the normalised cone resistance (see section 4.2) over the ratio between the diameters of the cell and cone (D/B). It can be concluded that Bolton et al. (1999) find that around a ratio of 30 the normalised cone resistance does not longer depend on the D/B -ratio. This does not fully correspond to the results from Salgado et al. (1998) and Ahmadi and Robertson (2004) for a relative density of 70%.

Because the difficulty of layered sample preparation was yet unknown and it was assumed that preparing larger diameter samples is more difficult and time consuming, it was preferred to use the available $\varnothing 60$ cm cylinder. However, when looking at the discussed researches, the use of

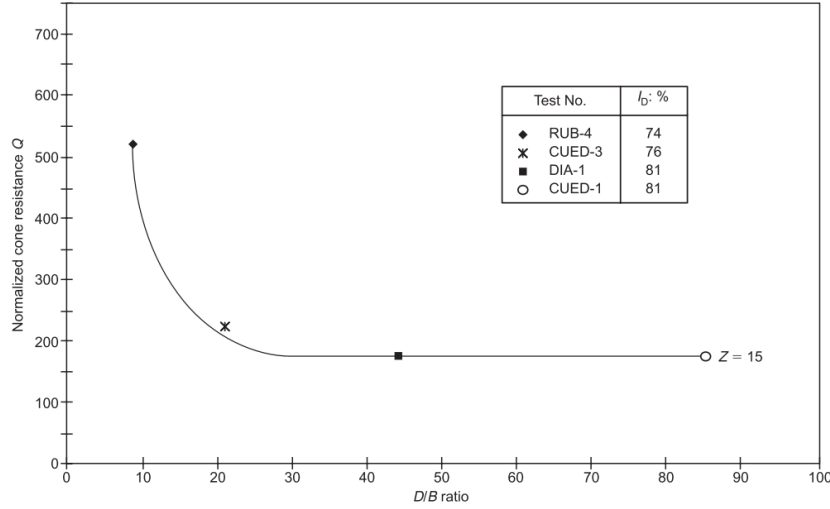


Figure G.4: Normalised cone resistance over D/B ratio (after Bolton et al. (1999).)

this size will lead to the occurrence of boundary effects in the results, which is certainly not desired. Nevertheless, the tests commenced using the $\varnothing 60$ cm cylinder with a cone diameter of 25 mm (D/B ratio of 24) since the use of a larger cell was not considered to be feasible.

Moreover, it seems that different authors draw different conclusions from their research. Ahmadi and Robertson (2004) give a fairly positive conclusion on BC3:

“The result of this study also indicate that the boundary condition BC3 appears to represent the best boundary condition with the least affect on the measured cone resistance.”

On the other hand, Salgado et al. (1998) state about BC2 and BC3 conditons on the basis of their research:

“So ideal BC2-BC3 conditions would represent free-field conditions poorly and introduce unneeded complexities into the analysis of the problem.”

It can therefore be concluded that different sources in literature do not entirely agree on the value of boundary conditions. Because of limitations in time and means, it was not an option to think about using different kinds of boundary conditions (e.g. constant lateral pressure instead of no lateral displacement at the boundaries), but it may be interesting to look at in future research.

G.1.4 Sample pressurisation

It turned out that in the course of this research it was too complicated to achieve a higher stress level in the sample. For sample pressurisation using air pressure the cell and other equipment were not The most simple way of obtaining some level of stress, to apply surcharge, would mean that with a 60 cm diameter cell a 10 kPa increase in stress would require an extra 282 kg of dead weight equally divided over the whole area of the cell. In combination with the requirement to test multiple locations on the sample sample pressurisation was believed not to be feasible.

For future research using a comparable testing setup could be focussed more on using surcharge. In order to have some level of pressure in the sample without using equipment like a triaxial test cell, a steel disk with similar diameter as the inner diameter of the cylinder could be placed on top of the soil. On this disk extra dead weight can be placed. A hole needs to be installed in the disk to allow the cone to penetrate the sample. By making on hole in the centre and two holes eccentricly a wide rang of test locations can be tested by rotating the disk.

G.1.5 Multiple tests on one sample

To obtain reliable results and to know where possible flaws in the cone resistance trend could come from, it was preferred to conduct multiple tests on a single sample. Because the cylinder diameter is already relatively small compared to the cone diameter, the results from the first (uniform sand) sample with multiple tests was needed to be analysed before deciding to continue performing multiple tests on a single sample and to continue preparing samples using the same preparation method. When results would show that the first penetration gives significantly different results than subsequent penetrations, it was concluded that only one penetration per sample is preferable for result analysis. Subsequent tests on a single sample would be used merely for checking whether flaws in the data would come from the way the sample was prepared or errors from the cone.

G.1.6 Layer thicknesses

Layers in Groningen are considered to have a thickness of 3 to 15 mm. Because it was not known whether it would be feasible to prepare clay layers of this size, it was believed to start testing with thicker layers. From simulations described in appendix F it was determined that performing tests on 30 cm, 8 cm and 2 cm thick layers with same thickness for clay and sand layers could give distinctive results between tests.

G.1.7 Sand density

High density is easier to obtain uniformly, but is not a good representation of the situation in Groningen, where a fairly loosely packed sand is found. Low density samples will mean that the sand will behave contractive, while high density samples tend to behave dilative during penetration, which causes differences between the field and laboratory situation. Since it was fairly easy to obtain homogeneous high density samples the first samples contained highly compacted sand. After evaluation of the results of the first tests it was decided to continue with lower relative densities for sand, making it necessary to test new sand preparation techniques on beforehand.

G.1.8 Penetration rate

Standard penetration rate as described in NEN-EN-SO 22476-1 (Nederlands Normalisatie-instituut (2012)) is (20 ± 5) mm/s. Since the data-acquisition hardware is capable of recording at a maximum of 4 Hz, keeping the penetration rate at 20 mm/s would mean that only every 5 mm a sample is taken. This interval is considered to be too large, so therefore a penetration rate of 4 mm/s with a sampling frequency of 4 Hz was chosen.

Choosing a different penetration rate could mean that CPT correlations valid under standard circumstances do not apply entirely on the tests on the layered samples, especially when looking at pore pressure development. Applying a lower penetration rate leads to lower excess pore pressures, so pore pressure data should be considered carefully when lower penetration rates are applied.

This way a lower penetration rate may lead to higher cone resistances in clayey soils, since effective stresses become higher as water pressures are less compared to higher penetration rates. Moreover the soil ahead of an advancing cone has more time to consolidate with a lower penetration rate than with higher penetration rates, developing larger shear strength and stiffness (Kim et al. (2010)). In permeable soils lower penetration rate should therefore have less effect on cone resistance measurements.

G.1.9 Repeatability

Since tests needed to be comparable with each other it was important to keep the preparation techniques repeatable so sample properties do not change much when prepared using the same preparation technique. Especially obtaining constant relative sand density proved to be a challenge, but looking at the results for cone resistance it can be concluded that a fair level of repeatability has been achieved with the preparation techniques used.

G.2 Indicative tests Baskarp sand

Baskarp sand can be classified as graded sand, which is encountered in Sweden and similar to sand found in the Eastern Scheldt region (Ibsen and Bodker (1994)). Ibsen and Bodker (1994) have conducted multiple tests on Baskarp sand, including sieve tests, maximum and minimum void ratios and drained and undrained triaxial tests.

G.2.1 Sieving characteristics

Sieving characteristics of the delivered batch of Baskarp sand can be found in figure G.5. The steep inclination of the sieving curve indicates a fairly uniform grain size. The parameter d_{50} is 151 μm .

After all the samples were tested the recycled sand was sieved as well. The sieving characteristics of the Baskarp sand after testing can be found in figure G.6. It can be concluded that no significant changes have in grain size distribution have taken place during recycling of the sand, only the fine fraction ($<0.063\text{ mm}$) slightly increased from 0.1% to 0.3% after testing. This may be a result of particle crushing due to high cone resistances encountered with testing sample 1 and 2. Although most of the clogs of crushed material were removed after drying the tested sand for recycling purposes, a small amount of fine fraction remained. Regarding these two results from sieving tests, for result analysis it is assumed that the grain size distribution remained the same after recycling and therefore that a tiny change in grain size distribution did not have influenced penetrometer measurements.

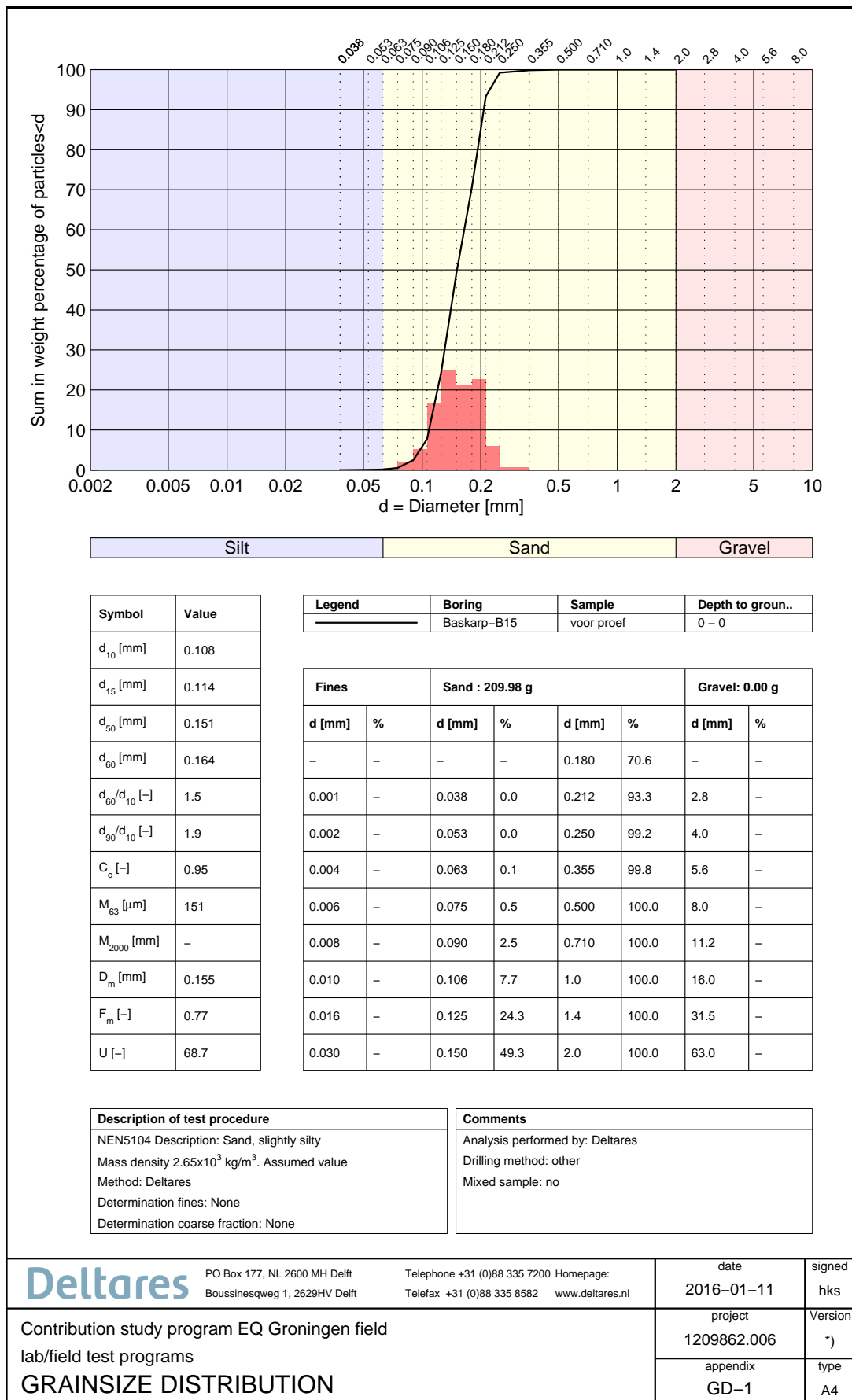


Figure G.5: Sieving characteristics of Baskarp sand before testing

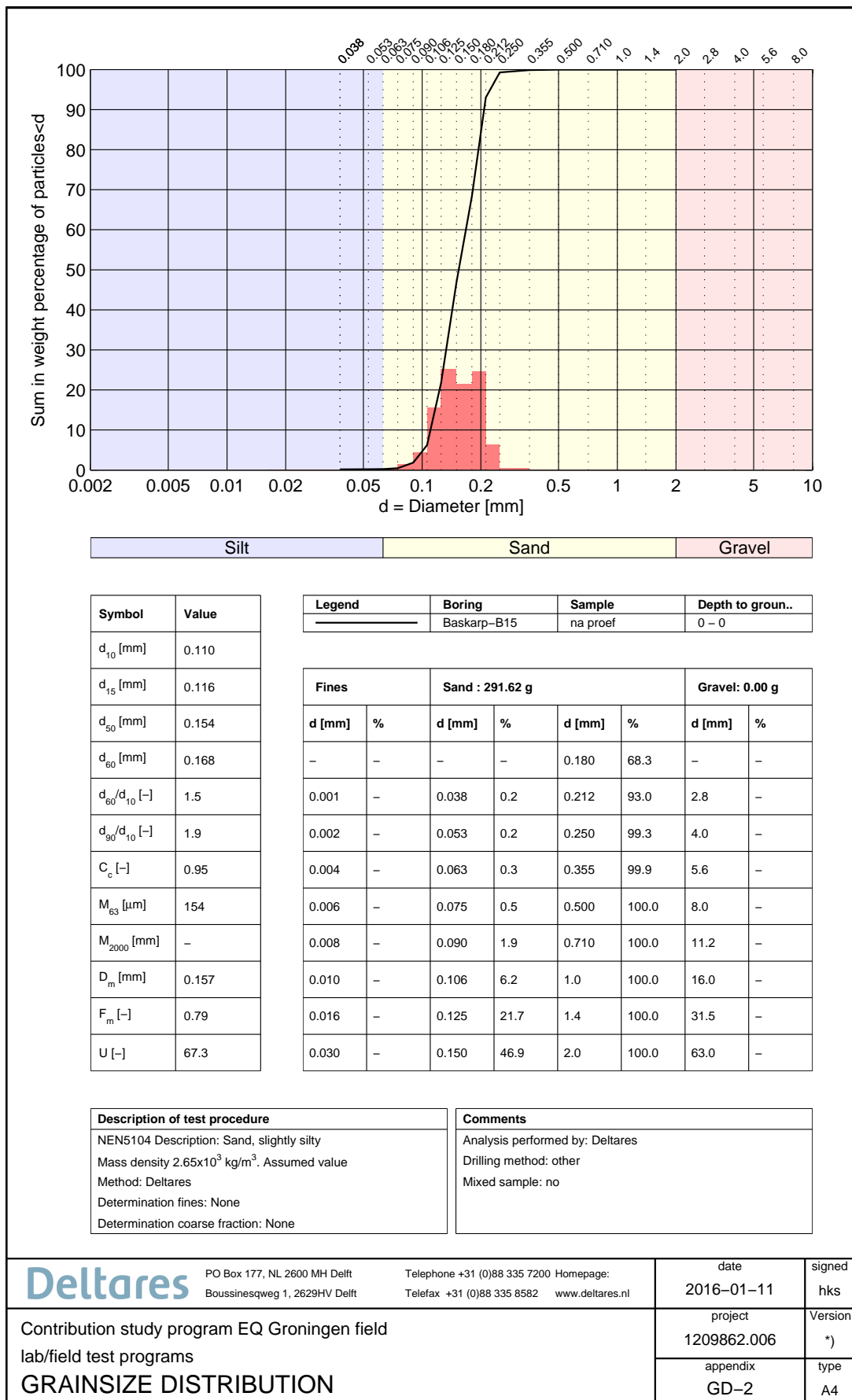


Figure G.6: Sieving characteristics of Baskarp sand after testing

G.2.2 Minimum and maximum density

Minimum and maximum densities of the Baskarp sand were determined using a 528 cm³ steel mould, a balance and a bowl with a certain amount of sand from the Deltares laboratory. For determining the maximum density also a stamper is needed. An overview of this equipment can be found in figure G.7. By measuring the weight of the sand before and after filling the mould an fairly accurate estimation can be made of the density of the sand in the mould. Minimum density was achieved by very carefully spreading the sand into the mould which is partly filled with water. This was done without touching or hitting the mould to avoid any compaction. Maximum density was achieved by also spreading the sand into the mould, but after each pour the sand was firmly compacted using the stamper.



Figure G.7: Equipment needed for determination of the minimum and maximum sand density, the balance has not been included in the photo

Table G.1: Overview of the density measurements

Measurement	Start weight [g]	End weight [g]	Net weight [g]	Density [g/cm ³]	Porosity [-]	Void ratio [-]
Max. density 1	1957.92	1056.18	901.74	1.7078	35.55%	55.17%
Max. density 2	2989.60	2088.14	901.46	1.7073	35.57%	55.21%
Max. density 3	2793.35	1892.18	901.17	1.7068	35.59%	55.26%
Min. density 1	2088.12	1347.94	740.18	1.4019	47.10%	89.04%
Min. density 2	2812.30	2067.93	744.37	1.4098	46.80%	87.97%
Min. density 3	2067.93	1320.48	747.45	1.4156	46.58%	87.20%
			n_{max}	47.1%	e_{max}	89.0%
			n_{min}	35.6%	e_{min}	55.2%

It is determined that the minimum and maximum porosity are 35.6% and 47.1% respectively. The value of 35.6% for n_{min} is determined from the mean of the three measurements, the value of 47.1% for n_{max} is determined with the help of measurements from other Baskarp sand deliveries. Previous measurements have been giving higher values for the maximum porosity and during sample preparation some sand has been spilled during measurements 2 and 3, so the result of measurement 1 is taken as leading maximum density.

Since the method of determining minimum and maximum density used during these tests is

not described in codes or standards, determination of minimum and maximum density of the sand was also done at the Fugro laboratory in Leidschendam, The Netherlands. In this lab the method designed by the Danish Geotechnical Institute is used: the DGI method. This method is performed using dry pluviation. Determining minimum density is done the similar way as described above. For obtaining maximum density the sand is compacted using a falling weight on a certain amount of sand. This method gives values for minimum and maximum porosity of 37.9% and 46.8% respectively. This indicates that the method used by Deltares gives looser and denser samples but that the values are comparable. This comparison can be used when results of this research are compared with other researches using different methods of minimum and maximum density determination.

During the experiments 35.6% and 47.1% are used as minimum and maximum porosities to determine how much sand is required for proper sample preparation. This amount of sand is calculated using relative density. Relative density can be determined using porosity according to the following equation:

$$R_{d,n} = \frac{n_{max} - n}{n_{max} - n_{min}} \quad (G.4)$$

Which can be rewritten to:

$$n = n_{max} - R_{d,n} \cdot (n_{max} - n_{min}) \quad (G.5)$$

In these equations $R_{d,n}$ is the relative density based on porosity, n_{max} the maximum porosity, n the measured porosity and n_{min} the minimum porosity. It is also possible to express the relative density in terms of void ratio:

$$R_{d,e} = \frac{e_{max} - e}{e_{max} - e_{min}} \quad (G.6)$$

In which $R_{d,e}$ is the relative density based on void ratio, e_{max} the maximum void ratio, e the measured void ratio and e_{min} the minimum void ratio. Because of different definitions of n and e , their values of $R_{d,n}$ and $R_{d,e}$ also show a slight difference.

For convenience in calculations during the tests relative density based on porosity was used. During the experiments a relative density $R_{d,n}$ of $90\% \pm 2\%$ is considered to be achievable and conveniently repeatable using the preparation technique discussed in section G.4, and therefore the amount of sand needed is calculated using this value for relative density.

For example, when calculating how much sand is needed for 10 cm^3 to have a value of $R_{d,n} = 90\%$ the following calculation can be made: a relative density of 90% corresponds to a porosity of $-1 \cdot (0.9 \cdot (0.471 - 0.356) - 0.417) = 36.75\%$. Assuming the density of the sand grains to be $2650 \text{ kg/m}^3 (= 2.65 \text{ g/cm}^3)$, the bulk density is equal to $2.65 \cdot (1 - 0.3675) = 1.676 \text{ g/cm}^3$. So for a volume of 10 cm^3 a mass of 16.76 g of sand is needed for reaching a relative density $R_{d,n}$ of 90%.

During sample preparation quick calculations of relative densities were needed, which was more convenient using porosity as density indicator instead of void ratio. Since $R_{d,e}$ is commonly used in literature, values of $R_{d,n}$ determined and used during sample preparation are recalculated to and presented as values of $R_{d,e}$ in this report. For recalculating $R_{d,n}$ to $R_{d,e}$ the relationship between n and e ($e = n/(1 - n)$) and equations (G.5) and (G.6) are used. Bulk relative density determination was done with an uncertainty of about 0.6% if a measurement would give 50%. This is further elaborated in section H.1 of appendix H.

G.2.3 Previously conducted tests

From internal Deltares documentation tests conducted on Baskarp were available (triaxial tests), giving an indication of other characteristic parameters. It should be noted that these parameters have not been determined using the sand delivered for this research. Table G.2 provides an indication of other characteristic parameters.

Table G.2: Parameters from previously conducted research for Baskarp sand

	R_d 65%		R_d 50%	
ϕ_{max}	40.1 - 42.4	[°]	37.3 - 39.7	[°]
ϕ_{cs}	33 - 35	[°]	33 - 34	[°]
ψ_{max}	14.5 - 16.6	[°]	10.6 - 12.1	[°]
E_{50}	16 - 25	[MPa]	2.9 - 5.1	[MPa]

G.3 Indicative tests Vingerling clay

Vingerling clay is used in pottery and ceramics, and can be obtained from the supplier in bricks (*Sibelco*, clay type K147) with certain dimensions. Eventually small layers were cut from the bricks, resulting in a layer of certain thickness with an area of 25x10 cm² per brick.

As long as the sand and clay were not mixed during the penetration process, sand was reused in consecutive tests. It was assumed that clay cannot be reused after testing, since it could easily be contaminated with sand grains and the clay properties could have changed over the period of time the clay was surrounded by a saturated environment.

G.3.1 Atterberg limits

Tests for determining the liquid and plastic limit were performed on a sample of clay from a single brick. Liquid limit was determined using the Casagrande cup, of which the results can be found in figure G.8. A logarithmic trendline can be drawn through the points of measurement,

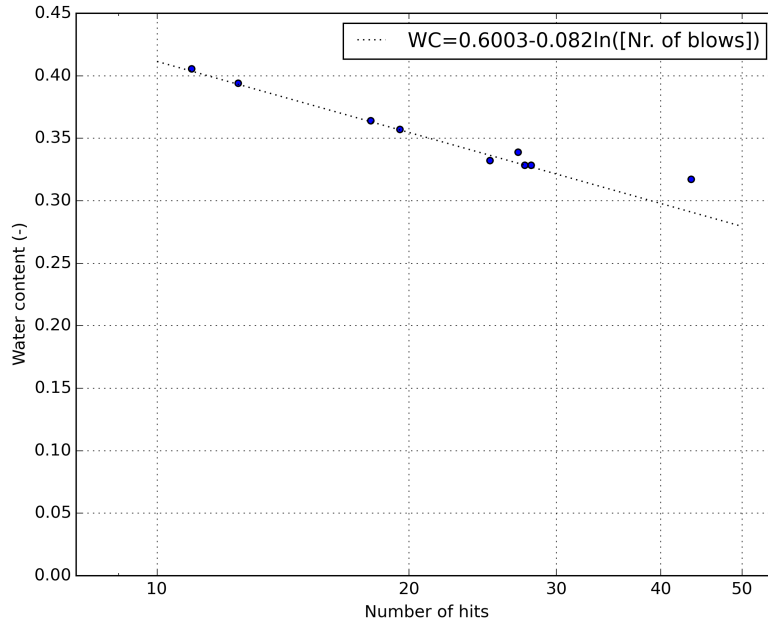


Figure G.8: Casagrande measurements and trendline

giving a relationship between the number of blows and water content WC:

$$WC = 0.6003 - 0.082 \cdot \ln([\text{nr. of blows}]) \quad (\text{G.7})$$

Since the liquid limit is defined in the Casagrande test as the WC at 25 blows, filling in the equation above gives a water content of 0.336.

The plastic limit was determined at a water content of 0.163. An overview of the consistency of the clay can be found in table G.3.

Table G.3: Values for Atterberg limits and soil consistency

Plastic limit	16.3%
Liquid limit	33.6%
Plasticity index	17.3%

These data can be used for determining the liquidity index of the clay, which is defined as:

$$\text{Liq. index} = \frac{\text{WC} - \text{Pl. limit}}{\text{Pl. index}} \quad (\text{G.8})$$

G.3.2 Undrained shear strength and water content

In order to know whether the different bricks of clay have comparable properties, each brick is tested for its undrained shear strength and water content. The undrained shear strength is indicatively determined with the use of a pocket-penetrometer. The water content is determined by weighing and drying a piece of clay. In table G.5 the results of the measurements on the bricks of clay can be found. In table G.6 statistical data can be found used for rejecting parts of the data, since the identifying of outliers on a dataset with a considerable amount of measurements is necessary. Rejection of data is done using the method of Chauvenet, described in appendix H.2.

The artificially produced clay was delivered as bricks with different serial numbers (example of a serial number can be found in figure G.17), indicating that the bricks delivered were produced in separate batches. This difference in moment of production may have influenced clay consistency, and therefore the two batches were analysed separately.

G.3.3 Previously conducted tests

From internal Deltares documentation tests conducted on Vingerling clay were available (oedometer tests), giving an indication of other characteristic parameters. It should be noted that these parameters have not been determined using the clay delivered for this research. Table G.4 provides an indication of other characteristic parameters.

Table G.4: Parameters from previously conducted research for Vingerling clay

c_v	$1.3 \cdot 10^{-8} - 2.0 \cdot 10^{-8}$	$[\text{m}^2/\text{s}]$
m_v	$1.4 \cdot 10^{-4} - 3.0 \cdot 10^{-4}$	$[\text{m}^2/\text{kN}]$

From the average value of m_v and with $E'_{oed} = m_v^{-1}$ the constrained modulus E'_{oed} is determined to be 4.5 MPa.

APPENDIX G. FACTUAL TESTING REPORT

Table G.5: Measurements of the tests regarding Vingerling clay

Brick nr.	Date	Batch nr.	Pocket pen.	S _u	Mass wet clay	Mass water	Water content	Chauv. nP	Chauv. nP
			[kg]	[kPa]	[g]	[g]	[-]	S _u	WC
1	17/08	11151103	5.20	14.24	42.06	7.99	0.235	10.774	14.856
2	17/08	11151103	5.15	14.11	29.73	5.63	0.234	7.676	12.483
3	17/08	11151103	5.40	14.79	N.A.	N.A.	N.A.	13.638	N.A.
4	17/08	11151103	5.30	14.52	57.28	10.21	0.217	18.368	0.008
5	17/08	11151103	5.35	14.65	59.51	11.58	0.242	17.557	5.767
6	17/08	11151103	5.30	14.52	20.37	3.87	0.235	18.368	14.932
7	17/08	11151103	4.80	13.15	20.35	3.91	0.238	0.154	14.022
8	17/08	11151103	5.40	14.79	20.29	3.93	0.240	13.638	8.338
9	18/08	11151103	5.60	15.34	20.22	3.91	0.240	3.029	9.387
10	18/08	11151103	5.00	13.70	20.32	3.95	0.241	2.023	6.287
11	18/08	11151103	5.20	14.24	40.52	7.79	0.238	10.774	13.566
12	18/08	11151103	5.30	14.52	50.37	9.64	0.237	18.368	17.157
13	18/08	11151103	5.50	15.07	31.77	6.00	0.233	7.129	10.574
14	18/08	11151103	5.70	15.61	44.35	8.37	0.233	1.031	10.110
15	18/08	11151103	5.40	14.79	46.13	8.76	0.234	13.638	14.576
16	18/08	11151103	5.20	14.24	44.51	8.57	0.238	10.774	12.422
17	18/08	11151103	5.45	14.93	49.83	9.41	0.233	10.108	10.519
18	18/08	11151103	5.45	14.93	20.36	3.91	0.238	10.108	14.405
19	18/08	11151103	5.30	14.52	20.27	3.95	0.242	18.368	5.085
20	18/08	11151103	5.40	14.79	20.30	3.91	0.239	13.638	12.153
21	18/08	20151205	5.70	15.61	20.29	3.95	0.242	20.993	1.562
22	18/08	20151205	5.75	15.75	20.27	3.92	0.240	13.891	6.273
23	18/08	20151205	5.80	15.89	42.13	8.05	0.236	8.584	32.491
24	18/08	20151205	5.60	15.34	39.33	N.A.	N.A.	39.580	N.A.
25	19/10	20151205	5.40	14.79	29.52	5.68	0.238	13.062	14.263
26	19/10	20151205	5.30	14.52	37.51	7.17	0.236	4.556	31.310
27	19/10	20151205	5.50	15.07	40.86	7.74	0.234	28.451	26.573
28	19/10	20151205	5.20	14.24	34.54	6.54	0.234	1.185	25.372
29	19/10	20151205	5.55	15.20	32.21	6.11	0.234	38.195	30.637
30	19/10	20151205	5.50	15.07	39.74	7.52	0.233	28.451	23.715
31	19/10	20151205	5.30	14.52	38.90	7.45	0.237	4.556	25.668
32	19/10	20151205	5.35	14.65	44.81	8.54	0.235	7.995	40.645
33	20/10	20151205	5.55	15.20	35.16	6.65	0.233	38.195	22.401
34	20/10	20151205	5.50	15.07	36.12	6.82	0.233	28.451	18.249
35	20/10	20151205	5.70	15.61	46.37	8.79	0.234	20.993	28.610
36	20/10	20151205	5.60	15.34	48.61	9.11	0.231	39.580	5.905
37	20/10	20151205	5.40	14.79	47.26	8.96	0.234	13.062	29.030
38	20/10	20151205	5.70	15.61	40.85	7.74	0.234	20.993	27.266
39	20/10	20151205	5.55	15.20	43.77	8.30	0.234	38.195	29.619
40	20/10	20151205	5.50	15.07	43.52	8.36	0.238	28.451	17.862
41	20/10	20151205	5.50	15.07	48.16	9.18	0.236	28.451	40.103
42	20/10	20151205	5.60	15.34	33.39	6.32	0.233	39.580	24.400
43	20/10	20151205	5.75	15.75	44.07	8.35	0.234	13.891	27.230
44	20/10	20151205	5.40	14.79	35.97	6.84	0.235	13.062	38.221
45	20/10	20151205	5.45	14.93	39.32	7.48	0.235	19.922	39.485
46	20/10	20151205	5.40	14.79	43.73	8.32	0.235	13.062	39.895
47	20/10	20151205	5.55	15.20	36.81	7.03	0.236	38.195	34.023
48	20/10	20151205	5.35	14.65	40.84	7.79	0.236	7.995	37.928
49	4/11	20151205	5.50	15.07	24.88	4.69	0.232	28.451	14.696
50	4/11	20151205	5.70	15.61	20.49	3.80	0.228	20.993	0.637
51	4/11	20151205	5.70	15.61	18.79	3.54	0.232	20.993	13.583
52	4/11	20151205	5.80	15.89	25.27	4.85	0.238	8.584	19.978
53	4/11	20151205	5.80	15.89	23.11	4.43	0.237	8.584	23.152
54	5/11	20151205	5.55	15.20	16.65	3.21	0.239	38.195	10.598
55	5/11	20151205	5.45	14.93	22.26	4.25	0.236	19.922	34.928
56	5/11	20151205	5.55	15.20	31.60	6.09	0.239	38.195	11.228
57	5/11	20151205	5.80	15.89	19.58	3.62	0.227	8.584	0.284
58	5/11	20151205	5.50	15.07	17.63	3.40	0.239	28.451	10.084
59	5/11	20151205	5.90	16.16	23.61	4.54	0.238	2.643	15.575
60	5/11	20151205	5.95	16.30	20.59	3.92	0.235	1.311	42.003
61	5/11	20151205	5.85	16.02	22.03	4.24	0.238	4.940	13.710
62	5/11	20151205	5.75	15.75	24.59	4.76	0.240	13.891	5.250
63	5/11	20151205	5.60	15.34	18.40	3.55	0.239	39.580	9.416
64	5/11	20151205	5.60	15.34	18.87	3.53	0.230	39.580	4.237

Table G.6: Statistical data of the measurements from table G.5, before and after rejecting data

<i>Before identifying outliers</i>						
Batch number	S_u	S_u	S_u	WC	WC	WC
	Readings	Mean	St. dev.	Readings	Mean	St. dev.
11151103	20	14.57	0.535	19	0.2360	0.00543
20151205	44	15.28	0.468	43	0.2352	0.00310
<i>After identifying outliers</i>						
Batch number	S_u	S_u	S_u	WC	WC	WC
	Readings	Mean	St. dev.	Readings	Mean	St. dev.
11151103	17	14.65	0.457	17	0.2370	0.00319
20151205	42	15.26	0.470	42	0.2354	0.00285

The dataset after identifying and eliminating outliers is used for liquidity index and S_u determination. Figure G.9 displays the dataset after elimination of the outliers including overall mean, showing limited spreading of the data. It can be concluded that batch 11151103 has a slightly lower S_u and a comparable mean WC as batch 20151205, therefore it is chosen not to focus much on differences between the batches.

From the pocket penetrometer measurements the undrained shear strength S_u can be calculated using the following empirical relationship:

$$S_u = \frac{Q}{\pi \cdot R^2 \cdot 11.4} \cdot 98.1 \quad [\text{kPa}] \quad (\text{G.9})$$

In which Q is the pocket penetrometer measurement in kg and R resembles the radius of the pocket penetrometer in cm (which has a diameter of 2.0 cm). This relationship between the penetrometer measurement and the undrained shear strength has been determined by Laboratorium voor Grondmechanica (1982) and has been used for determining the undrained shear strength S_u in table G.5.

Using equation (G.8) and the data from table G.3 the liquidity index is calculated taking the mean WC values of both batches with different serial numbers. Results are presented in table G.7:

Table G.7: Liquidity index of the Vingerling clay used during testing

Batch number	Mean WC	Liq. index
11151103	23.70%	42.8%
20151205	23.54%	41.8%
Mean		40.9%

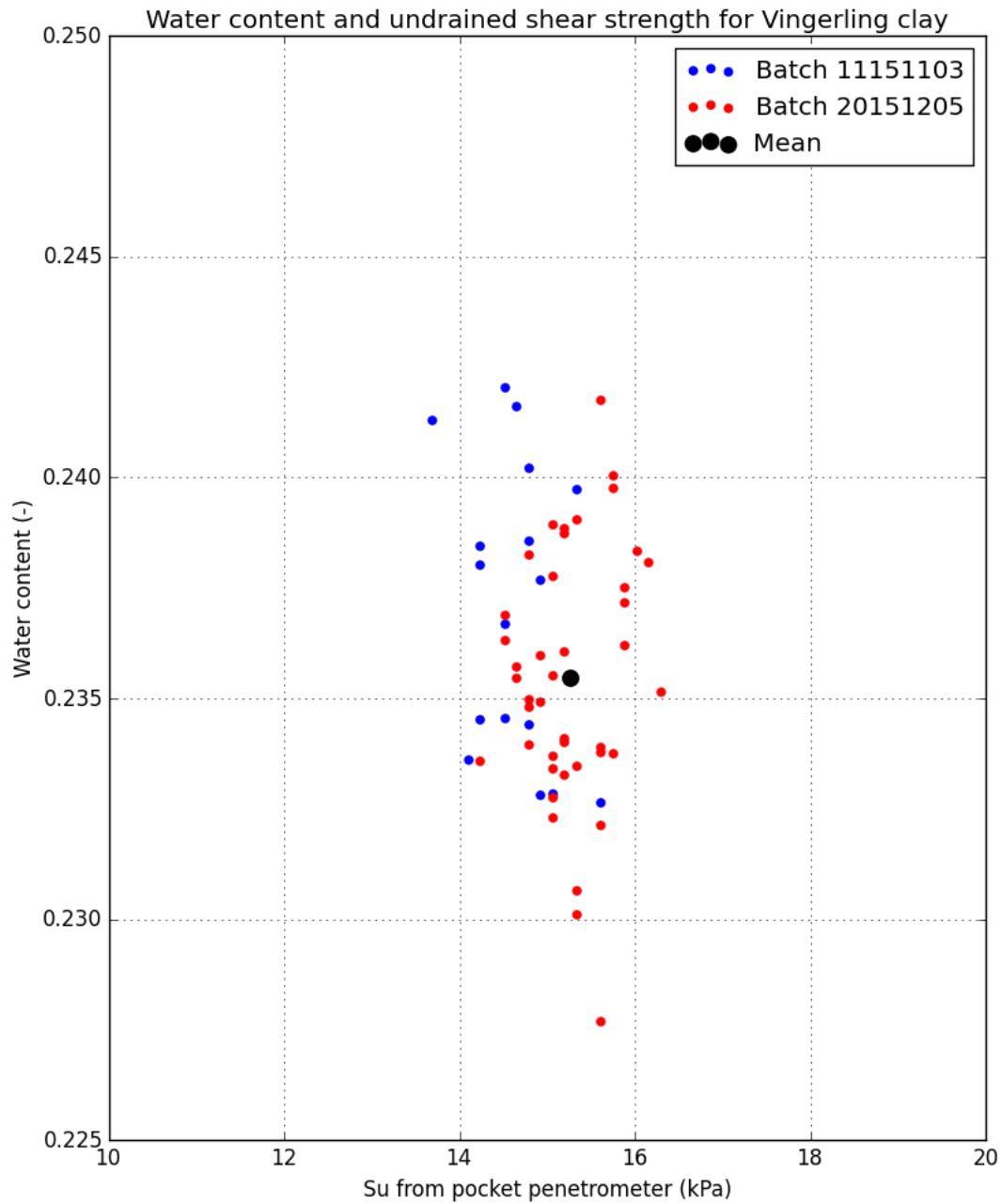


Figure G.9: Undrained shear strength plotted against water content obtained from tests on Vingerling clay

G.3.4 Swelling of Vingerling clay

In order to have an idea whether the Vingerling clay is susceptible to swelling when it is in contact with water, a small cylinder has been filled with a 3 cm circular clay layer surrounded by fully saturated sand. The sand has been prepared with a relative density of $R_{d,n} = 90\%$ ($R_{d,e} = 91.6\%$) using the method that will be used to prepare the samples in the large cylinder. After sample preparation the boundaries of the clay layer have been marked on the side of the transparent cylinder, which can be seen in figure G.10a. After 12 days it was concluded that the boundaries of the clay layer have not been moved, which can be concluded comparing figures G.10a and G.10b. Since it was expected that testing will happen before a period of 12 days has

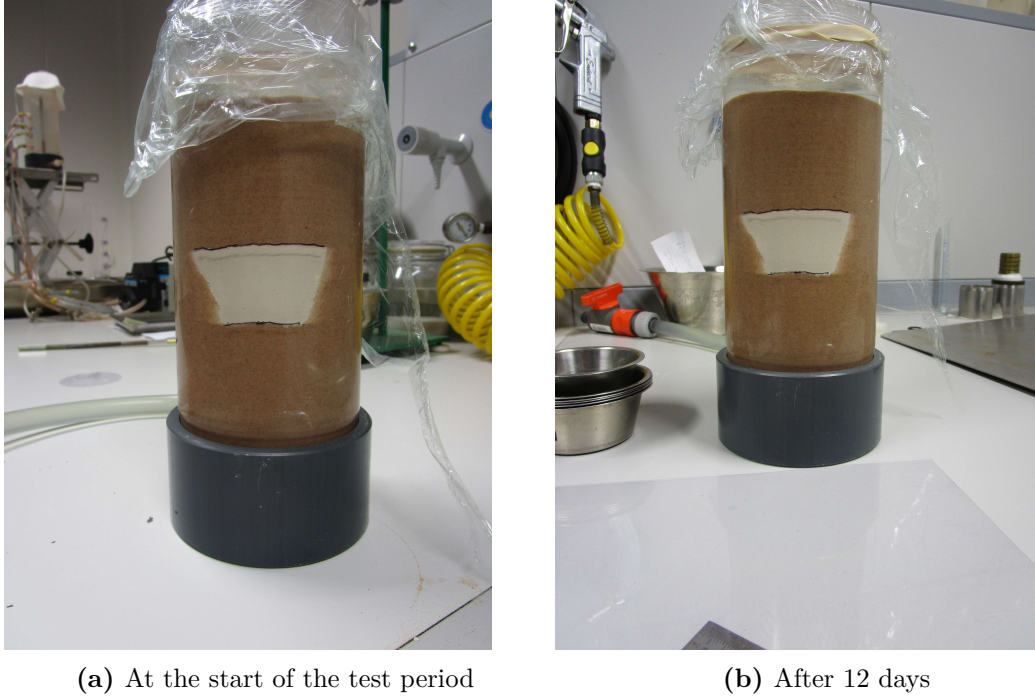


Figure G.10: Figures of the test cylinder at the start and at the end of the testing period

expired, it is assumed that swelling will not be an issue with this type of clay.

From the same brick of clay used for setting up the test cylinder, a measurement with the pocket penetrometer has been made, giving a value of 4.4 kg. After the 12 day period the clay from the cylinder has also been tested with the pocket penetrometer, giving a value of 3.7 kg. Although only one pair on measurements has been taken, the outcome indicates that the surface of the clay layer becomes softer after a period of rest in a saturated environment. This needs to be considered when evaluating the CPT results, therefore it may be best to perform the CPTs shortly after sample preparation.

G.4 Preparation techniques

G.4.1 Sand preparation

For preparation of the sand layer, multiple kinds of preparation techniques were used on different samples. All methods use the method of wet pluviation, but the method of compaction varies between different samples, described in sections below. Sand was delivered in big bags displayed in figure G.15a and prepared using a setup shown in figure G.15b.

Tamping technique

For the first and second sample, the sand was compacted up to a relative density $R_{d,n}$ of 90% ($R_{d,e} = 91.6\%$). The sand was prepared using a tamping technique which leads to a dense, homogeneous sample. By first carefully spreading dry sand in the cell filled with de-aired water enclosure of air pockets in the sand is prevented. After a layer of approximately few millimeters has been formed in the cell, continuous tamping starts. After half a minute of tamping more sand is spreaded into the cell while tamping continues. This process is continued until the amount of sand weighed at the start or the desired sample height has been reached. Figure G.11 shows a sketch of how the tamping technique is executed (1: sand is poured in the cell filled with water, 2: during pouring of the sand a tamper constantly compacts the sand which is poured in the cell over the whole area of the sample).

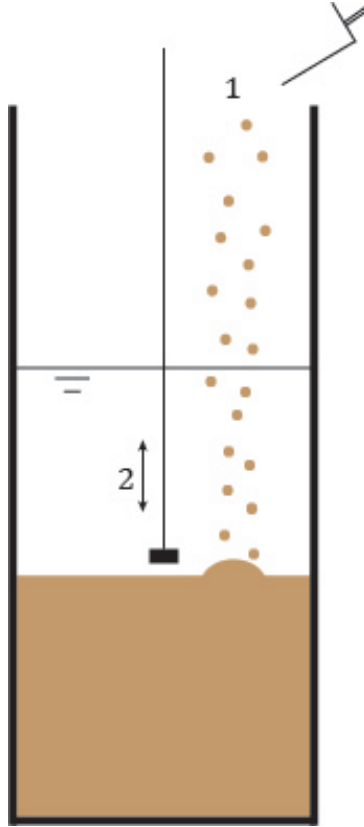


Figure G.11: Tamping technique

Verical shock wave technique

For the third and fourth sample, the tamping technique could not be used since a less dense sample was preferred. For this sample use was made of vertical shock waves in order to densify the sample. Because the technique results in a sample with certain relative density, the amount of sand can be calculated on beforehand. Because the sand compacts after pouring of the sand,

extra cell height is needed for pouring the sand which can be removed after compaction. After filling the cell by carefully spreading the sand in the cell without densifying the sand in any way, the cell was gently dropped on the floor in a controlled way after lifting the cell about 1 cm, until the desired sample height resulting in a $R_{d,n}$ of 70% ($R_{d,e} = 74.0\%$) was reached. According to Van der Poel and Schenkeveld (1998) this method gives an acceptable amount of homogeneity in relative density $R_{d,n}$. Figure G.12 shows a sketch of how the vertical shock wave technique is executed (1: sand is poured in the cell filled with water without any compaction, 2: a top plate is placed on the sand which is kept straight during compacting for giving stability to the top part of the sand, 3: vertical shock waves are applied on the sample).

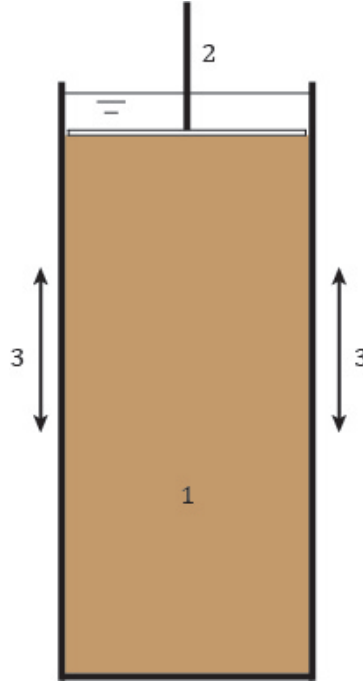


Figure G.12: Vertical shock wave technique

Thin layering compacting technique

For samples 5, 6 and 7 the two previous techniques could not be used, since a lower density than 70% was preferred and vertical shock waves are not suitable to use for building layered samples. Using vertical shock waves a sample of about 70% can be obtained which will not compact further after a certain amount of shocks. For lower densities in combination with layering this would cause the layers below the prepared clay layer to compact further as the top sand layer needs to compact as well, causing shifts in the location of the layering, which is certainly unwanted. Figure G.13 shows a sketch of how the thin layering compacting technique is executed (1: gently pouring the sand in the container in such amount that a height of 5 cm is reached after compacting up to $R_{d,n} = \%$, 2: compacting the sand by gently nudging the sand layer with a small plate and measuring the height of the layer as indication for the density achieved). Before using this technique on the actual samples, first a dummy layered sample was prepared with the thin layering compacting technique. During this test 2 clay layers were built between three sand layers, which were built in parts of 4 cm and compacted with the new technique. The bulk density of these layers seemed to be quite controllable and clay layer installation did not influence sand layer levels considerably. Figure G.14 shows a photo of the dummy sample after completion.

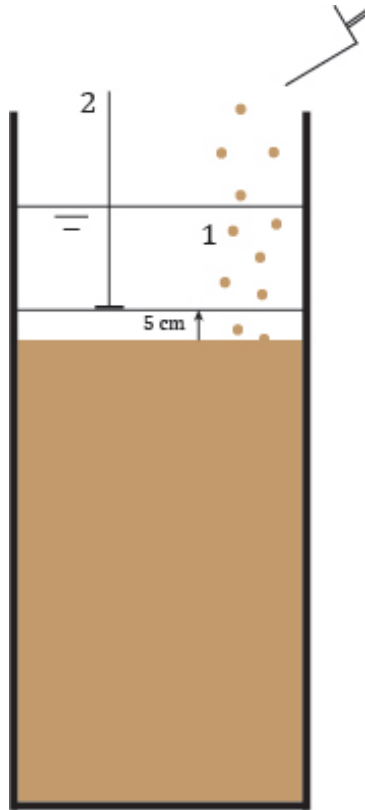


Figure G.13: Thin layering compacting technique



Figure G.14: Experimental setup for investigating preparation method for building a layered sample

Completing sand preparation

In order to have a clear and tight interface between sand and clay, the sand layers were prepared with extra height of which a few centimetres were removed before clay was placed, shown in figure G.16. This way the top of the layer, showing different sand properties than the rest of the sand layer, could not influence measurements and a smooth interface between sand and clay could be achieved. For the preparation method for obtaining a $R_{d,e}$ of 50% no extra height was removed, only the surface was smoothed. By lowering the water table below the level up to which the sand was prepared, capillary forces would give extra strength to the sand surface in order to keep the sand intact when placing the layers of clay on top. This way also height differences on the surface could be detected, making it easy to obtain a smooth surface were clay could be placed upon.



(a) Original delivered big bag of Baskarp sand



(b) Construction phase of sample 1

Figure G.15: Sand preparation



Figure G.16: Sand trimming technique for achieving a flat surface

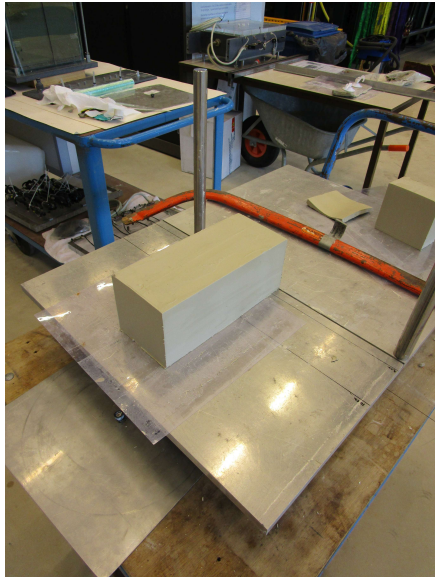
G.4.2 Clay preparation

The Vingerling clay was delivered in bricks of approximately 12.5x12.5x32 cm, which were trimmed into bricks of 10x10x25 cm. Figure G.17 shows an original brick the way it was delivered with the batch serial number printed on the side of the packaging.



Figure G.17: Original clay brick sealed with the batch serial number printed on the side of the packaging

Because the bricks of clay were delivered sealed in plastic but damaged and partly dried out on the outside during the production process and transport, the surface parts of the bricks were removed by slicing the bricks with a steel wire, which can be seen in figure G.18a. With the same steel wire the thinner slices of clay were cut from the reshaped brick. The thin clay slices were lifted by using two suckers on a plastic sheet sticking to the clay (see figure G.18b).



(a) Reshaping the clay by trimming



(b) Lifting method for thin layers

Figure G.18: Clay preparation techniques

After preparing the clay bricks the bricks were placed in the cell and pushed tightly together to prevent formation of air pockets between bricks as much as possible. An example of configuration of the clay from the second sample can be found in figure G.19.

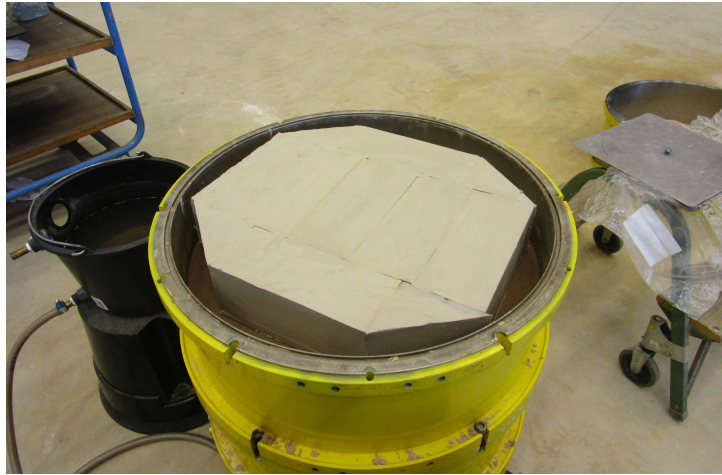


Figure G.19: Clay configuration in the cell

G.5 Experimental setup

G.5.1 Cell and driving equipment

In the testing hall of Deltares a number of steel cylindrical segments were available with an outer diameter of 60.0 cm and inner diameter of 58.9 cm, of which an example is shown in figure G.20a. Together with a bottom construction containing a bottom filter and drain a vertical construction was made allowing drainage at the top and bottom of the sample. Segments with different heights were available and combining different segment heights a wide range of sample heights could be achieved. The segments were fixed together with O-rings in between, ensuring the joints to be watertight.



(a) A 60 cm cylindrical segment with height of 23.1 cm

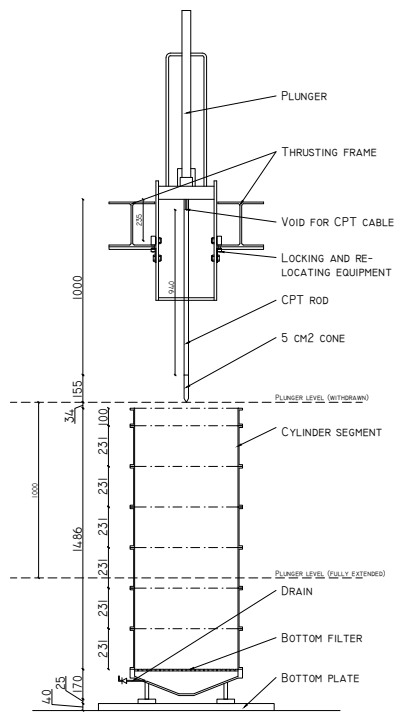


(b) Driving plunger, frame and tank in which the cell containing the sample was placed

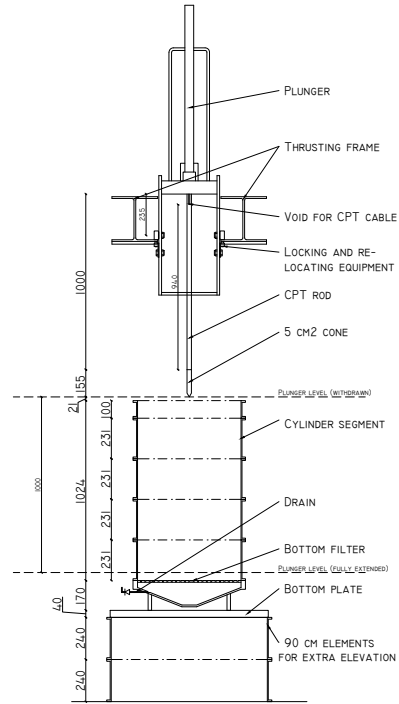
Figure G.20: Cell elements and testing location

As driving equipment a hydraulic plunger installed on a frame was chosen, shown in figure G.20b. The frame could be moved parallel to the tank and in lateral direction, allowing multiple testing locations without having to move the sample. A detailed cross-sectional overview of the test equipment and their positioning can be found in figure G.21. Equipment configuration was adjusted for different tests, resulting in different configurations for different tests. For example a different bottom plate was used after tests on sample 3, giving more stability to the cell.

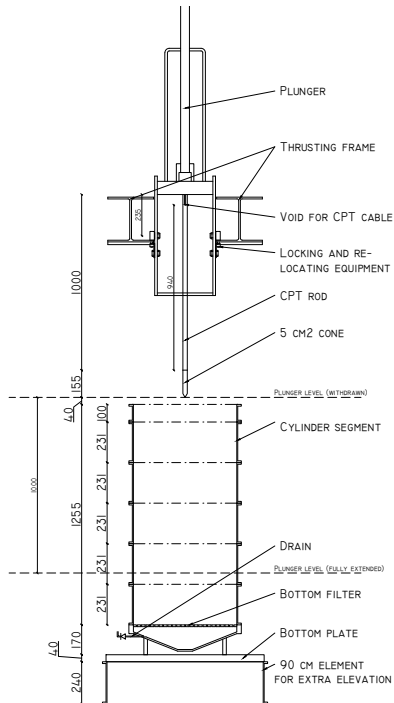
In order to avoid penetration through the joints in the clay layer caused by installation of the bricks, attention was paid where the bricks were placed and where the tests were performed. An overview of the brick configuration can be found in figure G.22. For the separate samples the test locations are displayed in their respective sections (figures G.28b, G.35b, G.43b, G.47b, G.53b, G.61b and G.69b).



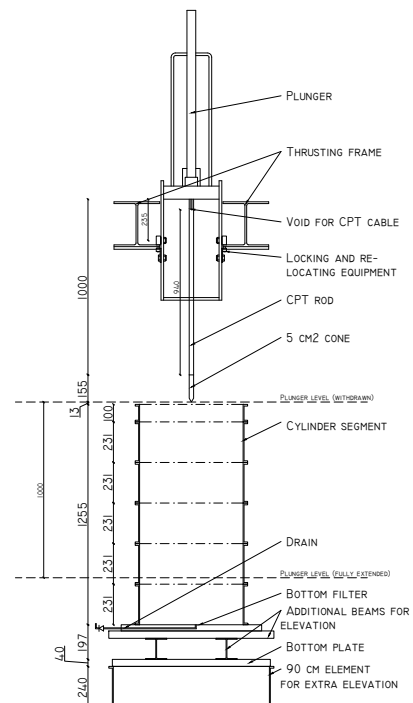
(a) Equipment configuration sample 1



(b) Equipment configuration sample 2



(c) Equipment configuration sample 3



(d) Equipment configuration sample 4, 5, 6 and 7

Figure G.21: Equipment configurations for different samples

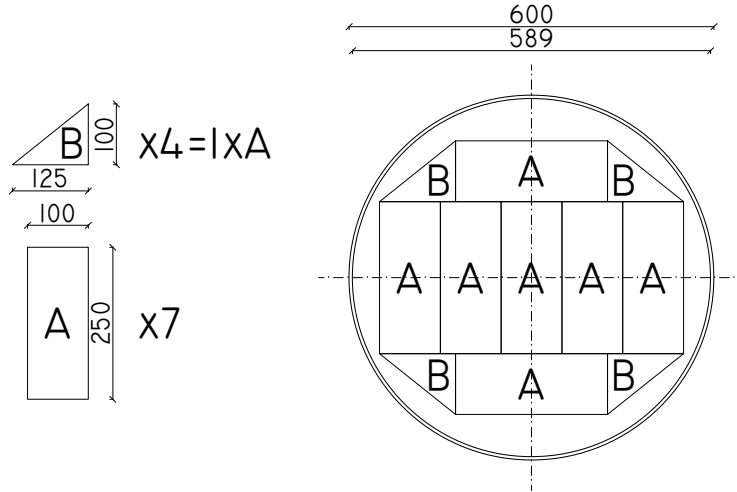


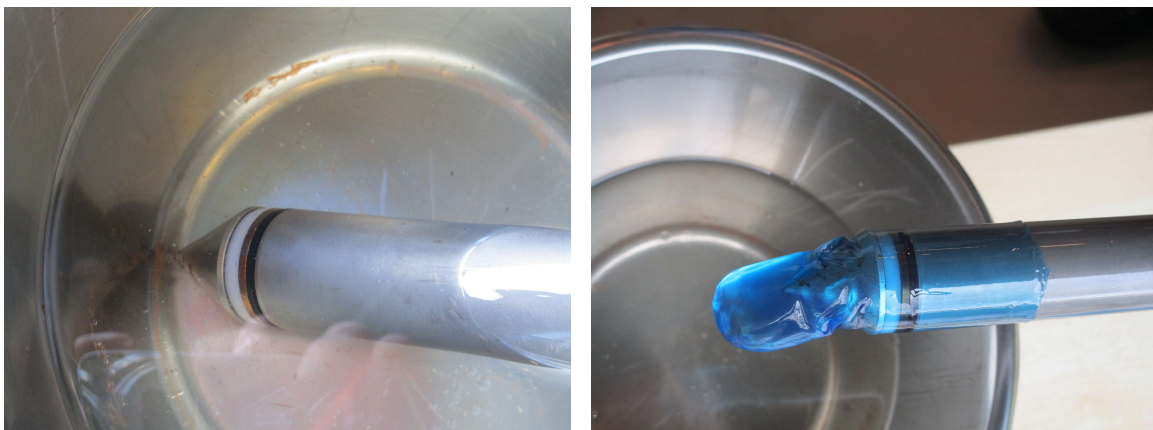
Figure G.22: Cross section of the cell with plan view of the clay brick configuration

G.5.2 Cone and data-acquisition

Since the cell diameter would give low D_{cell}/d_{cone} ratio (see section G.1.3), a smaller cone than used in usual field tests was used. A 5 cm² cone (having a d_{cone} of 25.2 mm \approx 25 mm) with u_2 pore pressure transducer (see figure 2.1a) was used for testing. Table G.8 gives cone dimensions displayed in figure G.25 of the cone used for testing.

The cone used for testing was a subtraction cone, meaning that the total load on the force on the penetrometer (tip and friction sleeve) is measured together with the force on the tip. By subtracting the total resistance with the tip resistance sleeve friction is obtained.

To prevent air from damping the pore pressure reaction of the pore pressure transducer, the filter and cone were put in silicone oil and treated with vacuum overnight. Before testing vacuum pressure was removed and a rubber seal was placed over the pore pressure filter while in silicone oil to prevent air intrusion. Just before penetration started the seal was removed from the cone. Figure G.23 shows figures of different stages of the saturation process.



(a) Photo of the cone during the saturation process of the pore pressure sensor **(b)** Photo of the cone sealed for preventing air intrusion in the pore pressure sensor

Figure G.23: Different stages in saturating pore pressure transducer and filter

After testing and dismantling of the sample the cone could be pulled out of the cross-section. The friction sleeve appears to have changed of colour after retrieving it from the sample (comparing figures G.23a and G.24). This happens when the cone is left in the soil for a while (which happened during dismantling), giving the metal alloy of the friction sleeve to react with its

environment. During testing with high density samples a broken O-ring was found in the path of cone while missing between the pore pressure filter and friction sleeve. It is assumed that the influence of a broken O-ring has insignificant effects on measurements, unless the watertightness of the cone is affected and measuring instruments and gauges start to fail. The data-acquisition program would give notifications when instruments fail.



Figure G.24: Photo of the cone after excavation

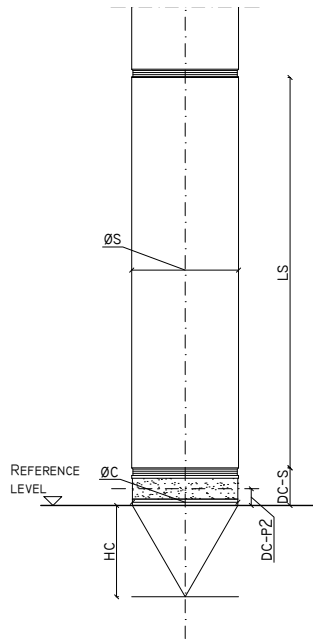


Table G.8: Table with typical dimensions of the cone used during testing, displayed in figure G.25, partly after the cone calibration certificate

Typical dimensions		
Ac	Cross-sectional projected area of the cone	0.0005 m ²
As	Surface area of the friction sleeve	0.0075 m ²
af	Cone net area ratio	0.5
scf	Friction sleeve net area ratio	0.01669
ϕ_c	Diameter of the cylindrical part of the cone	25.3 mm
ϕ_s	Diameter of the friction sleeve	25.6 mm
ls	Length of the friction sleeve	93.6 mm
dc-s	Cone - friction sleeve distance	9 mm
dc-p2	Cone - pore 2 distance	4 mm
Apex	Cone apex	60°
Hc	Cone height	21.9 mm

Figure G.25: Sketch of the typical dimensions of a cone with u_2 measuring possibilities

Just before testing starts a zero load check is done. During this check the cone is left hanging above the sample for about 30 seconds during which the data is recorded and checked for critical peaks, checking the stability of the signal and sensors. If this check is not passed the data-acquisition system notifies the user, leaving the decision to the user whether to start testing or not.

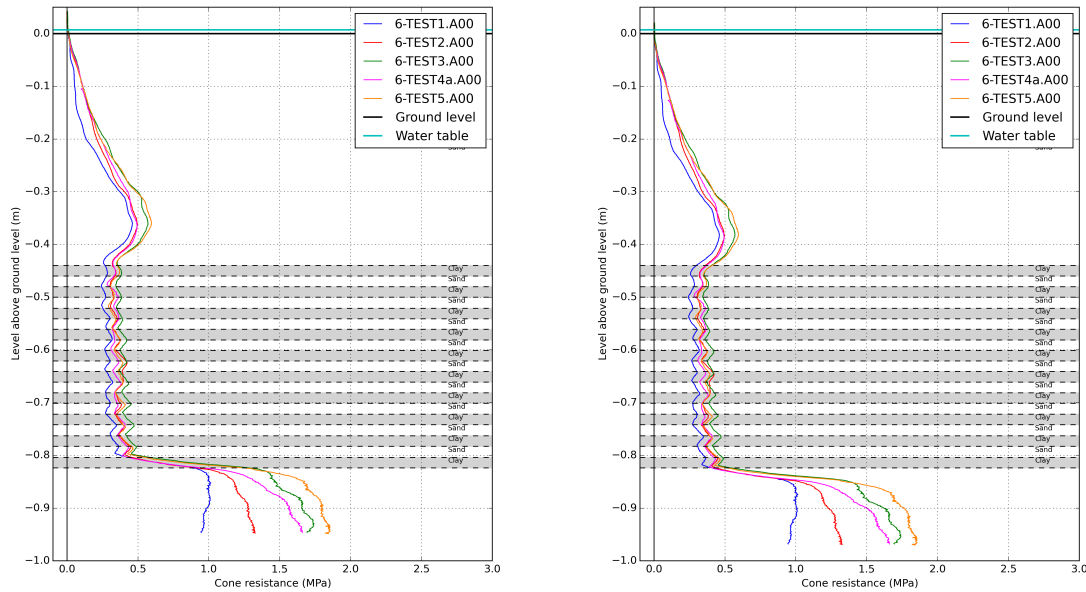
Reference levels

The location on the cone taken as reference point for the cone resistance measurements is drawn in figure G.25. Taking location at the shoulder of the cone as point of reference is done since the cone resistance is defined as the total force on the cone tip divided by the cone area. When choosing the reference point at the tip of the cone, cone resistance would not make sense since the area on the cone tip approaches zero.

Choosing the location on the shoulder of the cone causes the cone resistance to react at pressure differences at the cone tip. For instance, as the cone tip enters the soil but the reference point has not yet entered the soil, a stress increase is recorded while it seems that the cone is above ground level. This difference in choosing the reference level at either shoulder or cone tip can be found in figure G.26.

In fact the cone resistance is 'averaged' over the total cone height, making it a parameter which is valid over a depth equal to the cone height. When looking at a level of layer thicknesses smaller than d_{cone} this feature of the cone resistance becomes an important factor when looking at cone resistance data, also illustrated in the differences between figures G.26a and G.26b.

The cone signal provides data recordings including cone resistance, cone + friction, u_2 , cone inclination for each moment in time a sample recorded. Therefore at a certain moment in time data is written valid at different levels than recorded, since the pore pressure sensor and reference point of the friction sleeve are located at different levels than the shoulder of the cone.



(a) Cone resistance with reference level at shoulder of the cone (b) Cone resistance with reference level at tip of the cone

Figure G.26: Differences in cone resistance interpretation for different reference levels

G.6 Testing procedure

For layers of sizes smaller than 20 mm sampling frequency combined with penetration rate become quite significant, since choosing to have a low sampling frequency and high penetration rate, effects on the clay-sand interface could be missed. For example, the default Fugro sampling frequency is 2 Hz at a penetration rate of 20 mm/s, thus writing measurements every 1 cm of depth, which can make it more difficult to detect layers smaller than 1 cm simply because no measurements are taken in those layers. Since in this research samples are tested with 2 cm layers, it was desired to have a measurement taken every vertical millimetre and the maximum possible sampling frequency of the data-acquisition system was 4 Hz, it was decided to perform all tests with a penetration rate of 4 mm/s with a sampling frequency of 4 Hz. Some tests were performed at different penetration rates to compare results. In this case the penetration rate is stated in the test description.

The first test performed on the samples was always done in the centre of the cell. Since the first test was performed on a virgin sample and with the least boundary effects of all locations, the first test on a sample is considered to be the leading and most important one. After the first test other penetration were made at several locations on the sample, of which the locations are shown in their respective sections. These tests were done to check the overall of results from test 1 and to see whether sudden changes in data occur at one or more locations, so that measuring errors could be determined or excluded.

G.6.1 Data processing

Data files contain recordings of the cone signal taken with certain frequency (4 Hz in this research). Since the difference in location of the reference point of different sensors the raw data needs to be processed before being able to use the data. Using the distances from table G.8 the shift in depth for u_2 and sleeve friction measurements can be determined.

Since sensors do not give a value of 0 at the start of the test, this also needs to be corrected. The values for each different parameter recorded just before difference in depth measurement is measured (when the plunger starts to lower) are taken as zero values. These zero values are used to let measurements start at 0. In the test results this causes a shift on the x-axis of the plots. Determining the correct reference levels and zero values in the raw data was done using Fugro in-house software, which works as described above.

Especially with the pore pressure measurements the data for most of the tests show the same trend but are located in the graph as if horizontal shift of the results has taken place. In most cases the first test on a sample shows an increasing pore pressure as the cone enters the soil, after which the pore pressure transducer starts to react on different soil conditions, such as differences in relative density or sand-clay interfaces. In subsequent tests the trend most of the time resembles the trend from the first test, but pore pressures do not show an increase as the soil is entered. A possible explanation can be a temperature effect on the penetrometer, recognized by Lunne et al. (1997). Since the pore pressure transducer and filter are saturated in room temperature conditions while it is believed that sample temperature is lower, temperature may also have affected the pore pressure transducer. Another explanation can be that just before testing starts the seal to prevent air to intrude in the pore pressure filter is removed, which can cause suction in the filters and therefore lower pore pressures at the start of the tests. Since the zero values are taken just before the plunger drops, this can cause a different horizontal shift than for subsequent tests, when the seal is not removed.

G.6.2 Sample dismantling

The last testing stage is dismantling of the sample. During dismantling a cross-section of the sample can be made and/or density samples can be taken to have an idea of the relative density of the sample over its depth.

A cross-section can be made along the cone rod when the cone was left in the sample after testing, or along the path of a retracted cone. The water level in the cell is lowered slowly to that capillary forces can keep the sand from collapsing when the cross-section is made. Sand was removed by scraping it away from the vertical plane with a measuring ruler, while clay was cut using a tightened steel wire. Cross-sections have been made for samples in which layers of clay were tested, which were sample 2, 5 and 6 (see upcoming sections). Sample 1 has also been cross-sectioned, although the purpose of this cross-section was to investigate the feasibility of making cross-sections.

Density samples were taken when cone resistance data indicated the presence of heterogeneities in the sample or when it was uncertain if the preparation method used produced homogeneous samples. Density samples were taken with a 6.65 cm diameter cylinder, generally over an height of 5.00 cm. After pushing the cylinder in the sand, a scraper transported the sand upward to separate the sand from the rest of the sample. Figure G.27 displays the sample cylinder with scraper and a sand sample taken out of the sampler. Density samples were taken after testing, so values of relative density cannot be considered to be sample density before testing, since cone penetration affects the sample by causing local compaction and relaxation of the sample. Compaction will occur next to the cavity of the cone over an area of several cone diameters during penetration in loosely packed samples (dilation in densely packed samples), sample loosening will occur during cone retraction since the cavity left by the cone is filled due to under pressure from the retracting cone. Since almost all density samples are taken in an untested area next to test locations, it is assumed that a higher density is measured after penetration than what would be measured when density samples would be taken from untested samples. Besides this errors were made during sampling, which are more closely considered in section H.1 of appendix H. Since it was not the main goal of this research not enough time and means were available to built a sand sample merely for taking density samples at several depths, which would be a good way of investigating the change in local relative density due to cone penetration.



(a) Sampling cylinder with scraper



(b) Density sample taken out of the sampler

Figure G.27: Density sampling

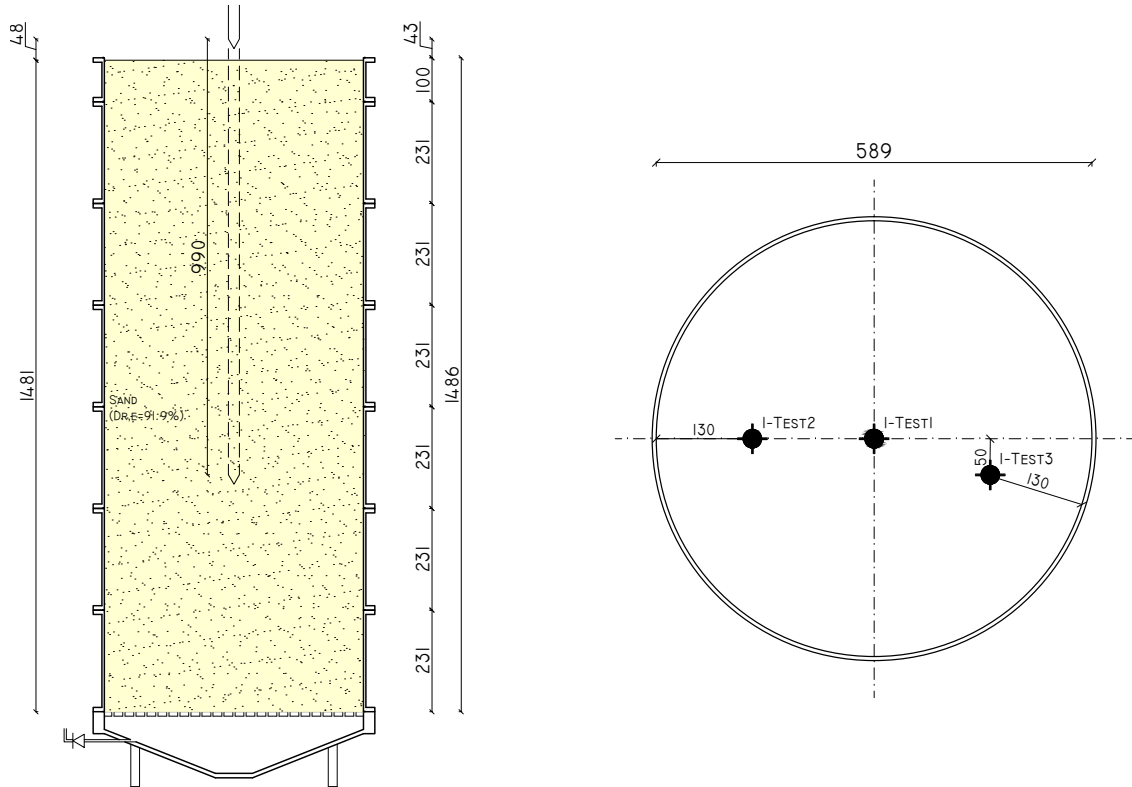
G.7 Sample 1: Uniform dense sand layer

During the first test setup the cell contains a sample with an approximate height of 1.5 m. The sample consists of a uniform densely packed sand with an relative density $R_{d,n}$ close to 90% ($R_{d,e} = 91.6\%$). Goals of the first sample were:

- To experience the procedure of sample preparation and testing,
- To see whether the use of an extension rod is feasible,
- To obtain a characteristic cone resistance for Baskarp sand (with $R_{d,n} \approx 90\%$) as input parameter for the scripts described in section 3.1.

G.7.1 Sample configuration

The high relative density was chosen for convenience during sample preparation. Lower relative densities require more experience with sample preparation which were not present at the start of building up sample 1. Sand was prepared using the method described in section G.4.1. Figure G.28a shows dimensions of the sample and an indication of the depth reached by the one without the use of an extension rod. In order to prevent the bottom of the cell to influence measurements, a sample height considerably larger than the maximum penetration depth was prepared. Given that sample height was larger than the penetration depth, an extension rod was used in 1-TEST2.



(a) Sample configuration for sample 1

(b) Top view of sample 1 with the test locations

Figure G.28: Sample configuration and test locations for sample 1

Three tests have been performed on the sample. The first test, which was located at the centre of the sample, is considered to be the leading test, since it was performed on a virgin sample without any disturbances by previous tests. Figure G.28b shows the test locations for sample 1 and figure G.29 shows the final position of the cone rod during testing. First 1-TEST1 was performed, after that 1-TEST2 and 1-TEST3.

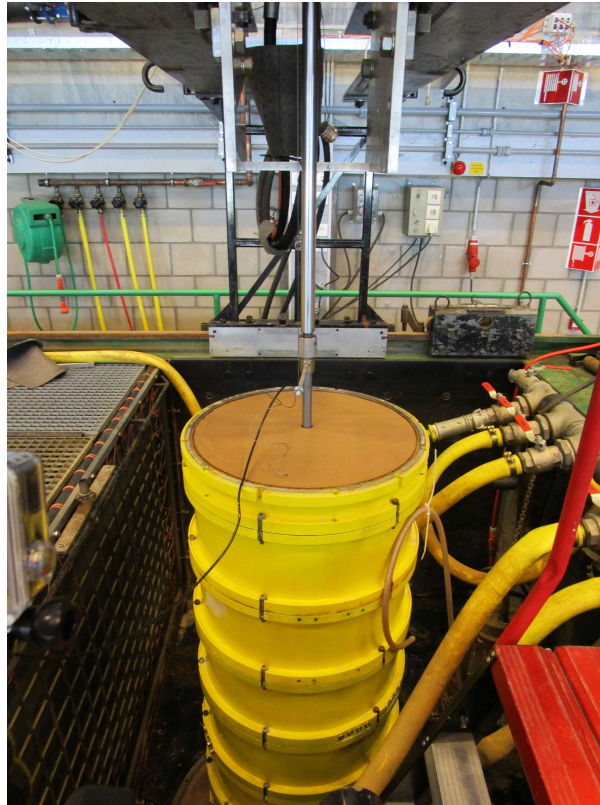


Figure G.29: Test setup after maximum testing depth has been reached

G.7.2 Tests

Since during the different tests on the first sample different testing circumstances were created (e.g. penetration rate and use of extension rod) which caused different issues for each test, the test are described separately below.

1-TEST1

- Due to dilatancy the water film on top ‘disappeared’ into the soil. One to two minutes after the penetration process was terminated, ‘free’ water reappeared on top of the sample.
- Slightly different configuration was used compared to 1-TEST2 and 1-TEST3. Configuration has been adjusted for subsequent tests to make sure that during the penetration process a water film stays on top of the sample.
- After retrieving the cone, crushed, grey coloured material was retrieved from the cone. It is uncertain why the material is grey. Figure G.34 shows the crushed material found in the sample.

1-TEST2

- 1-TEST2 was performed 5 days after 1-TEST2. Immediately after testing the cone was retracted.
- An additional extension rod with a length of 45 cm was used to be able to make use of the full sample.
- Installing the extension rod proved to be more difficult than expected, since disconnecting the 1-meter-rod from the join of the plunger was difficult. Installation of the extension rod may have influenced measurements.

- The extension rod buckled shortly after restarting the penetration process, after the additional extension rod was installed on the main extension rod. The extension rod buckled at the cable void.
- During buckling maximum plunger force was reached at which cone resistance reached values up to 60 MPa. In this configuration with dense sand it seems not possible with current configuration and/or equipment to reach a depth below 1 m and still receive usable data.

1-TEST3

- 1-TEST3 was performed right after 1-TEST2. After testing the cone was left in the soil for 5 days before dismantling of the sample and excavation of the cone.
- No use was made of additional extension rod, only the main extension rod was used.
- A penetration rate of 0.5 mm/s was applied to have an indication of what the influence of penetration rate is on different measurement parameters.
- A dissipation test was performed at the final penetration depth.
- During dismantling of the sample a clear bulge can be observed on the surface of the sample. See figure G.32.
- After excavation of the cone, the friction sleeve appeared to have changed in colour. Before entering the soil the friction sleeve had a shiny grey colour, after excavating the cone it was black. According to Fugro the metal of the friction sleeve reacts with the environment when a cone stays into the soil for a longer period of time.

G.7.3 Results

Results of the tests can be found in figure G.30 as CPT data, figure G.31 presents each measured parameter separately. The Fugro algorithm for soil classification could not deal with the detailed depth range, therefore the classification column contains white blocks. Measurements are indicating that the sample has been prepared fairly homogeneously, especially when looking at the friction ratios. Nevertheless it can be concluded that the effect of the density of the sand together with the stiff boundaries of the cell could have caused the high resistances measured.

Cone resistance (fig. G.31a)

Below a depth of about 35 cm ($14 \cdot d_{cone}$) cone resistance increases proportionally with depth. The first $14 \cdot d_{cone}$ can be described as the area where the cone resistance is developing before critical depth is reached, as displayed in figure 2.10. Below a depth of $14 \cdot d_{cone}$ the cone resistance is increasing at considerable rate of 8 MPa per 10 cm. This rate is believed to be caused by the boundary effects because of the limited cell dimensions in combination with the high relative density. Therefore it is not possible to obtain a characteristic cone resistance at shallow depth for Baskarp sand with a high relative density.

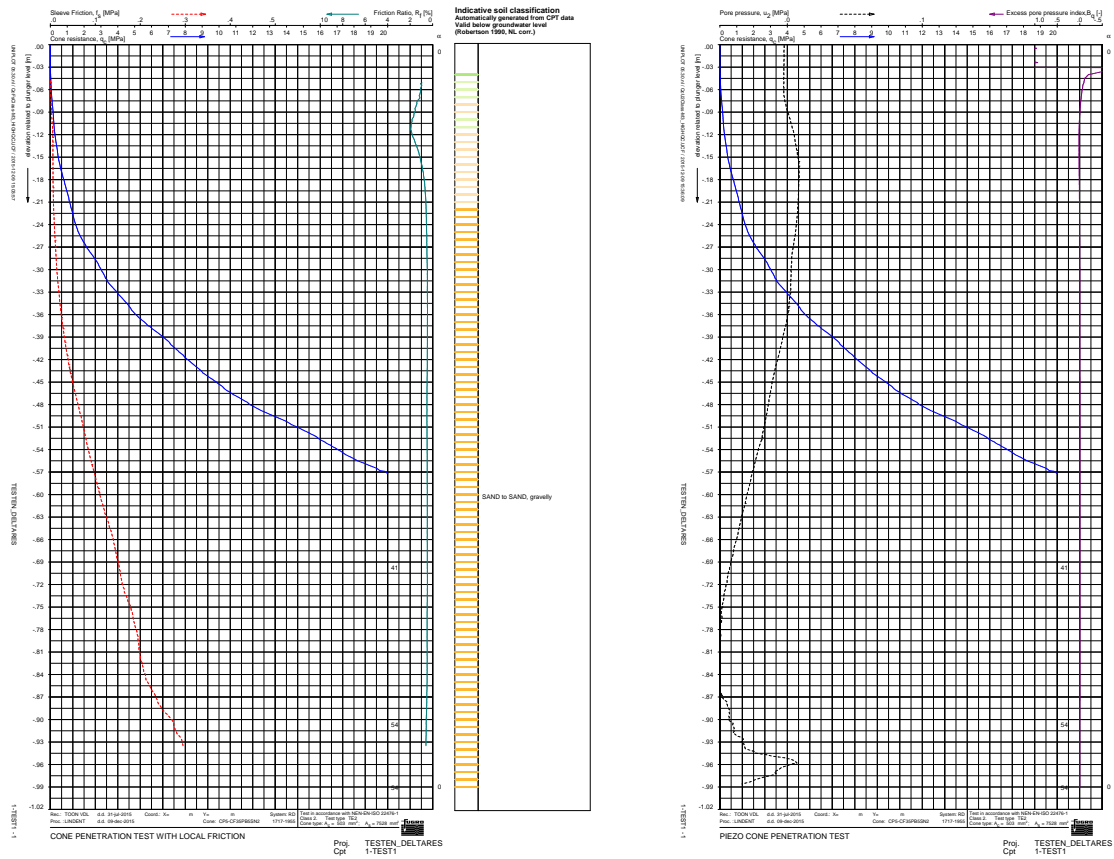
Regarding the overall trend in cone resistance measurements it can be concluded that with each consecutive test a lower cone resistance is measured, indicating that penetration and especially retraction of the cone may loosen the sample when it is very dense. Literature indicates that a lower penetration rate allows more water to drain resulting in higher cone resistances (e.g. Kim et al. (2010) and Poulsen et al. (2013)). This can be another reason to believe the sample loosens during testing, since 1-TEST3 was performed with lower penetration rate and also lower cone resistances than measured during tests before.

Sleeve friction and friction ratio (fig. G.31b and fig. G.31c)

Sleeve friction measurements are showing the same trend as for the cone resistance regarding critical depth and increase in resistance. This is confirmed by the friction ratios, where below a depth of 15 cm ($6 \cdot d_{cone}$) the friction ratio remains fairly constant just over 0.5%. No reasonable conclusions can be drawn regarding the effect of penetration rate on sleeve friction, because sleeve friction values of 1-TEST1 interfere with values from the two other test. This is confirmed by the study of Poulsen et al. (2013).

Pore pressure (fig. G.31d)

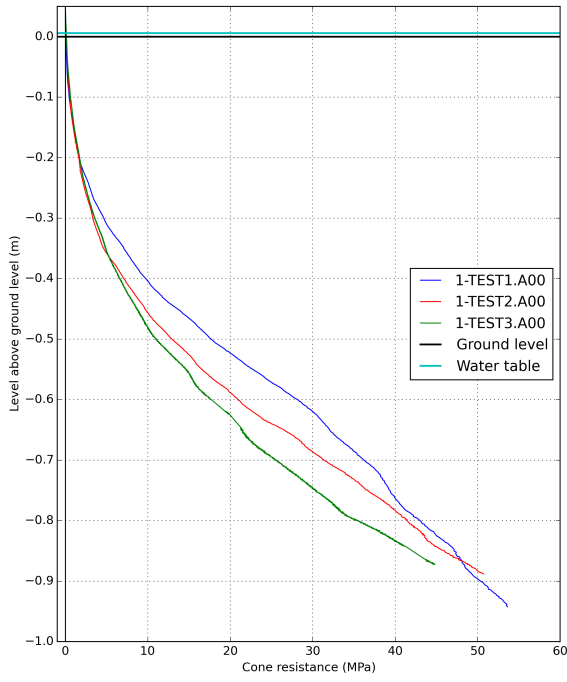
Pore pressure measurements indicate that under pressures occur due to dilation during penetration, which is normal in dense sands. Pore pressures are increasing over the first centimetres (perhaps some compaction takes place in this part), but after 10 cm pressures are continuously decreasing. Measurements of 1-TEST1 show below a depth of 75 cm an increase in pore pressure over a depth of 15 cm, after which pressure drops suddenly back to negative values. This behaviour is something no explanation could be given for in this research.



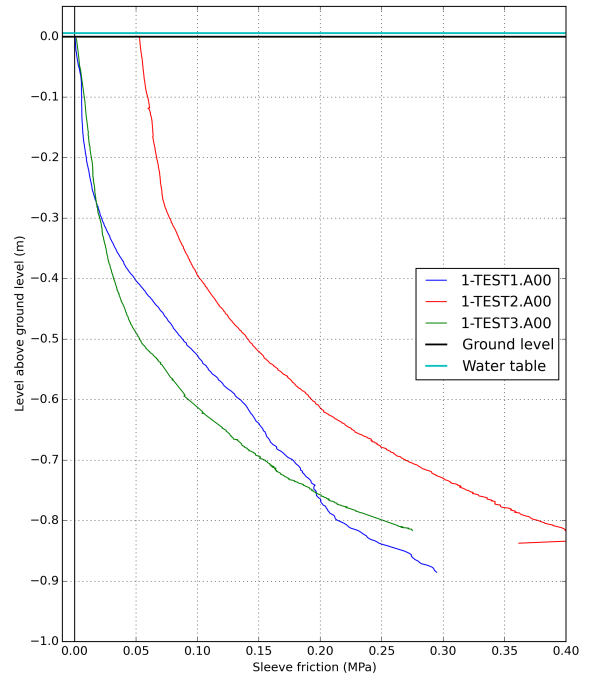
(a) Results for q_c , f_s and friction ratio

(b) Results for q_c and u_2

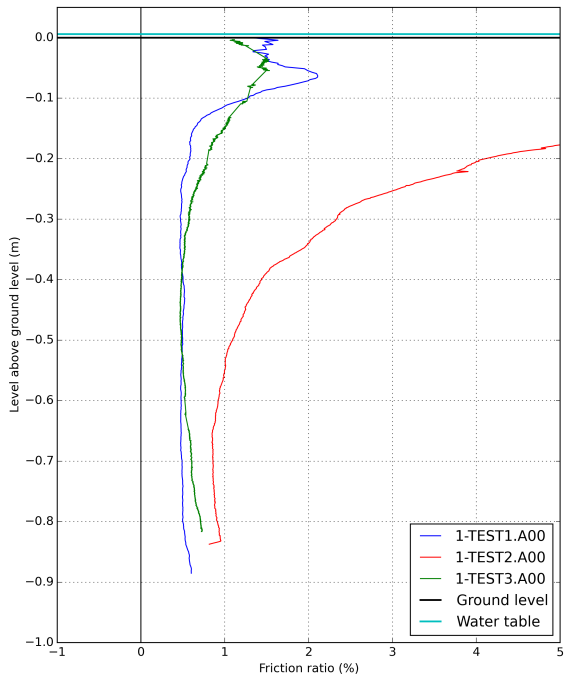
Figure G.30: CPT data for test 1-TEST1 including classification



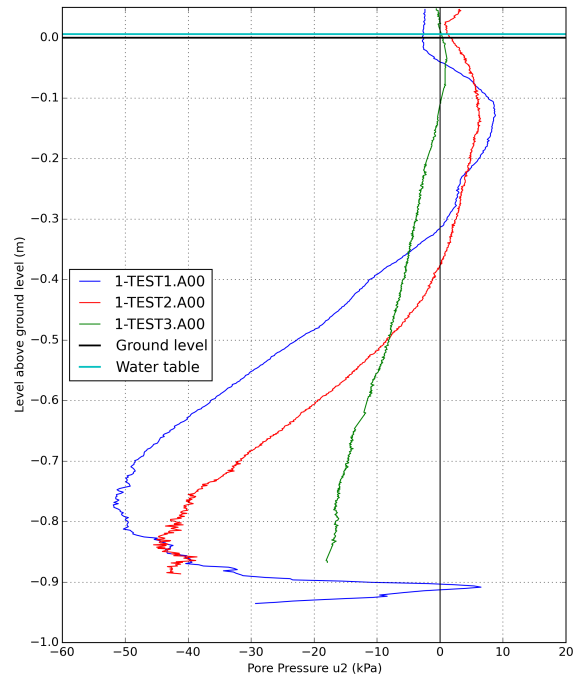
(a) Cone resistances



(b) Sleeve friction measurements



(c) Friction ratios



(d) Pore pressure u_2 measurements

Figure G.31: Results of the tests on sample 1

G.7.4 Sample dismantling

Since the feasibility of a cross-section over 1 m was not yet known, also a cross section was made from the uniform sand sample. Before making the cross-section it was concluded that the sample surface had lifted, shown in figure G.32. A clear bulge can be distinguished by looking at the marks made with a ruler. This confirms that dilation has taken place because of the sand density. The cone and rod were left in the soil to make a cross-section along the cone rod as well



Figure G.32: Bulge on the surface caused by expansion of the sample due to penetration

as cross-sections along the path of a retracted cone. An overview of the cross-section and detail near the cone tip can be found in figure G.33. Although corrosion causes the sand to have a brownish colour, a lighter coloured area between the corroded area and less disturbed sand can be distinguished. This may indicate differences in permeability and water content, since changes in colour are mostly caused by wetness of the sand. Because the sand was already very densely packed, this difference in colour may be caused by local change in grain size distribution of the sand due to crushing of the sand when high cone resistances are measured. Another reason



(a) Overview of the dismantling phase of sample 1



(b) Cross section of sample 1 near the cone tip

Figure G.33: Dismantling sample 1

to believe this colouring comes from change in grain size distribution is because grey material

can be found in the path of the cone rod. After drying of the sand with greyish material some little clods of very fine material can be picked out of the sand. Since grain size distribution of untested Baskarp sand is fairly homogeneous, this fine material could be formed during testing. Photos of the retrieved material can be found in figure G.34.



(a) Crushed material (grey) as found in the course of the CPT rod



(b) Crushed material as obtained after drying of the sand

Figure G.34: Crushed material removed from the sample after testing

G.7.5 Conclusions

- In order to prevent dilatancy from causing the sample to be drained dry of water on top of the sample, a sufficient amount of water should be present to form a water layer on the sample.
- An extension rod cannot be used, unless a new rod has enough strength to withstand high pushing forces and a method is found to prevent the process of installing the extension rod to influence the measurements as little as possible.
- Cone resistances measured indicate that the cell boundaries influence measurements, facilitated by high relative density of the sand.
- Measurements influenced by boundary effects are not very usable for studying thin layer effects, therefore the chance of encountering boundary effects in measurements should be minimized in next tests.
- A characteristic cone resistance for uniform sand was not found during tests on sample.
- Because sleeve friction is influenced by the cell boundary as much as the cone resistance, 'normal' values for friction ratio in sand are found.
- High relative density leads to dilatancy during testing, which causes under pressures in the sample during testing.
- High cone resistances can be a cause of the fine (crushed) material found in the course of the cone rod.

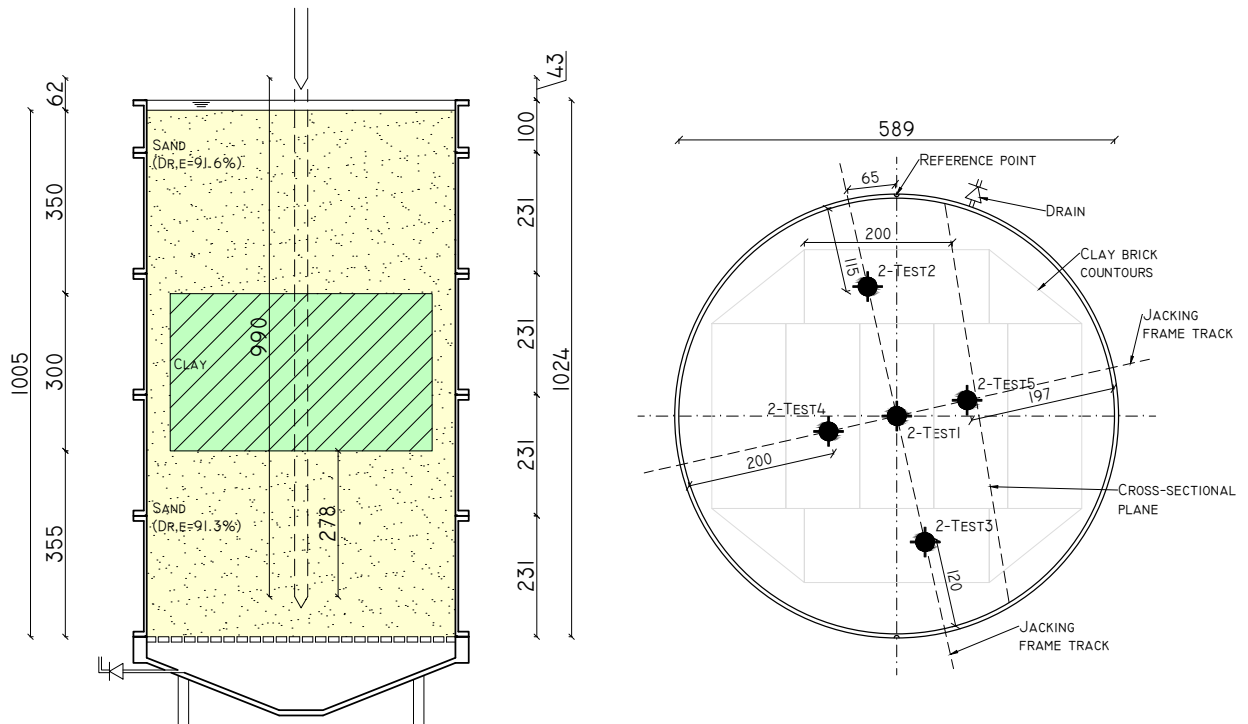
G.8 Sample 2: Single 30 cm clay layer between dense sand layers

After gaining experience with sample preparation, handling of the tools and using the cone, a clay layer with 30 cm thickness surrounded by a dense sand layer was tested. The goals of the second sample were:

- To get experience with handling of the bricks of clay,
- To obtain a characteristic cone resistance for the Vingerling clay as input parameter for the scripts described in section 3.1,
- To see how the cone resistance develops in boundary areas between sand and clay.

G.8.1 Sample configuration

A figure of the sample configuration can be found in figure G.35a. The sand layers were prepared the same way as for sample 1, meaning that the sand was compacted using the tamping method. In the top layer $R_{d,e}$ was 91.6% and in the bottom sand layer 91.3%, both for their bulk. Because this test aimed to obtain the resistance in clay and because it was not yet clear how exactly lower relative densities could be achieved, it was decided to continue using the tamping method for sand preparation in this test. Clay was prepared as described in section G.4.2. With this test a reference point on the cell was chosen in order to know how the clay bricks were configured when commencing testing. An overview of the brick configuration can be found in figure G.36. The numbers on the bricks correspond to the brick numbers in table G.5. Because the use of



(a) Sample configuration for sample 2

(b) Top view of sample 2 with the test locations

Figure G.35: Sample configuration and test locations for sample 2

an extension rod was not an option considering the tests on sample 1, the sample height was reduced for sample 2. To have an idea of how cone resistance redevelops after entering the bottom sand layer, it was chosen to let the cone penetrate 30 cm into the bottom sand layer.

Figure G.35b shows the test locations with the brick contours. For avoiding potential clay brick

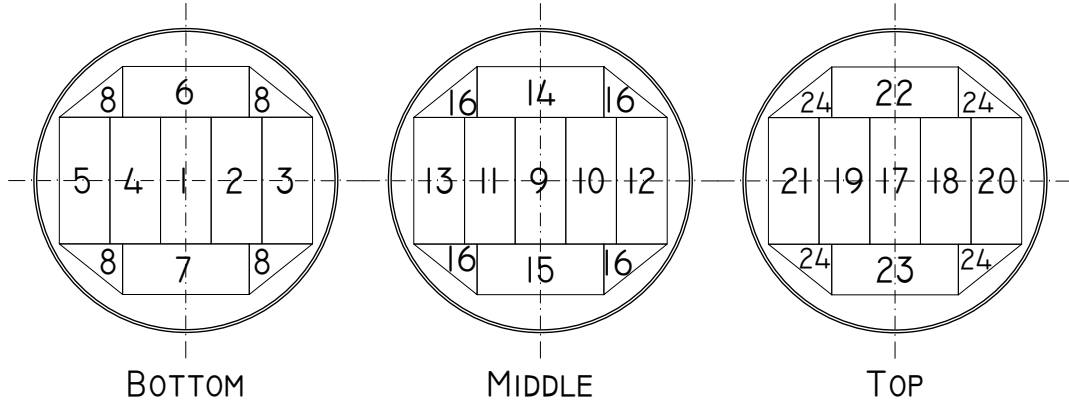


Figure G.36: Brick configuration corresponding to the brick numbers in table G.5

voids with the cone, testing locations were chosen such that the locations were as far from brick voids as possible. To see whether the test location has effect on the measurements, test 2 and 3 were performed closer to the cell boundary than test 4 and 5.

G.8.2 Results

Results of the first test can be found in figure G.37 presented as CPT data, figure G.39 presents each measured parameter separately for all tests. It can be concluded that the sample has been fairly homogeneously prepared since the results of all 5 tests are in the same range for each separate measured parameter.

Cone resistance (fig. G.39a)

As with sample 1 the cone resistance rapidly increases once entering the sand layer, indicating that the sand is indeed densely packed and that the effect of the cell boundaries may be seen in the results. The results for the cone resistance in the clay however seem so to be quite reasonable. Since figure G.39a does not show a correct scale for the cone resistance in clay, figure G.38 shows a detail of the cone resistance in clay. From the data presented in figure G.38 it is determined that the cone resistance in a thick clay layer (characteristic cone resistance) is 0.22 MPa for the test conditions considered. Figure G.39a seems to be very comparable to the result Xu found, shown in figure 2.17.

Figure G.38 displays characteristic points, distances and angles of the cone resistance regarding penetration through a single 30 cm clay layer. The first characteristic point is where the cone resistance stops increasing in the sand (it ‘senses’ the clay layer) and starts to decrease as it is approaching the sand-clay interface. For 2-TEST1 this point is at 82 mm ($3.3 \cdot d_{cone}$) above the interface, consecutive tests show measurements in which this point is located closer to the interface down to 69 mm ($2.8 \cdot d_{cone}$). It can be concluded that the cone can feel the clay layer at slightly more than $2 \cdot d_{cone}$ distance from the interface with this particular sand density. Boundary effects may have affected measurements at this depth, so the conclusion about at what point the clay layer influences the cone resistance is questionable.

Next characteristic point is the depth at which a (relatively) constant cone resistance is reached in clay. It is determined that this point lies 122 mm ($4.9 \cdot d_{cone}$) beneath the upper interface. Below this point an average constant cone resistance of 0.22 MPa is measured, until 32 mm ($1.3 \cdot d_{cone}$) above the bottom clay-sand interface. At this point the cone resistance is influenced by the bottom sand layer and immediately when entering the sand layer cone resistances reach considerable levels comparable to those measured during tests on sample 1.

Where no significant differences between testing locations are noticeable in cone resistances in clay, there are differences in cone resistance measurements in sand. Above the clay layer resistances of 2-TEST2 and 2-TEST3 are significantly higher than resistances of 2-TEST4 and 2-TEST5 (see figure G.38). This is also the case below the clay layer (see figure G.39a). Since 2-TEST2 and 2-TEST3 are performed more closely to the cell boundary than 2-TEST4 and 2-TEST5 (see figure G.35b), it is concluded that boundary effects are causing higher cone resistance for tests performed closer to the boundary. Besides, cone resistance for 2-TEST1 is higher than other tests above the clay layer and lower than other tests below the clay layer. Above the clay layer penetration and retraction might lead to loosening of the sand, causing lower cone resistances in consecutive tests, below the clay layer boundary effects may influence measurements taken closer to the boundary more as penetration progresses.

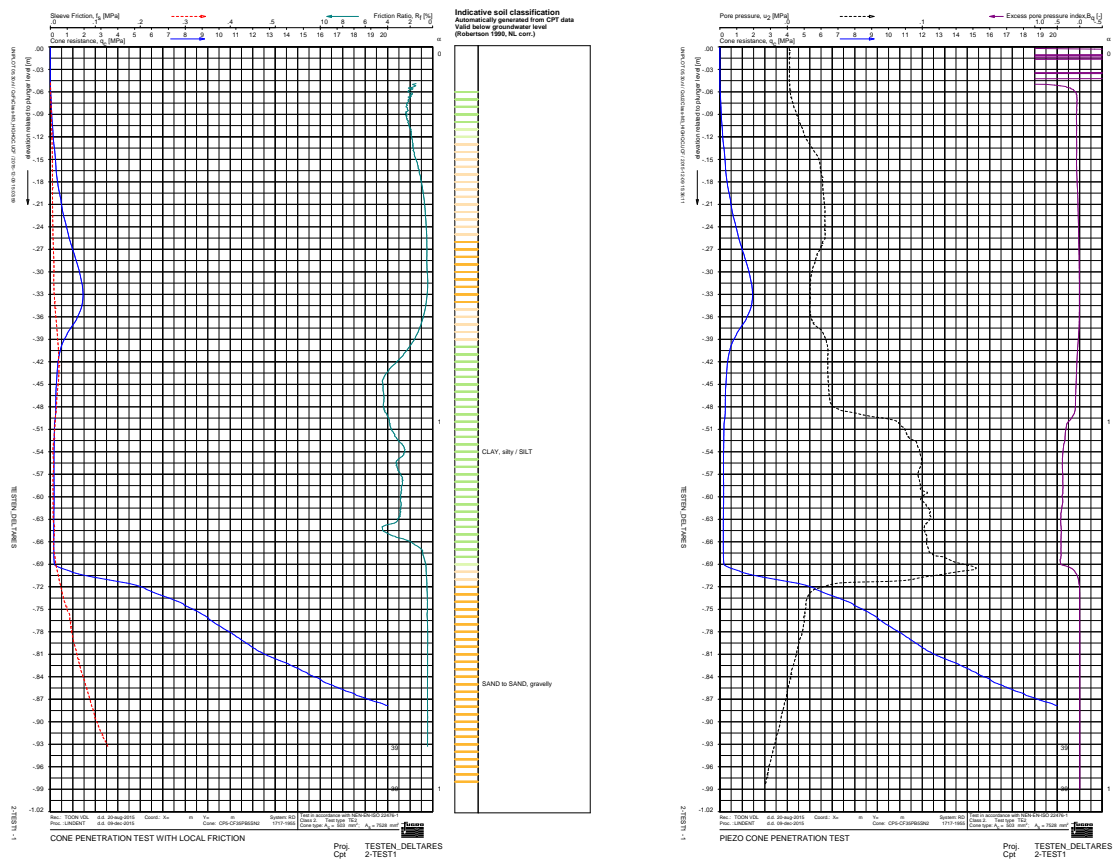
Sleeve friction and friction ratio (fig. G.39b and fig G.39c)

As the bottom part of the friction sleeve enters the clay before the reference point of the sleeve is in the clay, sleeve friction increases well before the clay layer is entered. After the first interfaces has passed, sleeve friction decreases again down to values it would show if it would be in sand, but for the friction ratio still values that would be expected in clay (2.5% to 3%) are found, indicating that the values for sleeve friction are reasonable (since the values for cone resistance are reasonable as well).

Pore pressure (fig. G.39d)

As expected an increase in pore pressure can be seen in the clay layer. However, pore pressures only start to increase after the reference level of the cone has penetrated approx. 7 cm into the clay. This may be explained by figure G.41, in which sand intrusion in the clay is shown. This may be a reason for the pore pressures to increase after 7 cm, since the pore pressure filter can be in contact with the sand up to that depth in the clay and so pore pressure which are built up when entering the clay can dissipate through this intrusion of sand. Just before the cone leaves the clay layer a sudden increase in pore pressure is measured. This can be caused by a difference in penetration mechanism between mechanisms in the clay and dense sand layer. As the cone tip already is displacing dense sand this displacement of sand particles that need to make place for the cone may cause pore pressure in the clay to increase, since the high density of the sand causes dilation and volume increase in the sand. This volume increase may cause the sand to rise locally, pushing upward into the clay and causing higher pore pressure in the bottom part of the clay.

Below the clay layer negative values for pore pressure are found, indicating that dilation takes place as expected in densely packed sand.



(a) Results for q_c , f_s and friction ratio

(b) Results for q_c and u_2

Figure G.37: CPT data for test 2-TEST1 including classification

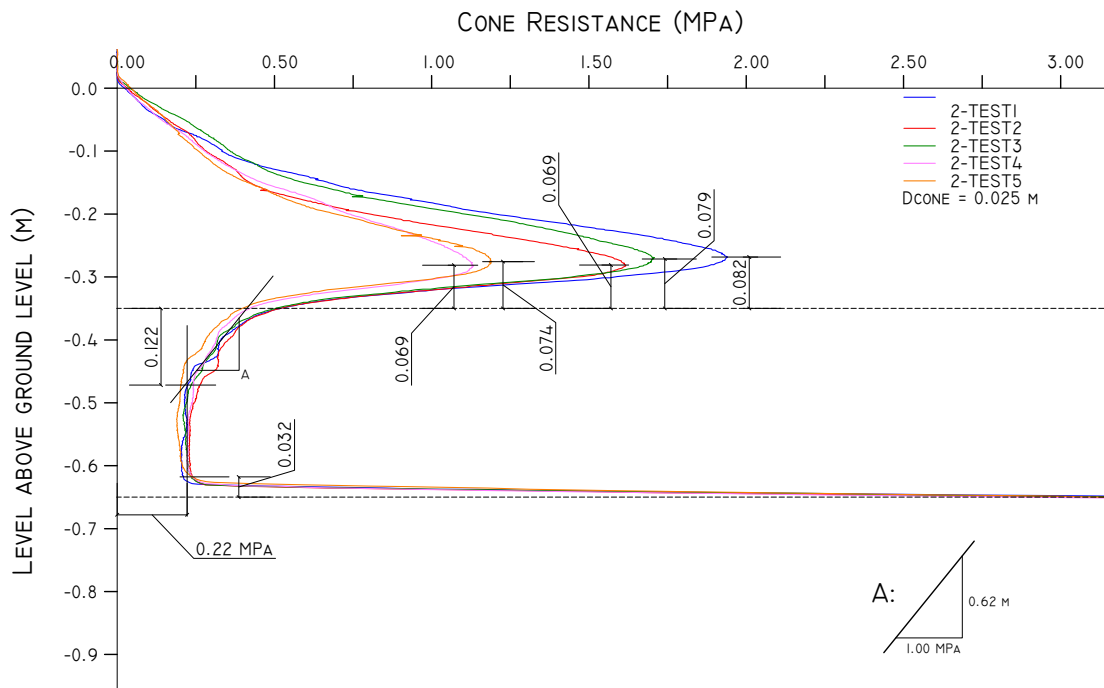
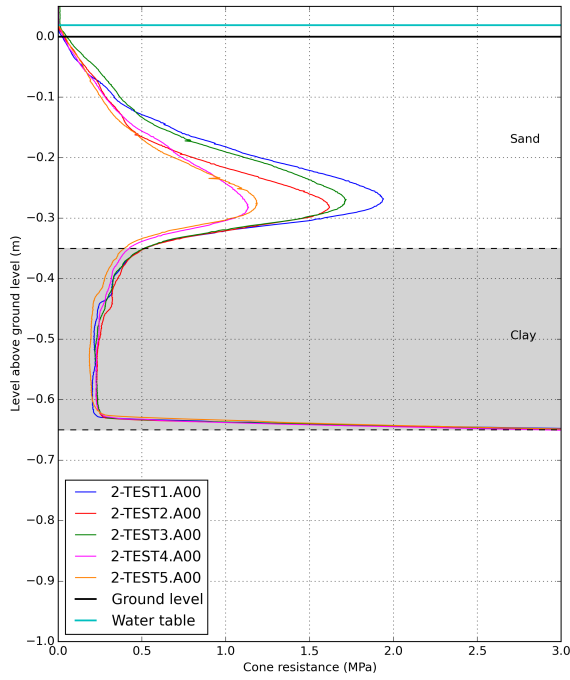
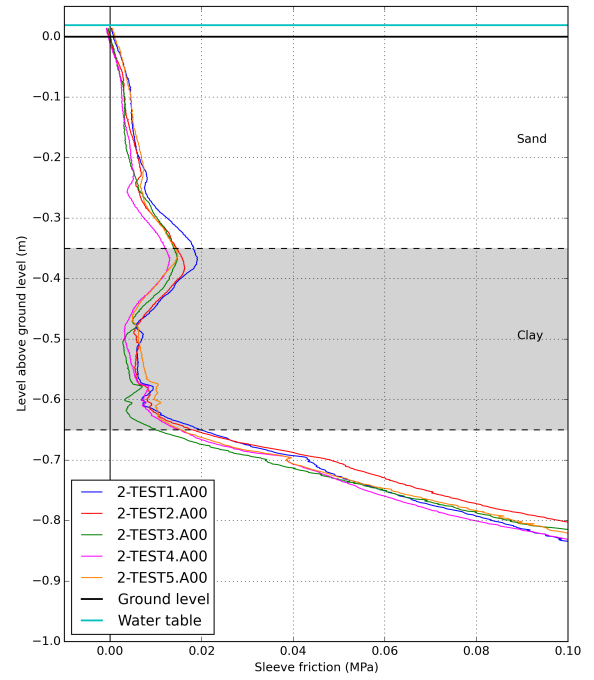


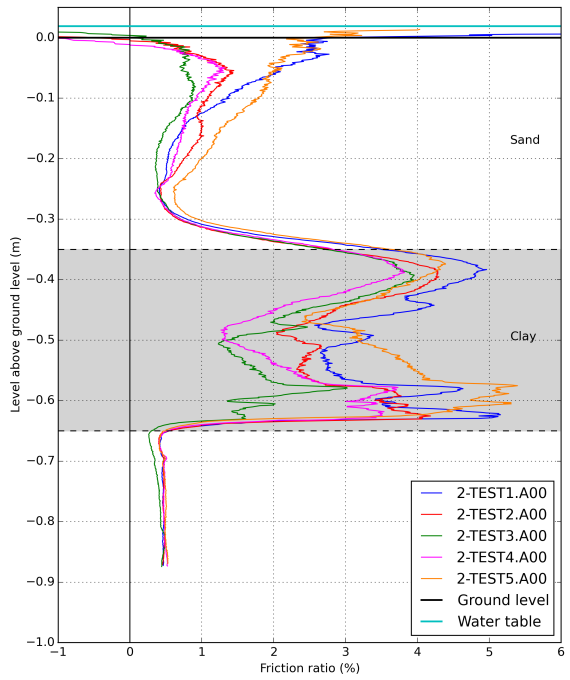
Figure G.38: Detail of the cone resistance in clay of sample 2



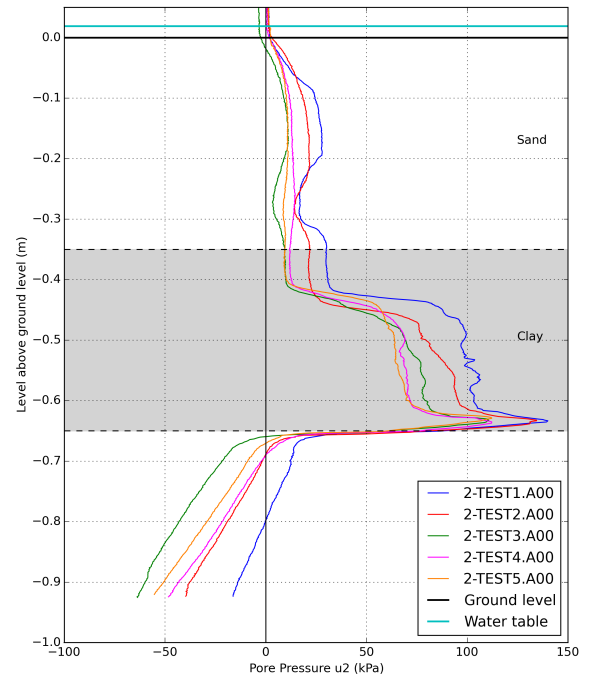
(a) Cone resistances



(b) Sleeve friction measurements



(c) Friction ratios



(d) Pore pressure u_2 measurements

Figure G.39: Results of the tests on sample 2

G.8.3 Dismantling

To see how the cone interacts with the soil and what happens with soil when the cone is retrieved, cross-sections were made along the cone rod and path of a retrieved cone. Location of the cross-section along the cone rod is drawn in figure G.35b. Figure G.40 shows a cross-sectional overview and detail of the cone penetrated in clay. Larger figures can be found in appendix I. For this sample no density samples were taken. It is clear that sand has intruded

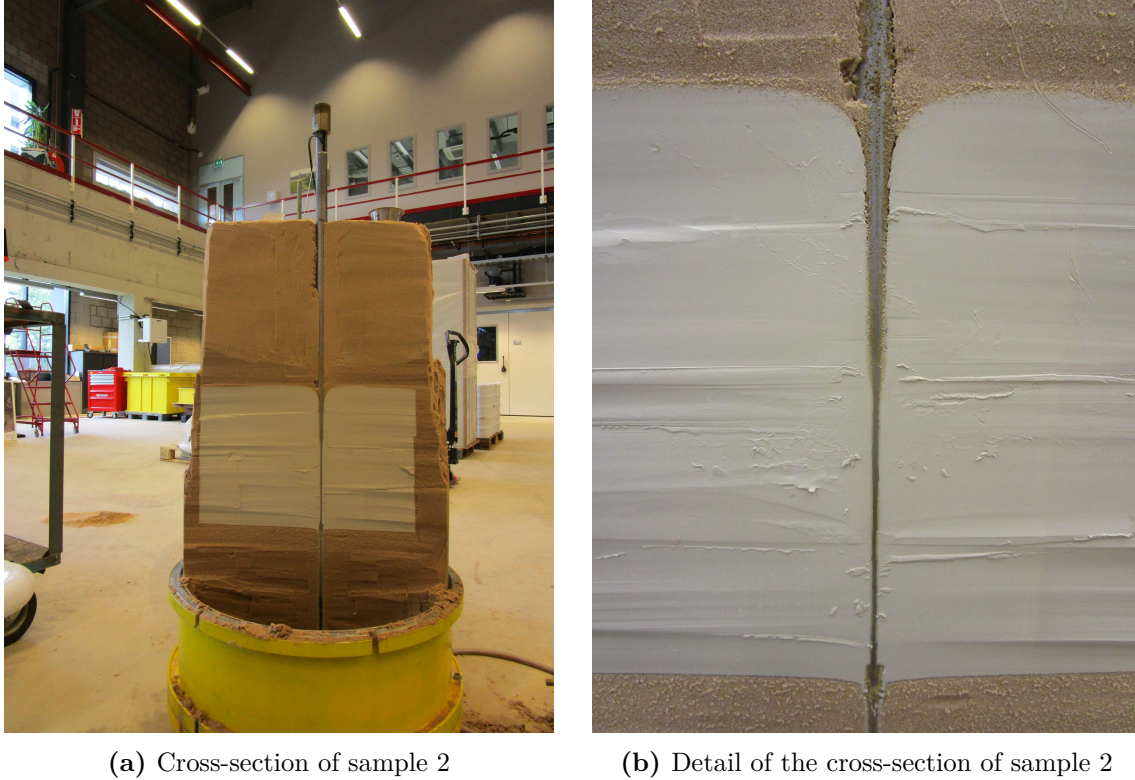


Figure G.40: Dismantling sample 2

in the clay up to about 12 cm into the clay, which can be seen in figure G.41. This may explain why pore pressures are not increasing over the first centimetres in clay, because excess pore pressures can drain along the intruded sand to the top sand layer. It cannot be determined from this cross-section whether sand intruded the clay by being pushed in front of the cone or if it intruded by being dragged into the clay by the passing rod behind the cone, although Xu (2007) observed a similar phenomenon and concluded that below the pile tip a sand cone with a height of 0.7 times the pile diameter had formed, meaning that sand was pushed in front of the cone. Cross-sections in samples with multiple clay layers may clarify the penetration mechanism around the interface and at which point sand intruded into the clay. While sand was able to enter the clay, it seems that clay has intruded far less into the bottom sand layer at the bottom clay-sand interface. This may have to do with the limited length of extension rod passing through this interface and/or with the density of the sand not allowing much less stiffer clay to intrude into sand.

Figure G.42 shows a cross-section of the sample through the path of a retracted cone. Clearly visible is the sand column which filled the cavity in the clay due to under pressure below the cone during retraction. It is therefore assumed that the sand forming the sand column in clay originates from the sand layer below the clay layer. Differences in sand pile diameter which can be noted in figure G.42b are likely to come from cutting the clay slightly non-symmetric through the cone path, since it is difficult to keep cutting over full diameter with only a steel wire and without a cone to let the wire slide along.

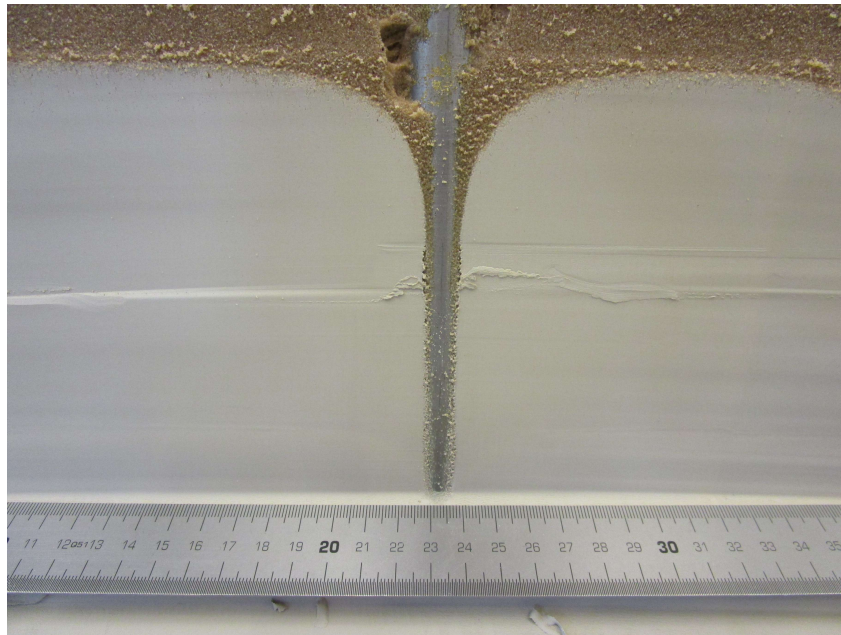
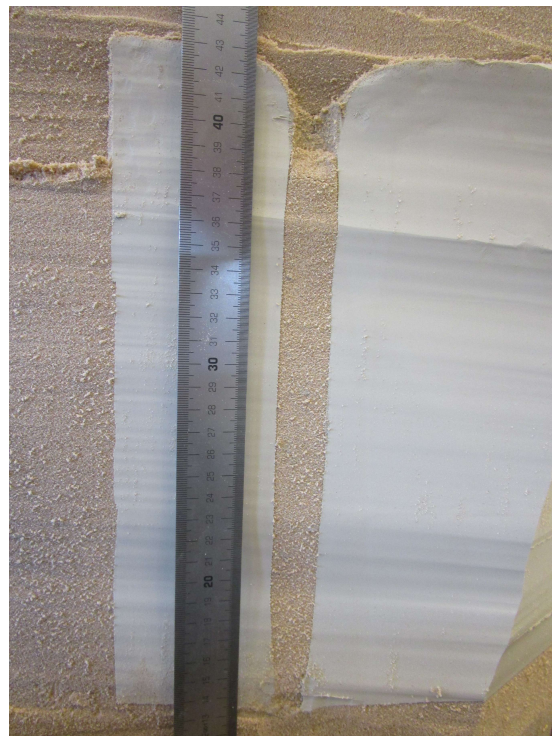


Figure G.41: Detail of the sand intrusion in the clay. Over a depth of 12 cm sand grains could be seen in the clay



(a) Cross section of the path of a retracted cone



(b) Detail of the sand pile

Figure G.42: Cross section of the path of a retracted cone. A sand pile formed during retraction can be clearly distinguished

G.8.4 Conclusions

- Characteristic cone resistance for clay is determined to be 0.22 MPa.
- Where the cone resistance in sand is affected by the relative density and boundaries, it seems that in clay the boundaries do not influence cone resistance measurements.
- When trying to estimate the size of the clay layer by looking only at u_2 measurements actual layer size will not come to mind since pore pressures do not increase at the moment the cone passes the sand-clay interface.
- Figure G.38 gives characteristic distances in the cone resistance measurements which can be compared to characteristic distances from in other sample configurations.
- Similar distance above the sand-clay interface at which the cone reacts on the presence of the clay is found in this test setup ($3.3d_{cone}$) as found by Xu (2007) ($3.8d_{cone}$, see figure 2.17).

G.9 Sample 3: Uniform medium dense sand layer

Since it was believed that the cone resistances during the tests on samples 1 and 2 were influenced considerably by the cell boundaries, it was decided that a lower relative density was needed in order to have useful results. In order to obtain a lower relative density than $R_{d,n} = 90\%$ ($R_{d,e} = 91.6\%$), the vertical shock wave method was used as described in G.4. Goals if this test were:

- To gain experience with sample preparation of samples with a relative density around $R_{d,n} = 70\%$ ($R_{d,e} = 74.0\%$),
- To see what the cone resistance would be at these particular range of relative densities,
- To obtain a characteristic cone resistance for Baskarp sand (with $R_{d,n} \approx 70\%$) as input parameter for the scripts described in section 3.1

G.9.1 Sample configuration

A figure showing the sample configuration can be found in figure G.43a and a top view of the test locations can be found in figure G.43b. After having results of four tests it was concluded that it would be useful to take samples of the sand in order to have an idea of the density at specific depths. Preparing a sample of this height has not been done by the authors (Van der Poel and Schenkeveld (1998)) from the vertical shock wave method, so it is not sure whether the sample compacts homogeneously over the total height. Therefore a part of the sample has not been tested by cone penetration, shown in figure G.43b.

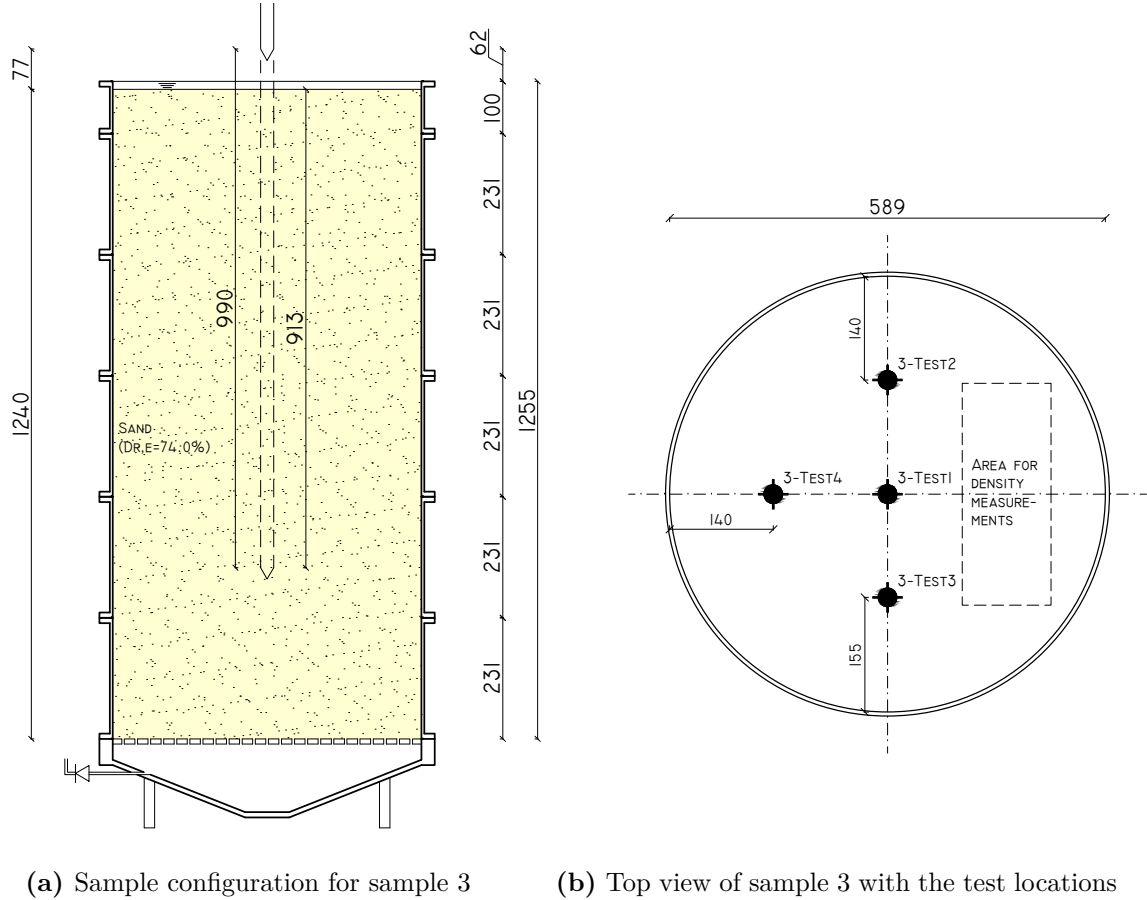


Figure G.43: Sample configuration and test locations for sample 3

During sample preparation execution of the vertical shock wave method did not go as planned. Vertical shocks were not applied properly, and because of an unstable bottom construction of

the cell shook during landing, which results in extra non-uniform compaction. Also the top plate was not able to move downwards freely with the sand level during compaction, causing an unconfined top layer with differential compaction as well. Therefore after preparing the sample there was not much confidence quality of the sample and the future test results. An indication of the bulk density after each shock cannot be given, since the top plate was not on top of the sand all the time so the real sand level could not be measured correctly. It is questionable whether this method can be used for preparing layered samples, since the sand must be prepared in different stages to allow the clay layering to be installed.

G.9.2 Results

Results of the first test can be found in figure G.44 presented as CPT data, figure G.45 presents each measured parameter separately for each test. From the results it can be concluded that the bottom part of the sample was more loosely packed as the middle and perhaps the top part.

Cone resistance (fig. G.45a)

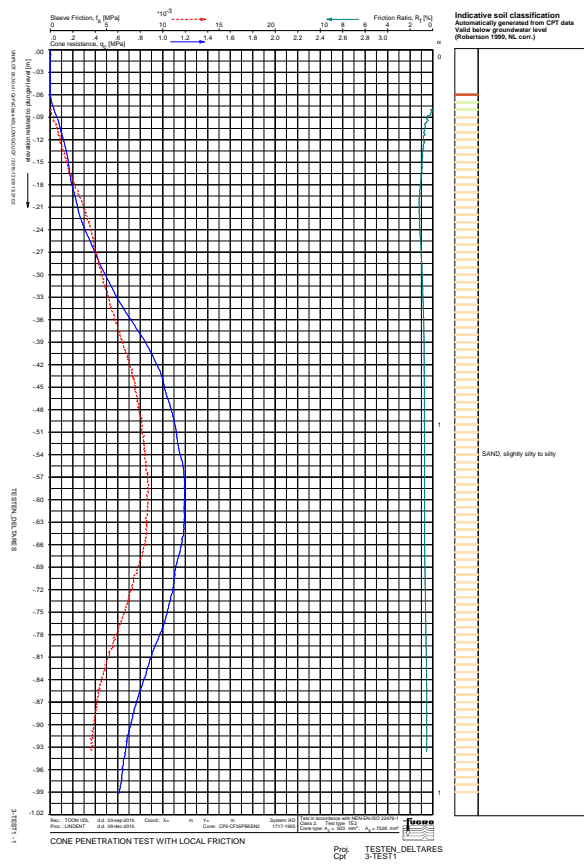
Significantly lower cone resistances were measured in the sample as during previous tests, which can conclude that boundaries have very little effect on measurements. After 60 cm, though, a decrease in cone resistance can be observed, indicating that the bottom part of the sample has a lower density as the top part. For determining a characteristic cone resistance the measurements taken from this sample cannot be used.

Sleeve friction and friction ratio (fig. G.45b and fig. G.45c)

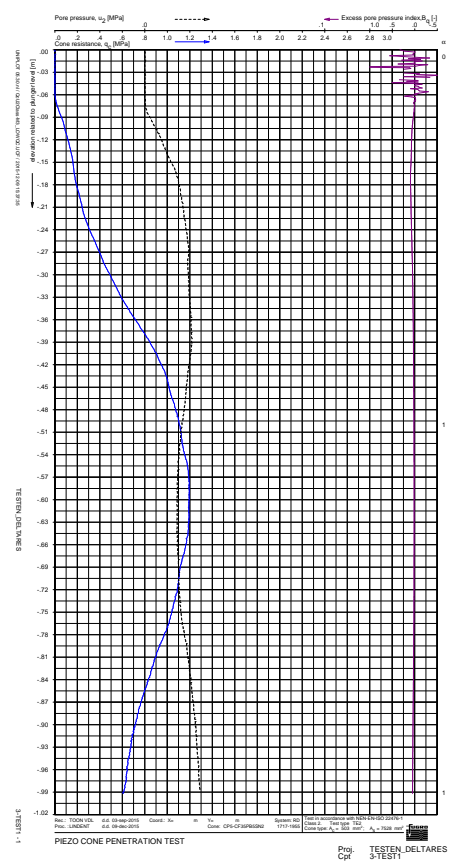
Sleeve friction measurements show similar behaviour as the cone resistance measurements, decreasing in value below a depth of 60 cm. This decline is less noticeable in the friction ratio since both cone resistance and sleeve friction show the same trend, though a slight decline in friction ratio can be observed at deeper levels. Values of friction ratio below 1% for sand can be considered to be normal values.

Pore pressure (fig. G.45d)

Pore pressure measurements show that around 40 cm depth dilation starts to occur since negative pressures are measured. After 70 cm pressures are becoming less negative, indicating looser sand at the bottom of the sample as in the middle, which is confirmed by the cone resistance. Because no negative pressures are measured above 40 cm, it can be concluded that no dilation takes place and that the top part is more loosely packed than lower parts, or that it is too shallow for pore pressures to become negative. Figures G.31d and G.39d shows no significant negative pressures for the top sand layers in previous tests, while those layers were densely packed, so shallow penetration effects can be an option here.

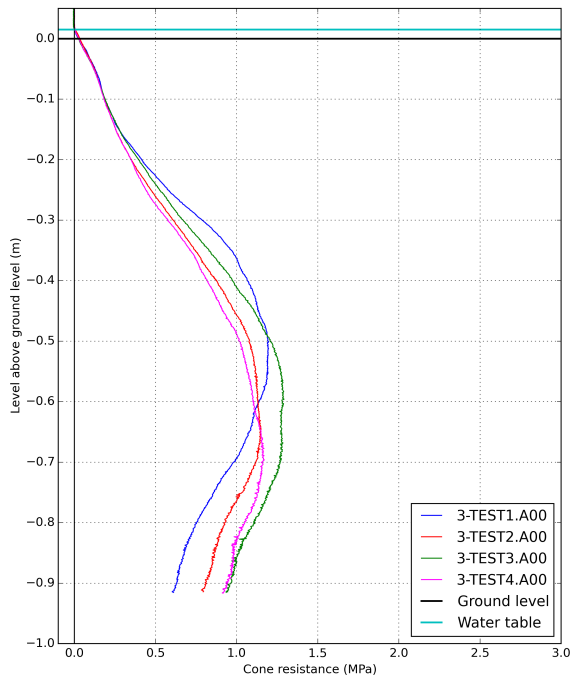


(a) Results for q_c , f_s and friction ratio

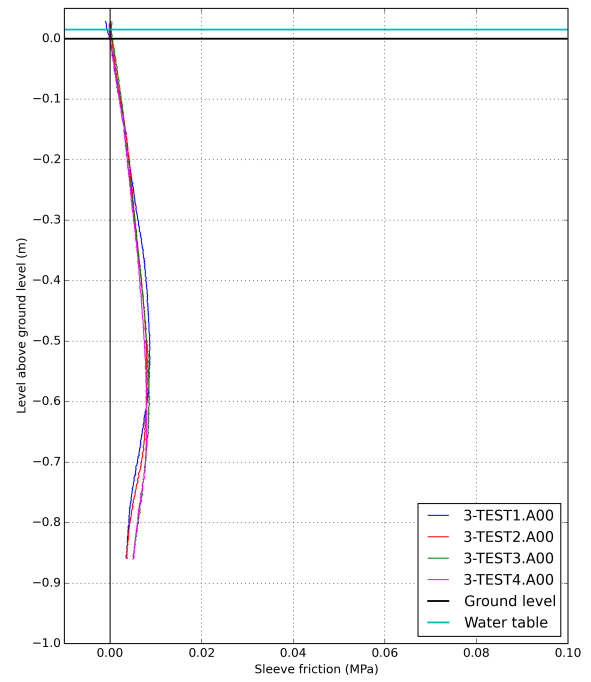


(b) Results for q_c and u_2

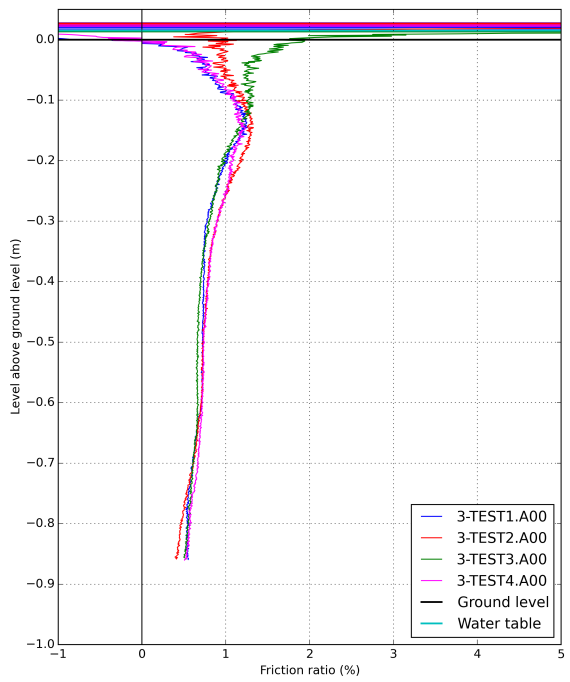
Figure G.44: CPT data for test 3-TEST1 including classification



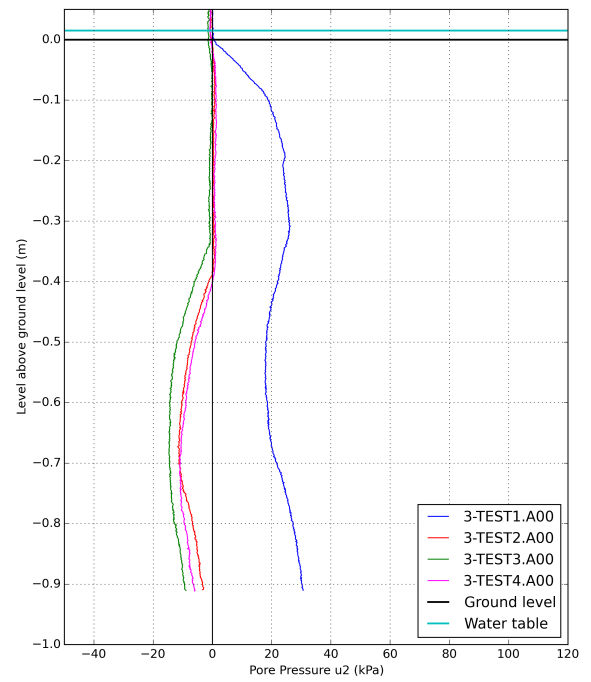
(a) Cone resistances



(b) Sleeve friction measurements



(c) Friction ratios



(d) Pore pressure u_2 measurements

Figure G.45: Results of the tests on sample 3

G.9.3 Dismantling

Dismantling sample 3 was done by taking density samples at various depths in the sample. Figure G.46 shows the relative densities based on void ratio at different levels in the sample. These samples were taken after CPTs were performed, during which some changes in density could be made to the sample. Relative density appears to decrease linearly over depth having a significant range from 80% to 30%. This confirms the lower cone resistances at the bottom of the sample. From these density samples it can be concluded that the sample was far from homogeneous and therefore not fit to use for determination of a characteristic cone resistance.

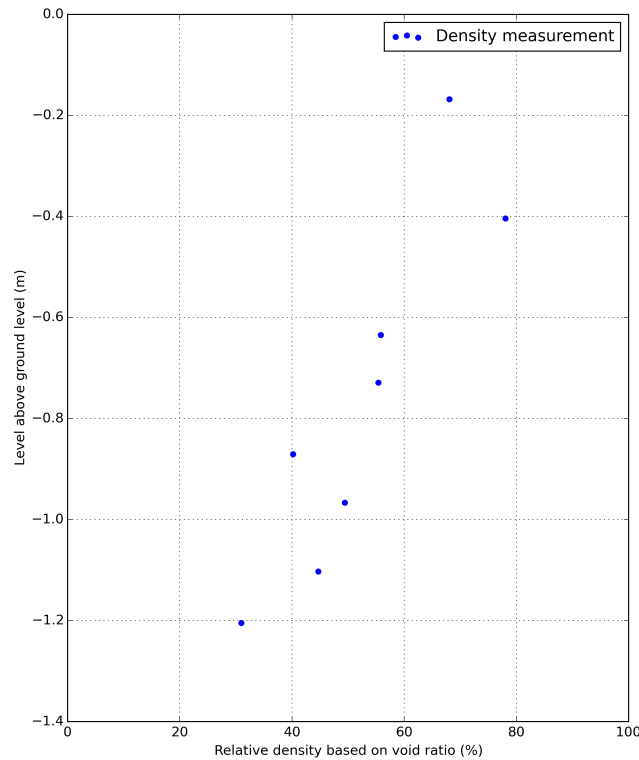


Figure G.46: Relative density based on void ratio over depth for sample 3

G.9.4 Conclusions

- When the vertical shock wave method is executed incorrectly, differential compaction can take place, making measurements for obtaining a characteristic cone resistance unreliable.
- No characteristic cone resistance could be determined from the tests on sample 3.
- A more stable bottom plate is needed for sample preparation. This also makes sure the sample does not change in density during transport to the testing location.
- Preparing and compacting the whole sample at once is not relevant for preparation of layered sample, so tests whether the vertical shock wave method is convenient for preparing layered samples should be performed.

top layer. To see if this assumption was correct a 1 mm thick coloured (Baskarp) sand layer was poured on top of the bottom layer. During dismantling the location of the coloured layer would indicate whether the bottom layer had compacted during compaction of the top layer.

Surface height was measured after each shock, giving an indication of relative bulk density of the bottom or top layer. Figure G.48 shows the development of the relative bulk density of each of the layers during their respective compaction phases, keeping in mind that the bottom layer also experiences the shocks of the compaction phase of the top layer.

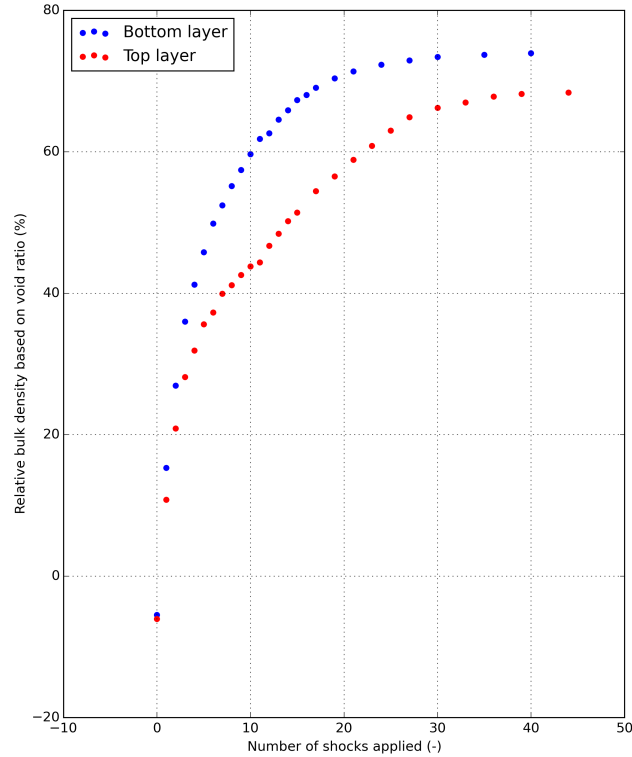


Figure G.48: Development of the relative bulk density $R_{d,e}$ over the number of shocks applied for the top and bottom layer

G.10.2 Results

Results of the first test can be found in figure G.49 presented as CPT data, figure G.50 presents each measured parameter separately for all tests. It can be concluded that the difference in bulk density between the top and bottom layer are clearly visible in the CPT data and that the sample is fairly homogeneous in the horizontal plane.

Cone resistance (fig. G.50a)

Above the top-bottom layer interface cone resistances are increasing up to 4 MPa before just below a depth of 60 cm cone resistances start to increase at a higher rate. In figure G.47a it can be seen that the interface between top and bottom layer is at 65 cm below ground level, meaning that the higher increasing rate comes from penetration through a denser layer. Cone resistance for the first test approaches a value of about 13 MPa with decreasing increasing rate near the bottom test level, while the increasing rate of subsequent tests does not change when

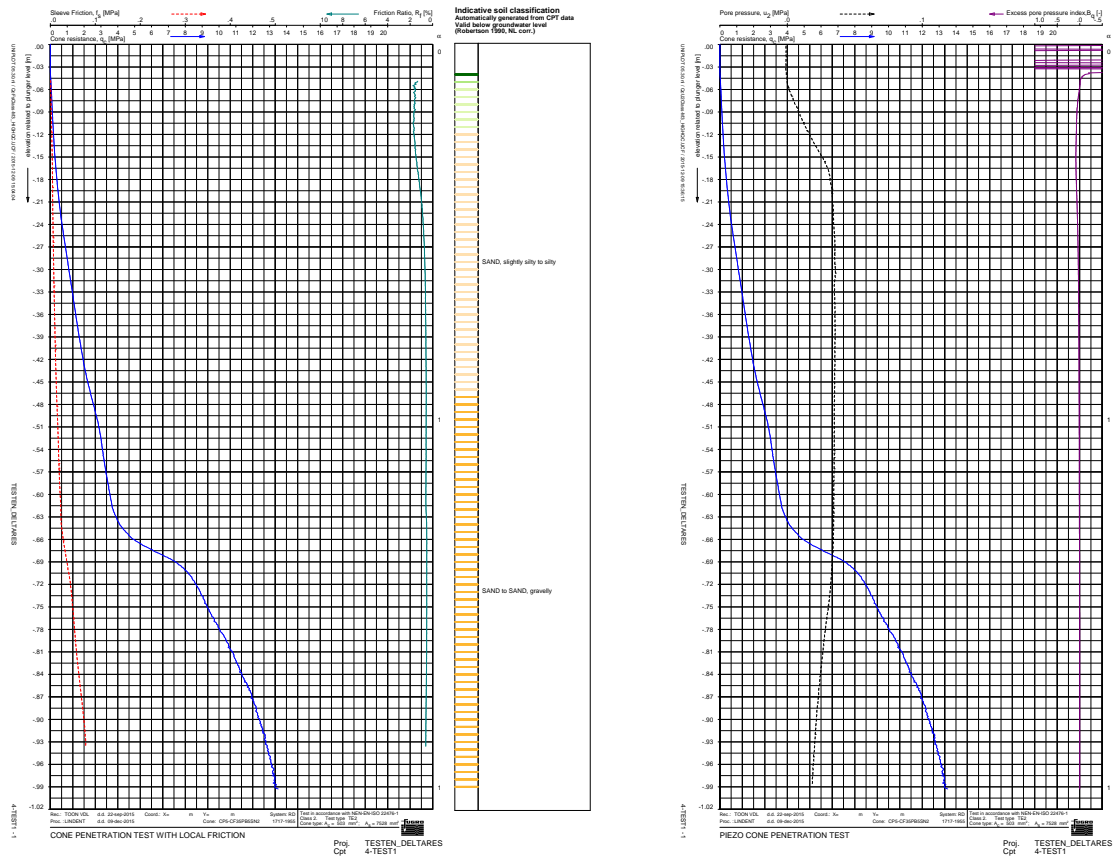
the lowest test level is reached. This may indicate a slight inhomogeneity in the sample or an increase in density by the cone penetrating the sample during the first test.

Sleeve friction and friction ratio (fig. G.50b and fig. G.50c)

Sleeve friction measurements show the same behaviour as the cone resistance, with the density boundary at the same level as the cone resistance. A little shift can be observed in the friction ratios at interface level, but generally the friction ratios for the top and bottom layer are of comparable values.

Pore pressure (fig. G.50d)

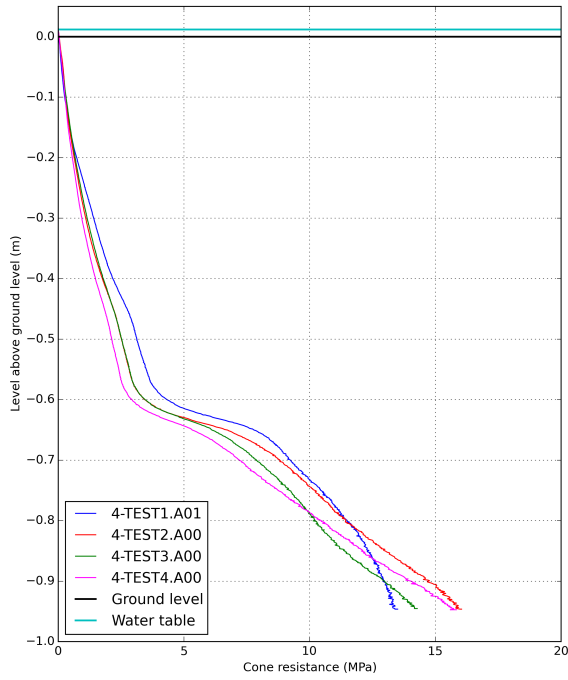
Pore pressure measurements show below interface level a decrease in pore pressure, where pore pressures in the top layer were have a more or less constant value. This indicates that in the bottom layer dilation occurs and therefore that the bottom layer has a higher density than the top layer. Moreover it could be concluded that the density at which compaction or dilation takes place for Baskarp sand may lay between $R_{d,e}$ 69.0% and 75.6%, since the top layer does not show dilative behaviour in pore pressure data while the bottom layer does. Differences in absolute values for pore pressure measurements are discussed in section G.6.1.



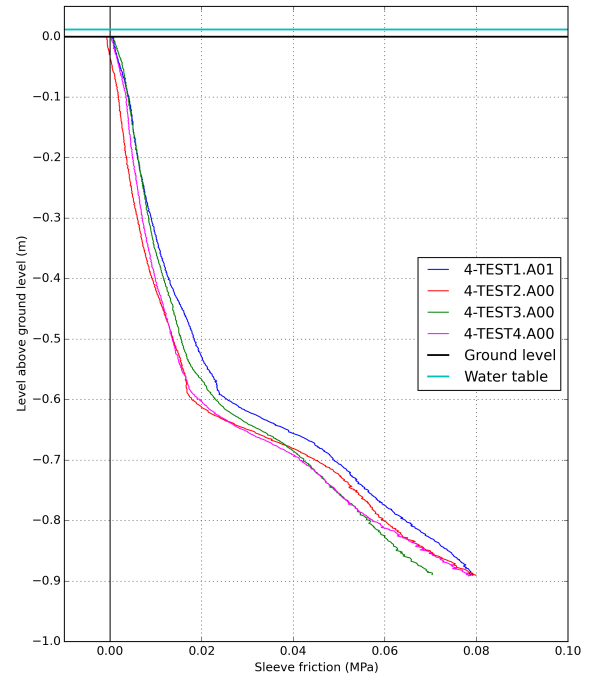
(a) Results for q_c , f_s and friction ratio

(b) Results for q_c and u_2

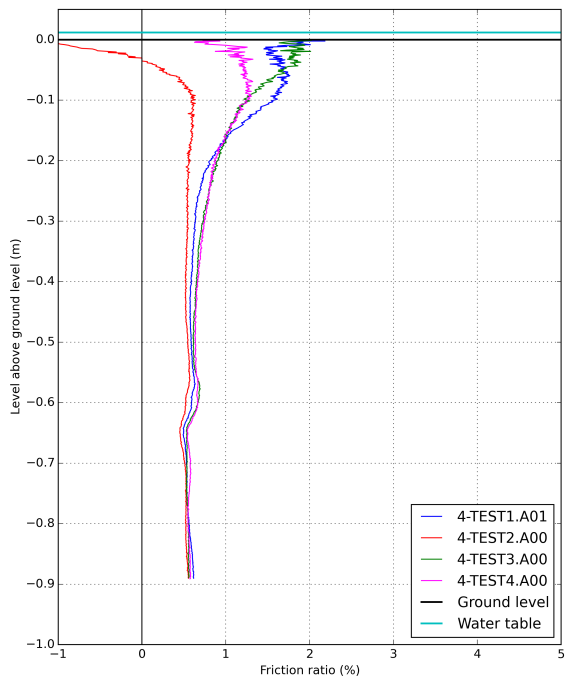
Figure G.49: CPT data for test 4-TEST1 including classification



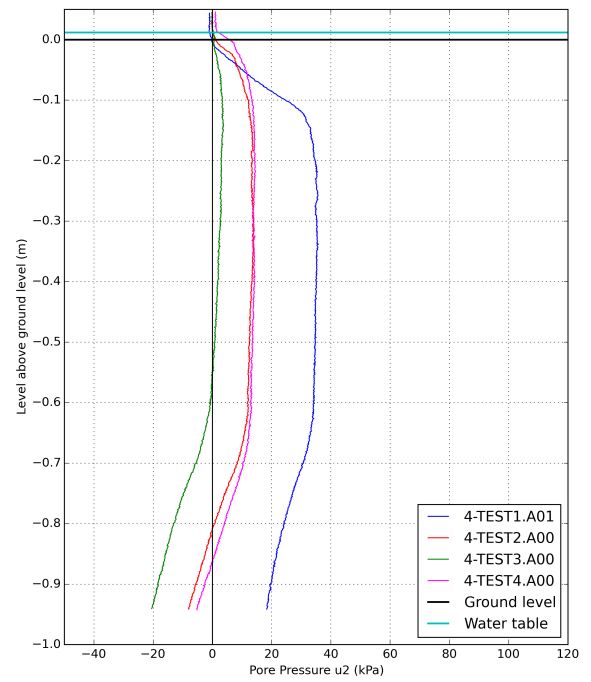
(a) Cone resistances



(b) Sleeve friction measurements



(c) Friction ratios



(d) Pore pressure u_2 measurements

Figure G.50: Results of the tests on sample 4

G.10.3 Dismantling

During sample dismantling density samples were taken and a cross section was made to check measure the final height of the coloured layer of sand and so to check whether the bottom layer was compacted during preparation of the top layer. Figure G.52 displays the way the coloured layer was encountered in the cross-section. After measuring the height of this layer is was concluded that the bulk of the bottom layer did not compact during preparation of the top layer.

Results of density measurements are found in figure G.51, in which the locations correspond to the locations drawn in figure G.47b. A clear division in density between the two layers can be observed in this figure. The average density of the top layer is lower than the average density of the bottom layer, which was expected considering the bulk densities reached during sample preparation. It can also be concluded that for each layer the top part of the layer is denser than the rest of the layer. It could be that arching occurs in the top part of the layers. Since this may be a results of the chosen preparation technique it is better to remove the denser top part of a layer (about 10 cm) to obtain a more homogeneous density in the sample when using the vertical shock wave method for future sample preparation.

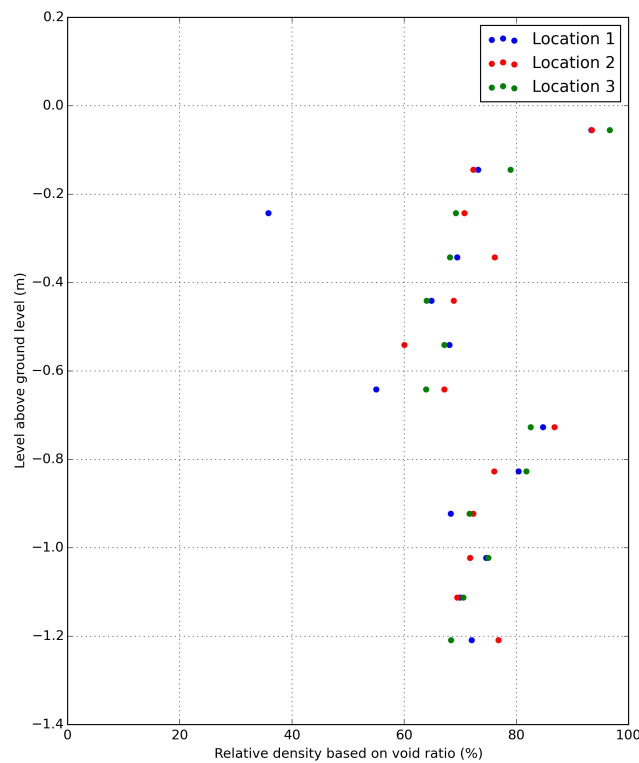


Figure G.51: Relative density based on void ratio over depth for sample 4



Figure G.52: Photo of excavation of the layer with coloured sand

G.10.4 Conclusions

- Using the vertical shock wave technique in multiple phases for preparing a single sample causes layering with significant differences in relative density.
- When applying an amount of shocks that causes the layer not to compact any more (around 35 shocks during preparing of sample 4), the layer will not compact any further during compaction of additional layers.
- The vertical shock wave technique is considered not suitable for preparing samples with layers of clay.
- The top part of a layer compacted using the vertical shock wave technique has a higher density than the rest of the layer, which may be caused by arching effects during compaction.

G.11 Sample 5: Three 8 cm clay layers between medium sand layers

Doing more tests on achieving a homogeneous sand sample would take too much time it was decided to start with layered samples. Since the vertical shock wave method and tamping technique are considered to be unable to be used in layered samples a new technique for sand preparation had to be developed. This method is described in section G.4.1 as the thin layering compacting technique. The goals of this test were:

- To gain experience with building up multiple sand layers with relative densities around 50%,
- To see how the cone reacts on layering (thickness $> d_{cone}$).

G.11.1 Sample configuration

A figure showing the sample configuration can be found in figure G.53a and a top view of the test locations can be found in figure G.53b. In order to make sure that the cone would fully penetrate all layers and that it has enough depth left to develop some cone resistance in sand, the vertical location of the clay layers had to be chosen carefully. To have the clay layers tested at some amount of stress the layers were placed as deep as possible, the sand layer on top was prepared with a thickness of 44 cm. Just as during tests on sample 2 test locations were chosen such that clay brick voids would be avoided as much as possible. An overview of the brick configuration can be found in figure G.54. The numbers on the bricks correspond to the brick numbers in table G.5.

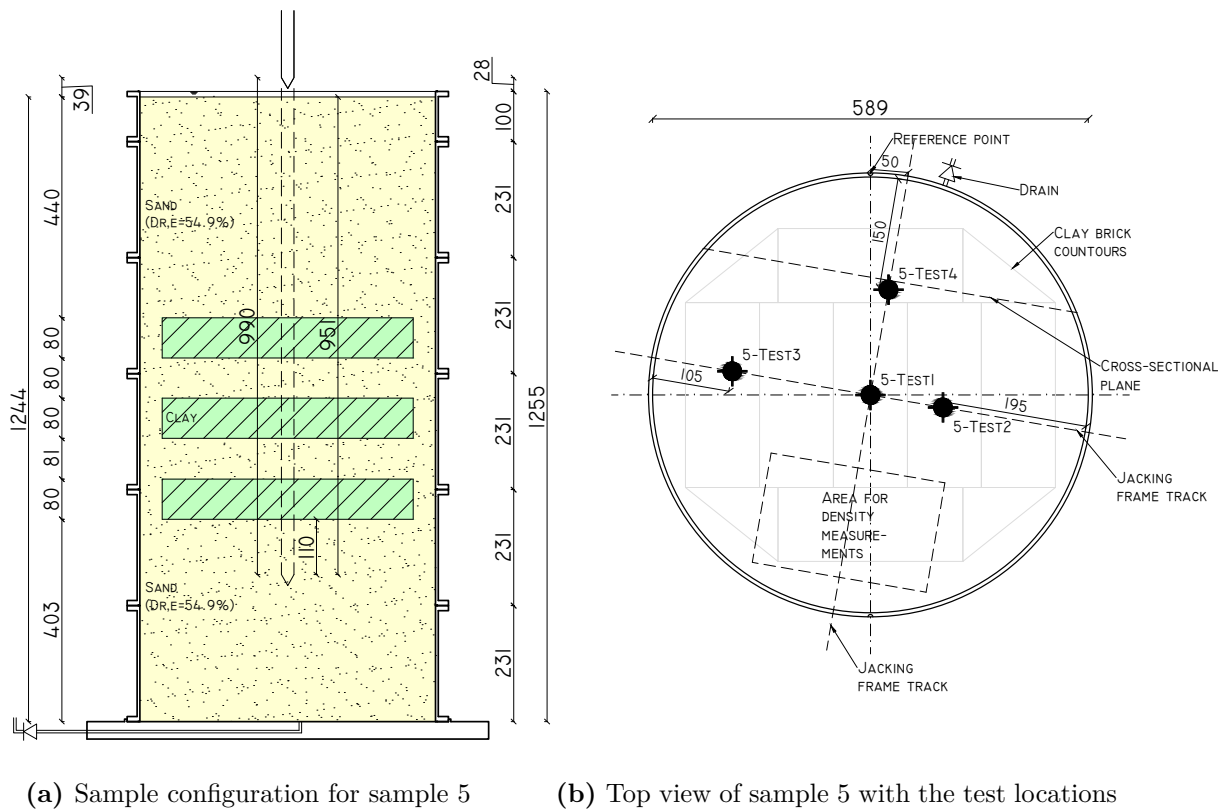


Figure G.53: Sample configuration and test locations for sample 5

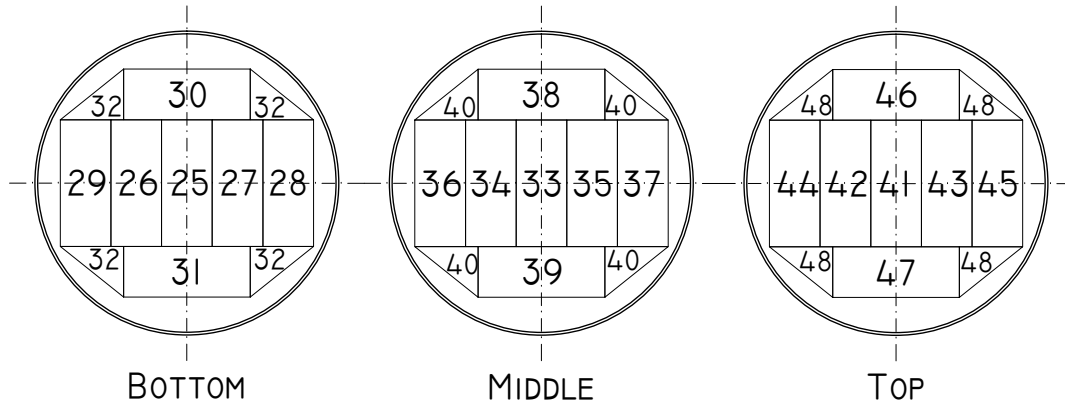


Figure G.54: Brick configuration for sample 5 corresponding to the brick numbers in table G.5

G.11.2 Results

Results of the first test can be found in figure G.55 presented as CPT data, figure G.57 presents each measured parameter separately for each test. Results of each test separately are in the same range (except for the cone resistance in the bottom sand layer), indicating that the sample has been fairly homogeneously prepared.

Cone resistance (fig. G.57a)

From the cone resistance the layers can be clearly distinguished. Maximum cone resistance reached with testing sample 5 lie between 1.3 and 2.5 MPa, which is considerably less than found in previous tests. This indicates that the thin layering compaction technique allows sand densities to be low and that boundary effects can be avoided. It is not sure whether variation in maximum density per tests comes from inhomogeneities or sample disturbance as more tests are performed. This can be concluded after testing more samples in which the thin layering compaction technique is used. Cone resistance in the clay layers shows a same pattern when comparing layers with each other, although with depth resistances rise slightly compared to clay layers above. This may come from difference in stress levels. The same goes for cone resistance in the sand layers.

Figure G.56 displays characteristic points, distances and angles of the cone resistance regarding penetration through three 8 cm clay layers with 8 cm sand layers in between. As for sample 2 the cone is influenced by the clay layer well before the actual layer is reached. It is not sure whether this point is at 105 mm ($4.2 \cdot d_{cone}$) or 61 mm ($2.4 \cdot d_{cone}$) from the first sand-clay interface. It could be that at the 105 mm point critical depth is reached after and that cone resistance has reached a characteristic cone resistance for sand between 105 mm and 61 mm, or that the 105 mm point originates from the influence of the clay layer.

In the clay layers two characteristic point can be distinguished: a point of inflection at 8 - 11 mm ($0.4 \cdot d_{cone}$) from the top interface at which cone resistance starts to decrease at a lower rate as above this point, and a point at 35 - 36 mm ($1.4 \cdot d_{cone}$) from the bottom boundary at which the cone resistance is increasing due to the sand below. The angles for the lines drawn between these two points are similar to each other (see A, B and C in figure G.56). For each separate layer these points and angles have comparable distances and values, therefore it is concluded that this behaviour in cone resistance is distinctive for this type of layering.

The same two characteristic points as for the clay layers can be distinguished for two 8 cm

layers, although the points are located at less distance from each other as in the clay layers. For both layers the points are at distances from layer interfaces comparable to the other layer. The lower of the two sand layers, however, shows a bigger variety in cone resistance than in upper sand layers.

Sleeve friction and friction ratio (fig. G.57b and fig. G.57c)

Sleeve friction shows results which are expected generally. Since the friction sleeve is 9.36 cm long and the layers are 8 cm thick, the friction sleeve should always detect clay as well as sand in this sample configuration. Just before the reference point of the friction sleeve (center of the sleeve) enters the first clay layer, half of it already has entered the layer and is experiencing the friction from that layer. Therefore sleeve friction starts increasing at the point where the sleeve reference point is half the sleeve length away from the layer boundary (46.8 mm, see table G.8). This is also the case for the points in the clay layers where the sleeve friction starts to decrease to values in sand, but this decrease can also come from the same decreasing trend as shown result of testing sample 2 (see figure G.39b).

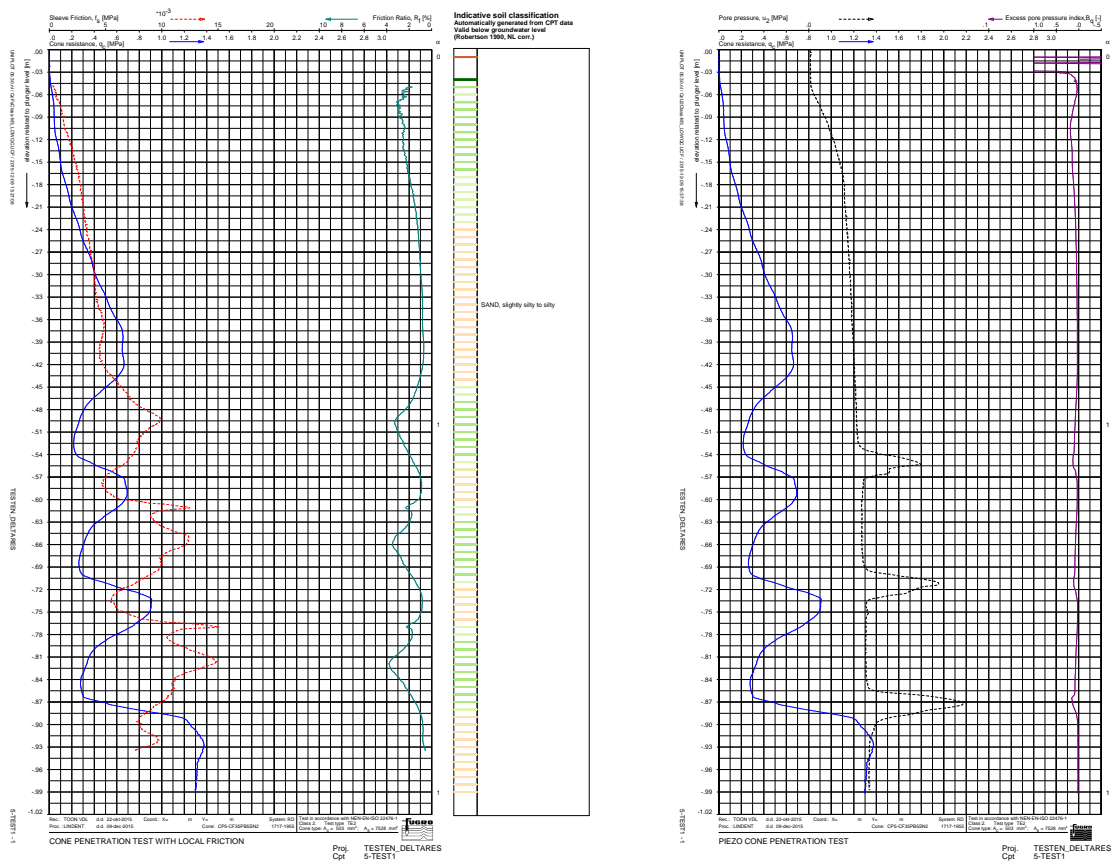
Around a level of -35 cm a slight increase and decrease can be observed in sleeve friction measurements. When the cone is approaching the clay layer, the penetration mechanism in sand as displayed in figure 2.10 is interrupted by the vicinity clay, causing the stresses along the friction sleeve to decrease, therefore lower values for sleeve friction are measured just before friction starts to rise again due to entering of the first clay layer.

In the middle of the 8 cm sand layers there are sudden increases in sleeve friction, also detectable in friction ratio data.

Apart from the either large or negative values for friction ratio at the top of the sample the layering is very well detected using friction ratio, though values between 3% and 4% are rather high for clay. Below the bottom clay layer values for friction ratio are just above 0.5%, which is considered normal in sand.

Pore pressure (fig. G.57d)

During tests on sample 2 the same behaviour in pore pressure measurements was seen as with tests on sample 5: in the majority of the clay pore pressure is not increasing, only until a clay layer is about to be exited. This indicates that increasing pore pressures can drain when the clay is penetrated, therefore it was expected that a cross-section of a penetrated layer would look the same as the cross-section of sample 2 (figure G.41). Increasing pore pressures right before entering a sand layer can be explained if clay is displaced into or plugged onto the sand enclosing the pore pressure filter and causing pore pressures to increase at those levels. From pore pressure measurements the number of layers would be estimated accurately, but the size of the layers would not.



(a) Results for q_c , f_s and friction ratio

(b) Results for q_c and u_2

Figure G.55: CPT data for test 5-TEST1 including classification

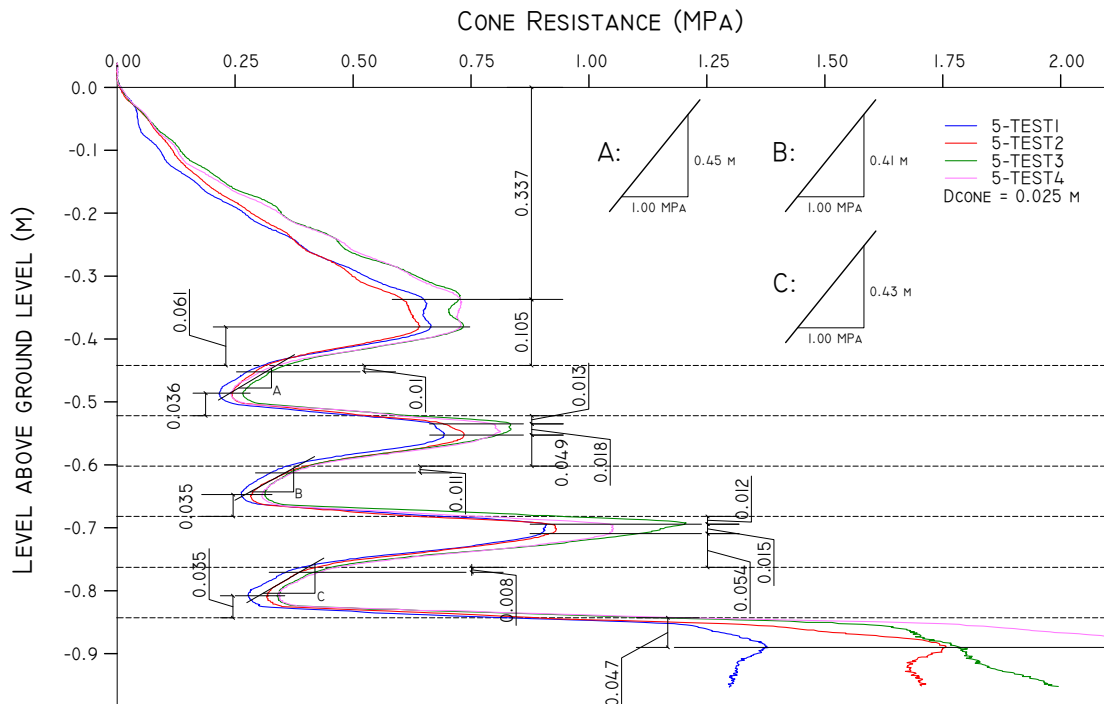
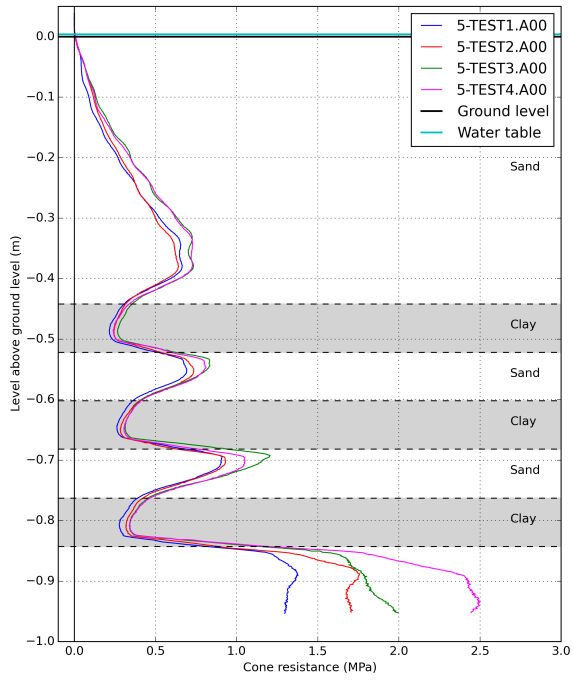
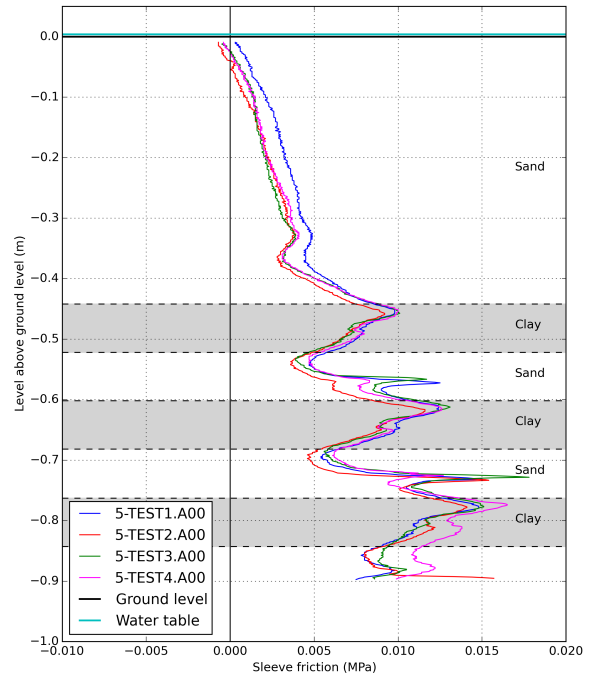


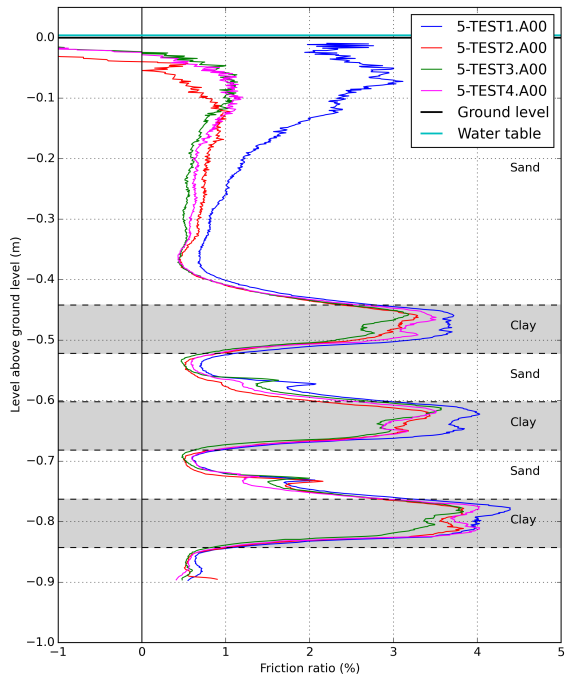
Figure G.56: Detail of the cone resistance in clay of sample 5



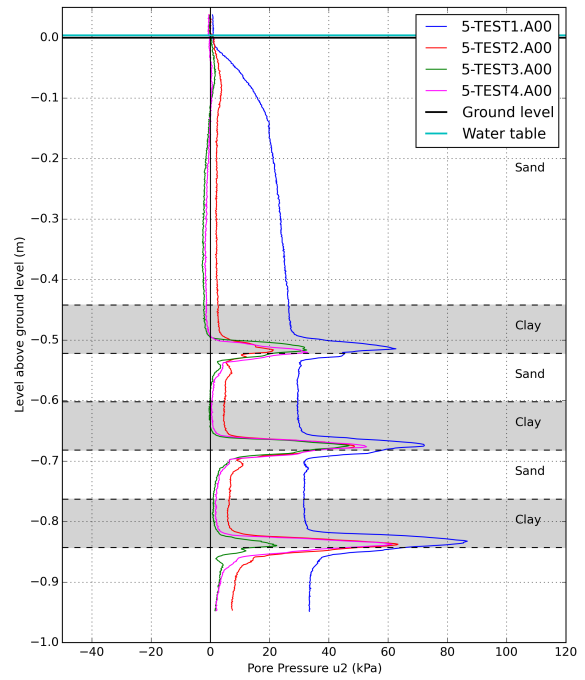
(a) Cone resistances



(b) Sleeve friction measurements



(c) Friction ratios



(d) Pore pressure u_2 measurements

Figure G.57: Results of the tests on sample 5

G.11.3 Dismantling

Sample dismantling of sample 5 comprised making a cross-section as well as taking density samples of the sand layers. Both are described in separate sections below.

Cross-section

Since making a cross-section of sample 2 proved to give additional information what happened during penetration, it was decided that for sample 5 a cross-section should be made as well. An overview of the cross-section of sample 5 can be found in figure G.58. Larger figures can be found in appendix I. Details of the cross-sections at each clay layer can be found in figure



Figure G.58: Overview of the cross-section during sample dismantling

G.59. The cross-sections at the top of the layers of clay resemble the cross-section of sample two regarding shape of clay and sand deformation, to be found in figure G.41. Where the sand intrusion has a width at the original layer interface in sample 2 of approximately 8 cm, the width of the shape in sample 5 is about 4 cm. This can be explained by the difference in sand density. The area of deformation surrounding the cone will be larger in dense sand than in looser sand, so the deformation around the layer interface is larger as well.

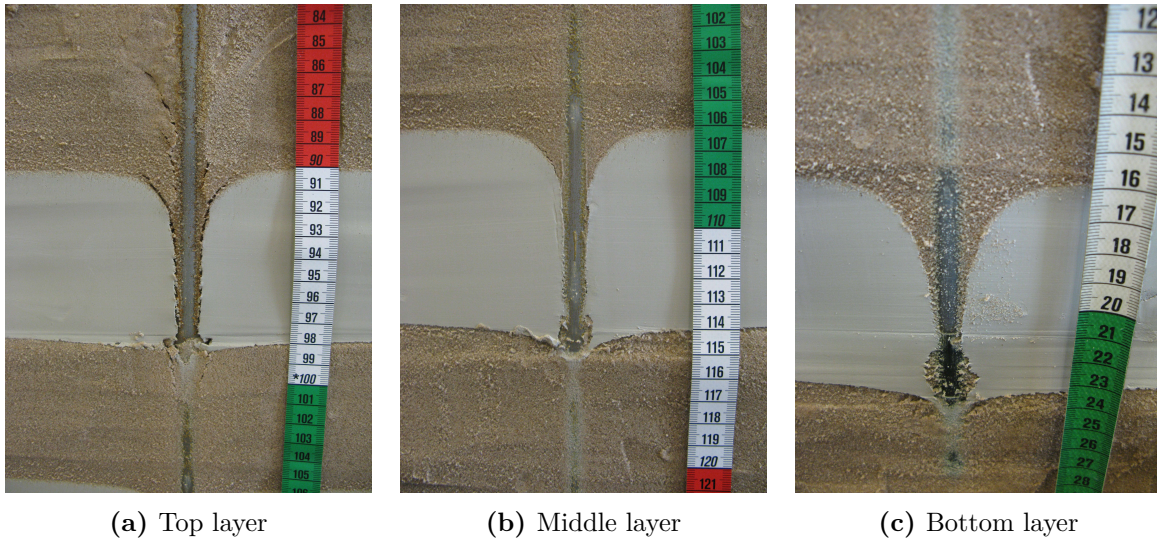


Figure G.59: Details of the separate clay layers

Especially visible in the middle and even more in the bottom layer is an accumulation of sand near the bottom clay-sand boundary. It seems that besides sand also clay is pushed in front of the cone. At some point in the clay the resistance of the clay pushed forward is larger than that of the sand that is being pushed in front, therefore at that point the sand is accumulated and the clay is pushed further forward. This may also explain why there is clay clogged around the rod just below the clay-sand interfaces.

In figure G.59 at the bottom clay-sand interfaces clay intrusions in the sand is visible. This clay sticking around the extension rod at those levels can explain why pore pressures are just increasing as the cone passes through the original clay-sand interface.

Density samples

Density samples were taken in the sand layers above, below and in the layering. Since measurements were taken after testing, it is believed that not much value should be given to the absolute values of density measurements. But measurements can be compared with each other, though. It can be concluded that the density around -70 cm is higher than density around -55 cm, which is where the second and first 8 cm sand layers are located. Considering cone resistance the bottom 8 cm sand layer seems to give higher cone resistances than the top 8 cm sand layer, which can be explained by the slightly higher densities measured in the bottom sand layer. Overall, the density measurements show a more or less constant trend, although the dispersion in measurements is significant.

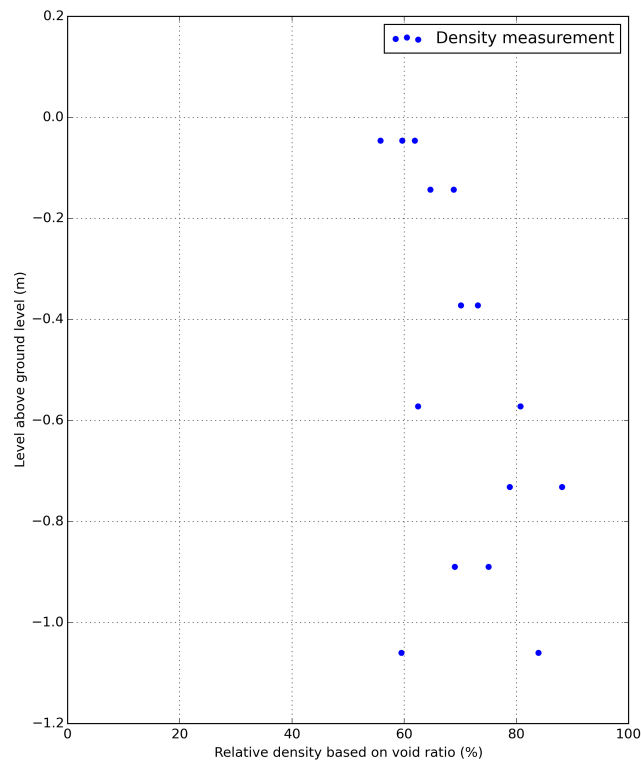


Figure G.60: Relative density based on void ratio over depth for sample 5

G.11.4 Conclusions

- Size of layering $> d_{cone}$ is detectable in cone resistance data and friction sleeve data as well.
- Pore pressure measurements (u_2) detect clay layers of this size but do not give a good indication of their sizes.

G.12 Sample 6: Ten 2 cm clay layers between medium sand layers

For the last test involving clay layers a sample with ten layers of clay with a thickness of 2 cm each was prepared. Sample 6 was prepared in a comparable way as the preparation of sample 5, only here more and thinner layers were needed to be prepared. The goal of this test was:

- To investigate the influence of layering (thickness $< d_{cone}$) on the cone resistance.

G.12.1 Sample configuration

A figure of the sample configuration can be found in figure G.61a and a top view of the test locations can be found in figure G.61b. Since the thin layering compaction technique seemed give reasonable results it was decided to use the method again for preparation of sample 6. As with sample 5, to have the clay layers tested at some amount of stress the layers were placed as deep as possible. Test locations were again chosen such that clay brick voids would be avoided as much as possible.

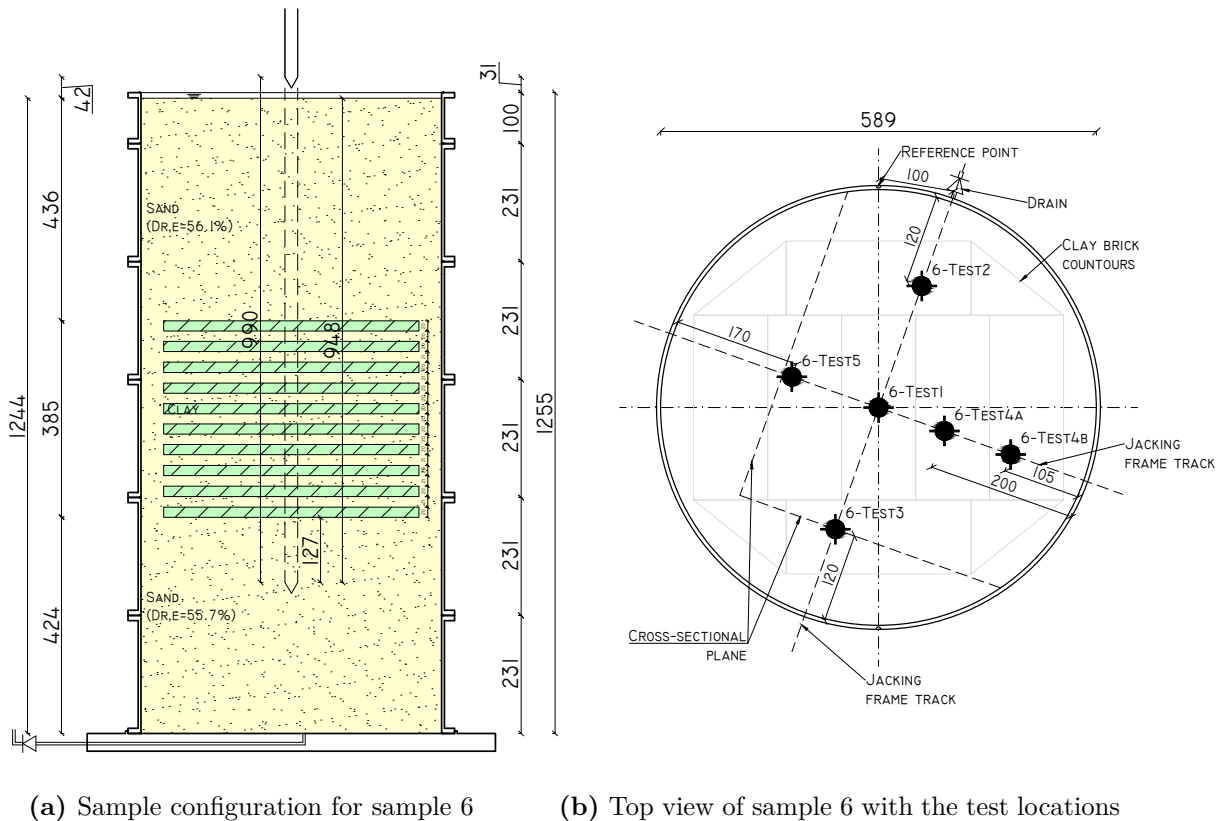


Figure G.61: Sample configuration and test locations for sample 6

G.12.2 Results

Results of the first test can be found in figure G.63 presented as CPT data, figure G.65 presents each measured parameter separately for each test. Regarding the zero output load check warnings, test results look reasonable comparing to test results from sample 5 and so there is reason to believe that these errors did not influence the test results significantly.

After the zero load check just before commencing testing the data-acquisition program indicated that the zero load output or calibration signal for the cone+friction measuring gauges was out of range and that the signals for cone and cone+friction were not stable (features of a subtraction cone), see figure G.62. Since it is believed that the sample could not remain untested too long because of possible changes in clay properties (softer edges), it was decided to let the tests continue and decide after result generation whether to redo the tests and prepare a new layered sample. After testing the cone was brought back to the Fugro workshop to have it checked, and there it turned out silicone oil had been able to get inside the cone. Since the test results, at least for the cone resistance, can be considered to be explainable and reasonable when comparing them to results from previous tests, it is believed that these errors did not have much effect on the measurements. But when looking at the results it should be kept in mind that the gauges may have been affected by silicone oil.

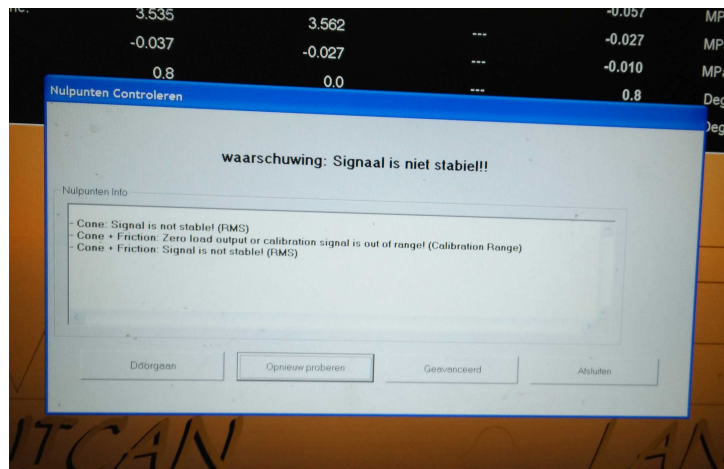


Figure G.62: Zero load output check warning

Cone resistance (fig. G.65a)

Size and location of the layers can be distinguished from cone resistance measurements. Maximum cone resistances reached with testing sample 6 lie between 1.0 and 2.0 MPa, comparable to but slightly lower than maximum values from sample 5 (1.3 to 2.5 MPa). Cone resistance seems to change between increasing or decreasing exactly at clay-sand interfaces, where the cone resistance increases when in a sand layer and decreases when in clay which would be expected in bigger layers. This behaviour occurring right at the clay-sand interfaces could be coincidence, while choosing another reference level on the cone would cause the results to shift significantly.

Figure G.64 displays characteristic points, distances and angles of the cone resistance regarding penetration through ten 2 cm clay layers with 2 cm sand layers in between. Although at 126 mm ($5.0 \cdot d_{cone}$) from the first sand-clay interface a point of inflection can be seen it is believed that at 78 mm ($3.1 \cdot d_{cone}$) from the interface the cone resistance is influenced by the layers, where this point in tests on sample 2 was at 82 mm ($3.3 \cdot d_{cone}$) and sample 5 at 61 mm ($2.4 \cdot d_{cone}$) (figures G.38 and G.56).

It seems that once the layered part of the sample is entered the cone resistance behaves more or less linearly between the clay-sand and sand-clay interfaces. The difference between maximum and minimum cone resistance for one cycle varies over depth from 0.04 MPa to 0.055 MPa. The angle of these lines however is not constant for every layer, although variation is small. It can be concluded that vertical stress affects the absolute values of the cone resistance in the layers, since a slight inclination can be seen in the mean of the cone resistance in the layered part of the sample.

Sleeve friction and friction ratio (fig. G.65b and fig. G.65c)

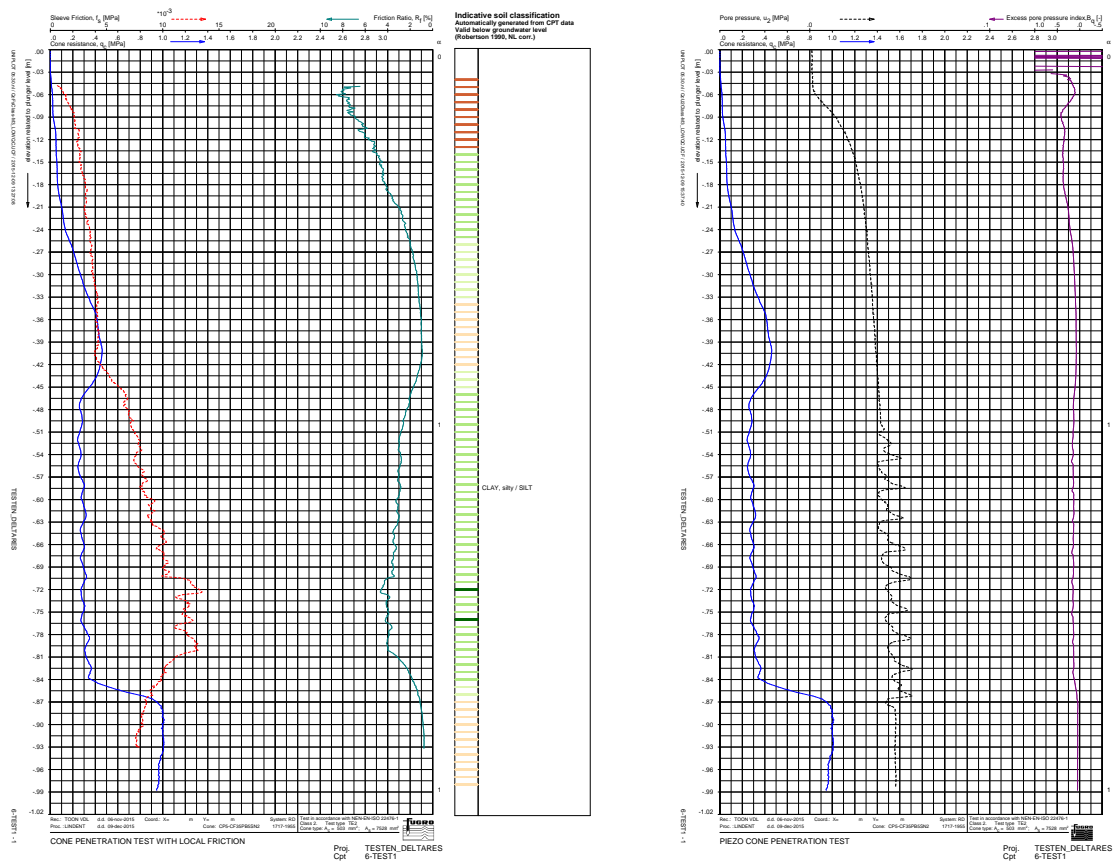
Since the friction sleeve has a length of 9.36 cm a lot of averaging takes place in the layered part of the sample. Therefore separate layers are not displayed in sleeve friction measurements as good as in cone resistance measurements, where averaging only applies to the height of the cone (2.17 cm). This explains the fuzzy course of sleeve friction measurements. About 76 mm above the first sand-clay interface sleeve friction starts to increase. This corresponds to the cone-friction sleeve distance of 56 mm plus cone height of 22 mm, together making 78 mm (see table G.8). When the cone approaches the interface and the cone tip enters the clay, the failure surface changes in shape and size and therefore the sleeve friction is affected. As the cone is entering the clay layer, the bottom part of the friction sleeve also encounters more resistance, although still sand is between the friction sleeve and actual clay, which can be seen in the cross-sections made during dismantling. As penetration continues a larger part of the friction sleeve enters the layered part, giving a constant increase in sleeve friction. The same goes for the point at the bottom of the layered part, when the friction sleeve starts to exit the layered part.

Besides this a constant increase in sleeve friction can be observed over depth in the layered part, indicating that here too stress level plays a role in sleeve friction measurements.

Because of the fuzziness of sleeve friction measurements, friction ratio does not give any additional information, besides that a mean maximum friction ratio of 3.5% is obtained in the layered part. The wide spreading of friction ratio in the top of the sample can be attributed to the top effects in sleeve friction, which even have negative values in some cases.

Pore pressure (fig. G.65d)

Because of sand entering the clay layers (see sample dismantling) the fist layer cannot be detected using pore pressure measurements, which could be seen during dismantling of the sample and from observations made previously dismantled samples. Looking at the lowest increase in pore pressure it can be concluded that the peaks in pore pressure data are caused by the clay layer above, so a clear ‘delay’ in pore pressure generation can be observed. If layer thickness and amount of layers would have to be determined from pore pressure measurements, layer thicknesses would be underestimated and only 9 layers would be detected.



(a) Results for q_c , f_s and friction ratio

(b) Results for q_c and u_2

Figure G.63: CPT data for test 6-TEST1 including classification

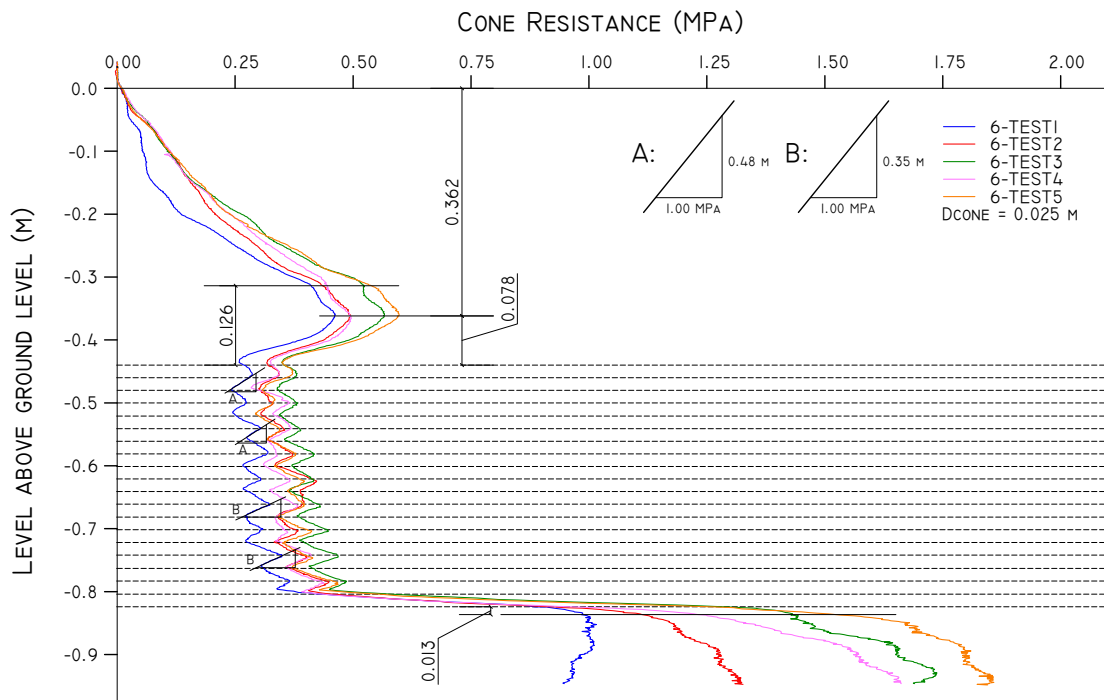
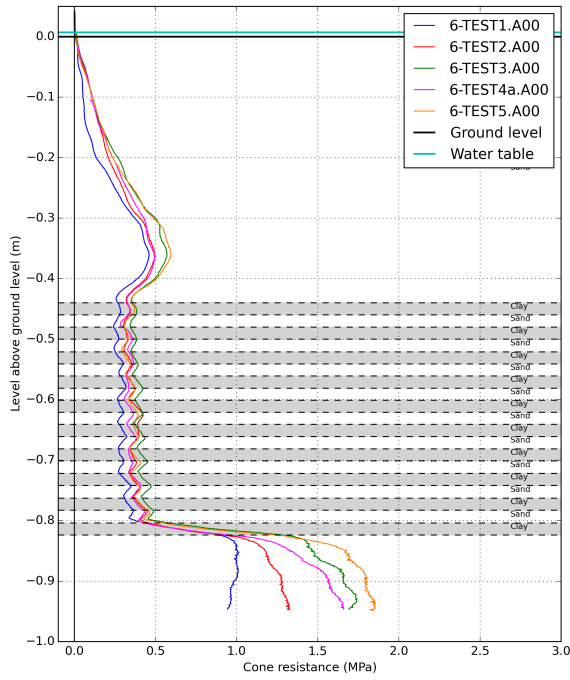
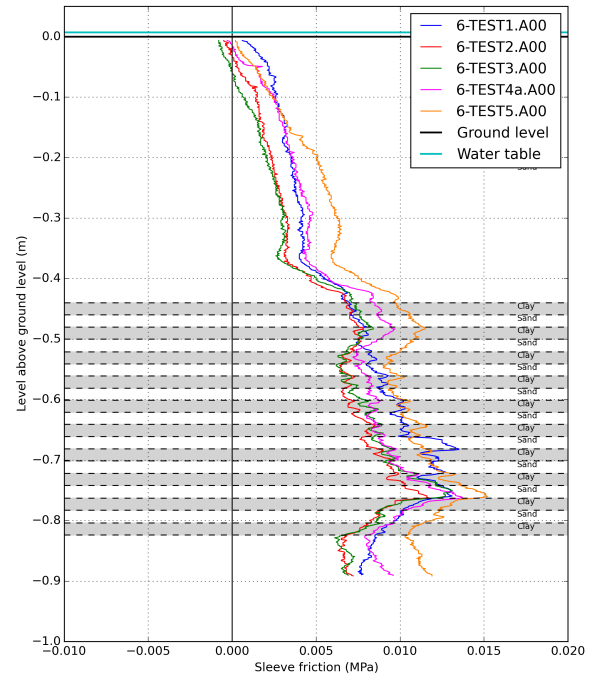


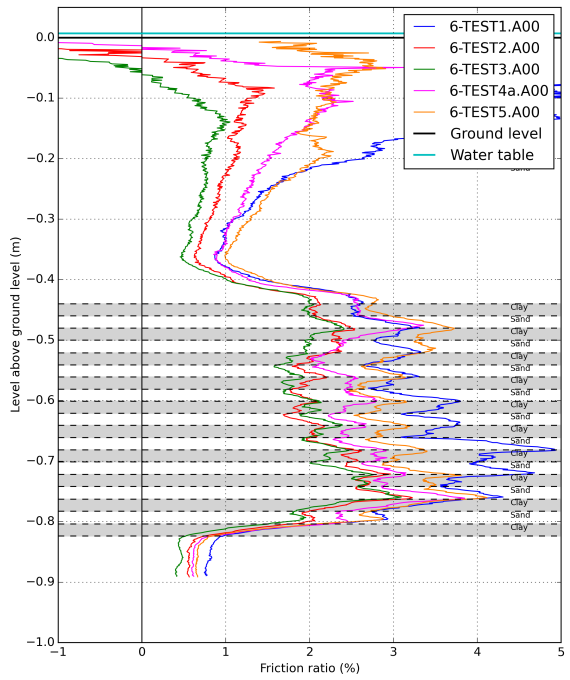
Figure G.64: Detail of the cone resistance in clay of sample 6



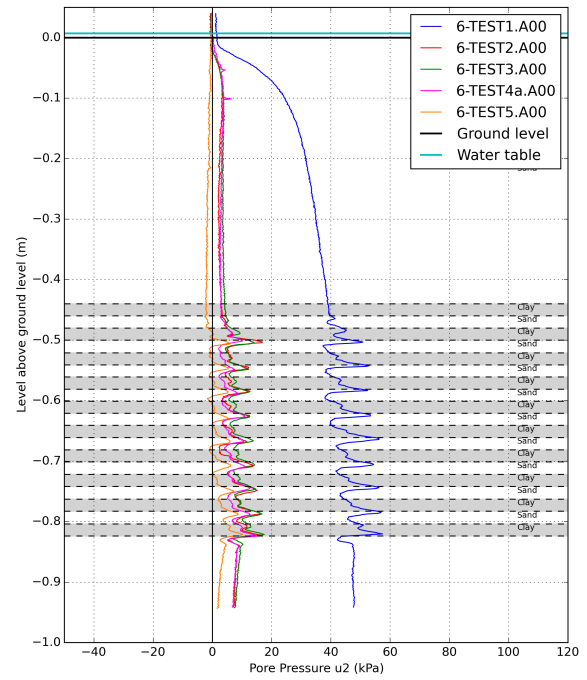
(a) Cone resistances



(b) Sleeve friction measurements



(c) Friction ratios



(d) Pore pressure u_2 measurements

Figure G.65: Results of the tests on sample 6

G.12.3 Dismantling

As for the other samples with clay layers, a cross-section was made along the cone rod left in the sample after testing. An overview of the cross-section of sample 6 can be found in figure G.66a. A detail of the layered part of the sample can be found in figure G.66b. Larger figures can be found in appendix I. Another type of shape is seen than in previous samples with layering. In figure G.68a it a cup-like shape can be recognized in the top clay layer. Below this shape smoothens and gets the form of shapes seen in previous samples, only here the clay attaches to the cone at less absolute depth from the top sand-clay interface. The smearing effect is clearly visible for all layers over the total depth of the layered section, indicating that this smearing is not an effect of the cone rod passing through the sample. For this sample also a cross-section

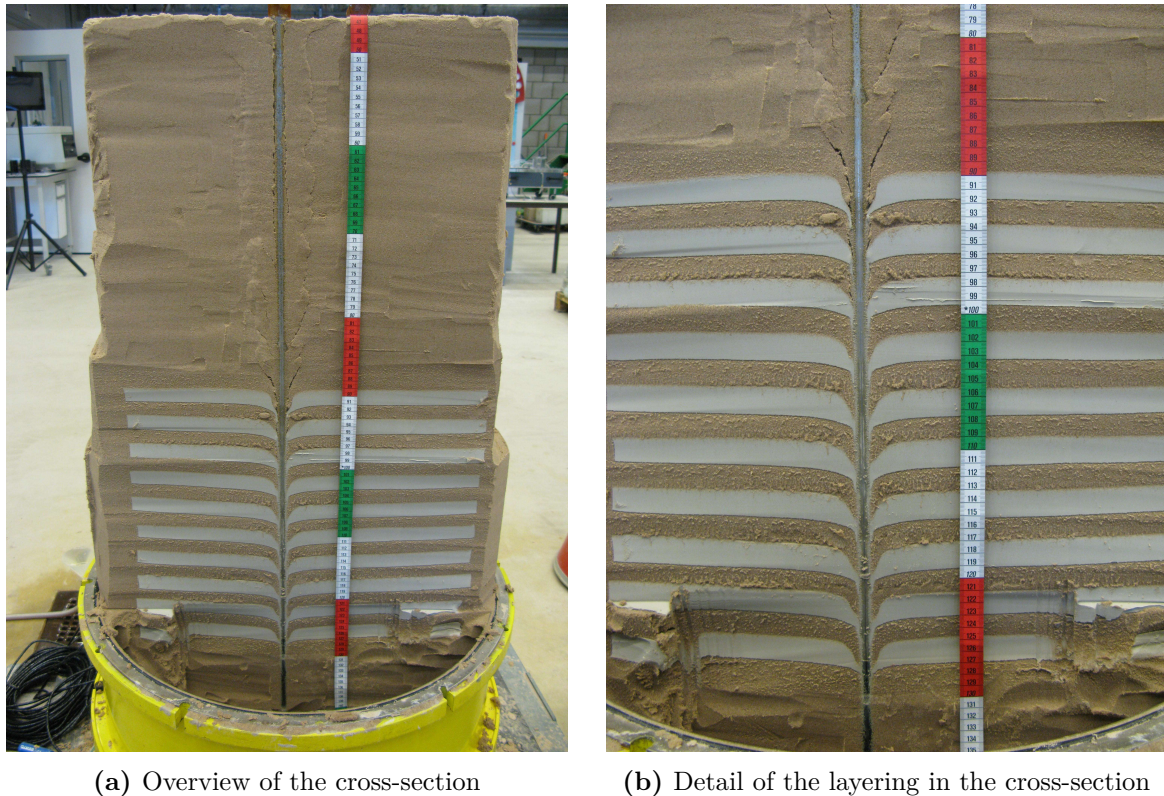
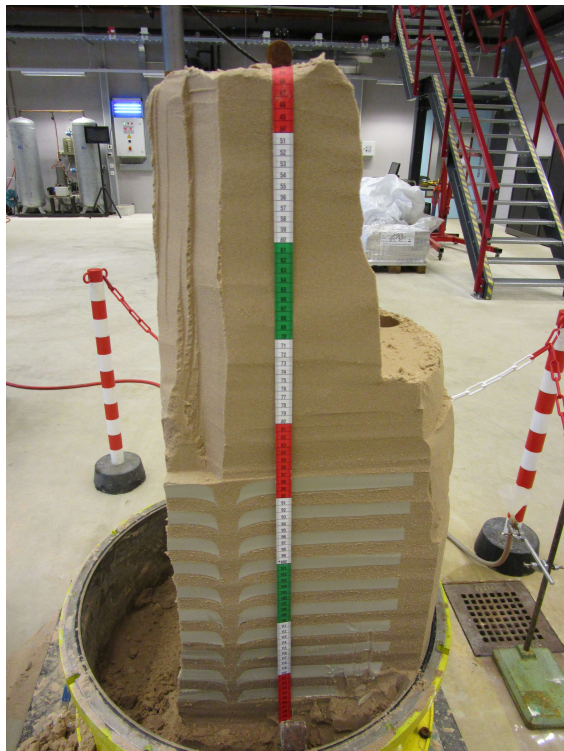


Figure G.66: Dismantling sample 6

was made through the path of a retracted cone. A clear sand column over the whole layered section can be seen in figure G.67b. In figure G.68b very thin horizontal clay layers can be seen in the path of the cone. This indicates that the sand which is filling the course of the retracted cone comes from the sand layers between the clay layers and not from below the layered section, since then the tiny slices of clay would not be horizontally oriented.



(a) Overview

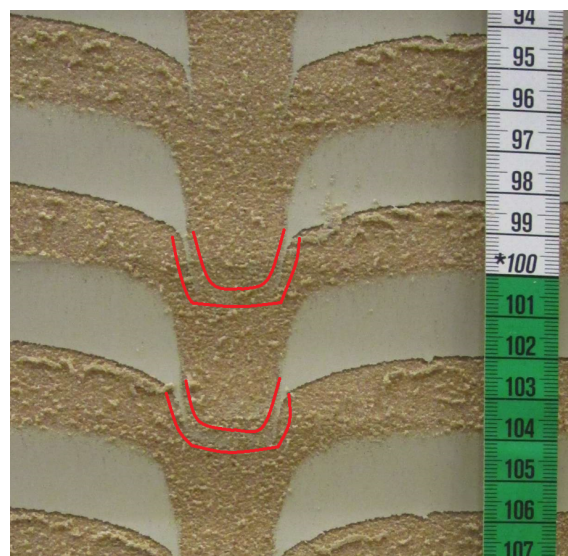


(b) Detail of the layering

Figure G.67: Cross-section through the path of a retracted cone



(a) Detail along the cone rod with horizontal thin clay lenses highlighted in red



(b) Detail of a sand column

Figure G.68: Details of the cross-sections along the rod and through the path of a retracted cone

G.12.4 Conclusions

- Cone resistance can give a good view on how many layers there are and how thick they are when layer thickness is in the range of the cone height.
- Sleeve friction data in layered samples with layer thicknesses far less than the length of the friction sleeve cannot be used to determine layer configuration.
- Pore pressure u_2 measurements do not give a correct indication of layer location and size for layers thinner than the cone diameter.
- Since other parameters measured give less insight in layer configuration, it seems that cone resistance is the best parameter to detect layering when layer thickness is in the range of the cone height.

G.13 Sample 7: Uniform medium sand layer

To obtain a characteristic cone resistance for sand at a relative density of 50% a reference test was needed. This reference test was done in a sample with only sand, prepared in the same as the sand for the layered samples using the thin layering compaction technique. The goal of this test was:

- To obtain a characteristic cone resistance for sand

G.13.1 Sample configuration

A figure of the sample configuration can be found in figure G.69a and a top view of the test locations can be found in figure G.69b. An area for taking density samples after testing was reserved. The sample was built in stages of 5 cm height using the thin layering compaction technique. After having problems with the zero load check of the cone before testing sample

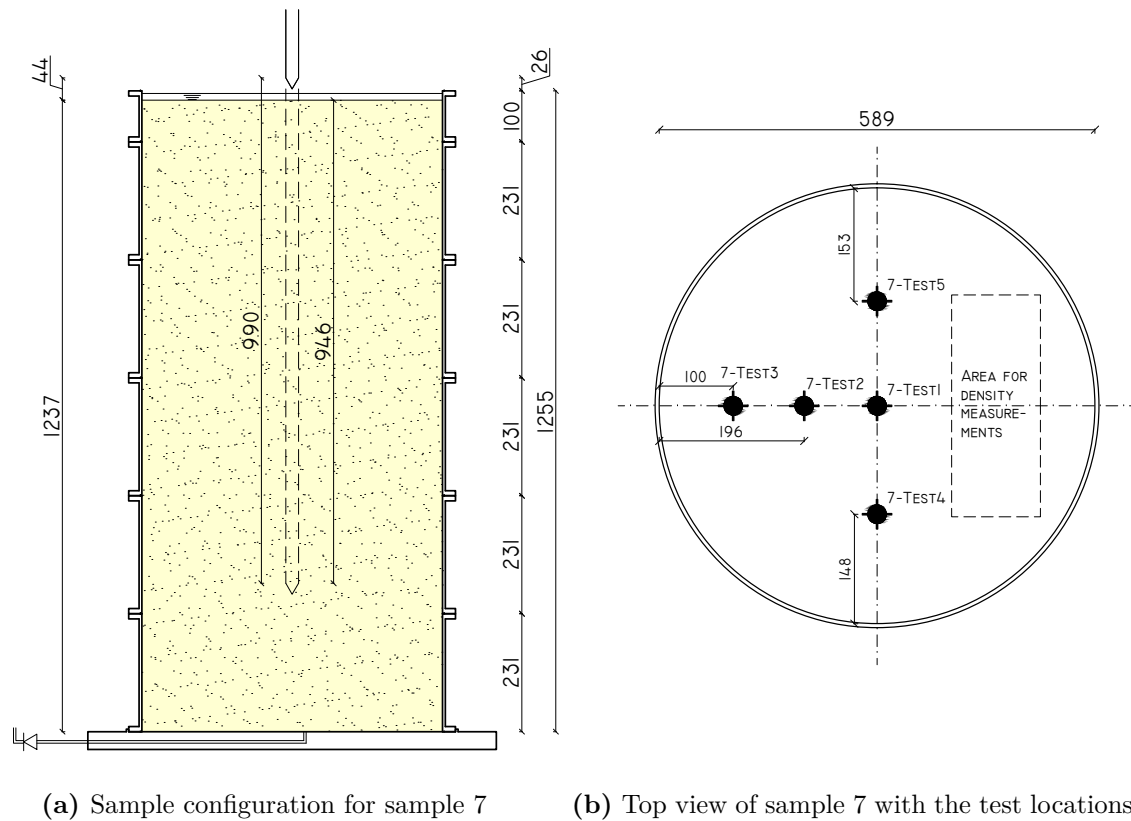


Figure G.69: Sample configuration and test locations for sample 7

6, the cone was calibrated and repaired at the workshop. The cone passed the zero load check before tests on sample 7 without any issue.

G.13.2 Results

Results of the first test can be found in figure G.70 presented as CPT data, figure G.72 presents each measured parameter separately for all tests. It can be concluded that the sample was prepared fairly homogeneously and that after penetration compaction of the sample takes place causing higher resistances.

Because during the first test (7-TEST1) the depth encoder was not working properly, sampling was done without depth data which needs to be derived from plunger data: lowest plunger level and plunger rate. After 7-TEST1 test proceeded after the weekend. Since this process has not yet been finished data for 7-TEST1 are not yet available in this report, except for cone resistance data.

Cone resistance (fig. G.72a)

After 55 cm of penetration through the sand a point of inclination is reached in all tests. This may indicate that this could be the critical depth of the sample with the achieved relative density and cone dimensions. If this point is caused by an inhomogeneity in the sample this would be visible in density samples taken after the test. This is why at the area around 55 cm where cone resistance has a section of constant value is chosen to take density samples from. This also goes for the decrease in cone resistance at 70 cm depth. and increase around 90 cm. Again it can be concluded that compaction takes place during sample penetration, since consecutive tests show higher cone resistances after a depth of 60 cm.

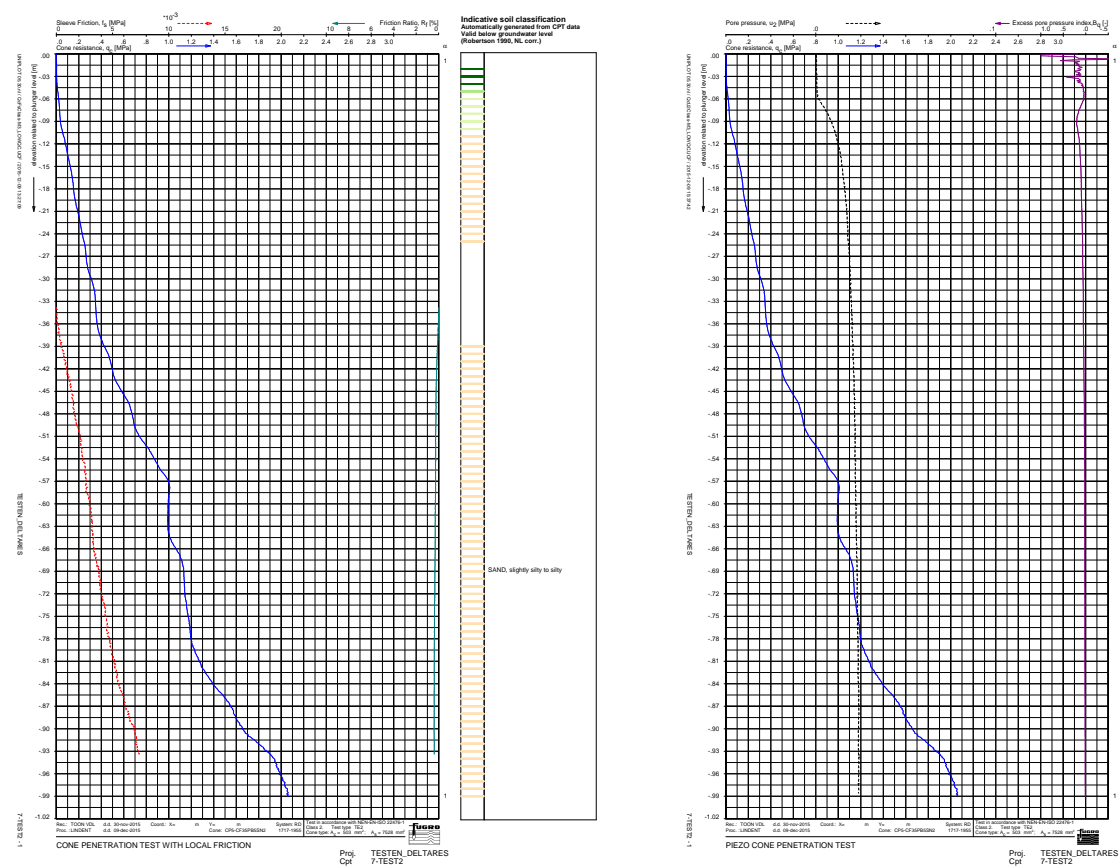
The sudden backdrop in cone resistance of 7-TEST1 can come from punching through the pore pressure filter seal (see figure G.23b), which was left on the cone when the first test started. Looking at the bottom part of 7-TEST1 (from 85 cm), it can be concluded that the characteristic cone resistance can be 1.30 MPa, although this resistance depends on local stress level.

Sleeve friction and friction ratio (fig. G.72b and fig. G.72c)

Results of both sleeve friction measurements and friction ratio are as expected without signs of problems or inhomogeneities. Friction ratio reaches values around 0.5%, which can be considered to be normal in sand.

Pore pressure (fig. G.72d)

Except for pore pressures measured during 7-TEST2 being the first one after saturating the sample using vacuum pressure, which is discussed in section G.6.1, pore pressure data are as expected, only without seeing hydrostatic water pressure back in the results.



(b) Results for q_c and u_2

Figure G.70: CPT data for test 7-TEST2 including classification

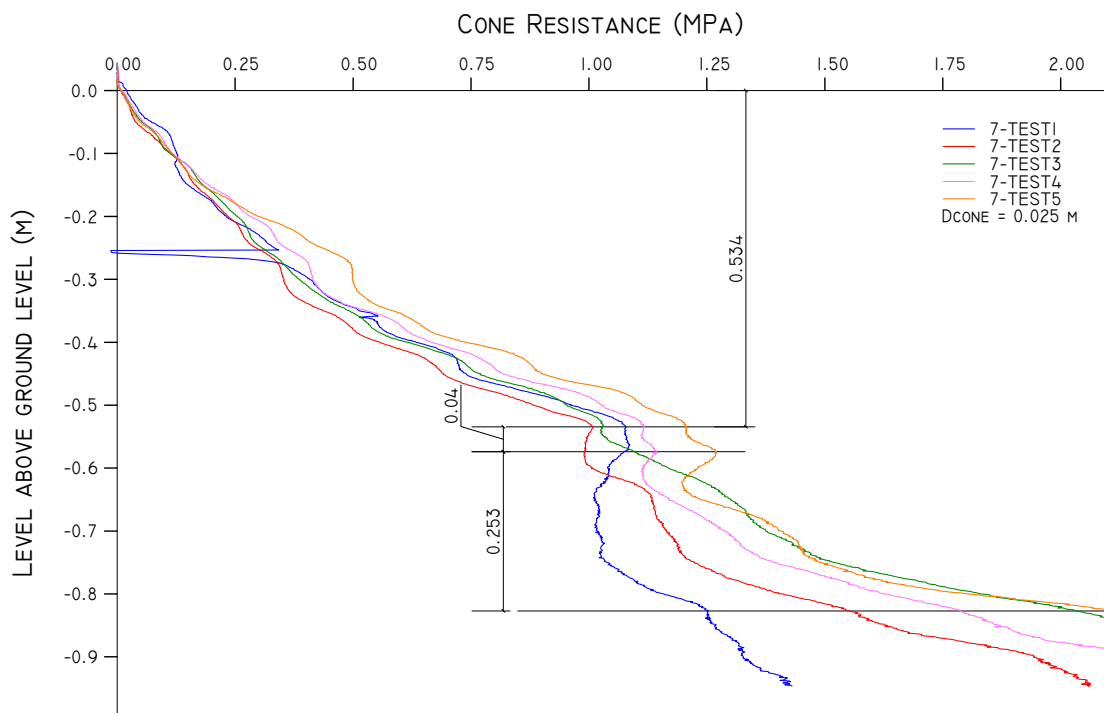
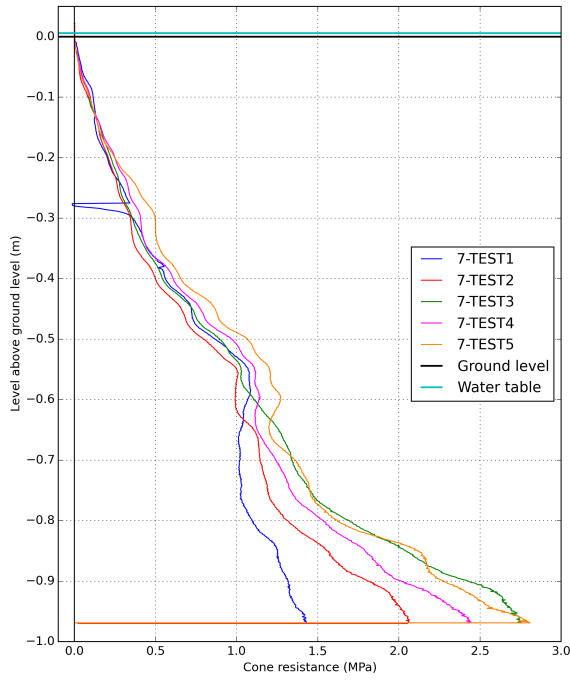
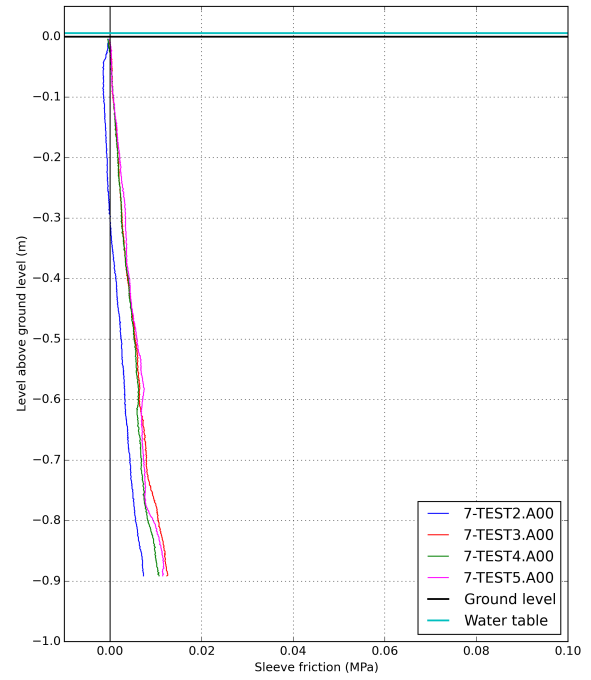


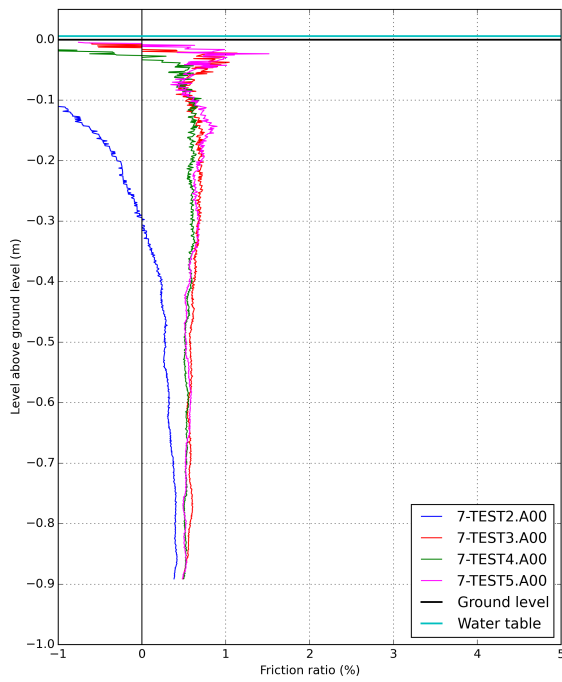
Figure G.71: Detail of the cone resistance in clay of sample 7



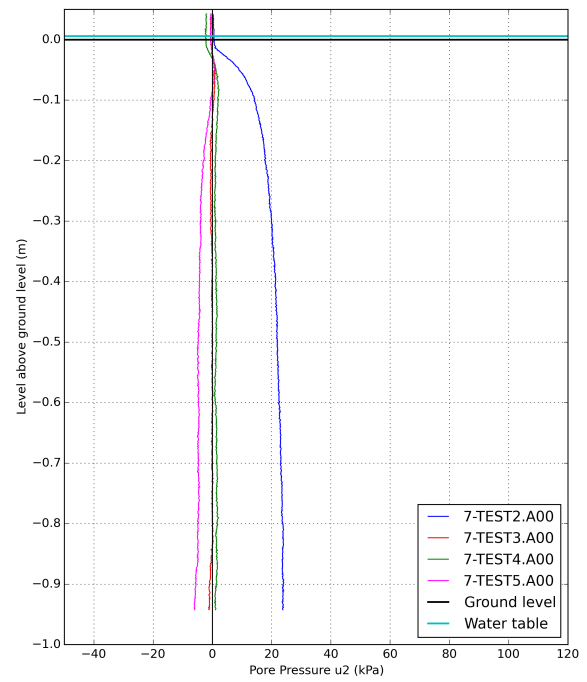
(a) Cone resistances



(b) Sleeve friction measurements



(c) Friction ratios



(d) Pore pressure u_2 measurements

Figure G.72: Results of the tests on sample 7

G.13.3 Dismantling

Dismantling of sample 7 was done by taking density samples at depths determined by features in cone resistance data. Figure G.73 gives the values of $R_{d,e}$ over depth. Again it is noted that these samples were taken after testing, therefore after the sample was penetrated several times and changes in density could have taken place. The measurement just above 80 cm depth in fact is two density measurements with exactly the same outcome.

Density measurements give an image of a homogeneous sample with densities slightly higher than 60%. Only around 60 cm depth a slightly looser section can be distinguished. This is the point where cone resistance starts to decrease. At a depth of approximately 90 cm density stabilizes again. This also is the point where the characteristic cone resistance for Baskarp sand of $R_{d,n} = 50\%$ is determined.

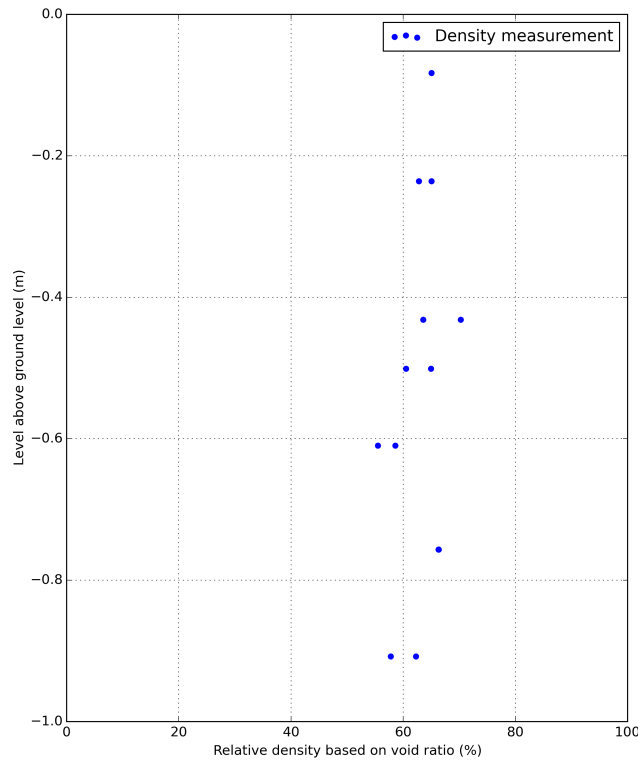


Figure G.73: Relative density based on void ratio over depth for sample 7

G.13.4 Conclusions

- Characteristic values for cone resistance in sand depend on the stress level, but below a depth of 85 cm an average cone resistance of 1.30 MPa can be distinguished.
- A sample prepared using the thin layering compaction technique can be considered to be homogeneous if preparation was done properly and without problems.

H Data management

Contents

H.1 Error analysis	H-1
H.1.1 Measuring errors	H-1
H.1.2 Handling errors	H-1
H.1.3 Uncertainty in relative density determination	H-2
H.2 Chauvenet's criterion	H-4

H.1 Error analysis

Since taking measurements implies making errors also uncertainties are present in the results presented in the main report. To have an idea of the magnitude of the errors, some examples are presented in this section. These kinds of errors are not presented for measurements taken with the cone penetrometer.

It is assumed that two kinds of errors are most important when looking at test measurements: measuring and handling errors, which are addressed in upcoming sections.

H.1.1 Measuring errors

Scales, rulers and other measuring devices and tools have a certain accuracy with which measurements can be taken. Some devices can provide more accurate measurements than others. This can be seen in table H.1, in which the measuring tools used during sample preparation can be found. Since the scales have a maximum allowable weight to be measured, the amount of sand had to be weighed in stages. Each time a certain amount of sand is weighed a measuring error is made. Since all the sand was put in containers before pouring it into the cell, the container had to be weighed as well causing another measuring error for each amount of sand weighed and therefore each time a portion of sand is weighed two measuring errors are made.

Table H.1: Measuring devices used with corresponding accuracy or measurement error made with each reading.

Quantity	Type	Error
Mass	Mettler Toledo TE 120	50 g
Mass	Mettler Toledo SB32001 DeltaRange	1 g
Mass	Mettler Toledo PM6100	0.02 g
Mass	Sartorius BP 3100 P	0.02 g
Length	Calliper	0.05 mm
Length	Ruler	0.5 mm
Length	Tapeline	0.5 mm

H.1.2 Handling errors

During sample preparation the vast amount of sand weighed with the scale did not end up entirely into the cell, so an error is made with the determination of the bulk density. It was estimated that for each sample 700 grams of sand were not included in the bulk density.

A same kind of error is made during determination of the local relative density, where not all grains of sand within a certain volume end up in the mass of sand weighed for determining

the relevant mass. It is believed that this handling error could be 0.5 g. For determination of minimum and maximum porosity the handling error is believed to be of the same magnitude.

H.1.3 Uncertainty in relative density determination

Say the highest and lowest probable values of x are $x \pm \delta x$ and those of y are $y \pm \delta y$. According to Taylor (1997), if the quantities x and y have uncertainties δx and δy and $q = x + y$, then:

$$\delta q \approx \delta x + \delta y \quad (\text{H.1})$$

If $q = x - y$, the combined uncertainty δq is the same as in equation (H.1).

If $q = x \cdot y$, then their fractional uncertainties may be summed:

$$\frac{\delta q}{|q|} \approx \frac{\delta x}{|x|} + \frac{\delta y}{|y|} \quad (\text{H.2})$$

This is also valid for $q = x/y$.

The next subsections contain examples of the magnitude of error made during testing. These examples have been made using measurements from sample 7.

Minimum and maximum porosity

Since all relative density calculations use the values for minimum and maximum porosity, the uncertainty with determination of these porosities is needed. During porosity determination the particle density is assumed to have a certain value of 2.65 g/cm³:

$$n = 1 - \frac{m_{por}/2.65 \text{ [g/cm}^3\text{]}}{V_{tot}} \quad (\text{H.3})$$

The fractional uncertainty of the porosity, in which it is believed that the uncertainty of the mould used for determining minimum and maximum porosity is $\pm 1 \text{ cm}^3$ and the measuring error made with weighing is two times 0.02 g:

$$\frac{\delta n}{|n|} = \frac{\delta m_{por}}{|m_{por}|} + \frac{\delta V_{tot}}{|V_{tot}|} = \frac{0.5 + 2 \cdot 0.02 \text{ g}}{900 \text{ g}} + \frac{1 \text{ g/cm}^3}{528 \text{ g/cm}^3} = \frac{1}{401.0} \quad (\text{H.4})$$

Therefore the value for maximum porosity should be presented as $0.471 \pm \frac{1}{401.0} \cdot 0.471 = 0.471 \pm 0.0012$. This uncertainty is assumed for every porosity determination, so:

$$\frac{\delta n}{|n|} = \frac{\delta n_{max}}{|n_{max}|} = \frac{\delta n_{min}}{|n_{min}|} \quad (\text{H.5})$$

Bulk relative density determination

For determining the achieved density of sample 7 the bulk density is defined as total mass over total volume:

$$\rho_{bulk} = \frac{m}{V} = \frac{m}{0.25 \cdot \pi \cdot D_{cell}^2 \cdot h_{cell}} \quad (\text{H.6})$$

This results in an uncertainty of:

$$\frac{\delta \rho_{bulk}}{|\rho_{bulk}|} = \frac{\delta m}{|m|} + \frac{\delta V}{|V|} = \frac{\delta m}{|m|} + 2 \cdot \frac{\delta D_{cell}}{|D_{cell}|} + \frac{\delta h_{cell}}{|h_{cell}|} \quad (\text{H.7})$$

Total sand weighed for sample 7 was 528477 g with a measuring error of 102 g and handling error of 700 g. This gives a fractional uncertainty for bulk density:

$$\frac{\delta \rho_{bulk}}{|\rho_{bulk}|} = \frac{102 + 700 \text{ g}}{528477 \text{ g}} + 2 \cdot \frac{0.05 \text{ cm}}{58.9 \text{ cm}} + \frac{0.05 \text{ cm}}{123.7 \text{ cm}} = \frac{1}{276.3} \quad (\text{H.8})$$

Calculation of the bulk porosity was done using:

$$n_{bulk} = 1 - \frac{\rho_{bulk}}{2.65 \text{ g/cm}^3} \quad (\text{H.9})$$

Which leads to:

$$\frac{\delta n_{bulk}}{|n_{bulk}|} = \frac{\delta \rho_{bulk}}{|\rho_{bulk}|} = \frac{1}{276.3} \quad (\text{H.10})$$

Relative density based on porosity was determined using:

$$R_{d,n} = \frac{n_{max} - n_{bulk}}{n_{max} - n_{min}} \quad (\text{H.11})$$

And the fractional uncertainty (using equation H.5):

$$\frac{\delta R_{d,n}}{|R_{d,n}|} = \frac{\delta n_{bulk}}{|n_{bulk}|} + 3 \cdot \frac{\delta n}{|n|} = \frac{1}{276.3} + 3 \cdot \frac{1}{401.0} = \frac{1}{90.1} \quad (\text{H.12})$$

Assuming that a relative density $R_{d,n}$ of 50% was determined, this should be presented as 0.5 ± 0.006 or $50\% \pm 0.6\%$

Local relative density determination

For local relative density determination the same equations can be used as for the bulk density, only other parameter values should be used:

$$\rho_{loc} = \frac{m}{V} = \frac{m}{0.25 \cdot \pi \cdot D_{loc}^2 \cdot h_{loc}} \quad (\text{H.13})$$

This results in an uncertainty of:

$$\frac{\delta \rho_{loc}}{|\rho_{loc}|} = \frac{\delta m}{|m|} + \frac{\delta V}{|V|} = \frac{\delta m}{|m|} + 2 \cdot \frac{\delta D_{loc}}{|D_{loc}|} + \frac{\delta h_{loc}}{|h_{loc}|} \quad (\text{H.14})$$

For the first local density measurement taken 413.91 g of sand was weighed with a measuring error of 0.04 g and a handling error of 0.5 g. This gives a fractional uncertainty for local density:

$$\frac{\delta \rho_{loc}}{|\rho_{loc}|} = \frac{0.04 + 0.5 \text{ g}}{413.91 \text{ g}} + 2 \cdot \frac{0.005 \text{ cm}}{|6.69 \text{ cm}|} + \frac{0.005 \text{ cm}}{|5.00 \text{ cm}|} = \frac{1}{263.2} \quad (\text{H.15})$$

Like with the bulk density the fractional uncertainty of the porosity is equal to that of the local density:

$$\frac{\delta n_{loc}}{|n_{loc}|} = \frac{\delta \rho_{loc}}{|\rho_{loc}|} = \frac{1}{263.2} \quad (\text{H.16})$$

And also similar to the uncertainty in bulk density the definition of the local relative density can be determined with:

$$\frac{\delta R_{d,n}}{|R_{d,n}|} = \frac{\delta n_{loc}}{|n_{loc}|} + 3 \cdot \frac{\delta n}{|n|} = \frac{1}{263.2} + 3 \cdot \frac{1}{401.0} = \frac{1}{88.6} \quad (\text{H.17})$$

This particular measurement gave a value of $R_{d,n} = 60.7\%$, which should be presented as $60.7\% \pm 0.7\%$ when considering uncertainty in the measurements.

For other measurements the magnitude of uncertainty is different since the fractional uncertainties are different. However, these differences are small and so the magnitude of uncertainty is assumed to be valid for comparable types of measurements.

H.2 Chauvenet's criterion

In a certain dataset some readings or values may deviate considerably from values believed to be normal. Using Chauvenet's criterion it can be determined which readings are 'allowed' to be discarded. The method assumes a data set to have a normal distribution. Therefore, if the data in the dataset is not normally distributed, Chauvenet's criterion might not be the correct way of identifying outliers in datasets. In this appendix the explanation of Taylor (1997) is used for explaining Chauvenet's criterion.

Chauvenet's criterion states that "if the expected number of measurements at least as deviant as the suspect measurement is less than one-half, then the suspect measurement should be rejected" (Taylor (1997)).

$$t_{sus} = \frac{|x_{sus} - \mu|}{\sigma} \quad (\text{H.18})$$

In which t_{sus} is the number of standard deviations by which x_{sus} differs from μ , x_{sus} the data point suspected to be an outlier, μ the mean of the dataset and σ the standard deviation of a data set. For a number of n measurements μ is defined as:

$$\mu = \frac{\sum_i^n x_i}{n} \quad i = 1, 2, \dots, n \quad (\text{H.19})$$

and σ as:

$$\sigma = \sqrt{\frac{\sum_i^n (x_i - \mu)^2}{n - 1}} \quad i = 1, 2, \dots, n \quad (\text{H.20})$$

The probability that x_{sus} can be considered an outlier is determined with the Gauss function:

$$P(\text{outside } t_{sus}\sigma) = 1 - P(\text{inside } t_{sus}\sigma) \quad (\text{H.21})$$

$$P(\text{inside } t_{sus}\sigma) = \frac{1}{\sqrt{2\pi}} \int_{-t_{sus}}^{t_{sus}} e^{-z^2/2} dz \quad (\text{H.22})$$

With:

$$z = \frac{x - \mu}{\sigma} \quad (\text{H.23})$$

In this equation x is a continuous variable of a measurement in the normal distribution. According to the criterion, if the expected number as deviant as x_{sus} is smaller than 0.5, the measurement should be rejected. For n measurements a single measurement should thus be rejected if:

$$n \cdot P(\text{outside } t_{sus}\sigma) < 0.5 \quad (\text{H.24})$$

Each measurement is tested using equations (H.18) to (H.24). Chauvenet determined acceptable values for t_{sus} for a certain number of readings. After applying the criterion on a dataset, new values for μ and σ can be found, but Chauvenet's criterion is not meant to be applied more than once on a dataset.

I Full page figures



Figure I.1: Overview of the cross-section of sample 2



Figure I.2: Detail of the clay layer of the cross-section of sample 2



Figure I.3: Overview of the cross-section of sample 5

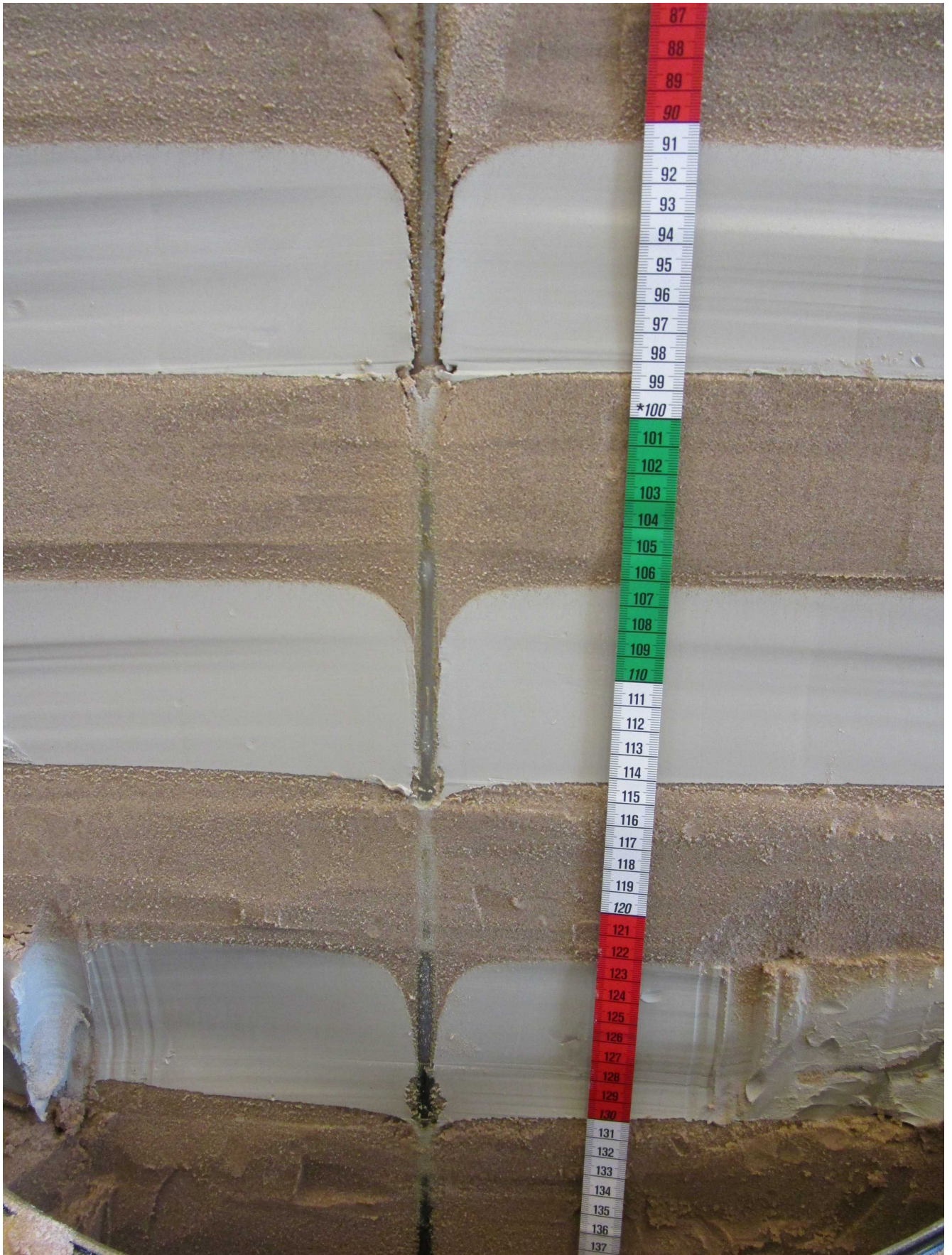


Figure I.4: Detail of the layered part of the cross-section of sample 5

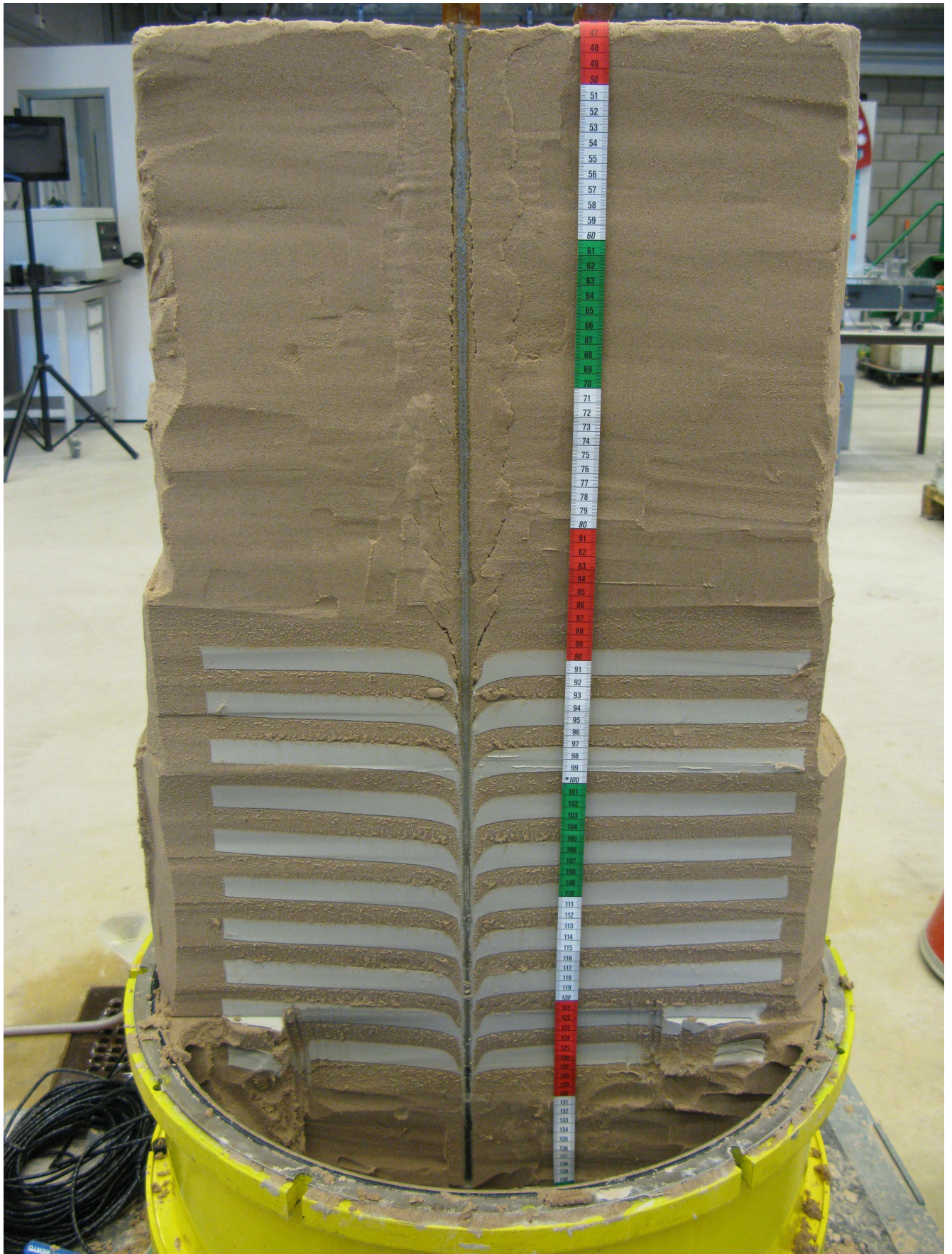


Figure I.5: Overview of the cross-section of sample 6

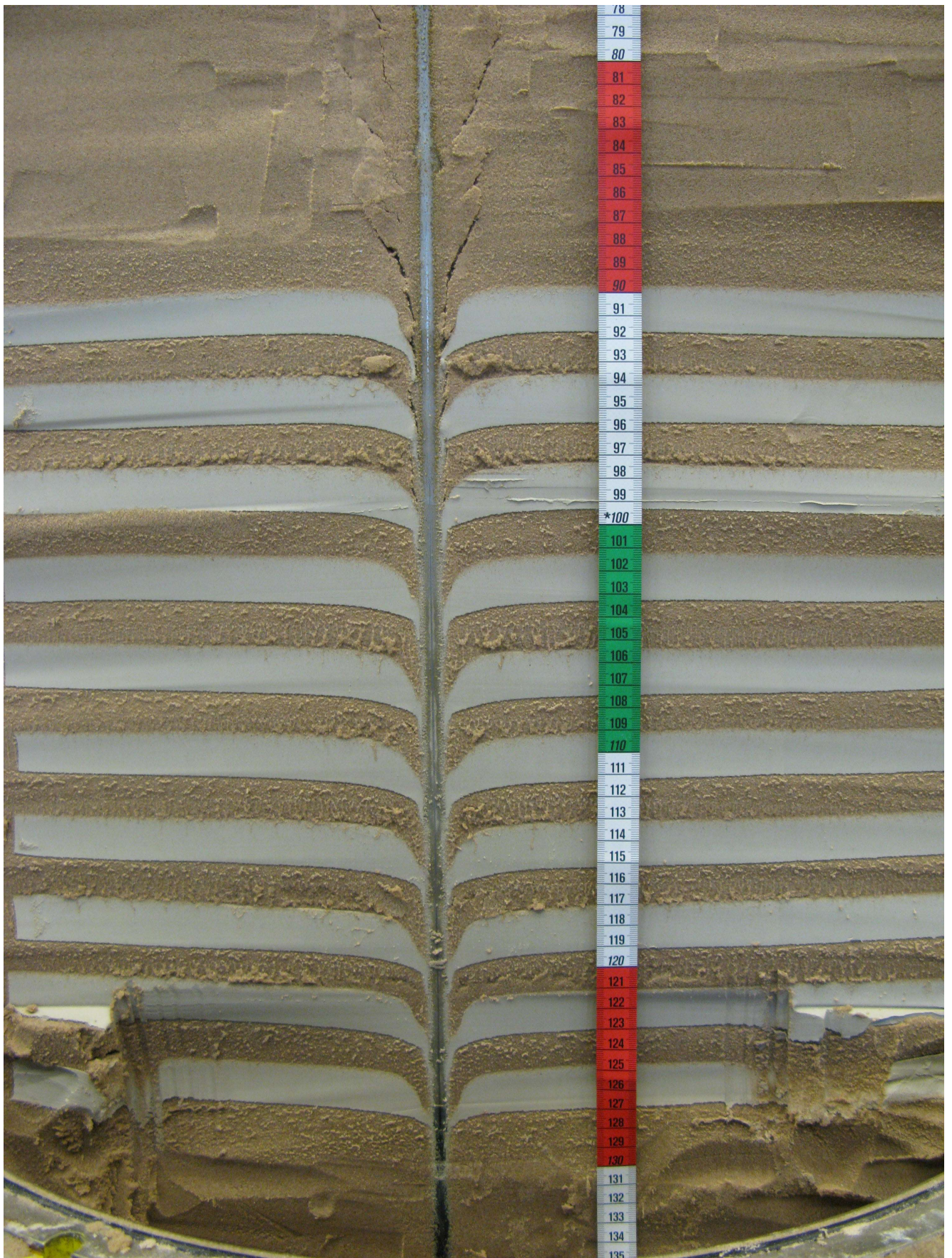


Figure I.6: Detail of the layered part of the cross-section of sample 6

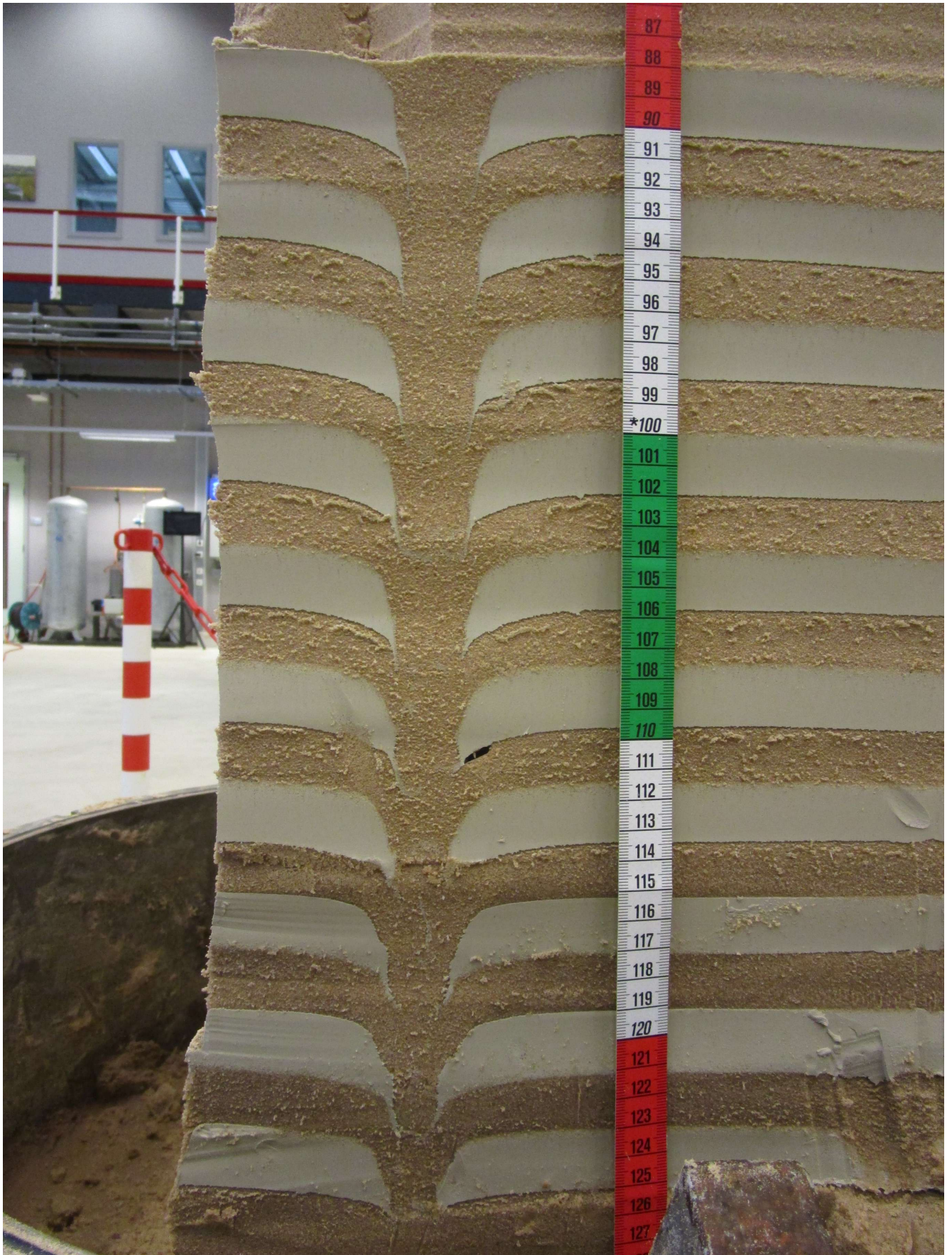


Figure I.7: Detail of the path of a retracted cone in the cross-section of sample 6

